Enabling Technologies for Co-Robotic Translational Ultrasound and Photoacoustic Imaging

by

Haichong Zhang

A dissertation submitted to The Johns Hopkins University in conformity with the requirements for the degree of Doctor of Philosophy.

Baltimore, Maryland

September, 2017

Abstract

Among many medical imaging modalities, medical ultrasound possesses its unique advantages of non-ionizing, real-time, and non-invasive properties. With its safeness, ease of use, and cost-effectiveness, ultrasound imaging has been used in a wide variety of diagnostic applications. Photoacoustic imaging is a hybrid imaging modality merging light and ultrasound, and reveals the tissue metabolism and molecular distribution with the utilization of endo- and exogenous contrast agents. With the emergence of photoacoustic imaging, ultrasound and photoacoustic imaging can comprehensively depict not only anatomical but also functional information of biological tissue.

To broaden the impact of translational ultrasound and photoacoustic imaging, this dissertation focuses on the development of enabling technologies and the exploration of associated applications. The goals of these technologies are;

(1) Enabling Technologies for Translational Photoacoustic Imaging. We investigated the potential of maximizing the access to translational photoacoustic imaging using a clinical ultrasound scanner and a low-cost light source, instead of widely used customized data acquisition system and expensive high power laser.

ABSTRACT

(2) Co-robotic Ultrasound and Photoacoustic Imaging. We introduced a co-robotic paradigm to make ultrasound/photoacoustic imaging more comprehensive and capable of imaging deeper with higher resolution and wider field-of-view.

(3) Advancements on Translational Photoacoustic Imaging. We explored the new use of translational photoacoustic imaging for molecular-based cancer detection and the sensing of neurotransmitter activity in the brain.

Together, these parts explore the feasibility of co-robotic translational ultrasound and photoacoustic imaging.

Advisor/Primary Reader:

Emad M. Boctor, Ph.D.

Secondary Readers

Russell H. Taylor, Ph.D.

Jin U. Kang, Ph.D.

Acknowledgments

This thesis is the culmination of the four years of PhD studies in the Medical Ultra-Sound Imaging and Intervention Collaboration (MUSiiC) lab at The Johns Hopkins University.

I would like to express my deepest graditude to my advisor Dr. Emad M. Boctor for being my mentor and a role model as an innovator and a team leader. I have received countless inspirations from his advice and support both academically and in my personal life.

I also would like to thank my thesis committee, Drs. Russell H. Taylor and Jin U. Kang. Dr. Russell H. Taylor has been a superb instructor for the courses "Computer Integrated Surgery", where I have been involved as a student, student mentor, and course assistant. He also has been directing and supervising the LSCR comminity where my research home is, and where I could grow up as a Ph.D. student. Dr. Jin U. Kang has been my generous mentor and supporter through collaborations under several projects.

Outside the commiteee, I was fortunate to be able to work with so many great

ACKNOWLEDGMENTS

mentors and collaborators including: Dr. Martin Pomper, Dr. Dean F. Wong, Dr. Arman Rahmim, Dr. Ying Chen, Dr. Nicholas J. Durr, Dr. Abhay Moghekar, Dr. Muyinatu Lediju-Bell, Dr. Gregg E. Trahey, and Dr. Leslie Loew. I especially acknowledge Dr. Gregory S. Chirikjian for being my advisor on the qualify project related to ultrasound calibration.

Further, my PhD work would not have been possible without support from my friends and colleagues in the MUSiiC lab, LCSR, and collegues at medical campus including: Dr. Peter Kazanzides, Dr. Iulian Iordachita, Dr. Ralph Etienne-Cummings, Dr. Noah J. Cowan, Dr. Yoshito Otake, Dr. Ken Taguchi, Dr. Xiaoyu Guo, Dr. Hyunjae Kang, Dr. M. Kendal Ackerman, Dr. Alexis Cheng, Younsu Kim, Dr. Qianli Ma, Dr. Jeeun Kang, Dr. Chloe Audigier, Dr. Nishikant Deshmukh, Dr. Fereshteh Aalamifar, Dr. Behnoosh Tavakoli, Dr. Lei Chen, Dr. Seth Billings, Dr. Cai Meng, Joshua Davis, Zerui Wang, Ezgi Ergun, Yuttana Itsarachaiyot, Singchun Lee, Long Qian, Li Chi, Xiang Xiang, Dr. Sungmin Kim, Dr. Nathan Cho, Taesoo Kim, Tutkun Sen, Rob Grupp, Dr. Nick Bottenus, Yixuan Wu, Angel Feng, Sipu Ruan, Keisuke Sakaguchi, Ryo Tsumura, Dr. Futoshi Yokota, Ryutah Kato, Hirofumi Kawaguchi, Ehsan Azimi, Joshua Liu, Mahsan Bakhtiari-Nejad, and Ala Lisok.

I would like to acknowledge ITO Foundation for finantially supporting two years of my PhD studies. Research financial supports were provided by Johns Hopkins University internal funds, NSF Grant RI-Medium No. IIS-1162095, NIH Grant No. R21CA202199, NIBIB-NIH Grant No. EB015638, NIGMS-/NIBIB- NIH Grant No.

ACKNOWLEDGMENTS

1R01EB021396, and NSF Grant No. IIS-1653322.

Dedication

This thesis is dedicated to my parents for their support throughout my life, Airi for being together with me during this journey, and Kyle for being my joy and motivation.

Contents

Abstract **ii**

Acknowledgments **iv**

List of Tables **xx**

List of Figures **xxi**

1 Introduction **1**

1.1 Ultrasound and Photoacoustic Imaging 1

1.2 Challenges and Thesis Objective 2

1.3 Thesis Statement and Outline 5

1.4 Summary of Contributions 9

1.4.1 Enabling Technologies for Translational Photoacoustic Imaging 9

1.4.2 Co-robotic Ultrasound and Photoacoustic Imaging 9

1.4.3 Advancements on Translational Photoacoustic Imaging 10

CONTENTS

I Enabling Technologies for Translational Photoacoustic Imaging 11

2 Photoacoustic Imaging Using Ultrasound Beamformed RF Data 12

2.1 Introduction . . . 13

2.2 Contributions . . . 15

2.3 Theory . . . 15

2.3.1 Ultrasound Beamforming . . . 15

2.3.2 Synthetic-Aperture Based Photoacoustic Re-Beamforming . . 16

2.3.3 Resolution and SNR . . . 19

2.3.4 Optimum Aperture Size . . . 22

2.4 Methods . . . 22

2.4.1 Simulation . . . 22

2.4.2 Experimental Setup . . . 23

2.5 Results . . . 24

2.5.1 Simulated Waveform and Images . . . 24

2.5.2 Resolution Evaluation . . . 26

2.5.3 SNR Evaluation . . . 28

2.5.4 PA re-beamforming for Dynamically Focused Beamformed Ultrasound RF Data . . . 30

2.5.5 Experiment Evaluation . . . 31

2.6 Discussion . . . 32

2.7 Conclusions 38

3 Photoacoustic Imaging Using Ultrasound B-mode Data 39

3.1 Introduction 40

3.2 Contributions 41

3.3 Methods 43

3.3.1 Retrieving Ultrasound Post-Beamformed RF Data from B-mode Data 43

3.3.2 Reconstructing PA image from Ultrasound Post-Beamformed RF Data 45

3.3.3 Simulation and Experimental Setup 46

3.4 Results 47

3.5 Discussion and Conclusions 50

4 Photoacoustic Imaging System Using LED Light Source and Clinical Ultrasound Scanner 52

4.1 Introduction 52

4.1.1 Contributions 55

4.2 Methods 55

4.2.1 Synthetic Aperture Based Re-Beamforming 55

4.2.2 Simulation Setup 56

4.2.3 Experimental Setup and LED Light Source 57

4.3 Results 58
4.3.1 Simulation Analysis 58
4.3.2 LED Light Source 60
4.3.3 *In Vivo* Evaluation 61
4.4 Discussion and Conclusions 63

II Co-Robotic Ultrasound and Photoacoustic Imaging 68

5 Cooperatively Controlled Robotic Ultrasound System 69

5.1 Introduction 70
5.2 Contributions and Acknowledgements 72
5.3 Materials and Methods 72
5.3.1 System Overview 72
5.3.2 Handheld Ultrasound Component 73
5.3.3 Admittance robot control 75
5.3.4 Velocity Gain Variable 77
5.4 Experimental setup 80
5.5 Results 83
5.5.1 Applied Force Reduction 83
5.5.2 Stability of Contact Forces 84
5.5.3 Stability of Ultrasound Images 86
5.6 Discussion and Conclusions 88

6 Synthetic Tracked Aperture Ultrasound (STRATUS) Imaging 92

6.1 Introduction . . . 93

6.2 Contributions . . . 96

6.3 Approach . . . 96

6.3.1 Synthetic Aperture Imaging . . . 96

6.3.2 Synthetic Tracked Aperture Ultrasound Imaging . . . 98

6.3.3 Implementation Strategies . . . 99

6.4 Materials and Methods . . . 103

6.4.1 Robot Motion Generation in Pure-translation Scenario . . . 103

6.4.2 Simulation . . . 104

6.4.3 Experiment Implementation . . . 105

6.4.4 Ultrasound Calibration Using Active Echo Phantom . . . 106

6.4.5 Image Quality Assessment Metrics . . . 108

6.5 Results . . . 110

6.5.1 Simulated Point Spread Function . . . 110

6.5.2 Experimental Phantom Validation . . . 113

6.6 Discussion . . . 116

6.6.1 Comparison of Experiment to Simulation . . . 116

6.6.2 Error Sources Affecting STRATUS Imaging . . . 119

6.6.3 Effect of Tracking Systems and Ultrasound Calibrations . . . 121

6.7 Conclusion . . . 122

7 Synthetic Tracked Aperture Ultrasound Imaging with Virtual Fixture Control and Motion Compensation 124

7.1 Introduction . . . 125

7.2 Contributions . . . 128

7.3 Methods . . . 128

7.3.1 Synthetic Tracked Aperture Ultrasound Imaging . . . 128

7.3.2 Curvilinear Array . . . 130

7.3.3 Co-Robotic Control with Virtual Fixtures . . . 130

7.3.3.1 Stay on Line . . . 133

7.3.3.2 Maintain A Direction . . . 134

7.3.3.3 Plane Related Constraints . . . 135

7.3.4 Cross-Correlation Based Dynamic Error Compensation . . . 135

7.3.5 Experimental Setup . . . 136

7.3.5.1 Virtual Fixture Evaluation . . . 136

7.3.5.2 *In Vivo* Experiment . . . 137

7.4 Results and Discussion . . . 138

7.4.1 STRATUS Images with Virtual Fixture . . . 138

7.4.2 Dynamic Error Compensation . . . 140

7.4.3 *In Vivo* Evaluation Results . . . 142

7.5 Conclusion . . . 147

8 Three-dimensional Synthetic Tracked Aperture Ultrasound Imaging 148

8.1 Introduction 149
8.2 Contributions 150
8.3 Methods 151
8.3.1 Synthetic Tracked Aperture Ultrasound Imaging in Elevation Direction 151
8.3.2 Three-Dimensional Visualization 153
8.3.3 Experimental Setup 155
8.4 Results 156
8.5 Discussion and Conclusions 159

9 Photoacoustic Synthetic Tracked Aperture Imaging and Application on Transrectal Ultrasound Probe 160

9.1 Introduction 161
9.2 Contributions 163
9.3 Methods 164
9.3.1 Photoacoustic Computed Tomography Reconstruction and Synthetic Aperture Focusing 164
9.3.2 Robotically Tracked photoacoustic Imaging 165
9.3.3 Robotically tracked Transrectal Photoacoustic Imaging 166
9.3.4 Simulation Setup 167
9.3.5 Experiment Setup 169
9.4 Results 170

9.4.1 Rotational Angle Effect on Photoacoustic Computed Tomography 170

9.4.2 Effect of Tracking Error on Photoacoustic Computed Tomography 173

9.4.3 Experiment Result of Photoacoustic Computed Tomography . 175

9.4.4 Experimental Result of Transrectal Photoacoustic Imaging . . 175

9.5 Discussion and Conclusions 176

10 Ultrasound Calibration Using A Phantom with Multiple Active Points 179

10.1 Introduction 180

10.2 Contributions 183

10.3 Theory 184

10.3.1 Solving Ultrasound Calibration Problem 184

10.3.2 Ultrasound Calibration Using Multi Active-Point Phantom . . 186

10.4 Methods 191

10.4.1 Calibration Workflow 191

10.4.2 Simulation 193

10.4.3 Experimental Implementation 193

10.4.4 Evaluation Methods 194

10.5 Results 196

10.5.1 Geometrical Simulation 196

10.5.2 Experimental Results 200

10.6 Discussion and Conclusions 201

11 Single Element Synthetic Tracked Aperture Ultrasound Imaging 204

11.1 Introduction 205

11.2 Contributions 208

11.3 Approach 209

11.3.1 Single Element Ultrasound Sensing and Imaging 209

11.3.2 Back Projection Based Synthetic Aperture Reconstruction . . 212

11.4 Methods 215

11.4.1 Simulation 215

11.4.2 Experimental Implementation 215

11.4.2.1 Needle with PZT Element Fabrication 215

11.4.2.2 Ultrasound Tracking 216

11.4.2.3 Data Collection 217

11.5 Results 218

11.5.1 Simulation Results 218

11.5.2 Needle Sensing Evaluation 220

11.5.3 Single Element Ultrasound Imaging with Controlled Scan . . . 221

11.5.4 Single Element Ultrasound Imaging with Free-hand Scan . . . 223

11.6 Discussion and Conclusions 224

III Advancements on Translational Photoacoustic

Imaging **228**

12 *In Vivo* Photoacoustic Prostate Cancer Imaging Using PSMA-Targeting Contrast Agents **229**

12.1 Introduction 230

12.2 Contributions 232

12.3 Methods 233

12.3.1 Synthesis of PA Agents 233

12.3.2 Animal Preparation 233

12.3.3 Ultrasound Imaging 234

12.3.4 Photoacoustic Imaging 235

12.3.5 Material Decomposition 236

12.3.6 Fluorescence imaging 237

12.4 Results and discussion 237

12.5 Conclusions 241

13 Photoacoustic Voltage-Sensitive Dye Recording **242**

13.1 Introduction 243

13.2 Contributions 245

13.3 Theory and Principle 246

13.3.1 Design of a PA-VSD Based on Photophysics and Photochemistry 246

13.3.2 Thermal Confinement and Fluorescence Emission 249

13.4 Materials and Methods 251
13.4.1 Synthesis of PAVSD800-2 251
13.4.2 Lipid vesicle preparation 253
13.4.3 Experimental Setup for Photoacoustic Voltage-Sensitive Dyes Characterization 254
13.4.3.1 Spectroscopic/fluorometric voltage sensitive dyes characterization 254
13.4.3.2 Phantom experiment setup for photoacoustic voltage-sensitive dyes sensing 254
13.5 Results 256
13.5.1 Spectrophoto/fluorometric Photoacoustic Voltage-Sensitive Dyes Characterization 256
13.5.2 Photoacoustic Characterization of the Photoacoustic Voltage-Sensitive Dyes 259
13.6 Discussion 263
13.7 Conclusions 267

14 Conclusions **268**

A Technical Terms and Acronyms **270**

B Supplemental information for Chapter 6 **272**

B.1 Tracking Systems and Ultrasound Calibration 272

B.2 Error Terms in Rigid-body Transformation 274

B.3 Error Propagation Analysis of BXp formulation 276

C Supplemental information for Chapter 10 **281**

C.1 Recovering A using multiple active-point phantom involves 1 DOF deficiency 281

C.2 Alternative Solution of Recovering A using Multiple Active-Point Phantom 282

Bibliography **284**

Vita **309**

List of Tables

4.1 Specifications of the near-infrared, pulsed LED illumination system. . 59
4.2 FWHM of the simulated point targets for corresponding beamforming methods. 61

5.1 The calibrated model for the load cell. Note F stands for contact force, and v is voltage reading. 81
5.2 T-test results confirm the force stability improvement of the system. The p-values for the hypothesis that SD of the contact force is the same for any pair of cases occurs by accident are shown. Note H_0 : mean of σ_i = mean of σ_j, and H_A : mean of $\sigma_i \neq$ mean of σ_j. 86
5.3 T-test results confirm the US image stability improvement through the system. The p-values for the hypothesis that the cross-correlation comparing pair of cases occurred by accident are shown. Note H_0 : $\beta_i = \beta_j$, and $H_A : \beta_i \neq \beta_j$. 88

7.1 Quantitative analysis on ultrasound images. 142

10.1 General characteristics of ultrasound calibration phantoms. 181
10.2 1D probe calibration accuracy using multi active point phantom. . . . 199
10.3 1D probe calibration precision using multi active point phantom. . . . 199

List of Figures

2.1 (a) Example of ultrasound beamforming for photoacoustic signals. When five point targets are placed, the points are extended with orbits in the reconstructed image due to incorrect delays. (b) Diagram of proposed synthetic aperture beamforming. 17
2.2 Illustration of channel data and the SPARE beamforming process. (a) In channel data, the wave front of receive RF signals expands corresponding to the depth (green line). The red lines indicate fixed focus delay function. (b) When fixed receive focusing is applied, the delay function is only optimized to the focus depth (red line). (c) As a result of fixed receive focusing, the focal point can be regarded as a virtual point source, so that inverse and forward delay and sum can be applied. (d) Similarly, dynamic focusing could be regarded as a specific case of that in which the virtual element depth z_F is the half distance of re-beamforming focal depth z_R. 18
2.3 The beamforming geometry when line n is beamformed. (a) The effective aperture size of the first beamforming is defined as D_{1st}^{a} and D_{1st}^{b} when $z_R = a$ and $z_R = b$ is chosen, respectively. (b) The effective aperture size of the second beamforming (SPARE) is defined as D_{2nd}^{a} and D_{2nd}^{b} when $z_R = a$ and $z_R = b$ is chosen. 20
2.4 (a) Experimental setup diagram. (b) Picture of the setup. 24
2.5 Simulated photoacoustic waveforms, PA images from channel data, and PA images using SPARE beamformer are shown. Fixed focusing at 20 mm depth was used for SPARE beamforming. (a) 1 mm and (b) 0.5 mm diameter objects with N-shape impulse responses were simulated. For a point source, (c) 2 MHz, (d) 5 MHz center frequency waves were simulated assuming that a band-limited ultrasound transducer was used to receive these signals. 25

2.6 The FWHM of the proposed re-beamforming for the designated focusing depth, and varying the aperture size in the (a) first beamforming and (b) the second beamforming. (c) The ground truth FWHM results using a delay-and-sum algorithm with dynamic focusing. (d) The focusing depth and aperture size parameters in Figs. 2.6(a-c) were compressed into the metric of fnumber. The theoretical ground truth values were computed by fitting the ground truth data from Fig. 2.6(c) into Eq. 2.5. 27
2.7 (a) The measured SNR of proposed beamformer varying the aperture size in the first beamforming (left) and the second beamforming. One beamformer aperture size was fixed to be maximum when the other aperture size was varied. (b) The ground truth SNR results using a delay-and-sum algorithm with dynamic focusing. (c) The focusing depth and aperture size parameters in Figs. 2.7(a-b) were compressed into the metric of f-number. To compensate the SNR variance for the same f-number but different target depth, the SNR of f-number 1.04 was normalized to be 0 dB. The theoretical ground truth values were computed by fitting the ground truth data from Fig. 2.7(b) into Eq. 2.9. 29
2.8 (a) The reconstructed PA image from channel data as a ground truth. (b-c) The reconstructed images through ultrasound and SPARE beamforming. Dynamic focusing is applied as ultrasound beamforming. Grating lobe artifacts are visible in the near field of ultrasound beamforming result (b) when a large aperture is used in 1st ultrasound beamforming, but it is drastically reduced when a small aperture size is used (c). 31
2.9 Experimental SPARE beamforming results. (a) Reconstructed photoacoustic images of conventional dynamic focusing for channel data, 9 mm, 12 mm, and 31 mm fixed focal depths. (b) Lateral profile of the point target. (c) Measured FWHM and SNR for various fixed focal depths. 33
2.10 Experimental SPARE beamforming results with dynamic focusing. Original channel data, intermediate ultrasound post-beamformed result, and final SPARE post-beamformed result are shown from left to right, respectively. The dynamic range of 20 dB was used for display. 34

3.1 Diagrams of ultrasound (US) and photoacoustic (PA) image formation. (a) Conventional image formation in US and PA imaging. (b) Proposed PA image formation using B-mode image from clinical ultrasound systems. 42
3.2 An example of PA re-beamforming from US post-beamformed RF data with dynamic receive focusing. 46

3.3 Experiment setup. A PZT element was used as a pseudo PA point source. 47
3.4 Simulation results. The input data of beamforming were shown in (a-c) and output was presented in (d-f). The profile of a point located at 30 mm depth for three different input data was shown in (g). 48
3.5 (a) US image formation in clinical ultrasound system. (b) Proposed PA image reconstruction processes. (c) PA image reconstruction from channel data. 49

4.1 Conventional PA imaging system (a) and proposed PA imaging system using clinical US scanners (b). Channel data is necessary for PA beamforming because US beamformed PA data is defocused with the incorrect delay function. The proposed two approaches could overcome the problem. 54
4.2 Illustration of synthetic aperture based re-beamforming processes. . 56
4.3 Experimental setup. (a) LED light source. (b) *In vivo* experiment configuration. 58
4.4 Simulation results. (a) Channel data. (b) US post-beamformed RF data. (c) Reconstructed PA image from channel data with an aperture size of 9.6 mm. (d) Reconstructed PA image through inverse beamforming. (e) Reconstructed PA image through SA re-beamforming. . 60
4.5 Experiment results with LED light source imaging line phantom. (a) Comparison of control using channel datafrom and SPARE results using ultrasound post-beamformed data. (b) SNR analysis of both control and SPARE results. (c) Resolution analysis of SPARE results. Resolution improvement was hindered at FWHM of 2 mm due to the aperture size. 62
4.6 *in vivo* PA imaging of piglet head using LED light source. Experimental configuration, ultrasound and PA images of piglet head are shown. PA images were reconstructed using channel data from DAQ device and beamformed RF data with the SPARE algorithm. 63
4.7 *in vivo* PA imaging of human fingers using LED light source. Experimental configuration, ultrasound and PA images of human fingers are shown. PA images were reconstructed using channel data from DAQ device and beamformed RF data with the SPARE algorithm. 64
4.8 Numerical estimation of frame rate using a LED system. Frame rate (a,d) and estimated energy (b,e) by varying the number of averaging, and the relationship between frame rate and estimated energy (c,f) are shown using a DAQ device (a-c), and using a clinical ultrasound system (d-f) for data collection. 66

5.1 The co-robotic ultrasound system with dual force sensing. The US probe is actuated by a 6-axis robotic arm through the users force input on the handheld device. 73
5.2 The design of the handheld US device. (a) The exploded CAD model of the handheld US device. (b) The probe holder **4-9** can be smoothly detached from the robotic arm to perform freehand scanning, while the contact force information remains accessible. 74
5.3 The free body diagram of the system under different scenarios. (a) The probe stays in free space. (b) The user is moving the probe in free space. (c) The user is scanning the object using the system. (d) The user released the probe during scanning. 76
5.4 The diagram summarizing modified admittance robot control and velocity gain calculation. 79
5.5 The estimated linear regression model for 1 DOF load cell. (a) Comparison of the measured data and the estimated regression model. (b) The residual error plot of the estimated model. 81
5.6 The scanning position is roughly the same in the four cases. (a) The position and the orientation of the US probe relative to the phantom. (b) An example of the scanned US image. 82
5.7 The comparison of the force applied to the tissue and from the operators for four cases. Co-robotic systems (#3 and #4) shows a substantial reduction in applied force compared to freehand scanning (#1 and #2). 84
5.8 The contact force stability with 20 N contact-force application over 20 seconds of scanning. The standard deviation of the contact force in four distinct scenarios is shown. 85
5.9 The US image stability with 20 N contact-force application over 20 seconds of scanning. The image cross-correlation relative to the initial image in four distinct scenarios is shown. 87

6.1 Synthetic tracked aperture ultrasound (STRATUS) imaging compared to conventional synthetic aperture ultrasound imaging. (a) Synthetic aperture ultrasound imaging with a single pose, and (b) STRATUS imaging with multiple poses. 95
6.2 The coordinate systems involved in synthetic tracked aperture ultrasound (STRATUS) imaging. 98
6.3 Scanning strategies: (a) freehand scanning, and (b) robotic scanning. (c) Diagrams visualizing STRATUS image acquisition and formation under different scanning approaches. 102
6.4 Experimental setup for synthetic tracked aperture ultrasound (STRATUS) imaging. (a) Robot control and ultrasound data acquisition system. (b) Wire phantom design. (c) General ultrasound phantom design.106

6.5 (a) Simulated point source by utilizing single pose, three poses, and five poses. (b) Simulated point source from five poses with image tracking error. Rotational error in X was 0.7 degree, and rotational and translational error in B was 0.1 degree and 0.1 mm, respectively. 111
6.6 Simulation results of image quality evaluation. (a) Quality of images of proposed method with different level of uncertainty in X and B. (b) As a normalized result, the pixel count for single pose was taken as the maximum value to show that the area the image quality did not improve. 114
6.7 A line phantom was imaged using two different calibrated transformation. When Xs was close to the true transformation between the robot end effector to the image, the effect of aperture extension was clearly observable (a, trial 1). However, if inappropriate X was chosen, the merged image was blurred, and that can be compensated by shifting each pose based on the amount of error in rotation (b, trial 2). 115
6.8 General ultrasound phantom was imaged. (a) The result from a single pose and three poses of the entire structure of the phantom is shown. (b) The anechoic region is magnified. 117
6.9 Evaluation of experimental results based on simulation. (a) Analysis of precision in B in UR5. (b) Analysis of a possible range of rotational error in X, (c) the possible image quality improvement in the best case. 119
6.10 The image quality corresponding to precision in B and segmentation error. The bold line represents the line of image quality for a single pose case. 122

7.1 The system diagram and the workflow of co-robotic STRATUS imaging system. 127
7.2 Co-robotic STRATUS system diagram. 132
7.3 Robotic tracking under virtual fixture control compared with automatic scanning. (a) The raw robotic tracking information with and without virtual fixture control, and (b) The robotic tracking information normalizing slope and intersect to cut the effect of velocity difference. 139
7.4 (a) Single pose B-mode ultrasound image. (b-c) STRATUS images synthesized the range of 10 mm (b) and 60 mm (c) motion data. The yellow solid circle region was used for FWHM and SNR measurement, and the dot circle region was used for contrast measurement. 141
7.5 STRATUS imaging results with and without dynamic error compensation, compared to conventional B-mode image. Scale bar represents 10 mm. 143

7.6 The reconstructed image of the human forearm under the water tank. (a) Single pose result represents conventional ultrasound image, (b) the STRATUS imaging result using 10 poses data corresponding to 19.5 mm motion, and (c) the STRATUS imaging result using 20 poses data corresponding to 36 mm motion. (d) Illustration of the scanning path. (e) Contrast comparison between single pose case and multiple poses case are shown. The solid line circle and the dot line circle in the image was regarded as the target region and the background region, respectively. 144
7.7 The reconstructed image of the human forearm with the probe touched. (a) Single pose result represents conventional ultrasound image, (b) the STRATUS imaging result using 10 poses data corresponding to 19.5 mm motion, and (c) the STRATUS imaging result using 20 poses data corresponding to 36 mm motion. (d) Illustration of the scanning path. (e) Contrast comparison between single pose case and multiple poses case are shown. The solid line circle and the dot line circle in the image was regarded as the target region and the background region, respectively. 146

8.1 The coordinate systems involved in STRATUS imaging system. The transformations associated with pose i and j are shown. 152
8.2 The illustration of synthetic aperture focusing on elevational axis. Inverse and forward delay-and-sum algorithm was applied from the single focal point regarded as virtual element. 153
8.3 The methodology of visualizing 3D ultrasound volume. (a) Transforming 3D volume with a desired rotation. (b) Projecting the 3D volume into 2D x-y plane with respect to the world frame. 155
8.4 The experiment setup. A pure translational motion in the elevation direction is assigned. The ultrasound data at each tracking timing has been recorded through a clinical ultrasound machine. 157
8.5 The tracked motion from the robotic arm on ultrasound image coordinate for three axes. 157
8.6 Elevational plan (a) and (b) 3D visualization results in conventional B-mode (left), and STRATUS imaging (right), comparing with and without synthetic aperture focusing (SAF). 158

9.1 Three ways to scan in circular geometry. (a) Placing transducers around the contrast agent, (b) rotating the target, and (c) moving ultrasound transducer around the target using a robot arm. 163

9.2 Concept of 3D PA image utilizing robotically tracked transrectal ultrasound probe. (a) Picture of setup. (b) Virtual element could be formed for each elevation line scan, and a collection of rotation scan earns a virtual probe surface. Forward and inverse dynamic receive focusing (DRF) is applied based on virtual elements location. (c) Conventional single slice elevational beam width. The target is defocused if it is away from the focal point. (d) New elevational beam with synthetic aperture focusing. 166
9.3 Concept of 3D PA image utilizing robotically tracked transrectal ultrasound probe. (a) Picture of setup. (b) Virtual element could be formed for each elevation line scan, and a collection of rotation scan earns a virtual probe surface. Forward and inverse dynamic receive focusing (DRF) is applied based on virtual elements location. (c) Conventional single slice elevational beam width. The target is defocused if it is away from the focal point. (d) New elevational beam with synthetic aperture focusing. 168
9.4 Experimental setup. 170
9.5 Simulation results of (a) single pose and (b) two poses with 60 degree rotation. The center region is zoomed in the bottom right image. . . 172
9.6 Zoomed sphere target around 50 mm depth with different rotation angles. 172
9.7 Full with at half maximum of the center sphere target. 172
9.8 The effect of error in lateral and axial direction. The measured FWHM is shown in the right bottom corner. 174
9.9 The experimental result. (a) Reconstructed image of single pose and three poses with consecutive 10 degree rotation angle, and (b) the profile of the center pose and three poses combined result. 176
9.10 Experiment results. (a) Both lateral and elevation plane were cut from the PA point location. The elevation plane after scan conversion is shown. (b) PA images before and after elevation synthetic aperture focusing. (c) PA images with -6dB background noise. 177

10.1 Illustration of multiple active-point phantom concept. (a) The conventional single point target phantom, and BXp framework. (b) The proposed multiple active-point phantom, and associated $AX = XB$ framework. 186
10.2 Diagram showing ultrasound calibration procedures using multiple active-point phantom. 191
10.3 Experimental setup. (a) Active point phantom, (b) Transrectal probe mounted on the robotic arm. 194
10.4 The experimental design and the scanning field in the transrectal probe. 195
10.5 Calibration error of BXp in (a) accuracy and (b) precision for corresponding segmentation and elevational error. 196

10.6 Calibration error of $AXXB$ for different size of point phantom. . . . 197
10.7 The effect of out-of-plane error on the calibration error. 198
10.8 Before (a) and after (b) recovering the unknown rotation. 201

11.1 The concept of single element ultrasound sensing and imaging system for dynamic lumbar puncture guidance. (a) The layers of tissue from skin to spinal cord. Conventional LPs require advancing a needle through a small target window that is difficult to identify in obese patients. (b) the illustration of the needle-based single element ultrasound imager. The blue piece of the attachment will guide the location of the ultrasound element. (c) The workflow diagram of the blind needle insertion, compared with the proposed procedure with dynamic ultrasound guidance. The proposed workflow reduces re-attempts that could be necessary in conventional workflow without guidance. Note that the needle sweep occurs only up to subsurface adipose tissue. . . 210
11.2 The back projection reconstruction process corresponding poses. Left: A position -6 degree from the center pose was back-projected. Middle: Position in the range from -6 degree to the 0 degree position were back-projected and summed. Right: Positions in the range from -6 degree to +6 degree position were back-projected and summed. The yellow line represents the back projection geometrical loci of the point at 30 mm depth point target. 214
11.3 Experimental setup. (a) The pictures of the needle transducer mounted on the holster and the metal wire phantom design. (b) Diagram of hardware integration for the single element ultrasound system. 217
11.4 Simulated point targets and corresponding received RF data of a point at 30 mm depth. (a) ground truth image with no error. (b) The result with error in the axial axis, and (c) the result with error in the rotation axis. 219
11.5 The full-width at the half maximum (FWHM) of the point targets for different error sources. (a) The resolution in the presence of error in axial direction for each receive line. (b) The resolution in the presence of error in rotational angle tracking. 220
11.6 The evaluation results of the needle (a) and the rotation encoder (b). (a) The distance from the needle reading was compared to the designated motion distance, and (b) the angle measurement for the encoder was compared to the actual angle. The correlation function for both the depth sensing and rotation encoder sensing was higher than 99.99 and 99.94, respectively. 222

11.7 The imaging result of the metal wire phantom. (a) The B-mode image of pre- and post-beamforming. The angle axis profiles of two metal wire targets are shown in (b) and (c), corresponding to wire 1 and 2, respectively. For each profile, the results before and after applying synthetic aperture reconstruction are compared. 223
11.8 (a) The spine phantom picture and the scanned plane. (b) The ultrasound image of the spine phantom. The contrast from the center region indicates that the needle cannot go through without changing the insertion orientation. 224
11.9 The freehand scanning result of single element ultrasound imaging system. (a) The measured angle for 500 needle positions. (b) The metal wire phantom design, and (c) the ultrasound image from the data of 500 positions corresponding to 61 degrees sweeping. 225

12.1 Proposed image based prostate cancer screening. 231
12.2 Structure of PSMA targeted PA agent. 233
12.3 (A) Xenograft tumor preparation. The xenograft tumors (PIP and FLU) were inclubaed on the back of mice. (B) Photoacoustic (PA) imaging setup. Laser was illuminated through bar-type fiber bundles, and PA signals were collected by a linear array transducer. 235
12.4 PA spectroscopic characteristics. (a) The PA spectrum of IRDye800CW-Ulea. (b) The PA intensity versus the dye concentration. 238
12.5 PA and ultrasound imaging of PSMA negative (FLU) and positive (PIP) tumors. (a) Image comparison of the tumor before injection and after 2 hours and 24 hours injection. (b) Quantified the PA intensity of FLU and PIP tumors. (c) Quantified the fluorescence (FL) intensity of FLU and PIP tumors. 240
12.6 (A) PA intensity comparing before injection and after injection 24 hours and 13 days. * stands for p-value lower than 0.01. (B) Fluorescence intensity comparison after injection 24 hours and 13 days. (C) Comparison of PA and fluorescence, and its correlation. 241

13.1 The principle of the fluorescence quenching effect on the developed VSD (PAVSD800-2) according to a varying membrane potential: typically -70mV and 0mV in the polarized / depolarized states of neurons, respectively. 248
13.2 PAVSD800-2 synthetic scheme. Conditions: (a) CH_3CN, 130°C, 14 h, 64; (b) Ac_2O, 130°C, 1 h; and (c) 11 Ac_2O/pyridine, 100°C, 40 251
13.3 Phantom experiment setup for PA characterization of PAVSD800-2. Near-infrared light excited the sample in the tubing (green) through the optical fiber bundle, and the generated PA signals were captured by a clinical linear array transducer (10-MHz center frequency). . . . 255

13.4 The spectrophotometric characteristics of the (a and b) PAVSD800-2 and (c) the di-$SC_2(5)$ at the simulated resting/action states using valinomycin (Val) and gramicidin (Gra). (a) Absorbance spectrum of the dye PAVSD800-2 for the concentration of 6 μM. (b) Absorbance spectra at the wavelength of 800 nm for different dye concentrations. (c) Absorbance spectrum of the dye di-$SC_2(5)$ for the concentration of 6 μM. 257
13.5 The spectrofluorometric characteristics of the PAVSD800-2 (a-b), and the di-$SC_2(5)$ (c). (a) The emission spectrum of the dye PAVSD800-2 at 6 μM concentration. (d) The fluorescence emission at 820 nm for different concentrations. (c) Fluorescence emission spectrum of the dye, di-$SC_2(5)$ at 6 μM concentration. 258
13.6 The fractional change of absorbance at 800 nm and fluorescence signal at 825 nm between the simulated resting to action states by adding valinomycin. 259
13.7 (a) PA spectra of the PA-VSD for different concentrations at the pre-stimulus (black) and stimulated polarized (red) and depolarized (green) states using valinomycin (Val) and gramicidin (Gra). (b) Voltage-dependent PA intensity at 800 nm for different concentrations. 260
13.8 The PA images for three conditions: the depolarized state from the PAVSD800-2 only, the valinomycin-induced polarized state, and the gramicidin-reinduced depolarized state. 261
13.9 Stimulated resting and action state contrast change relative to the pre-stimulus state intensity. (a) Image produced by subtraction of the gramicidin data from the initial PA dye image is considered a negative control. (b) The difference between the initial PA dye image and the valinomycin-induced polarized state. Magnitude represents the fractional change of the intensity relative to the pre-stimulus state intensity. 262
13.10 The theoretical PA signal change based on the absorbance change and fluorescence change from the experimental data. 265

B.1 The relationship between rotational and translational components to the overall precision error. 276
B.2 Result of error propagation analysis based on BXp formulation. . . . 280

Chapter 1

Introduction

1.1 Ultrasound and Photoacoustic Imaging

Ultrasound imaging, also known as ultrasonography, is an imaging technique that visualizes internal body structures utilizing the physical reflection of high frequency sound waves. Among other medical imaging modalities such as X-ray computed tomography (CT) and magnetic resonance imaging (MRI), medical ultrasound possesses its unique advantages of non-ionizing, real-time, and non-invasive properties. With its safeness, ease of use, and cost-effectiveness, ultrasound imaging has been used in a wide variety of diagnostic applications including abdominal, cardiac, breast and urological examinations as well as in pediatric to monitor fetus growth.

As an emerging advanced ultrasound imaging method, photoacoustic (PA) imaging, is a hybrid imaging modality merging light and ultrasound. Non-invasive molecular light absorbance dependent acoustic signal occurs at depths of up to several centimeters in biological tissue, with a micro to millimeter spatial resolution that is limited by the acoustic bandwidth and focusing. The mechanism behind PA imaging is that upon excitation by a short-pulsed laser, thermal relaxation of the absorber induces local thermal elastic expansion. Using near-infrared laser excitation and ultrasound detection enhances the light-penetration and resulting imaging depth by minimizing the absorptive and scattering attenuation during the light propagation through the biological tissue. PA imaging has the potential of revealing the tissue metabolism and molecular distribution with the utilization of endo- and exogenous contrast agents. Ultrasound and PA imaging comprehensively cover both anatomical and functional information of biological tissue.

This dissertation investigates the challenges on clinical translation of ultrasound and PA imaging, and explore enabling technologies to overcome them. The potential future applications of PA imaging are also introduced.

1.2 Challenges and Thesis Objective

Although ultrasound imaging has been widely used in clinic, we are aware that it has several limitations that hinder its effectiveness in challenging environments such

as obese patients. PA imaging has several obstacles before it can be smoothly applied in clinic including its hardware cost. This dissertation particularly focuses on the following challenges:

- **Hardware requirements on photoacoustic imaging**

  PA imaging has been a promising modality to visualize optical absorption based functional information for pre-clinical and clinical applications. However, there are several factors that prevent PA imaging from being more widely used in clinical research and applications. The first limitation is the light source. Most of the laser systems used for PA imaging have high power and with low pulse repetition frequency (PRF). These laser systems are expensive, bulky, and not portable. This prevents PA system from being integrated to the existing clinical ultrasound scanners. The second limitation is the necessity of using channel data, which has not been well studied. PA reconstruction requires a delay function calculated based on the time-of-flight (TOF) from the PA source to the receiving probe element, while ultrasound beamforming considers the round trip initiated from the transmitting and receiving probe element. Thus, the reconstructed PA image with ultrasound beamformer would be defocused due to the incorrect delay function. Real-time channel data acquisition systems are only accessible from a limited number of research platforms. Most of them are not FDA approved, which hinders the development of PA imaging in the clinical setting.

- **User dependency**

  Ultrasound and PA imaging are considered a user dependent modality compared to other major imaging tools. Due to the requirement of acoustic coupling, ultrasound systems require the probe to be touched subject during a scan. The image quality highly depends on the probe position, orientation, and force applied. These parameters are barely reproducible throughout a medical treatment and between different sonographers. In addition, the ultrasound scanning process sometimes requires applying large forces over extended periods of time, often in an awkward posture to maintain the desired orientation. This physical requirement over a sonographer's career often leads to musculoskeletal pain and strain.

- **Imaging field and resolution**

  The image resolution of ultrasonography is affected by several factors including the center frequency of the transmission wave and the F-number, which represents the ratio of the focusing depth to the aperture size. F-number increases corresponding to the rise in the focusing depth, and it is challenging to acquire acceptable image quality in deep tissue, and accordingly a large aperture size is desired to decrease the F-number. In the clinic, diagnosing obese patients with the current ultrasound imaging system is challenging, as the target region may be too deep due to a thick fat layer, and the maximum available aperture size

is determined by the physical size of the ultrasound probe.

- **Translational photoacoustic imaging**

  Toward translational PA imaging research, many internal and external contrast agents have been previously evaluated for use with PA imaging to selectively visualize tumor tissue or metabolic properties. Molecular PA imaging utilizes the characteristics of highlighting specific material contrast and its applications on breast and prostate cancer has to be investigated. Clinical and scientific application of PA imaging has not been fully explored especially in the field of cancer imaging and neuro/brain imaging.

1.3 Thesis Statement and Outline

To broaden the impact of translational ultrasound/PA imaging, this dissertation explores the potentials on cancer detection and brain imaging, without compromizing the advantage of existing clinical ultrasound. Utilization of clinical ultrasound system is a core concept that enables low cost, safe, and high accessibility, in that the FDA-approved ultrasound scanner has been widely used. However, using existing ultrasound system will face the present challenges as listed in the previous section including applicability on PA imaging, user-dependency, and image quality.

I hypothesize that clinical ultrasound system may provide a substantial impact on translational PA imaging; Existing limitations on ultrasound may be overcome

through enabling technologies. The goals of these technologies are; (1) to broaden the accessibility to PA imaging and demonstrate the translational applicability, (2) to make both ultrasound and PA imaging be more comprehensive and capable of imaging deep by incorporating co-robotic paradigm, and (3) to explore new usage of translational PA imaging for cancer detection and brain imaging.

Along the goals given, I introduce three research topics in this thesis. **Part I** presents the enabling technique to maximize the access to PA imaging by using a clinical ultrasound scanner and a low-cost light source. *Chapter 2* devises a new PA reconstruction approach that uses ultrasound post-beamformed radio frequency (RF) data rather than raw channel data, because this type of data is readily available in both clinical and research ultrasound systems. In our proposed Synthetic-aperture based PA re-beamforming (SPARE) approach, post-beamformed RF data from a clinical ultrasound scanner are considered as input data for an adaptive synthetic aperture beamforming algorithm. *Chapter 3* extends the SPARE method to B-mode image data that is even more accessible than beamformed RF data. *Chapter 4* builds an *in vivo* PA imaging system using a LED light source and a clinical ultrasound scanner with ultrasound beamformed data.

Part II is the integration of a robot with both ultrasound and PA imaging systems with human robot cooperative control capability. *Chapter 5* introduces a co-robotic ultrasound system that assists the sonographer to reduce the force applied during the scan. Under this system, Sonographer can still have the control of the ultra-

sound probe, while the scan requires less force and has more stablility with robot assistance. *Chapter 6* discusses the integration between tracking technology and ultrasound beamforming for achieving high resolution deep-tissue imaging. We propose a novel method to extend the available aperture size for synthetic aperture, called synthetic tracked aperture ultrasound (STRATUS) imaging, by sweeping an ultrasound transducer while tracking its orientation and location. *Chapter 7* presents a use of STRATUS imaging through a mechanical tracking configuration using a 6 degree-of-freedom (DOF) robotic arm with force sensors that not only provides a robust tracking accuracy, but also enables co-operative control. Furthermore, we developed an algorithm to mitigate the potential errors between consecutive poses, such as tracking inaccuracy, tissue deformation, and phase aberration. *Chapter 8* extends the STRATUS concept into out-of-plane to enable high resolution 3D ultrasound imaging system. Ultrasound calibration is a pre-operational procedure to recover the transformation, bridging the tracking sensor to the ultrasound image coordinate systems, which is required in the STRATUS imaging. *Chapter 9* envisions the integration of co-robotic system with PA imaging for high resolution three-dimensional imaging. Aperture extension improves the spatial resolution and imaging contrast. The general framework was investigated through PA computed tomography, and a specific application on prostate and brachytherapy monitoring was tested using a translational ultrasound transducer. *Chapter 10* presents a new phantom design and the associated mathematical framework enabling a fast and accurate ultrasound cal-

ibration. *Chapter 11* explore the usage of tracked ultrasound from the point of view of point-of-care ultrasound (POCUS) by minimizing the ultrasound scanner to be a needle. Lumbar punctures (LPs) are interventional procedures used to collect cerebrospinal fluid (CSF). Because the target window is small, physicians have a limited success rate of the procedure, and the procedure is especially difficult for obese patients due to the distance between bone and the skin surface. A simple and direct the needle insertion platform enables image formation from sweeping a single ultrasound element at the needle tip.

Part III is the demonstration of translational PA imaging on brain imaging and cancer detection. Together, these parts explore the feasibility of co-robotic translational PA imaging. *Chapter 12* presents an application of translational PA imaging on prostate cancer screening. We proposed a PA imaging approach to non-invasively distinguish indolent from aggressive prostate tumors in vivo using PSMA targeting molecular probe. *Chapter 13* explores the ambitious future application of PA imaging for building a comprehensive map of brain function using special contrast dyes: voltage sensitive dye (VSD). We developed a novel near infrared PA VSD whose PA intensity change is sensitive to change in membrane potential.

Chapter 14 summarizes the findings of the thesis, discusses the limitations, and proposes potential future works.

1.4 Summary of Contributions

1.4.1 Enabling Technologies for Translational Photoacoustic Imaging

My major contributions to Part I are the following:

- Development of photoacoustic re-beamforming algorithm utilizes ultrasound beamformed RF data
- Development of advanced photoacoustic re-beamforming algorithm utilizing ultrasound B-mode image for point targets
- Development of low cost translational photoacoustic imaging based on a LED light source and a re-beamforming algorithm

1.4.2 Co-robotic Ultrasound and Photoacoustic Imaging

My major contributions to Part II are the following:

- Development of force assisted co-robotic ultrasound imaging system
- Introduction of synthetic tracked aperture ultrasound (STRATUS) imaging concept

- Development of co-robotic synthetic tracked aperture ultrasound imaging with virtual fixture control
- Development of synthetic tracked aperture ultrasound imaging with motion error compensation
- Development of single element ultrasound imaging based on synthetic tracked aperture
- Development of 3D synthetic tracked aperture ultrasound imaging
- Development of synthetic tracked aperture imaging for photoacoustic tomography
- Multiple active-point phantom based ultrasound calibration

1.4.3 Advancements on Translational Photoacoustic Imaging

My major contributions to Part III are the following:

- *In vivo* prostate specific membrane antigen (PSMA) targeted photoacoustic imaging
- Demonstration of photoacoustic voltage sensitive dye
- Theoretical derivation for quenching based photoacoustic voltage sensitive dye

Part I

Enabling Technologies for Translational Photoacoustic Imaging

Chapter 2

Photoacoustic Imaging Using Ultrasound Beamformed RF Data

This chapter has been published as: *H. K. Zhang, M. Bell, X. Guo, H. J. Kang, Emad M. Boctor, "Synthetic-aperture based photoacoustic re-beamforming (SPARE) approach using beamformed ultrasound data" in Biomedical Optics Express, 7(8), 3056-3068, 2016.*

I was responsible for the project design, system integration, data collection, analysis and writing. Dr. Xiaoyu Guo and Dr. Hyun Jae Kang assisted experiemntal data collection. Dr. Muyinatu A. Lediju Bell helped on constructing the theoretical model. Dr. Emad M. Boctor supervised the project.

2.1 Introduction

Photoacoustic (PA) imaging is an important tool for various clinical and pre-clinical applications [1], providing functional information by visualizing optical absorption properties, and offering great synergy with conventional ultrasound imaging, which delineates anatomical structures. In order to construct a PA image, it is necessary to receive signals from different locations through scanning. While various scanning strategies are considered, the ultrasound array transducer can be regarded as the most accessible receiver because it is widely used in the clinic for ultrasound imaging [2–4]. In addition, receiving PA signals from the same ultrasound imaging array simplifies fusion of PA and ultrasound images [5].

When forming PA images, acquiring pre-beamformed channel data is essential because typical clinical ultrasound systems only provide access to delay-and-sum beamformed data [2,6]. Accessing pre-beamformed channel data requires custom hardware and parallel beamforming software, and is available for a limited number of research ultrasound platforms with dedicated channel data acquisition devices such as the Ultrasonix DAQ system [7]. These systems are generally expensive with fixed data transfer rates that prohibit high frame-rate, real-time imaging [8]. More importantly, most clinical ultrasound systems do not offer PA beamforming which hinders clinical transition. Harrison et al. [9] studied this issue and suggested changing the speed of sound parameter of clinical ultrasound systems. However, software access to change the speed of sound is not common and when available, the range for this change is

limited, making this option insufficient for PA beamforming. In addition, this concept is limited to linear arrays, because angled beams (e.g. as in curvilinear arrays) alter the geometry of beamformer, as well as the speed of sound. Thus, it is not possible to compensate by simply chaning the speed of sound. In contrast, post-beamformed radio frequency (RF) data is readily available with several clinical and research ultrasound platforms, thus to broaden the impact of clinical PA imaging, our goal is to devise a new PA image reconstruction approach based on ultrasound RF data that has already been beamformed by the system.

We therefore propose a synthetic aperture-based beamforming algorithm, named Synthetic-aperture based PhotoAcoustic RE-beamforming (SPARE), utilizing ultrasound post-beamformed RF data as the pre-beamformed data for PA beamforming. When receive focusing is applied in ultrasound beamforming, the focal point can be regarded as a virtual element [10–12] to form a set of pre-beamformed data for PA beamforming. The SPARE beamformer takes the ultrasound data as input, and reconstructs a PA image with the correct focal delay.

In this chapter, we first introduce the theory of the synthetic aperture based PA beamformer. Then, the resolution and signal-to-noise ratio (SNR) of the proposed method are evaluated through simulation, and an experiment is conducted to validate its feasibility. Finally, the limitations and the potential applications of this algorithm are discussed.

2.2 Contributions

The main contributions of this chapter are the following:

- Development of PA re-beamforming algorithm without using conventional channel data but ultrasound beamformed data that are available in a clinical ultrasound scanner
- Theoretical derivation of the SPARE beamforming algroithm and its quality
- Concept validation of the SPARE beamforming through simulation and experiment

2.3 Theory

2.3.1 Ultrasound Beamforming

In ultrasound image reconstruction, the delay function in delay-and-sum beamforming is computed from the distance between receivers and the target [13]. The acoustic wave is first transmitted from the ultrasound transducer, through a medium with a specific velocity, reflected at boundaries with impedance mismatching, and the backscattered sound is received by the ultrasound transducer. The entire acoustic time-of-flight (TOF) during this process can be formulated as,

$$t_{US}(r_F) = \frac{1}{c}(|r_T| + |r_R|). \tag{2.1}$$

where r_F is the focus point originating from the ultrasound image coordinates, r_T is the vector from the transmit element to the focal point, r_R is the vector from the focal point to the receive element, and c is the speed of sound. In clinical ultrasound systems, sequential beamforming with dynamic focus or fixed focus is generally applied as a delay-and-sum algorithm. In dynamic focusing, the axial component z_F of the focusing point varies with depth, while a single fixed depth focus is used for the fixed focusing.

The acoustic TOF of PA signals is half of that of ultrasound, because the acoustic wave is generated at the target by absorbing light energy, and the optical transmission side of time travel is negligible. Therefore, the acoustic TOF for photoacoustic imaging becomes

$$t_{PA}(r_F) = \frac{|r_R|}{c}. \tag{2.2}$$

Considering the differences between Eqs. 2.1 and 2.2, when beamforming is applied to the received PA signals based on Eq. 2.2, the beamformed RF signals are defocused, as shown in Fig. 2.1(a).

2.3.2 Synthetic-Aperture Based Photoacoustic Re-Beamforming

In SPARE beamforming, the beamformed RF data from the ultrasound scanner is not considered as defocused useless data, but as pre-beamformed RF data for

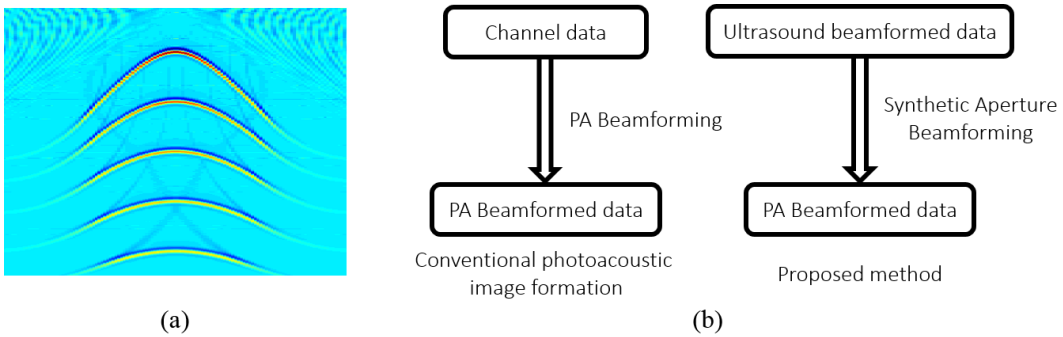

Figure 2.1: (a) Example of ultrasound beamforming for photoacoustic signals. When five point targets are placed, the points are extended with orbits in the reconstructed image due to incorrect delays. (b) Diagram of proposed synthetic aperture beamforming.

PA beamforming. The additional delay-and-sum step is applied on the beamformed RF data, and the new photoacoustically beamformed RF data can be reconstructed. When fixed focusing is applied in the ultrasound beamforming process, the focus point in the axial direction is constant with depth, indicating that ideal focusing was applied at the specific focal depth with defocused signals appearing elsewhere. Starting from the single focal depth, the defocused signals appear as they were transmitted from the focal point (i.e. a virtual element as illustrated in Fig. 2.2(b)). In this sense, the ultrasound post-beamformed RF data is regarded as PA pre-beamformed RF data. For convenience, we define the ultrasound beamforming with a fixed focus as the first beamforming, and the following SPARE beamforming as the second beamforming. The TOF from the virtual element, when a fixed focus at z_F is applied, becomes

$$t(r'_F) = \frac{|r'_R|}{c}. \tag{2.3}$$

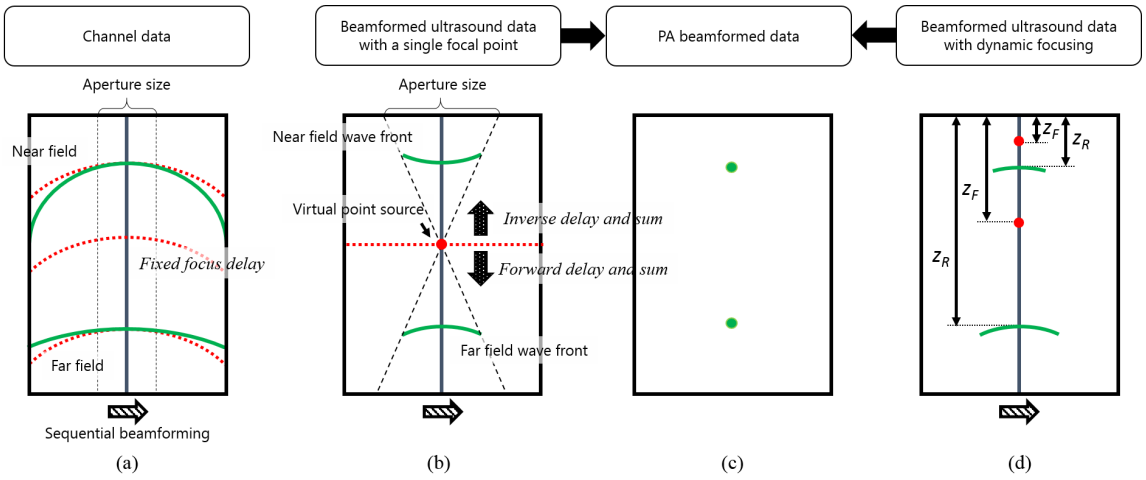

Figure 2.2: Illustration of channel data and the SPARE beamforming process. (a) In channel data, the wave front of receive RF signals expands corresponding to the depth (green line). The red lines indicate fixed focus delay function. (b) When fixed receive focusing is applied, the delay function is only optimized to the focus depth (red line). (c) As a result of fixed receive focusing, the focal point can be regarded as a virtual point source, so that inverse and forward delay and sum can be applied. (d) Similarly, dynamic focusing could be regarded as a specific case of that in which the virtual element depth z_F is the half distance of re-beamforming focal depth z_R.

where

$$|r'_R| = \sqrt{(x_R)^2 + (z_R - z_F)^2}, \tag{2.4}$$

and $r'_F = r_F - z_F$. x_R and z_R is the lateral and axial components of r_R, respectively. The dynamic receive delay function will be applied in the positive axial direction when $z_R \geq z_F$, and negative dynamic focusing delay will be applied when $z_R \leq z_F$. The diagrams in Fig. 2.2(b) and Fig. 2.2(c) show the re-beamforming process of the SPARE beamformer. Post-beamforming processes such as envelope detection and scan conversion will be applied on the reconstructed data for the PA image display.

Although derived for fixed focusing, this theory is applicable to both fixed and dynamic focused beamformed ultrasound RF data with the primary difference being

that in dynamic focusing, the round trip distance between the transmitter and the reflecting point in conventional ultrasound imaging must be considered along with the location of the virtual point source. Thus, in SPARE beamforming of dynamically focused data, we consider the virtual point source depth, z_F, to be dynamically varied by half of the photoacoustic beamforming focal point depth, z_R, as illustrated in Fig. 2.2(d). Note that $z_R = 2z_F$ is always true in this special case.

2.3.3 Resolution and SNR

The lateral resolution of photoacoustic imaging is proportional to the f-number, which is the ratio of aperture size to the focusing depth. In PA beamforming, the relationship between f-number ($F\#$) and lateral resolution can be described as

$$\text{Lateral Resolution} \propto \frac{F}{D} = F\#. \tag{2.5}$$

where F is focusing depth and D is the aperture size. Therefore, to achieve a high resolution PA image, a low f-number (i.e. a small focusing depth and/or a large aperture) is desired. In ultrasound imaging, the frequency of the received signals is another factor that affects the lateral resolution, which typically depends on the probe bandwidth in PA imaging.

In the proposed SPARE beamformer, four factors are involved to determine the lateral resolution: 1) the fixed focal depth z_F, 2) the SPARE beamforming focal depth z_R, 3) the fixed focus aperture size D_{US}, and 4) the aperture size for the SPARE

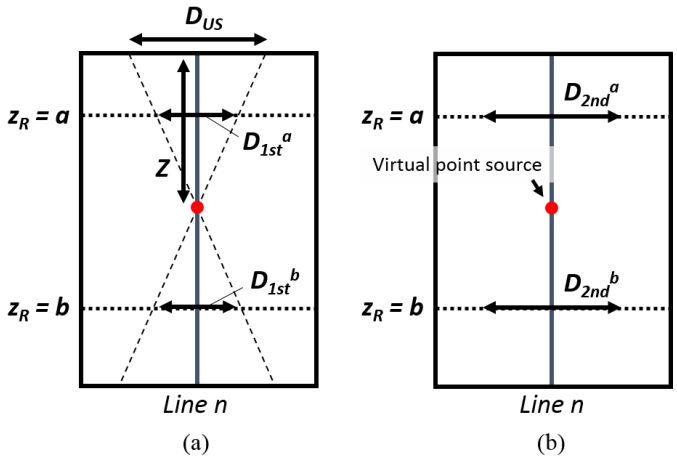

Figure 2.3: The beamforming geometry when line n is beamformed. (a) The effective aperture size of the first beamforming is defined as D^a_{1st} and D^b_{1st} when $z_R = a$ and $z_R = b$ is chosen, respectively. (b) The effective aperture size of the second beamforming (SPARE) is defined as D^a_{2nd} and D^b_{2nd} when $z_R = a$ and $z_R = b$ is chosen.

beamforming D_{SA}. The fixed focus depth and aperture size are determined by the ultrasound system as in conventional beamforming, and the SPARE beamforming parameters are determined based on the fixed focus parameters, as discussed in Section 2.3.4. The effective focusing depth and aperture of the SPARE beamformer, which defines the resolution of the reconstructed PA image, is

$$F_{SA} = |z_F - z_R|. \tag{2.6}$$

where z_F is considered as a virtual element point source, and the new focusing depth is computed starting from the virtual element.

The effective aperture size of the system is determined by both fixed focusing and the following second SPARE beamforming. For the fixed focusing, the effective aperture size in the first focusing step is affected by the fixed-focus aperture size and

depth as illustrated in the geometrical region covered by dotted lines in Fig. 2.3. The effective aperture size in the first ultrasound beamforming is

$$D_{1st} = \frac{D_{US} F_{SA}}{z_F}, \tag{2.7}$$

and that in second beamforming is

$$D_{2st} = D_{SA}, \tag{2.8}$$

The overall effective aperture size is the smaller of the two apertures for the first or the second beamforming step. Hence, the overall effect on lateral resolution can be expressed as

$$\text{Lateral Resolution} \propto \begin{cases} \dfrac{F_{SA}}{D_{1st}} & \text{if} D_{2nd} < D_{1st} \\ \dfrac{F_{SA}}{D_{2nd}} & \text{if} D_{2nd} \geq D_{1st} \end{cases}. \tag{2.9}$$

The SNR is another factor that represents the quality of beamforming defined as

$$SNR = 20\log_{10}\left(\frac{|A_{Max}|}{\sigma_{noise}}\right), \tag{2.10}$$

where A_{Max} is the maximum signal amplitude, and σ_{noise} is the RMS electrical noise level. The SNR of ultrasound signals depend on many factors including f-number, attenuation, reflection, and angle sensitivity of elements, etc. However, when all parameters except f-number are fixed, the SNR is determined based on f-number as

$$\text{SNR} = f(F\#). \tag{2.11}$$

In the proposed algorithm, therefore, Equation 2.9 determines SNR as well as lateral resolution.

2.3.4 Optimum Aperture Size

The appropriate aperture size in the SPARE beamforming can be determined by the effective aperture size in the first ultrasound beamforming. As the resolution is determined by the aperture size used for fixed focusing, using a wider aperture in the second SPARE beamforming than the original aperture size from fixed focusing is unnecessary and does not provide additional resolution. Therefore, the optimum aperture size for the second SPARE beamforming can be calculated based on the first beamforming aperture size. The aperture size for the SPARE beamforming is defined as

$$K(z_R) = \frac{(|z_R - z_F|)D_{US}}{z_F}. \tag{2.12}$$

2.4 Methods

2.4.1 Simulation

Various center frequency signals were simulated using Field II [14], and N-shape waveforms with different absorber sizes were simulated to evaluate their effects on different impulse responses. For the resolution and SNR analyses, five photoacoustic point sources were placed at 10 mm, 20 mm, 30 mm, 40 mm, and 50 mm depth, respectively to observe the proposed re-beamforming effect at different target depths. Beamforming with a fixed focal point at 20 mm depth and dynamic focusing was

applied to the simulated channel data, then the SPARE beamforming algorithm was applied. The center frequency of the impulse response was 2 MHz. A 128-element, 0.3 mm pitch, linear array transducer was assumed to be a receiver, which matches the setup of the experiment described in section 3.2. The received signals were sampled at 40 MHz. We varied the following parameters: the fixed focal depth, the SPARE beamformer focal depth, the fixed focusing aperture size, and the aperture size for the SPARE beamforming. To provide a ground-truth resolution value for this setup, the conventional delay-and-sum PA beamforming algorithm was applied to the simulated channel data. The full-width at half maximum (FWHM) was calculated to evaluate the resolution of the beamforming algorithm. For the SNR analysis, -20 dB Gaussian noise compared to the maximum intensity was added to the background, and the SNR was computed using Eq. 2.10.

2.4.2 Experimental Setup

The experimental setup is shown in Fig. 2.4. A 905 nm wavelength pulsed laser diode (PLD) (Laser Components) was used to irradiate a plastisol phantom with black ink. The diode laser was triggered by a function generator which was programmed through a PC. Since the light was absorbed by the surface of the phantom because of the high absorption coefficient of the black ink, PA signals could be generated from a tiny spot in the phantom, which could be regarded as a point source. The PLD is placed approximately 5 mm from the phantom surface, and the laser spot

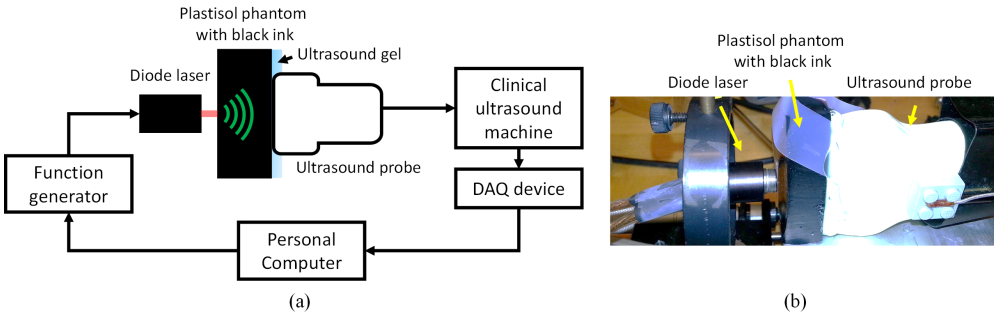

Figure 2.4: (a) Experimental setup diagram. (b) Picture of the setup.

size at the incident surface was 1mm. PA signals were generated at from the surface of the phantom and traveled toward the ultrasound probe, located on the opposite surface of the phantom. The generated PA signal was received by a 0.3 mm pitch, 128-element, linear array ultrasound transducer (L14-5/38, Ultrasonix). The received 128-element channel data were transferred to a channel data collection device (Sonix DAQ) via a clinical ultrasound machine (Sonix Touch, Ultrasonix), and saved to the PC. Beamforming algorithms were applied to the acquired channel data.

2.5 Results

2.5.1 Simulated Waveform and Images

Simulated waveforms and the resulting reconstructed PA images using channel data (center) and ultrasound beamformed RF data with a fixed focal point (right) are shown in Fig. 2.5.

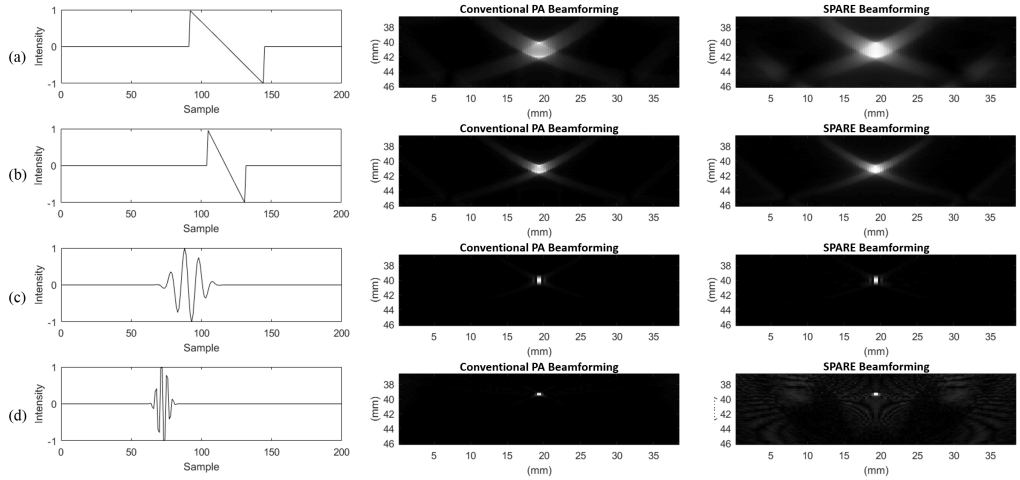

Figure 2.5: Simulated photoacoustic waveforms, PA images from channel data, and PA images using SPARE beamformer are shown. Fixed focusing at 20 mm depth was used for SPARE beamforming. (a) 1 mm and (b) 0.5 mm diameter objects with N-shape impulse responses were simulated. For a point source, (c) 2 MHz, (d) 5 MHz center frequency waves were simulated assuming that a band-limited ultrasound transducer was used to receive these signals.

The true PA signals from a cyliderical target is N-shape, and Figs. 2.5(a) and 2.5(b) shows the waveform when the absorber size was set to 1 mm and 0.5 mm, respectively. However, the ultrasound receiver is generally band-limited with a specific center frequency. When the PA signals are received by the ultrasound probe, the PA signals will be filtered at the probes center frequency. Figs. 2.5(c) and 2.5(d) demonstrate signals with center frequencies of 2 MHz and 5 MHz, respectively. The maximum available aperture size was used for all reconstructed images. PA images using the proposed SPARE beamformer were similar to that from conventional PA beamforming from raw channel data. These results indicate that our algorithm is independent of the impulse responses determined by the absorber size and the ultrasound probe.

2.5.2 Resolution Evaluation

To quantitatively evaluate the performance of the proposed SPARE beamformer, the resolution of reconstructed point targets was compared to the theoretical property introduced in Section 2.3.3. We first analyzed the FWHM of the PA point reconstructed with conventional delay-and-sum beamforming for each depth as a function of aperture size. In this simulation, the full aperture was used for the PA beamforming to estimate the maximum achievable resolution. As shown in Fig. 2.6(c), for conventional delay-and-sum photoacoustic beamforming, the FWHM decreased as the target depth decreased and the aperture size increased. In addition, the FWHM was evaluated as a function of f-number. For those data, the metric of f-number was computed for corresponding depth and aperture size using Eq. 2.5, and we present the average of FWHM values for the corresponding f-number [Fig. 2.5(d)]. This rearranged result was used as the ground truth control to compare with the proposed method.

Figures 2.6(a) and 2.6(b) show the resolution of SPARE beamformed images. When the first beamforming aperture was varied, the second beamforming aperture used all elements (Fig. 2.6(a)). Similarly, when the second beamforming aperture was varied, the maximum available aperture size was used in the first beamforming (Fig. 2.6(b)). Figure 2.6(a) shows the decrease of FWHM corresponding to the aperture size increase and the fixed focal depth reduction, and Figure 2.6(b) shows the FWHM reduction due to the aperture size increase in the second beamforming step. These

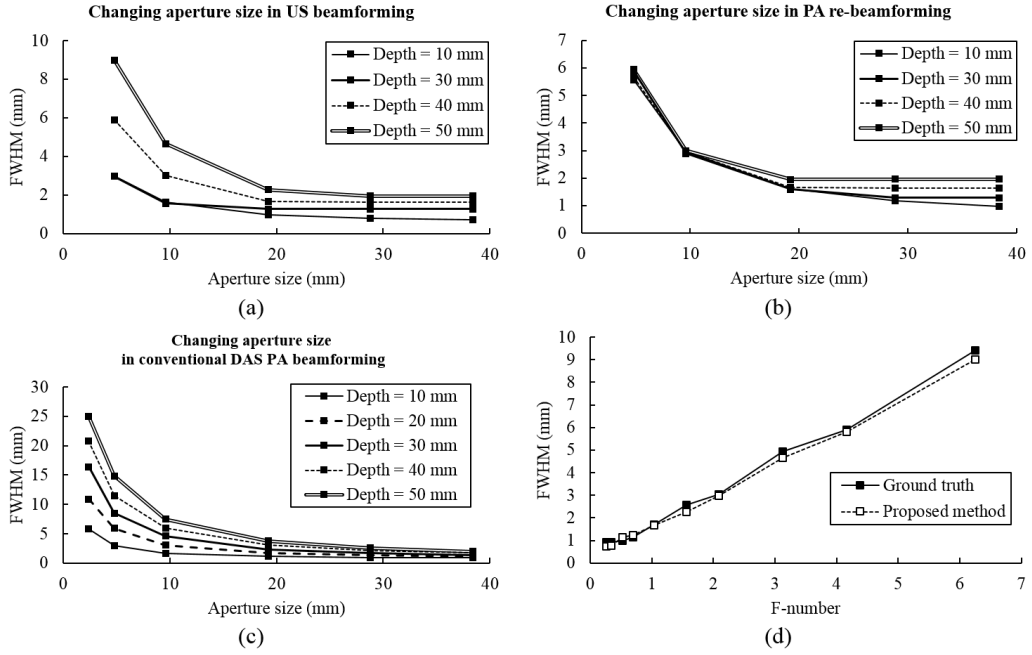

Figure 2.6: The FWHM of the proposed re-beamforming for the designated focusing depth, and varying the aperture size in the (a) first beamforming and (b) the second beamforming. (c) The ground truth FWHM results using a delay-and-sum algorithm with dynamic focusing. (d) The focusing depth and aperture size parameters in Figs. 2.6(a-c) were compressed into the metric of fnumber. The theoretical ground truth values were computed by fitting the ground truth data from Fig. 2.6(c) into Eq. 2.5.

SPARE beamforming results were rearranged based on the f-number of each depth and aperture size, and the FWHM value was compared to that of the ground truth values presented in Figure 2.6(c). Figure 2.6(d) shows the result of this comparison for various f-numbers. The resolution of the proposed method agrees well with the ground truth values with a correlation coefficient of 99.87 %.

2.5.3 SNR Evaluation

Following the evaluation scheme used in Section 2.5.2, the SNR of simulated beamformed data using the conventional PA beamformer and proposed re-beamforming algorithm were calculated using Equation 2.10 (Figs. 2.7(a-b)). For the proposed method, the aperture size was changed for either the first or second beamformer; when one was changed, the other aperture size was fixed to be the maximum aperture size [Fig. 2.7(a)]. The ground truth data was based on conventional PA beamforming by changing the aperture size and the focal depth [Fig. 2.7(b)]. To observe the characteristics of SNR for a corresponding f-number, the SNR at a f-number of 1.04 was normalized to be 0 dB throughout different target depth results. The comparison with ground truth is shown in Fig. 2.7(c). A shared trend could be seen between the proposed method and ground truth values, and the correlation coefficient obtained from comparison of the two plots in Fig. 2.7(c) was 91.56 %. One difference between the results for SNR (Fig. 2.7(c)) and resolution (Fig. 2.6(d)) is that the SNR is not solely proportional to the f-number, likely because other factors (e.g. attenuation difference at different depths) also affect the SNR.

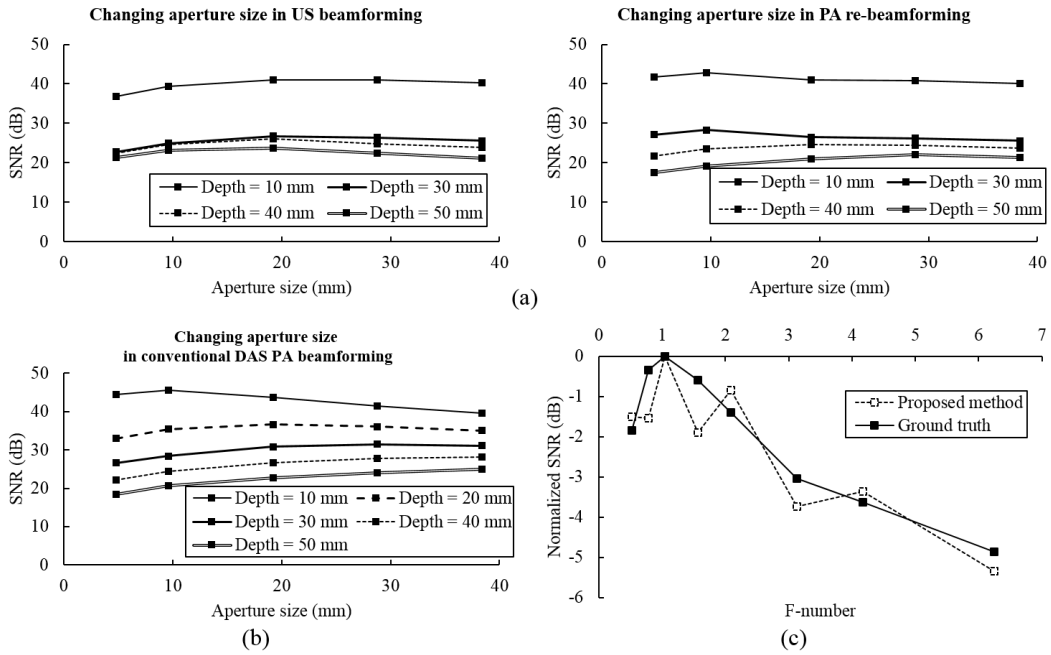

Figure 2.7: (a) The measured SNR of proposed beamformer varying the aperture size in the first beamforming (left) and the second beamforming. One beamformer aperture size was fixed to be maximum when the other aperture size was varied. (b) The ground truth SNR results using a delay-and-sum algorithm with dynamic focusing. (c) The focusing depth and aperture size parameters in Figs. 2.7(a-b) were compressed into the metric of f-number. To compensate the SNR variance for the same f-number but different target depth, the SNR of f-number 1.04 was normalized to be 0 dB. The theoretical ground truth values were computed by fitting the ground truth data from Fig. 2.7(b) into Eq. 2.9.

2.5.4 PA re-beamforming for Dynamically Focused Beamformed Ultrasound RF Data

Figure 2.8 shows the reconstructed results of SA beamforming using dynamically focused beamformed ultrasound RF data, displayed with a dynamic range of 30 dB. The defocused beamformed ultrasound data was re-beamformed through SPARE beamforming. Comparing the proposed method with the conventional PA beamforming (Fig. 2.8(a)), a similar sidelobe level is observed, while unique artifacts are visible in the SPARE beamformed results (Figs. 2.8(b-c)). The aperture size for the ultrasound beamforming was changed from 128 elements (Fig. 2.8(b)) to 16 elements (Fig. 2.8(c)). The point targets obtained with the ultrasound beamforming step were not only degraded due to incorrect delay functions, but a large grating lobe also appeared in the near field when a large aperture was used in ultrasound beamforming step. This grating lobe artifact remains in the SPARE beamforming result (Fig. 2.8(b)). When a smaller aperture was used in ultrasound beamforming, the grating lobe artifacts were mitigated, and therefore were less visible in the corresponding SPARE beamformed image (Fig. 2.8(c)). On the other hand, when a small aperture size was employed, the resolution of the deeper point targets were degraded compared to that obtained with the larger aperture. Thus, in the practical implementation, one solution to overcome these challenges to optimize image quality is a variable aperture size (e.g. fixed f-number throughout the image with a smaller aperture size in the

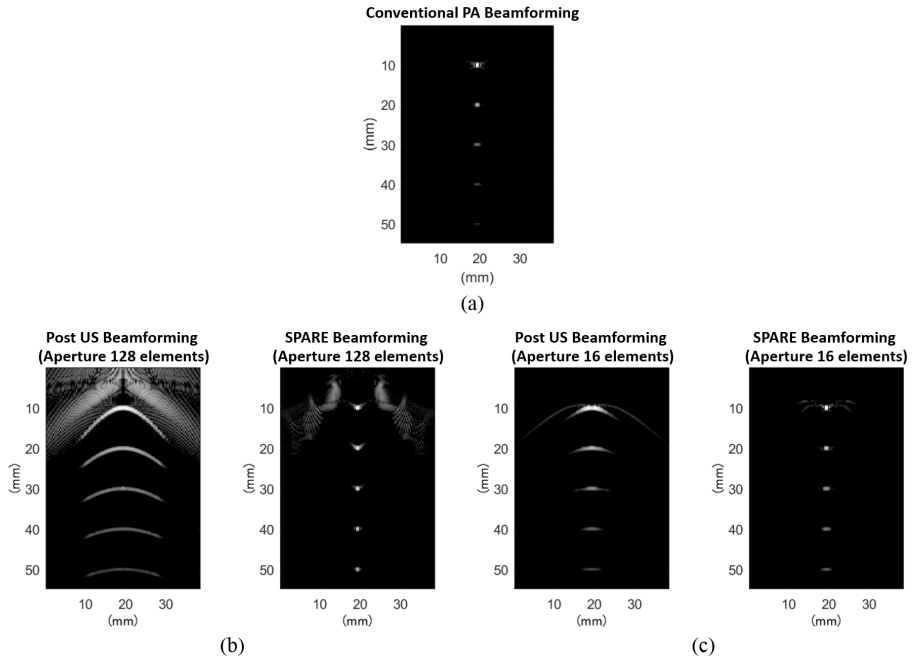

Figure 2.8: (a) The reconstructed PA image from channel data as a ground truth. (b-c) The reconstructed images through ultrasound and SPARE beamforming. Dynamic focusing is applied as ultrasound beamforming. Grating lobe artifacts are visible in the near field of ultrasound beamforming result (b) when a large aperture is used in 1st ultrasound beamforming, but it is drastically reduced when a small aperture size is used (c).

near region and a larger aperture size in the far region).

2.5.5 Experiment Evaluation

Ultrasound beamforming with fixed focusing and dynamic focusing was applied to experimental channel data to produce two types of ultrasound post-beamformed data. The experimental SPARE beamformer results from ultrasound beamforming with a single focal point are shown in Fig. 2.9, displayed with 20 dB dynamic range. The point source located at 12 mm was reconstructed for all fixed foci in the range of

3 mm to 45 mm. The FWHM and SNR of the point source was measured for different fixed focal depths in Fig. 2.9(c). The results of conventional PA beamforming using channel data is also shown as the ground truth. This ground truth result can be regarded as the lower boundary of achievable FWHM for these data because the maximum available aperture information is used. For SPARE beamforming results, the FWHM was similar to that of the ground truth when the fixed focusing was applied from 9 mm to 21 mm. However, the reconstructed point was degraded in the lateral direction when the fixed focal depth was far from the target. This degradation is likely due to an insufficient aperture size for the first and the second beamforming steps. In terms of SNR, a similar trend of image quality improvement was observed compared to the ground truth result, and the fixed focal depth over 21 mm shows a better SNR.

Figure 2.10 shows the experimental SPARE beamforming results from dynamically focused ultrasound beamforming. The defocused target in ultrasound post-beamformed result was re-focused with SPARE beamforming.

2.6 Discussion

Generally, the simulation results presented in this chapter have good agreement with theory, and the proposed method produces similar resolution and SNR to that obtained with conventional delay-and-sum beamforming. The agreement between

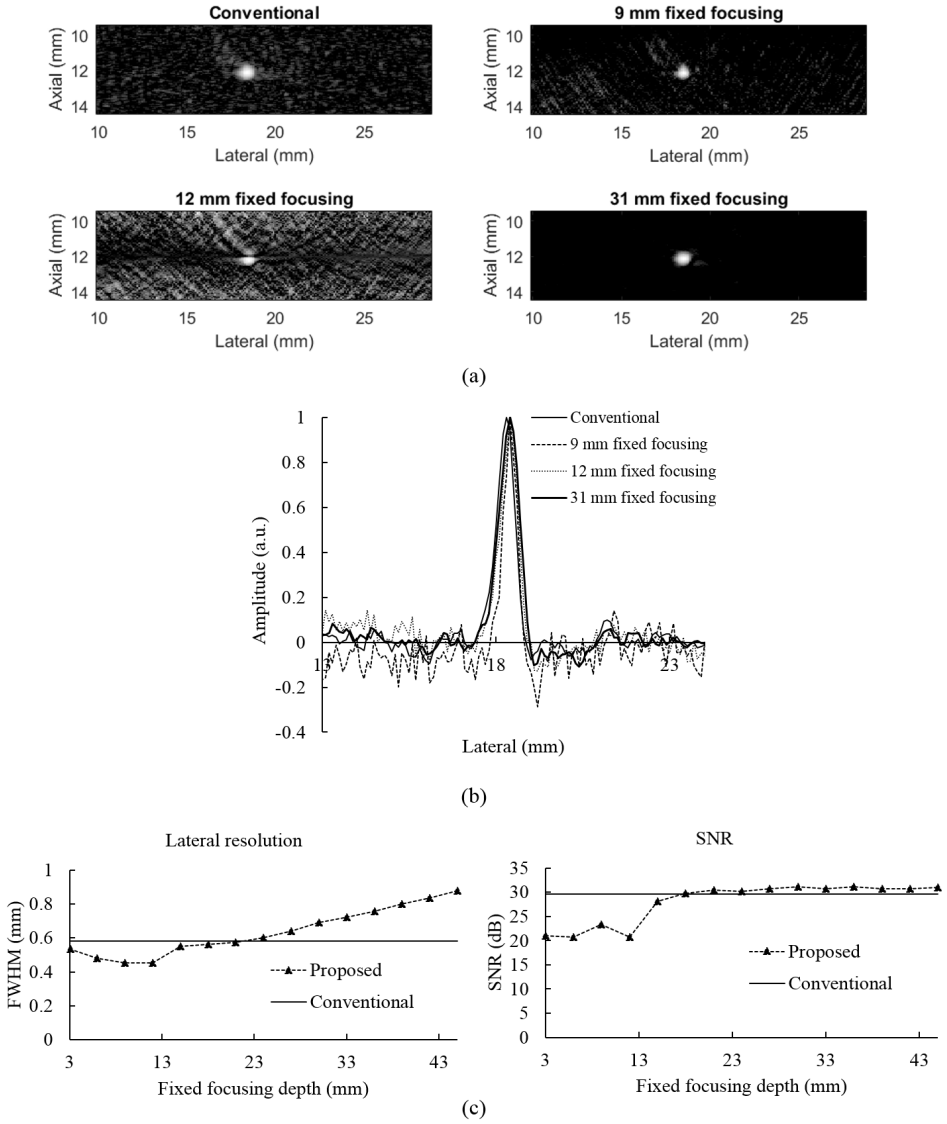

Figure 2.9: Experimental SPARE beamforming results. (a) Reconstructed photoacoustic images of conventional dynamic focusing for channel data, 9 mm, 12 mm, and 31 mm fixed focal depths. (b) Lateral profile of the point target. (c) Measured FWHM and SNR for various fixed focal depths.

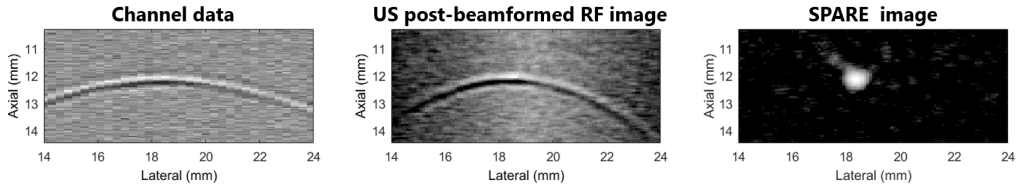

Figure 2.10: Experimental SPARE beamforming results with dynamic focusing. Original channel data, intermediate ultrasound post-beamformed result, and final SPARE post-beamformed result are shown from left to right, respectively. The dynamic range of 20 dB was used for display.

the theory and simulation for SNR was influenced by multiple confounding factors, additionally evidenced by the SPARE beamformer showing a better SNR compared to conventional PA beamforming in the experimental results [Fig. 2.9]. Theoretically, the SNR of both beamformers should be similar, and this discrepancy could be attributed to summing axially distributed coherent information twice, once for each beamforming step. If the waveform is not a simple point target, the axial components from the non-point wavefront are first summed during ultrasound beamforming. This accumulated information would be further summed after SPARE beamforming. When the SNR of the channel signals is significantly low, the reconstructed image may contain a noise-related gradation artifact as the number of summations varies for each focal point. Hence, beamforming with the full aperture is more appropriate in this high-noise case.

When fixed focusing is used as the ultrasound beamforming, the fixed focal depth should not be the same as the interested target location, as near field artifacts would appear as seen in Fig. 2.9(a) (compare 12 mm fixed focus result to 9 mm and 31

mm fixed focus results). Moreover, a deep fixed focal depth is desired to keep stable SNR, however, this depth should be sufficiently shallow to avoid degradation of the resolution,as demonstrated in the experimental results shown in Fig. 2.9(c). Dynamic focusing does not have this problem as the ultrasound focal depth is always shorter than the ideal PA focal depth.

A superiority of the proposed method over the speed of sound adjustment approach [9] is the generality to steered beams (e.g. phased arrays) or to beam geometries that differ from those of the linear array (e.g. curvilinear arrays). As formulated in equations 2.3 and 2.4, the proposed beamformer applys a delay-and-sum assuming the PA signals are received at the virtual element. Therefore, even if the ultrasound beam is angled, the delay-and-sum algorithm can still be applied with the virtual element created by the angled beam.

We expect that image quality improvement strategies (apodization, transmit gain compensation, etc.) will have a similar effect on the improvement of SPARE images. The effect of the beamformer for specific f-number parameter is shown and discussed in simulation. Apodization could improve the appearance of the reconstructed image, because it reduces the sidelobes in the ultrasound beam.

The effect of speed of sound variations with SPARE beamforming is expected to be similar to that of conventional PA beamforming if the same speed of sound is utilized for both ultrasound (the 1st beamformer) and SPARE beamforming. However, the SPARE beamformer has the added advantage of compensating for incorrect speed of

sound utilized during the ultrasound beamforming step by considering the true focal depth and speed of sound during the SPARE beamforming. This is, however, not possible if the speed of sound varies widely throughout the medium being imaged.

Although image formation was demonstrated with point-like targets throughout this manuscript, the SPARE beamformer has potential to be implemented to visualize any structure that has a high optical absorption property. Thus, the key contribution of the proposed SPARE algorithm is its potential for integration into real-time imaging systems using clinical ultrasound machines. Currently, most real-time photoacoustic imaging systems are based on open platform research systems [7]. However, the option to use an FDA-approved clinical ultrasound system eases the transition of photoacoustic technology into the clinic. Potential applications include real-time in vivo photoacoustic visualization for brachytherapy monitoring [15, 16], image-guided surgery [17, 18], interventional photoacoustic tracking [19], multispectral interventional imaging [20], and cardiac radiofrequency ablation monitoring [21].

A high pulse repetition frequency (PRF) laser system is one system requirement for the SPARE beamformer. Since the ultrasound post-beamformed RF data acquisition relies on a clinical ultrasound system, it is necessary to synchronize the laser transmission to the ultrasound line transmission trigger. To maintain similar frame rates to that of conventional ultrasound B-mode imaging, the PRF of the laser transmission should be the same as that of the ultrasound transmission frequency. Therefore, a high PRF laser system, like the PLD used in this chapter, is desirable.

Ultrasound transmission suppression can be considered as another system requirement. Turning off the transmit events is the most ideal solution. However, if this feature is unavailable, an alternative is to reduce the voltage of the transmission energy. Another approach is to use an electric circuit to control the laser transmit timing. The PA signals would be highlighted by subtracting the images with and without laser excitation.

In addition to enabling broader use of PA imaging through clinical systems, the SPARE beamformer applied to fixed focus data is also applicable to PA tomogram formation using a hydrophone combined with an acoustic lens with a focal point, as proposed by Li et al. [22]. Hydrophones are widely used as a PA signal receiver because of its wide frequency receiving capability and sensitivity compared to a clinical ultrasound array [23]. PA tomograms can be formed by sweeping the hydrophone using a Cartesian stage. Although large-diameter hydrophones have high sensitivity, their wide reception angles cause suboptimal lateral resolution [24]. Attaching an acoustic lens is a simple solution to provide a focus, but the higher resolution made possible by this lens is only available near the focal point, and the image is defocused outside of the focal point. The acoustic lens focuses the acoustic beam for a single depth, which is the same situation for the fixed beamformed data using a linear array. Thus, the proposed algorithm could be a solution to provide an opportunity to generate a dynamically focused PA tomograms with SPARE beamforming of the received data.

2.7 Conclusions

In this chapter, we propose a synthetic aperture based PA beamforming method utilizing ultrasound post-beamformed RF data. The goal is to reconstruct PA images utilizing data that can be acquired from any clinical ultrasound machine. The theoretical basis for quantifying the image resolution is introduced, and it is validated with simulations. As a result, it is possible to estimate the potential image resolution of this beamformer under various parameter definitions. In addition, we conducted a phantom experiment to beamform a point source using the SPARE beamformer. Results demonstrate the feasibility of the algorithm under practical data acquisition.

Chapter 3

Photoacoustic Imaging Using Ultrasound B-mode Data

This chapter has been published as: *H. K. Zhang, X. Guo, H. J. Kang, and E. M. Boctor, "Photoacoustic image reconstruction from ultrasound post-beamformed B-mode image", in Proceedings of SPIE Photonics West BiOS 2016, 9708, 970837, 2016.*

I was responsible for the project design, system integration, data collection, analysis and writing. Dr. Xiaoyu Guo and Dr. Hyun Jae Kang assisted experiemntal data collection. Dr. Emad M. Boctor supervised the project.

3.1 Introduction

A photoacoustic (PA) image is constructed by beamforming received channel data, and then applying signal processing methods to display it [2, 6]. Although acquiring channel data is essential, most clinical ultrasound systems do not offer an interface to obtain the synchronized channel data. Accessing these synchronized channel data requires expensive and sometimes bulky research systems such as DAQ system, and it is an obstacle to translate the PA imaging technique into clinical applications. Therefore, to broaden the impact of PA imaging, we investigate PA image reconstruction algorithm using the data accessible at clinical ultrasound systems. As clinical ultrasound systems have been widely used all over the world, this work connects PA research to the environment in which specialized research systems do not exist.

Previous chapter has demonstrated that the PA image reconstruction can be carried out from US beamformed RF data [25]. Nevertheless, the method requires clinical ultrasound system to have a functionality to provide a radio-frequency (RF) data. B-mode image, on the other hand, is the final product of ultrasound image, and accessible at most of the ultrasound systems. In this work, we present the possibility to recover US post-beamformed RF data from a B-mode image and re-beamform the recovered data to a PA image. Even though each vendor has its unique signal processing to form the final B-mode image, envelope detection and scan conversion including log compression are two major post processing after generating beamformed RF data. Figure 3.1(a) illustrates the major signal processing for ultrasound image

as well as PA image.

We divide the proposed approach into two major steps: 1) RF signal recovery from B-mode data, and 2) PA beamforming using US post-beamformed RF data. For the first step, the envelope data is recovered from B-mode image by applying log decompression. And since the RF information is discarded in the envelope data, we convolute an acoustic impulse response with the envelope data. For the second step, an adaptive PA beamforming algorithm is applied on US post-beamformed RF data. The US post-beamformed RF data is utilized as pre-beamformed RF data for PA re-beamforming, and the new delay function is used by taking into account that the focus depth in US beamforming is at the half depth of PA case. The stream of the proposed PA image formation is shown in Fig. 3.1(b).

In this chapter, we first introduce the theory behind the proposed PA reconstruction method. Then, the proposed method is evaluated through simulation, and an experiment is operated to validate its feasibility for the practical implementation. Finally, limitations of the system are discussed.

3.2 Contributions

The main contributions of this chapter are the following:

- Development of PA re-beamforming algorithm utilizing ultrasound B-mode image that are available in a clinical ultrasound scanner

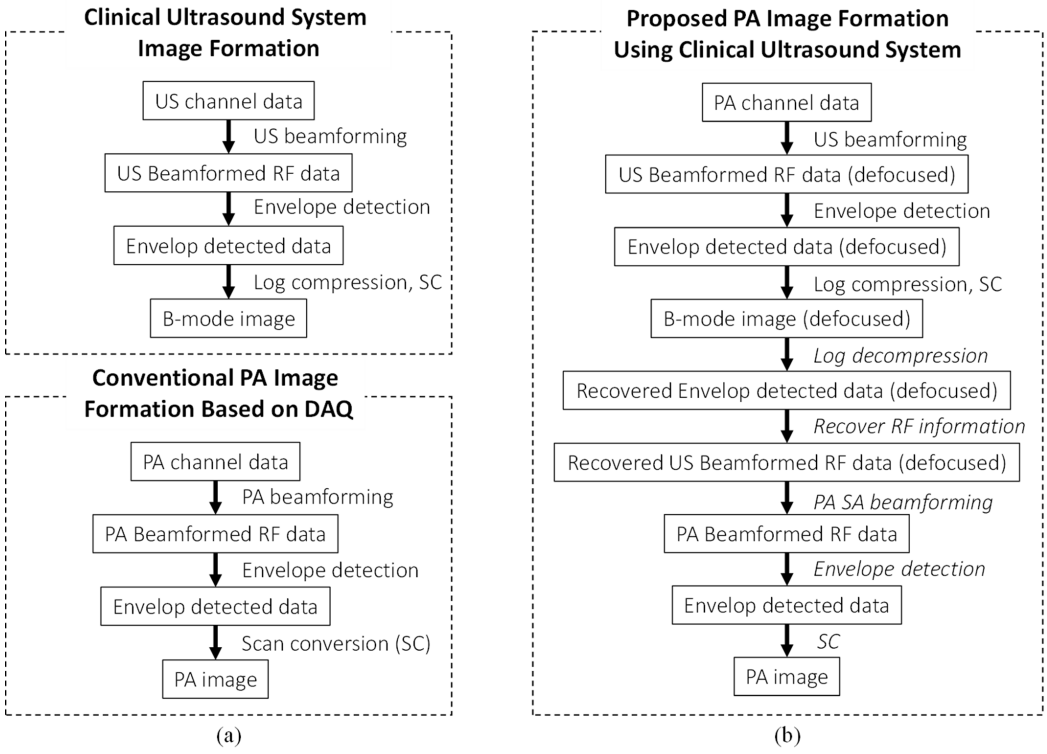

Figure 3.1: Diagrams of ultrasound (US) and photoacoustic (PA) image formation. (a) Conventional image formation in US and PA imaging. (b) Proposed PA image formation using B-mode image from clinical ultrasound systems.

- Concept Validation of the SPARE beamforming using ultrasound B-mode iamge through simulation and experiment

3.3 Methods

3.3.1 Retrieving Ultrasound Post-Beamformed RF Data from B-mode Data

A B-mode image is the final output from clinical ultrasound systems, in which the envelope detected acoustic signals are displayed in log scale. Detail signal processing techniques to produce a B-mode image could vary depending on vendor, but envelope detection and following log compression are two basic common signal processing techniques after ultrasound beamforming. Therefore, reversing two signal processing steps is necessary to retrieve US post-beamformed RF data. A general formulation of log compression is

$$z_{ij} = \alpha \ln(y_{ij}) + \beta, \tag{3.1}$$

where α and β are parameters indicating the contrast and brightness, respectively. y_{ij} is the envelope detected data, and z_{ij} is the observed intensity on a US B-mode image. Two parameters α and β could be recovered by analyzing the speckle property of a B-mode image [26, 27]. Thus, the estimated envelope detected data could be processed

as

$$\widehat{y_{ij}} = e^{(\frac{z_{ij}}{\alpha}^{\beta})}. \tag{3.2}$$

Contrast to log compression which is applied on the entire image, the envelope detection is applied to line by line. The beamformed RF signals of an A-line $x(t)$ could be expressed as

$$x(t) = y(t)cos(2\pi f_0 + \phi), \tag{3.3}$$

where $y(t)$ is the envelope data of the line, and f_0 and ϕ are its center frequency and phase, respectively. It is not difficult to multiple RF component to the envelope detected data, but the phase information will not be recovered. The phase information is essential to utilize the data for further PA beamforming, so that Eq. 3.3 is unavailable for the proposed method. Instead, we assumed the photoacoustic image as a collection of delta functions, and the RF component is added to each delta function through convolution.

$$\widehat{x(t)} = \sum_{s+1}^{S} y(t-s)H(s), \tag{3.4}$$

where $H(s)$ is an impulse response that corresponding to a cycle of cosine function. $\widehat{x(t)}$ is the recovered US post-beamformed RF data, and will be used for PA be-beamforming.

3.3.2 Reconstructing PA image from Ultrasound Post-Beamformed RF Data

The difference between ultrasound beamforming and PA beamforming is time-of-flight and accompanied delay function. Ultrasound beamforming takes into account the time-of-flight of the round trip of acoustic signals transmitted and received by the US probe elements, that is reflected at targets, while PA beamforming only counts one way trip from the PA source to the US probe. Therefore, the beamformed PA signals under ultrasound beamforming is defocused due to incorrect delay function. In our previous work, we proposed a synthetic aperture based PA beamformer using ultrasound post-beamformed RF data. Ultrasound beamformed RF data are considered as pre-beamformed input data, where its focal point is considered as a virtual element, and a new delay function is applied based on the acoustic wave travel starts from the virtual element [10–12]. Since, the delay function in dynamically focused ultrasound beamforming takes into account the round trip between the transmitter and the reflecting point, the focus point at each depth becomes the half distance for that in PA beamforming. Thus, it is possible to consider that the virtual point source is swept dynamically in the half distance of the true focal point. Figure 3.2 shows an example of implementing proposed algorithm based on back projection.

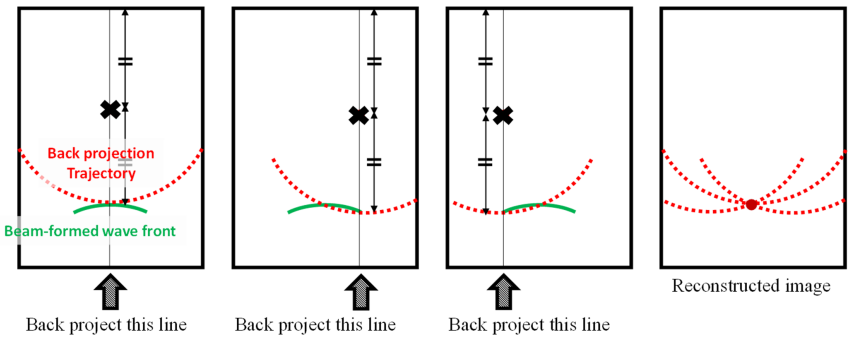

Figure 3.2: An example of PA re-beamforming from US post-beamformed RF data with dynamic receive focusing.

3.3.3 Simulation and Experimental Setup

For simulation, five point targets were placed at the depth of 10 mm to 50 mm with 10 mm interval. A 6 cm linear array transducer with 128 elements was designed to receive the photoacoustic signals. Delay-and-sum with dynamic receive focusing was used to beamform the simulated channel data assuming ultrasound delay. Envelope detection and log compression were applied on the received data and proposed PA re-beamforming process was applied on the data.

The experimental setup is shown in Fig. 3.3. Clinical ultrasound machine (Sonix Touch, Ultrasonix) was used to display and save the received data, and the acoustic wave transmission was turned off during receiving. A costume made piezo element was used to imitate a PA point target. The element has the center frequency of 10 MHz, and was attached to the tip of needle, and it was wired to an electric board controlling the voltage and transmission pattern. The acoustic signals transmission is triggered by the line generation trigger from clinical ultrasound machine. The

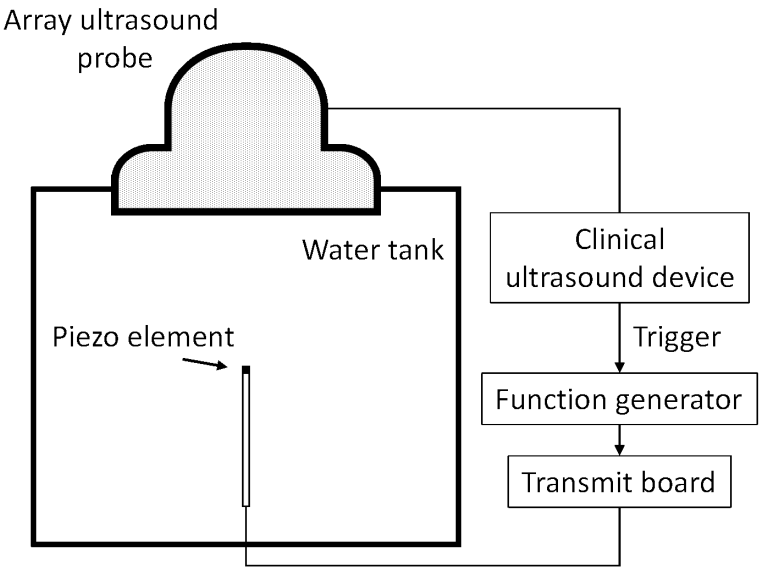

Figure 3.3: Experiment setup. A PZT element was used as a pseudo PA point source.

received RF data was saved and a B-mode image was formed. All elements on the probe were used to beamform each line. The proposed signal processing was applied on the B-mode image.

3.4 Results

The simulation result is shown in Fig. 3.4. A set of channel data simulates PA signals was beamformed using delay-and-sum with dynamic receive focusing. The US beamformed RF data was defocused due to incorrect delay function [Fig. 3.4(b)]. The US beamformed RF data could be re-beamformed to form a PA image using adaptive PA reconstruction algorithm [Fig. 3.4(e)]. Then, a B-mode image was formed using the US beamformed RF data. We applied the log decompression and RF information

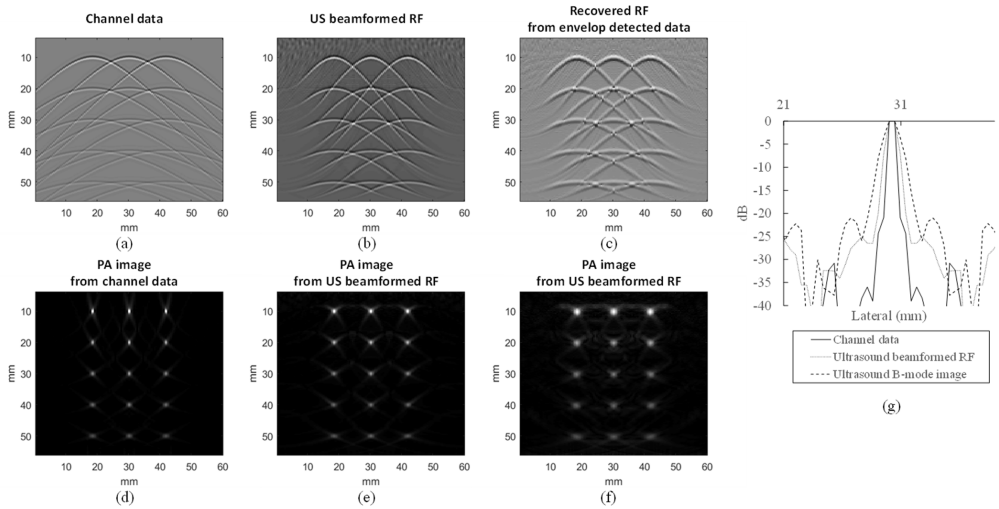

Figure 3.4: Simulation results. The input data of beamforming were shown in (a-c) and output was presented in (d-f). The profile of a point located at 30 mm depth for three different input data was shown in (g).

recovery through convoluting a cycle of sine function. The RF component was lost through envelope detection, but new RF wave was added to the envelope detected data [Fig. 3.4(c)]. The recovered RF data was re-beamformed, and finally a PA image was obtained [Fig. 3.4(f)]. Although the reconstructed point was larger than the point reconstructed from channel data, it is demonstrated that the defocused data could be beamformed through proposed processing.

Figure 3.5 shows the experiment results. A set of US post-beamformed RF data was collected from ultrasound machine, and a B-mode image is formed through envelope detection and scan conversion with log compression [Fig. 3.5(a)]. The processed US B-mode image was used as the input for the proposed signal processing and following PA image re-beamforming. US post-beamformed RF data was recovered through convolution with a cycle of sine function, and finally a PA image is reconstructed

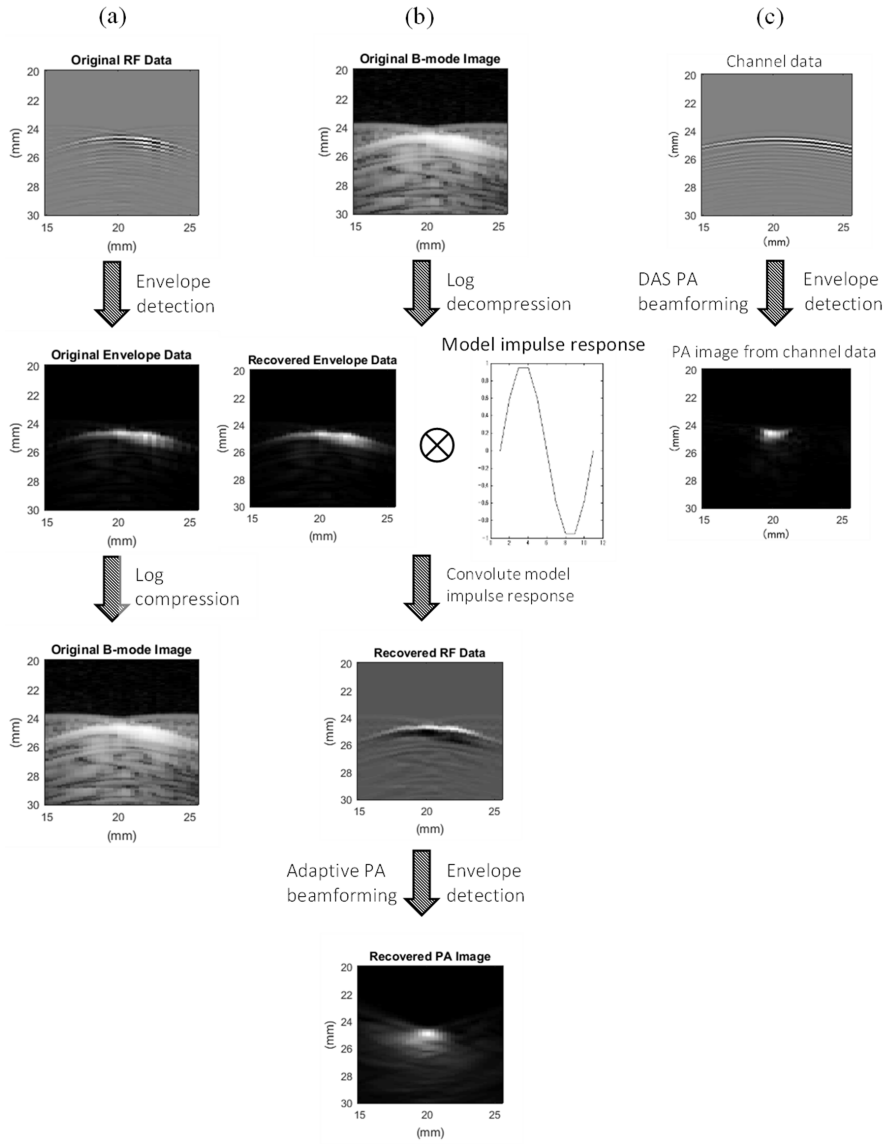

Figure 3.5: (a) US image formation in clinical ultrasound system. (b) Proposed PA image reconstruction processes. (c) PA image reconstruction from channel data.

using back projection based re-beamformer [Fig. 3.5(b)]. For the control, the channel data was collected and conventional delay-and-sum PA beamforming was applied [Fig. 3.5(c)]. The full width at half maximum (FWHM) of the US B-mode image was 7.50 mm, and it was improved to 1.89 mm through the proposed method. The FWHM for the PA image from the channel data was 1.48 mm. The degradation of point spread function could be due to signal loss during envelop detection, and blurring through convolution.

3.5 Discussion and Conclusions

In this chapter, we proposed a method to reconstruct a PA image utilizing US B-mode image, which can be acquired from clinical ultrasound machine. The proposed method could reconstruct point targets on simulation, and the experiment using an acoustic point source was conducted to validate the practical implementation.

The limitation of the current algorithm is that it only works when the image target is a point-like object. The convolution approach could recover the phase information of the wave-front, which is lost when simple multiplication is applied. However, the problem is the axial size growth of a RF signal as a large pulse was convoluted, so that the frequency and phase change when the input is the non-uniform wave-front such as targets that is not point object. Thus, photoacoustic based point targets tracking [28] or brachytherapy seed visualization [15] could be considered to be the

primary application.

Chapter 4

Photoacoustic Imaging System Using LED Light Source and Clinical Ultrasound Scanner

I was responsible for the project design, system integration, data collection, analysis and writing. Dr. Jeeun Kang and Dr. Xiaoyu Guo assisted experiemntal data collection. Dr. Emad M. Boctor supervised the project.

4.1 Introduction

The clinical accessibility of photoacoustic (PA) imaging is limited because of specific hardware requirements including channel data acquisition system and high en-

ergy pulsed laser. PA reconstruction requires a delay function calculated based on the time-of-flight (TOF) from the PA source to the receiving probe element [6-7], while US beamforming considers the round trip initiated from the transmitting and receiving probe element. Thus, the reconstructed PA image with US beamformer would be defocused due to the incorrect delay function (Fig. 4.1(a)). Real-time channel data acquisition systems are only accessible from limited research platforms. Most of them are not FDA approved, which hinders the development of PA imaging in the clinical setting. Therefore, there is a strong demand to implement PA imaging on more widely used clinical machines. As introduced in Chapter 2, Synthetic-aperture based photoacoustic re (SPARE)-beamforming algorithm regards the defocused RF data as a set of pre-beamformed RF data received by virtual elements; an adaptive synthetic aperture beamforming algorithm is applied to refocus it.

This chapter considers more general ultrasound beamformed data applied with delay-and-sum dynamic receive focusing. Ultrasound beamforming is a sequential process scanning line by line. Using those sequentially beamformed data as input, synthetic aperture (SA) based re-beamforming algorithm regards the defocused RF data as a set of pre-beamformed RF data from virtual elements; an adaptive synthetic aperture beamforming algorithm is applied on the RF data to refocus it.

Most of the laser systems used for PA imaging have high power and with low pulse repetition frequency (PRF). Those laser systems are expensive, bulky, non-portable, and not safe to be used without laser glasses. Thus, a portable low cost laser system

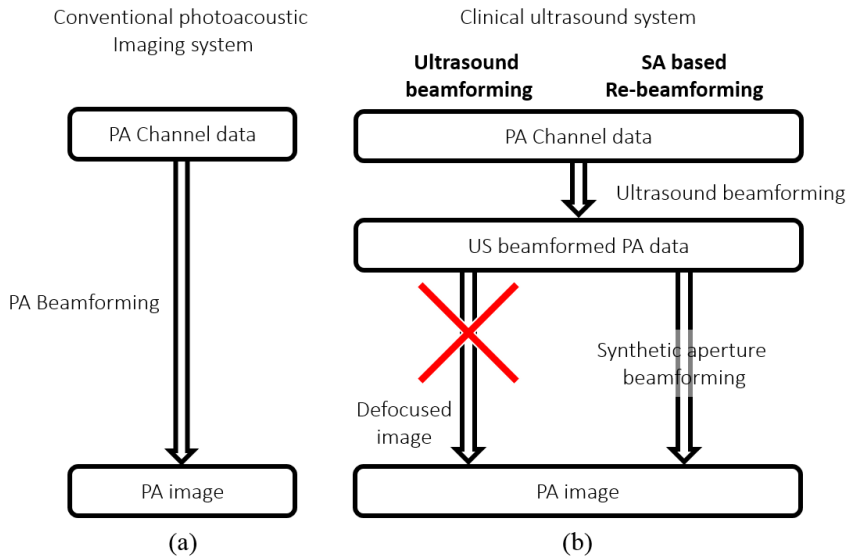

Figure 4.1: Conventional PA imaging system (a) and proposed PA imaging system using clinical US scanners (b). Channel data is necessary for PA beamforming because US beamformed PA data is defocused with the incorrect delay function. The proposed two approaches could overcome the problem.

with sufficient power output is desired for easier access to PA data acquisition.

To broaden the impact of clinical PA imaging, we propose a vendor-independent PA imaging system utilizing ultrasound post-beamformed radio frequency (RF) data, which is readily accessible in some clinical scanners. Light emitting diodes (LED) was used as a low energy high pulse repetition frequency light source to replace conventional high energy laser.

In this chapter, we first introduce the theory and methodology behind the proposed PA reconstruction method using LED light source. Afterwards, we present the evaluation of our method through simulation and experiments that validate its feasibility for practical implementation.

4.1.1 Contributions

The main contributions of this chapter are the followings:

- Development of low cost and safe PA imaging system using LED light source
- *In vivo* demonstration of the concept using clinical ultrasound scanner

4.2 Methods

4.2.1 Synthetic Aperture Based Re-Beamforming

The difference between ultrasound beamforming and PA beamforming is the TOF and accompanied delay function. ultrasound beamforming takes into account the TOF of the round trip of acoustic signals transmitted and received by the ultrasound probe elements (that is sent to and reflected from targets), while PA beamforming only counts a one way trip from the PA source to the ultrasound probe. Therefore, the PA signals under ultrasound beamforming is defocused due to an incorrect delay function.

The delay function in dynamically focused ultrasound beamforming takes into account the round trip between the transmitter and the reflecting point, thus the focus point at each depth becomes the half distance for that in PA beamforming. Thereby, it is possible to consider that there is a virtual point source, of which depth is dynamically varied in the axial dimension by a maximum value equal to half distance

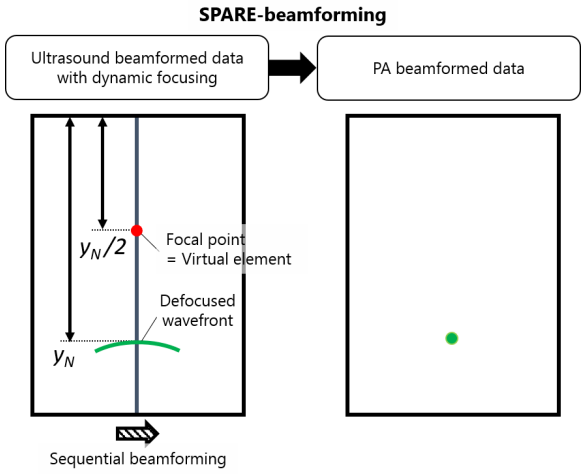

Figure 4.2: Illustration of synthetic aperture based re-beamforming processes.

of the true focal point. The TOF from the virtual element to the receiving elements can be formulated as

$$t = \frac{r}{c}, \tag{4.1}$$

where

$$r = \sqrt{\left(\frac{y_n}{2}\right)^2 + (x_m)^2}. \tag{4.2}$$

4.2.2 Simulation Setup

For the simulation, five point targets were placed at the depth of 10 mm to 50 mm with 10 mm intervals. A 0.3 mm pitch linear array transducer with 128 elements was designed to receive the PA signals. Delay-and-sum with dynamic receive focusing and an aperture size of 4.8 mm was used to beamform the simulated channel data assuming US delays.

4.2.3 Experimental Setup and LED Light Source

The PA sensing system was employed for evaluating the proposed LED-based PA imaging performance; A near-infrared pulsed LED illumination system (Prexion Inc., Japan) was used for PA signal generation. Table 4.1 summarizes the specifications of the compact and safe laser system; The arrays of HDHP LED light source can be comprised by various wavelengths throughout 365 to 1450 nm. Especially, near-infrared wavelengths such as 690, 760, 780, 850 nm can be used for diagnostic PA imaging with deep penetration depth. Also, the system supports combination mode between 690 and 850 nm. The effective illumination area of each LED head is 50 by 7 mm^2 which is compatible for common clinical ultrasound array transducer. The pulse energy is up to 200 μJ at variable pulse width from 30 to 135 nm. The pulse repetition rate is up to 4 kHz, which is desirable for high-speed PA imaging. To collect the generated PA signals, a clinical ultrasound machine (Sonix Touch, Ultrasonix) with a 10 MHz linear ultrasound probe (L14-5/38, Ultrasonix), which was used to display and save the received data. The laser transmission triggered the clinical ultrasound machine line reception. A line phantom made with fishing wire was imaged to evaluate the SNR and resolutional performance. The ultrasound post-beamformed RF data with dynamic receive focusing was then saved. To validate the channel data recovery through inverse beamforming, the raw channel data was collected using a data acquisition device (DAQ). For in vivo experiment, a open scalp piglet head and human fingers were imaged using 850 nm LED bars. The channel data was collected

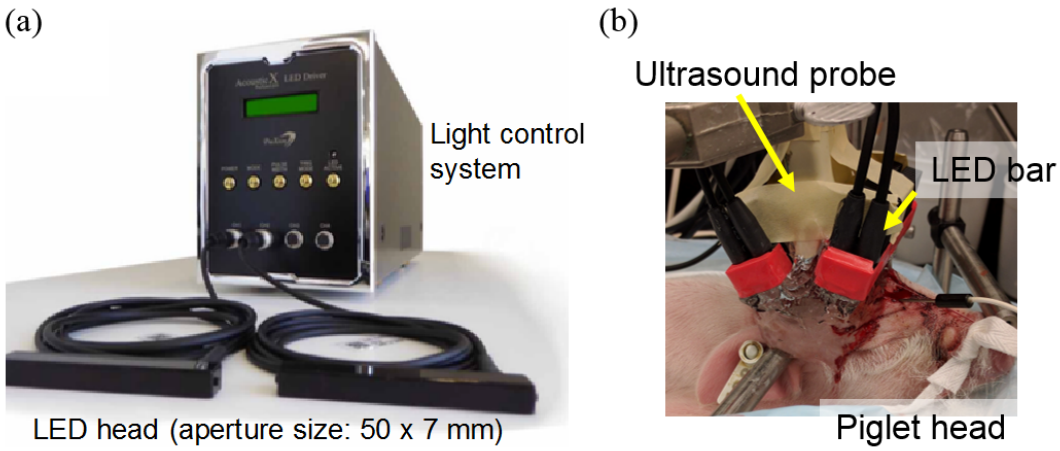

Figure 4.3: Experimental setup. (a) LED light source. (b) *In vivo* experiment configuration.

first, then the ultrasound beamformed data was generated to compare conventional and proposed beamforming approaches.

4.3 Results

4.3.1 Simulation Analysis

The simulation results are shown in Fig. 4.4. The US beamformed RF data was defocused due to an incorrect delay function (Fig. 4.4(b)). The reconstructed PA images are shown in Figs. 4.4(c-e). The proposed two approaches were compared to the ground truth conventional PA beamforming using channel data. The measured full width at the half maximum (FWHM) was shown in Table 4.2. The reconstructed point size was comparable to the point reconstructed using a 9.6 mm aperture on the

Table 4.1: Specifications of the near-infrared, pulsed LED illumination system.

	Specifications
Light source	HDHP LED
Maximum energy per pulse	850 nm: 20 J/pulse, 690 nm: 80 J/pulse, 925 nm: 80 J/pulse
Wavelength	365, 405, 525, 630, 690, 760, 780, 850, 930, 1050, 1200, 1450 nm (single mode), 690/850 nm (combination mode)
PRF	Variable up to 4 kHz
Pulse width	Selectable from 30, 45, 60, 75, 90, 105, 120, 135 nm
Driver ports	4
Pulse trigger mode	Normal or alternate drive mode for combination LED setup
Pulse trigger ports	Internal trigger output x 1, External trigger input x 1

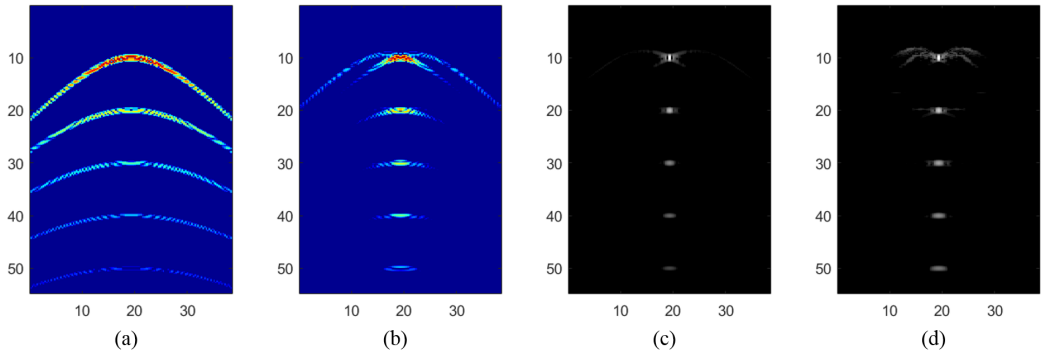

Figure 4.4: Simulation results. (a) Channel data. (b) US post-beamformed RF data. (c) Reconstructed PA image from channel data with an aperture size of 9.6 mm. (d) Reconstructed PA image through inverse beamforming. (e) Reconstructed PA image through SA re-beamforming.

conventional PA beamforming.

4.3.2 LED Light Source

Figure 4.5 shows the experimental results imaging the cross section of a line phantom. The control data was reconstructed from channel data collected using DAQ. The SPARE result used the ultrasound post-beamformed data collected from the ultrasound scanner as the input. Compering the inherent resolution of two methods, the proposed SPARE showed a better imaging contrast and SNR. By quantifying the SNR change over the number of averaging, these two were correlated in log-linear model for both with and without using channel data (Fig. 4.5(b)). The gradient of SPARE method was larger than conventional PA reconstruction from channel data in this result, because the ultrasound beamformed data was summed once already across the aperture even with incorrect focus, and the random noise can be suppressed in

Table 4.2: FWHM of the simulated point targets for corresponding beamforming methods.

FWHM (mm)	Control using channel data	SA Re-beamforming
10 mm depth	0.60	0.63
20 mm depth	1.02	0.99
30 mm depth	1.53	1.43
40 mm depth	1.94	1.91
50 mm depth	2.45	2.42

this process. For resolution, the control result showed better spatial resotuion compared to the SPARE result because the ultrasound beamformed data was formed from limited aperture size (maximum 32 elements) due to ultrasound scanner limitation, while the channel data could utilize the full aperture for reconstruction.

4.3.3 *In Vivo* Evaluation

Figures 4.6 and 4.7 show the results of *in vivo* study imaging a piglet head and human fingers. To maximize the imaging contrast, the raw channel data was averaged 3000 times. From piglet data, we demontrated the capability of imaging blood vessel transcranially. Piglet is known for an animal model similar to newborn baby especially for the head, so that this result indicates the potential application of LED-based PA imaging modality for measuring blood oxygenation level of newborn baby during labor (Fig. 4.6). Human fingers were imaged to show its inherent contrast applied

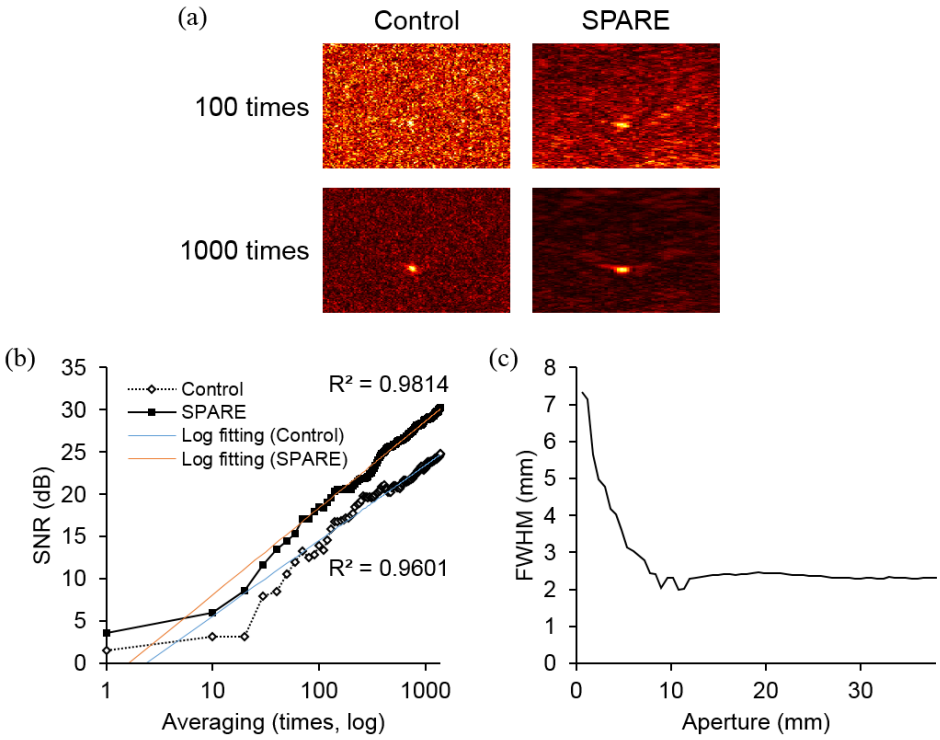

Figure 4.5: Experiment results with LED light source imaging line phantom. (a) Comparison of control using channel datafrom and SPARE results using ultrasound post-beamformed data. (b) SNR analysis of both control and SPARE results. (c) Resolution analysis of SPARE results. Resolution improvement was hindered at FWHM of 2 mm due to the aperture size.

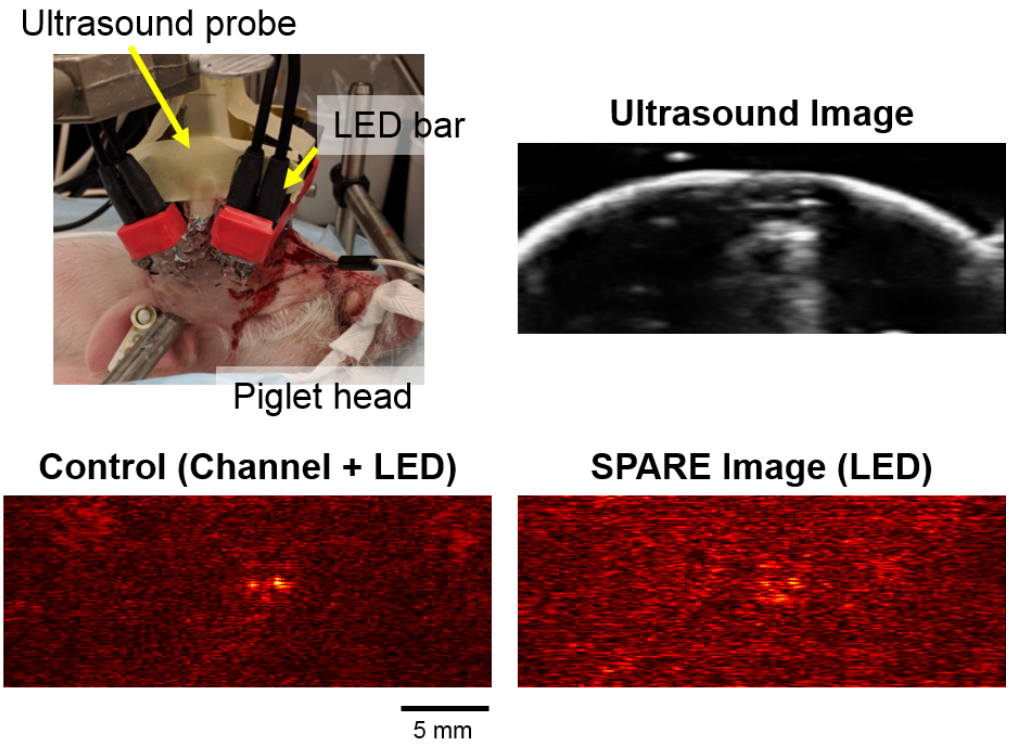

Figure 4.6: *in vivo* PA imaging of piglet head using LED light source. Experimental configuration, ultrasound and PA images of piglet head are shown. PA images were reconstructed using channel data from DAQ device and beamformed RF data with the SPARE algorithm.

on the human (Fig. 4.7). Melanin layer covering the skin could be depicted by the imager.

4.4 Discussion and Conclusions

The proposed algorithms would work for any structures that have high optical absorption such as a blood vessel that shows strong contrast for near-infrared wavelength light excitation. The reconstruction artifacts such as side lobe and grating

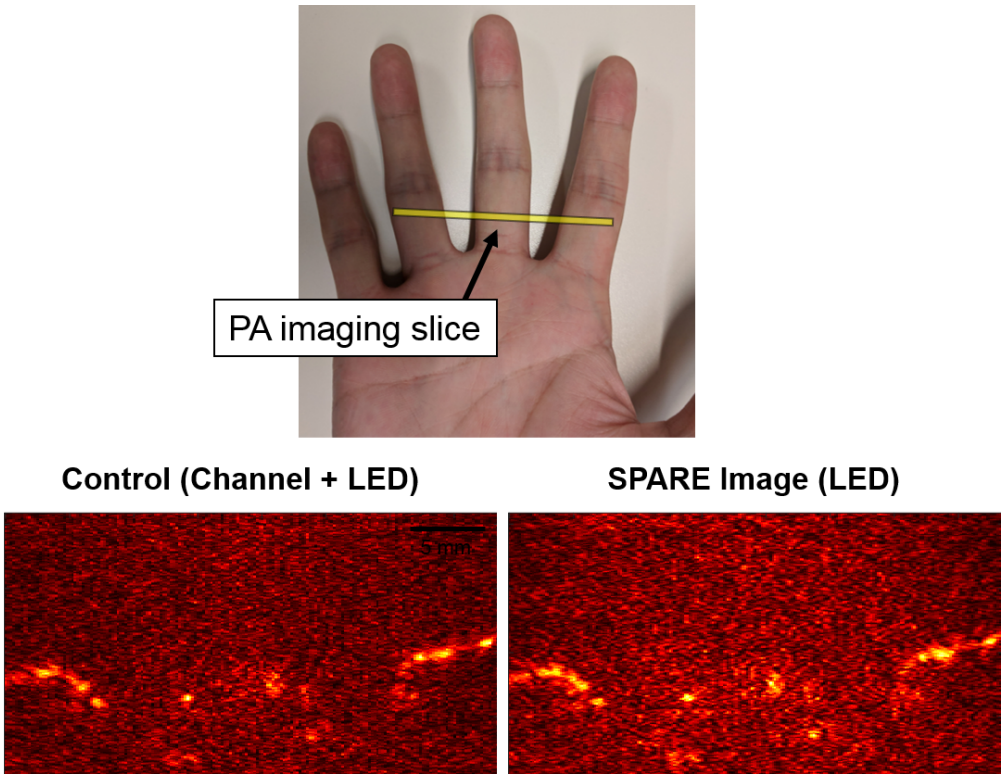

Figure 4.7: *in vivo* PA imaging of human fingers using LED light source. Experimental configuration, ultrasound and PA images of human fingers are shown. PA images were reconstructed using channel data from DAQ device and beamformed RF data with the SPARE algorithm.

lobe could be appeared and affect on non-point target as the image quality of SPARE image was worse compared to conventional PA image using channel data. This effect was more obvisous on high frequency signals as shown in simulation evaluation in Chapter 2. The algorithms could be also integrated into a real-time imaging system using clinical ultrasound machines.

A high PRF laser system is considered as a system requirement for using SPARE algorithm, as it is necessary to synchronize the laser transmission to the ultrasound line transmission trigger timing. To keep the frame rate similar to that of conventional ultrasound B-mode imaging, the PRF of the laser transmission should be the same as the transmission rate, in the range of at least several kHz. Therefore, a high PRF laser system such as a LED or a laser diode is desirable. Based on the assumption that the LED frame rate is 16,000 and the reception ultrasound has 128 lines acquistion, Figure 4.8 summarizes the estimated frame rate and laser energy by varying the number of averaging. Since SNR improvement under averaging is the square root of the number of averaging, outputing 1mJ and 5mJ light source energy requires 25 and 625 times averaging, respectively. When the daq device is accessible, the maximum available frame rate is 625 and 25.6 frame per second, respectively. When clinical ultrasound scanner was used for data acquisition, the frame rate becomes 5 and 0.2 frame per second, respectively. The maximum available frame rate using clinical ultrasound machine is 125 without averaging.

In this chapter, we proposed a new paradigm on PA imaging using a LED light

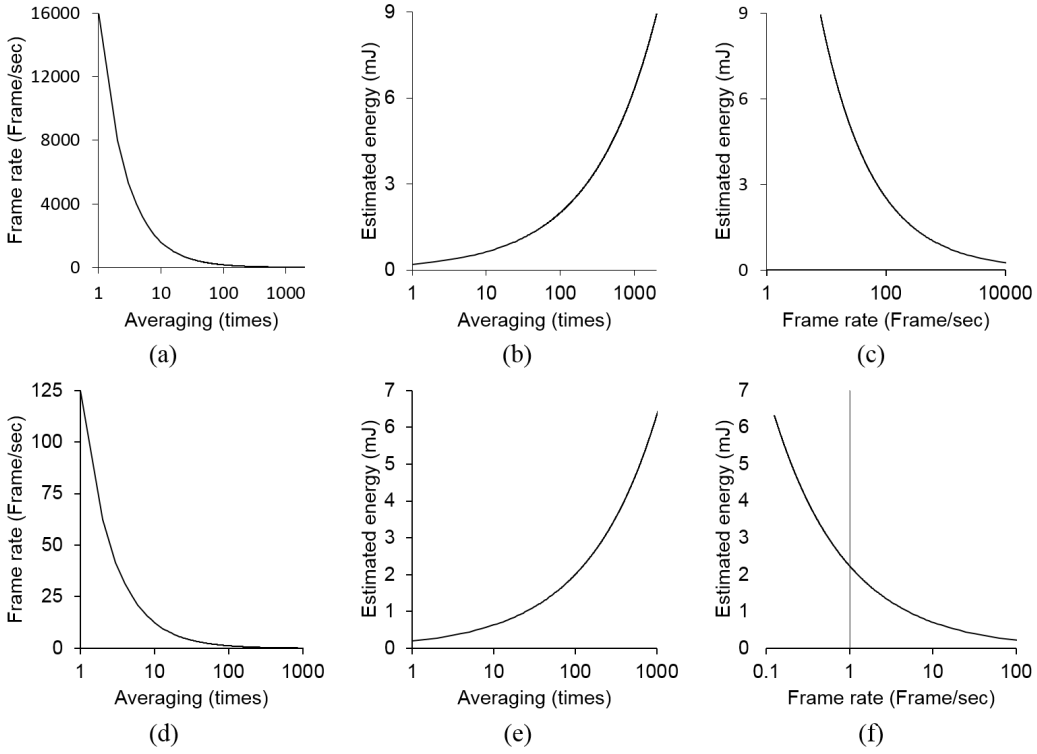

Figure 4.8: Numerical estimation of frame rate using a LED system. Frame rate (a,d) and estimated energy (b,e) by varying the number of averaging, and the relationship between frame rate and estimated energy (c,f) are shown using a DAQ device (a-c), and using a clinical ultrasound system (d-f) for data collection.

source and US post-beamformed RF data from a clinical ultrasound system. SA based re-beamforming was used and their performance was demonstrated in the simulation. In addition, low-cost light source using LED was introduced and the experimental study using a line phantom and *in vivo* targets revealed the validity and clinical significance of these methods, in that a similar resolution was achieved compared to PA imaging using channel data.

Part II

Co-Robotic Ultrasound and Photoacoustic Imaging

Chapter 5

Cooperatively Controlled Robotic Ultrasound System

This chapter has been published as: *T.-Y. Fang, H. K. Zhang, R. Finocchi, R. H. Taylor, E. M. Boctor, "Force Assisted Ultrasound Imaging System through Dual Force Sensing and Admittance Robot Control in International Journal for Computer Assisted Radiology and Surgery (IJCARS), 12(6), 983-991, 2017.*

This work was co-led with a master student, Ting-Yun (Angel) Fang. I was responsible for the project design, data collection, and part of writing especially skeleton preparation. Rodolfo Finocchi conducted a preliminary study that was the basis for this work. Dr. Russell H. Taylor and Dr. Emad M. Boctor supervised the anaysis and edited the manuscript.

5.1 Introduction

Ultrasound (US) imaging has served as a gold standard for various clinical diagnoses and applications. US imaging has unique advantages, including low-cost, non-invasiveness, and safety to the human body, compared to other major imaging modalities such as CT or MRI. Due to the requirement of acoustic coupling, US systems require the probe to touch the subject during a scan. The image quality highly depends on the probe position, orientation, and applied force. These parameters are barely reproducible throughout a medical treatment and through different sonographers. In addition, the ultrasound scanning process sometimes requires applying large forces over extended periods of time, often in an awkward posture to maintain the desired orientation. Echocardiography in particular requires larger contact forces in order to acquire a better image resolution of deep organs, and extra force is needed for scanning obese patients or pregnant women. This physical requirement over a sonographer's career often leads to musculoskeletal pain and strain injuries [29, 30].

To overcome these challenges, autonomous robotic or remotely operated (teleoperated) robotic US systems have been proposed [31, 32]. With robotic assistance, precise control of the US probe is possible, making the procedure repeatable and less user-dependent. Hennersperger et al. integrated an US probe onto a 7 degree-of-freedom (DOF) robotic arm for autonomous US scanning [33]. However, the limitation of autonomous robotic or remotely operated robotic US systems is the loss of haptic feedback for the user. Though some remote-control based US systems with

haptic feedback have been proposed, these systems are less likely to make it to clinical practice due to: 1) sonographers like to keep a close proximity to their patients since scanning protocols require communication, and 2) vendors dont provide remotely controlled US systems [34–36]. With the recent introduction of lightweight robotic systems, several groups have started to consider better execution of surgeonrobot cooperative control systems (also known as co-robotic systems) [31]. This control method senses the force applied on the probe by the operator, and asks the robotic arm to follow the operators intended motion. Sen et al. integrated the cooperative control on robotic US with virtual fixture constraints that provide haptic feedback and guide the probe motion [37].

Here, we propose a co-robotic US imaging system using a 6-axis robotic arm mounted with two force sensors - a 6 DOF force sensor and a 1 DOF load cell - integrated with a handheld US device. The combination of dual force sensors enables the differentiation of two types of forces: the users applied force and the contact force between the probe and the tissue. With the admittance force control, the robotic arm follows the motion of the operator, while adding forces during scanning. In addition to user-robot cooperative scanning, the handheld device can be smoothly detached from the robot to perform conventional freehand scanning. Furthermore, the robot assisted system can improve the steadiness of the contact force acting on the scanning target, and consequently provides stable and repeatable US scanning and image acquisition.

5.2 Contributions and Acknowledgements

The main contributions of this chapter are the following:

- Development and validation of force assisting co-robotic ultrasound system
- Development of dual-sensor based cooperative robot control

5.3 Materials and Methods

5.3.1 System Overview

The proposed co-robotic system is composed of a 6-axis robotic arm (UR5, Universal Robots, Odense, Denmark) mounted with a 6 DOF force/torque sensor (FT-150, Robotiq), a detachable handheld US device with a 1 DOF load cell (Model 31 Mid, Honeywell), and a US probe (L14-5W/60, Ultrasonix) (Fig. 5.1). When the handheld device is attached to the robot, the robot complies with the operators motion through cooperative control based on the reading of 6 DOF force sensor. The 1 DOF load cell on the handheld device measures the contact force between the US probe and the tissue surface. The force assisted mode is triggered by the contact between the US probe and tissue. To reduce the force applied by the user, the robotic arm magnifies the force input, and assists in reaching the target contact force under different scenarios (Sections 5.3.3 and 5.3.4). The handheld US device can be quickly detached and reattached to the robotic arm. The following section covers the design in detail.

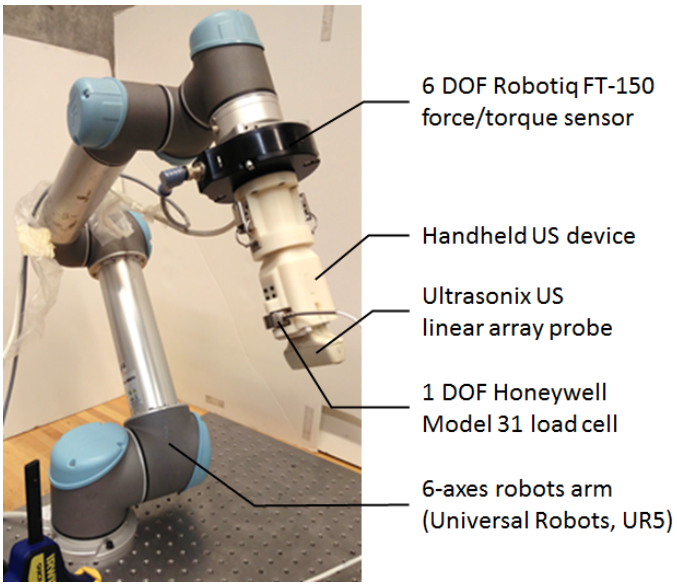

Figure 5.1: The co-robotic ultrasound system with dual force sensing. The US probe is actuated by a 6-axis robotic arm through the users force input on the handheld device.

5.3.2 Handheld Ultrasound Component

The handheld US device is designed with several features:

- Easy to use. The device is easy and comfortable for the operator to hold without drastically changing the size and shape of the US probe.
- Fast detachment/attachment. The sonographer can scan freehand by detaching the device from the robot, with contact force measurements still available.
- Compatible with different types of US probe. To meet the requirement of using different US probes under certain situations, the device can be reassembled by simply changing the inner case.

The device can be divided into two main parts (Fig. 5.2a). The first part is the

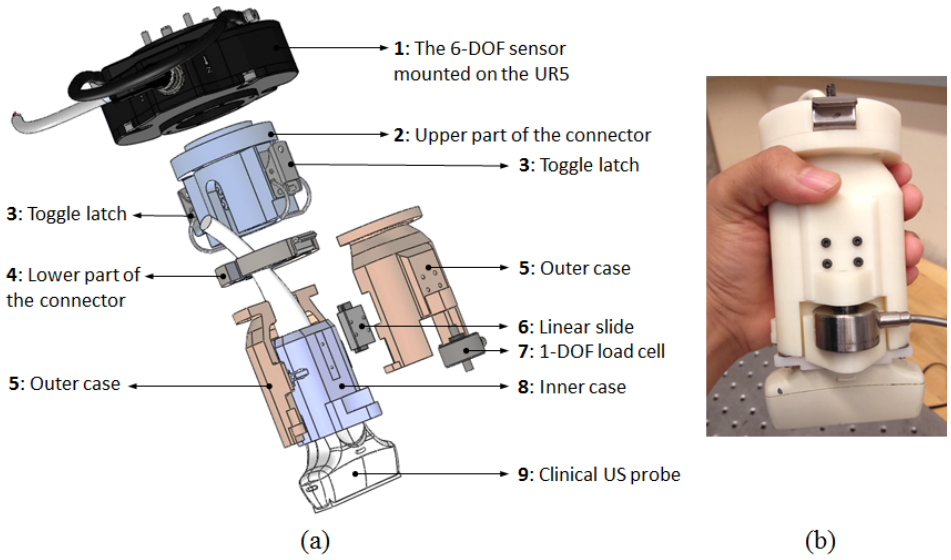

Figure 5.2: The design of the handheld US device. (a) The exploded CAD model of the handheld US device. (b) The probe holder **4-9** can be smoothly detached from the robotic arm to perform freehand scanning, while the contact force information remains accessible.

connector **2**, which is fastened to the robot body **1**. The second part **4-9**, the probe holder, is attached to the connector using two toggle latches **3**. Two additional slots on the bottom of the connector **2** restrict rotations between the probe holder and the connector.

The probe holder consists of an outer case **5**, an inner case **8**, a linear slide **6**, a 1 DOF load cell **7** and a US probe **9**. The outer and inner cases are assembled using the linear slide **6**. The linear slide permits the axial motion while minimizing the friction between the two cases. It also mitigates the torque generated by the contact force due to misalignment between the contact point and the axis of the load cell.

Most parts of the device, namely parts **2**, **4**, **5**, and **8**, were 3D printed with

Acrylonitrile-Butadiene-Styrene (ABS). This allows customization of the specific shape of the inner case 8 such that it can be modified to fit any US probe perfectly. With the toggle latches **3**, the probe can be detached from the robot and used to perform freehand scanning (Fig. 5.2(b)).

5.3.3 Admittance robot control

Admittance robot control is a force control approach for human-machine interaction, and allows the robot to perform a smooth and desired task from human force input [37–39]. Based on force scaling and contact force feedback, the equation for calculating the tool velocity is written as:

$$\dot{x_t} = K \cdot (F_t + \gamma F_c) = \text{diag}(K_1, K_2, \cdots, K_6) \cdot (F_t + \gamma F_c), \tag{5.1}$$

$$\dot{x_w} = Ad_{gwt}\dot{x_t}, \tag{5.2}$$

where $\dot{x_t}$ and $\dot{x_w}$ are the desired tool velocity with respect to (w.r.t.) the robot tool frame and the world frame, respectively; Ad_{gwt} is the adjoint transformation from the tool frame to the world frame; $F_t = [F_x, F_y, F_z, M_x, M_y, M_z]^T$ denotes the human handling force and torque, measured by the 6 DOF sensor w.r.t. the robot tool frame; $F_t = [0, 0, F_c, 0, 0, 0]^T$ denotes the US probe contact force obtained from the 1 DOF senor. F_c is always a positive number, as only the compression force is measured; K and $\gamma \in [0, 1]$ are the constant admittance gain and force scaling factor, respectively, which were empirically defined. The force applied by an operators hand

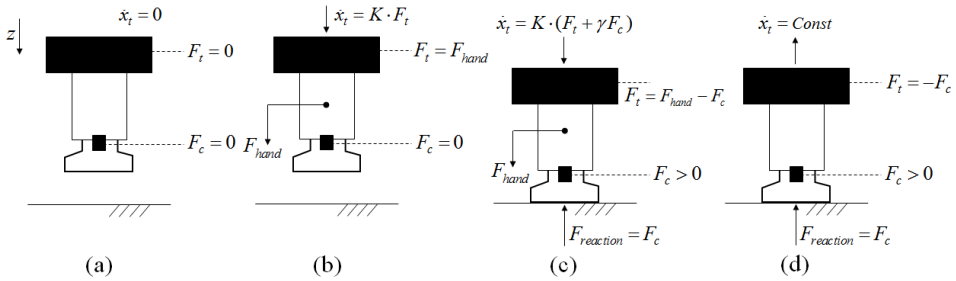

Figure 5.3: The free body diagram of the system under different scenarios. (a) The probe stays in free space. (b) The user is moving the probe in free space. (c) The user is scanning the object using the system. (d) The user released the probe during scanning.

can be magnified by the robot based on this force scaling factor γ.

Figure 5.3 illustrates the free body diagram (FBD) of forces, and the resulting robot command under different scenarios. When the probes is in free space (Figs. 5.3(a-b)), the contact force F_c equal to zero, and the robot follows the user's force input (Fig. 5.3(b)). When the probe is in contact with the tissue (Figs. 5.3(c-d)), the 1 DOF sensor senses the actual contact force between the probe and the object. If a force is applied by the user (Fig. 5.3(c)), the robot provides extra force assistance based on the admittance control equation 5.1. At the instance the user releases the US probe (Fig. 5.3(d)), the axial force reading of 6 DOF sensor becomes negative. This negative reading triggeres a preset of assigning a constant tool velocity, and the robot moves the probe upward until the probe has not more tissue contact.

The counter effect of enviornmental noise, such as robot vibration, on the human handling forces F_t, and subsequently the robot velocity commands $\dot{x}_t$, a One Euro filter is applied on the velocty command ($\dot{x}_t$) to smooth the robot motion [40].

5.3.4 Velocity Gain Variable

To further smooth and improve force assistance, we took advantage of dual force sensing that is capable of differentiating the applied force and the contact force, and defined an additional gain factor $\mu \in [0, 1]$ as

$$\dot{x}_{send} = \mu \dot{x_w}, \tag{5.3}$$

where $\dot{x}_{send}$ send denotes the actual speed command sent to the robot. The velocity gain μ can be considered as robot sensitivity or how fast the robot should follow the operator, and mainly depends on three factors: 1) whether the probe is in contact with tissue; 2) whether the contact force is out of a safety bound; 3) the direction and the magnitude of the applied force. The velocity gain varies based on different control regimens as follows:

a) Compliant mode: μ=1

   When the probe is not touching the tissue, and only the users force is present ($F_c = 0$), the velocity gain is set to 1, allowing freehand motion.

b) Force assisted mode: $\mu = \text{Const} \in (0, 1)$

   Force assisted mode is activated when the probe makes contact with the scanning object ($F_c > 0$). The velocity gain is set to a constant within the range $(0, 1)$. At this instance, dual sensors allow the robot to sense both the users force and the counterforce from the tissue, where the users force is the sum of the two sensors axial readings. In our setup, the constant velocity gain is set to

0.2 empirically.

c) Target force assisted mode: $\mu = \text{Variable} \in [0, 1]$

In addition to simply magnifying the force, this mode is designed to assist the user in smoothly reaching a specific target contact force. When the target force is set to a value larger than zero ($F_{Goal} > 0$), the velocity gain is set accordingly as

$$\begin{cases} \mu = \dfrac{F_{Goal} - F_c}{F_{Goal}} & \text{if } F_{Goal} \geq F_c \\ \mu = \text{Const} & \text{if } F_{Goal} < F_c \end{cases}. \tag{5.4}$$

Under this formulation, the robot speed decreases as the actual contact force approaches the goal force. It dynamically guides the operator to reach the target force. If the contact force goes beyond the goal force; the velocity gain would be set to a constant (0.01), in that no further force boost is required. In practice, the target contact force should be altered based on the patients physique and the sonographers experience.

d) Motion restriction mode: $\mu = 0$ or $\text{Const} \in (0, 1]$

When the contact force exceeds the safety boundary (or F_{Goal}), the robot restricts the operators motion from pushing further ($\mu = 0$), while allowing motions in the opposite direction ($\mu \in (0, 1]$). This safety feature is a maximum admittance force constraint that allows the operator to focus on the US images without being concerned with the current force or excessive force application.

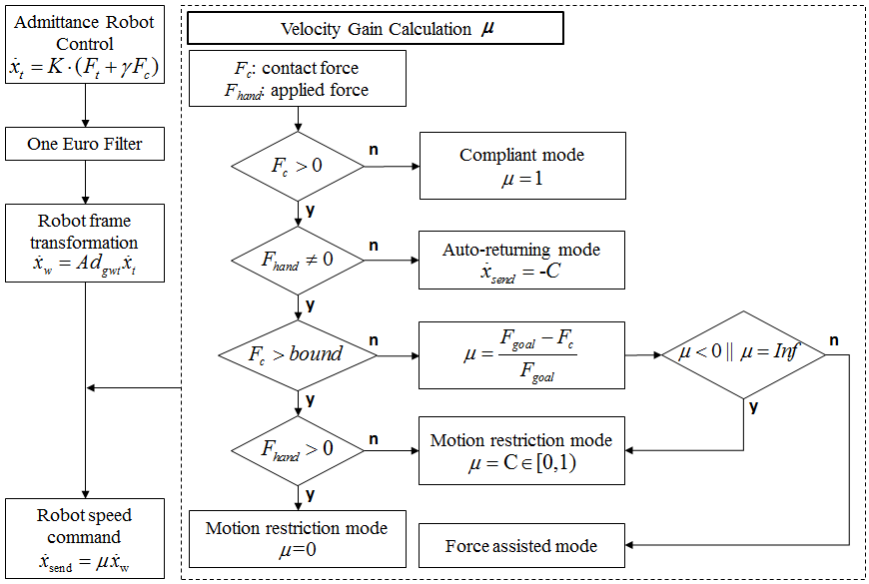

Figure 5.4: The diagram summarizing modified admittance robot control and velocity gain calculation.

e) Auto-Returning mode:

For safety, the robot is designed to automatically release the force from the tissue by sending a constant speed command (10 mm/s) in the opposite direction when no force input from the user is present. The auto-returning mode is active only when there exists a contact between the probe and the tissue. Thus, it is automatically terminated if there is no contact force (stops within 2s from experience).

Figure 5.4 summarizes the modified admittance controls step-by-step algorithm and velocity gain determination under different modes. Although the velocity gain theoretically could be incorporated with the constant admittance gain K in equation 5.1, we separated them for two reasons. The first reason is to enable a flexible gain

variation for different modes, and to simplify the robot control. The second, and more important, reason is to address the issue of sensor noise. Our approach can integrate additional filtering, such as the One Euro filter, to smooth the velocity command. Otherwise, undesired velocity commands could be contaminated when the velocity gain is smaller than the noise.

5.4 Experimental setup

We conducted a user study to evaluate the performance of the proposed system. The protocol was approved by the institutional review board at Johns Hopkins University. Before the study, the 1 DOF load cell was calibrated. We applied different forces to the load cell and recorded both the contact forces with an electric scale and the resulting output voltages (sensor readings). The relationship can be approximated with two linear equations (shown in table 5.1), where the intersection point of the two lines lays at 4 N. The estimated regression model is shown in Fig. 5.5. The estimated two linear models had mean square errors of 0.40 N and 0.49 N for forces smaller and larger than 4 N, respectively.

In the user study, six volunteers participated, including two experts, professional and licensed sonographers, and four non-experts. Non-experts included one layman who was briefly taught how to operate the ultrasound machine, and three researchers with a basic understand of US imaging, but without a license. Each volunteer subject

Table 5.1: The calibrated model for the load cell. Note F stands for contact force, and v is voltage reading.

Approximated model	$F(v) = a + b * v$	
	a	b
$F > 4N$	3.120	3.707
$F < 4N$	0.601	10.61

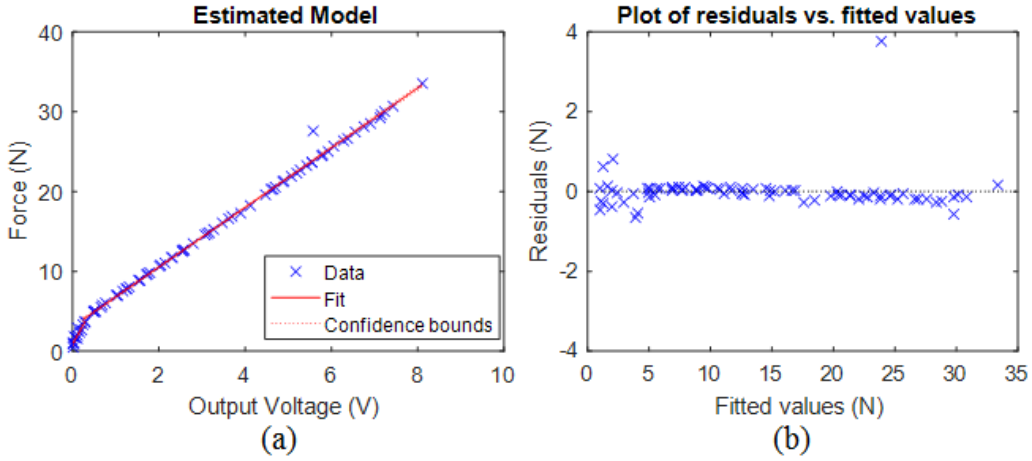

Figure 5.5: The estimated linear regression model for 1 DOF load cell. (a) Comparison of the measured data and the estimated regression model. (b) The residual error plot of the estimated model.

was asked to scan a female uterus phantom using the linear array US probe in a standing position and hold the position for 20 seconds (Fig. 5.6(a)). We assigned a target force of 20 N during the scan, emulating a typical procedure that requires application of relatively large force such as for obese patients or in obstetrics and gynecology. These time and force parameters were chosen to take the fatigue factor into account. The phantom was placed about 50 cm away from the operator at

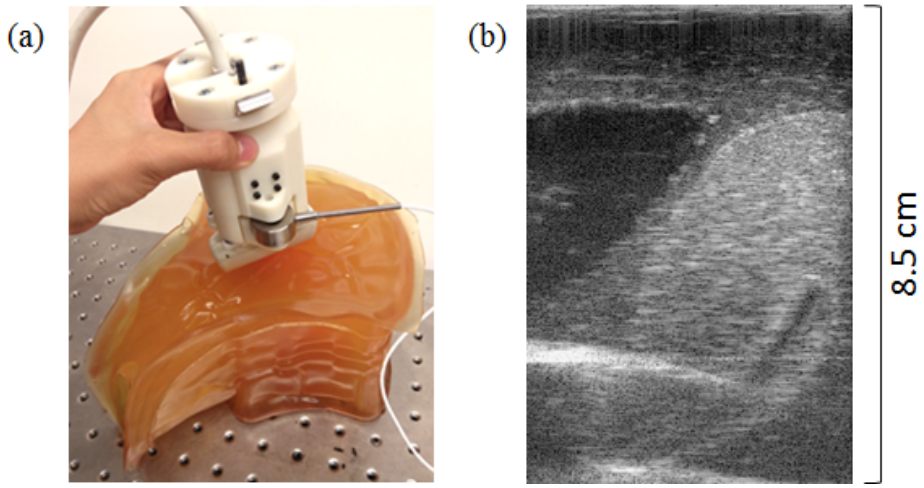

Figure 5.6: The scanning position is roughly the same in the four cases. (a) The position and the orientation of the US probe relative to the phantom. (b) An example of the scanned US image.

waist-height. This scanning procedure was conducted under four different scanning scenarios: 1) freehand scanning (detached from the robotic arm) without providing contact force information; 2) freehand scanning with real-time visual feedback of the contact force, where the force value was displayed on a GUI; 3) robot assisted scanning without maximum admittance force constraint; 4) robot assisted scanning with a maximum admittance force constraint. Note that to make a fair comparison, all case recordings started from the same initial pose with the same 20 N force applied, and the task was to maintain the pose under the different scenarios. Visual force feedback was allowed in Case 2 and 3, where the subject watched both the US images and the force reading (placed next to each other). For each scenario, the procedure was repeated five times. During the scan, the force readings from two sensors and the continuous US images were recorded (SonixTouch, Ultrasonix) for further analysis.

For evaluation, we calculated the contact force variation over time and used it as the metric for the applied force stability. To compare the stability on US images, the metric of image cross-correlation was used to quantify the subtle change in the US image appearance. The very first US image in a volume of dataset was set as the reference image, and the remaining images were compared with the reference using the normalized cross-correlation (NCC) method. The scanning position and orientation are shown in Fig. 5.6(a), and its US image appearance is shown in Fig. 5.6(b), where the scanning depth was set to 8.5 centimeters. We expect the NCC variation mostly came from the probe motion as other factors were consistent. To effectively evaluate the results, we collected a baseline data, where the US probe was placed on the phantom with 20 N using the robotic arm while the position is locked for 20 seconds. The NCC value resulted in 0.83-0.96. This could be due to the inherent image noise from the US system we used.

5.5 Results

5.5.1 Applied Force Reduction

The comparison of the human applied force and the measured phantom contact force are plotted in Fig. 5.7. This result indicates that the robot assistance in case 3 and case 4 reduces the force applied by the human participants from 20 N to an average of 5.48 N and 13.62 N, which are 73 % and 32 % reductions, respectively.

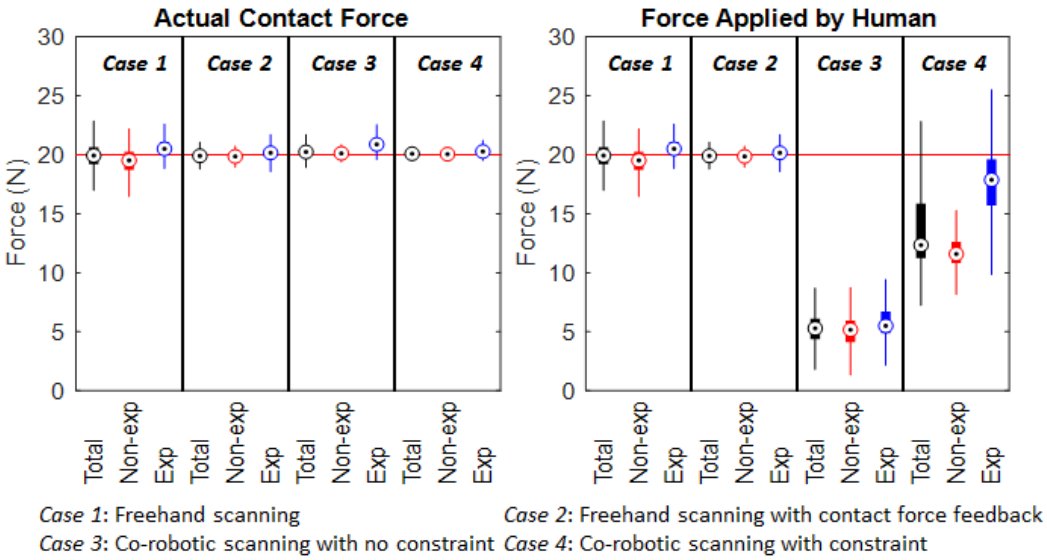

Figure 5.7: The comparison of the force applied to the tissue and from the operators for four cases. Co-robotic systems (#3 and #4) shows a substantial reduction in applied force compared to freehand scanning (#1 and #2).

The applied force in case 4 was higher than that in case 3 because the subject knew that applying a higher force was constrained to 20 N, and effectively utilized the force constraint feature to stabilize the scanning.

5.5.2 Stability of Contact Forces

To quantify the stability of the contact force, we analyzed the standard deviation (SD) of the 20 second data sets. Fig. 5.8 shows the SD of the contact force for the four scanning scenarios under different test subject groups. The average SD of all subjects (including the experts and non-experts) in case 2 ($\sigma_2 = 0.263$) decreased compared with case 1 ($\sigma_1 = 0.433$). In case 2, the 20 N force was better maintained than in case 1, since the subjects had the knowledge of the contact force value. In

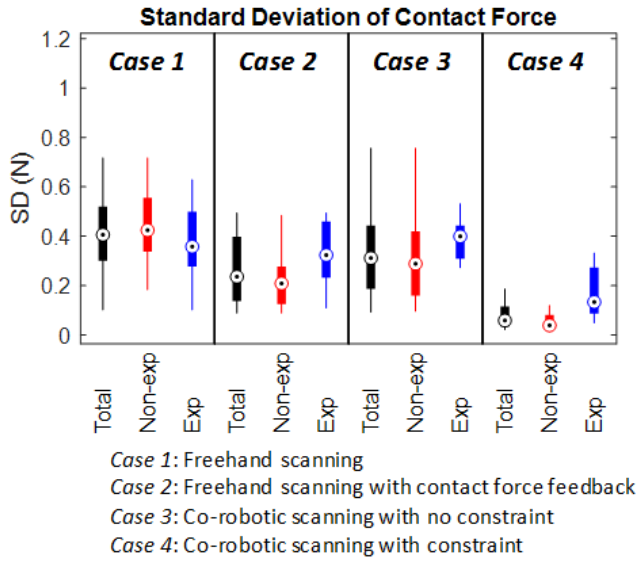

Figure 5.8: The contact force stability with 20 N contact-force application over 20 seconds of scanning. The standard deviation of the contact force in four distinct scenarios is shown.

case 3, the average standard deviation slightly increased ($\sigma_3 = 0.335$) under co-robotic operation. In case 4, the co-robotic system substantially stabilized the contact force ($\sigma_4 = 0.093$). With the maximum admittance force constraint, the operator can rely on the constraint feature, and is not required to monitor the contact force reading.

To verify the statistical significance of the result, we performed a two-tailed t-test for the SD of all subjects for every case combination. The null hypothesis was that the two means of the SDs in two cases were identical. For small p-values under 0.01 we reject the null hypothesis and the alternative hypothesis, the two means have difference, stands. The p-value results shown in Table 5.2 indicate statistical significance, confirming that our experiment results did not occur by accident.

Table 5.2: T-test results confirm the force stability improvement of the system. The p-values for the hypothesis that SD of the contact force is the same for any pair of cases occurs by accident are shown. Note H_0 : mean of σ_i = mean of σ_j, and H_A : mean of $\sigma_i \neq$ mean of σ_j.

$Case_{ij}$	1	2	3	4
1	-	<0.001	0.047	<0.001
2	<0.001	-	0.073	<0.001
3	0.047	0.073	-	<0.001
4	<0.001	<0.001	<0.001	-

5.5.3 Stability of Ultrasound Images

Fig. 5.9 shows the results of image similarity analysis through cross-correlation for all cases and different subject groups. The average NCC value of the two freehand cases 1 ($\beta_1 = 0.782$) and 2 ($\beta_2 = 0.729$) did not show a significant difference, indicating the images did not improve, although case 2 showed more stable force readings. This could be because in case 2, the user only had 1 DOF reading, and did not have access to other DOFs such as out-of-plane motion. The US images, on the other hand, were sensitive to these motions. In contrast with freehand scanning, the co-robotic system in case 3 slightly improved the image stability ($\beta_3 = 0.785$) by 8 % (compared with case 2), even though this case was less stable in the force measurement. This could be due to the fact that there is more restriction on the out-of-plane motion or probe orientation with the robotic arm than without. The robot made the US probe harder to rotate or move in elevation and lateral direction. In case 4, the co-robotic

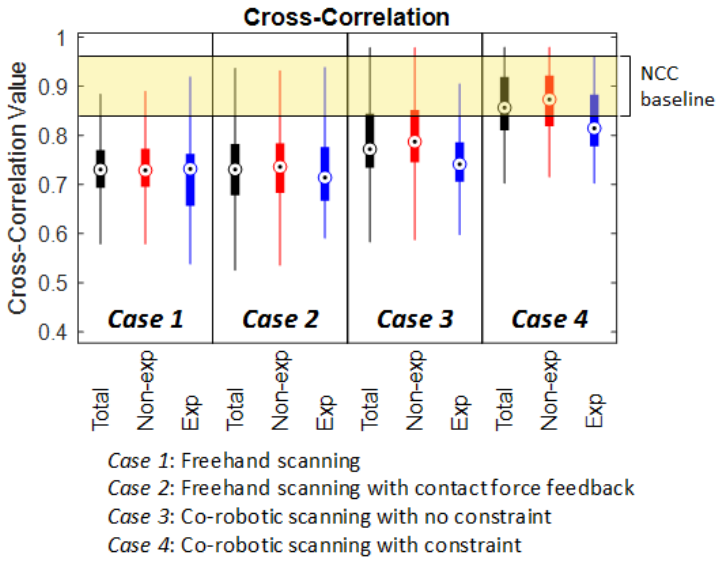

Figure 5.9: The US image stability with 20 N contact-force application over 20 seconds of scanning. The image cross-correlation relative to the initial image in four distinct scenarios is shown.

system improved image stability where the NCC value increased to be an average of 0.861, which is 18 % higher than the case 1. This is comparable to the baseline (0.83-0.96). The difference between maximum and minimum cross-correlation value was also smaller compared to the other three cases.

A two-tailed t-test was performed to verify the average cross-correlation value (β), and the p-value results are shown in Table 3. For case 1 and 2, we failed to reject the null hypothesis $\beta_1 = \beta_2$ which indicates that the stability of US image might not improve with the extra contact force feedback. The results using the co-robotic system in both cases 3 and 4 showed statistically significant improvements over freehand scanning, while case 4 was better than case 3.

Table 5.3: T-test results confirm the US image stability improvement through the system. The p-values for the hypothesis that the cross-correlation comparing pair of cases occurred by accident are shown. Note $H_0 : \beta_i = \beta_j$, and $H_A : \beta_i \neq \beta_j$.

$Case_{ij}$	1	2	3	4
1	-	0.786	<0.001	<0.001
2	0.786	-	<0.001	<0.001
3	<0.001	<0.001	-	<0.001
4	<0.001	<0.001	<0.001	-

5.6 Discussion and Conclusions

In this paper, we presented a co-robotic, dual force sensing system that assists sonographers performing US scanning with a reduced force and steady US imaging. Combining the two force sensors allows the robot to distinguish the human motion from the US probe contact force with the tissue. With the robot admittance force control law, the robot follows the intended motion of the operator while magnifying the human force input. The variable velocity gain facilitates the task of reaching a specific contact force and constrains the excessive force application. This system has a potential to minimize the risk of occupational injuries for sonographers, and to make the scanning tasks faster, easier, safer, and more repeatable.

The results of the user study demonstrated the reduction of human force from 20 N to $2 \sim 13N$ with the co-robotic system. With the maximum admittance force constraint, the operator is not required to monitor the contact force for safety, and this

feature makes the procedure easier and improves the stability of both the contact force and the US image. In addition, we quantitatively validated the stability improvement of the contact force and US imaging. The image stability is crucial in the clinical settings because some ultrasound procedures, such as first trimester fetal screening or US guided biopsy, require the operator to maintain the same pose for an extended period. Subtle probe misalignments could affect tissue deformation and result in destabilizing US scanning and degrading the NCC value.

In the baseline experiment, the NCC ranged from 0.83 to 0.96 instead of theoretically 1. To determine this difference, we compared two cases when the robot was on and off; the NCC showed 0.952 and 0.949 for on and off case, respectively. Thus, we concluded robot vibration had little effect on the values. While we think the main reason is the inherent NCC performance with our ultrasound system, another possible reason is the subtle motion of the phantom. Although the motion was unnoticeable from videos, the phantom gradually deformed under a fixed pressure. This small deformation could become considerable over time and introduce decorrelation on images.

The experts' results were worse than non-experts for both contact force and image stability analysis; possibly because the professional sonographers are experienced and are used to their own scanning workflow. They tend to touch the scanning object with US probe and rotate the probe around to observe the image. Actually, one of them preferred to touch the object with the side of his little finger during the scan to

stabilize his hand. In fact, our system has the potential to reduce these unnecessary motions and optimize their current procedure as the scanning is stabilized. The average force applied by experts was 17.9 N, which is higher compared to the average force of 11.6 N applied by non-experts, as shown in Fig. 5.5. However, in overall, it is demonstrated in both groups that our system reduced the amount of force execution and enhanced the scanning stability.

In this research, we chose to use a 1 DOF load cell for contact force sensing because the force applied to tissue is dominant in the axial axis [41]. Nevertheless, measuring forces in all directions could further improve the system for practical applications. As an example, in cardiac US, the sonographers have to push the probe hard and rotate it around to see the heart due to the limited scanning window; therefore, a system with higher dexterity is essential. We chose the target force of 20 N to demonstrate the performance of the system, but practically it should be adjustable during the procedure. This could be achieved by some triggers such as assigning the target force by probe motion or verbal command.

Considering the clinical transition, our prototype using the UR5 is suitable for bench-side investigation and feasibility studies. The UR5 in its current mode provides a safety stop according to end-point force output and does have virtual force sensors in all joints to detect collision. However, it does not equip joint force sensing for all joints, so that the hand-over-hand path planning or its work space wont be constrained. In order for our system to be translated to the bedside, another FDA-ready arm, such as

the new KUKA system (7 DOF robot) should be considered. The joint force sensing is a nice-to-have feature and can be used as additional safety assurance. Additionally, the reported minor vibration is coming from the UR5. Our experiments and results were not affected by the presence of this vibration because the condition was the same for all cases.

Our co-robotic system can be further improved, or effectively utilized, for many applications. Considering general clinical practice, higher dexterity of the system is desired. It can be achieved by replacing the 1 DOF load cell with a multi-axis force sensor because it can take into account more DOF contact force sensing for a higher flexibility on force control. Also, the design of the US probe holder can be further optimized by making its shape and size closer to the original US probe. It would be easier for sonographers to adapt to a new system if the device was similar to what they are used to. In addition, constrained control approaches such as virtual fixtures could be included into the proposed system to maximize the benefit of the co-robotic US system [42]. For instance, if the motion of the robot is constrained to pure in-plane or out-plane direction, there is a chance to integrate all robot tracking and US image data together to improve image resolution in deep tissue [43, 44] or to reconstruct wide-field 3D US volume [45]. These extensive utilizations of the robotic ultrasound system will be elaborated in the following chapters.

Chapter 6

Synthetic Tracked Aperture Ultrasound (STRATUS) Imaging

This chapter has been published as: *H. K. Zhang, A. Cheng, N. Bottenus, X. Guo, G. E. Trahey, Emad M. Boctor, "Synthetic Tracked Aperture Ultrasound (STRATUS) Imaging: Design, Simulation, and Experimental Evaluation", in Journal of Medical Imaging, 3(2), 027001, 2016.*

I was responsible for the project design, system integration, data collection, analysis and writing. Alexis Cheng and Nick Bottenus provided technical supports. Dr. Gregg E. Trahey and Dr. Emad M. Boctor supervised the project.

6.1 Introduction

Ultrasonography is a widely used medical imaging modality to visualize anatomical structures in the human body due to its low cost and ease of use. The image resolution of ultrasonography is affected by several factors including the center frequency of the transmission wave and the F-number, which represents the ratio of the focusing depth to the aperture size. Although a high center frequency is desired for high-resolution, high-frequency acoustic waves are easily absorbed and attenuated in the near field, resulting in degraded resolution and contrast in the far field. Consequently, only low-frequency acoustic waves are available if the region of interest is located in deep places. Similarly, F-number increases corresponding to the rise of the focusing depth, and it is challenging to acquire acceptable image quality in deep tissue, and accordingly a large aperture size is desired to decrease the F-number. In conventional ultrasound beamforming, some number of elements from an ultrasound transducer array are used as the aperture size. Synthetic aperture (SA) imaging is a technique that increases image resolution by synthesizing the information from multiple sub-apertures and extending the effective aperture size [46–48]. However, the maximum available aperture size in SA is still limited by the physical size of the ultrasound transducer. In the clinic, diagnosing obese patients with the current ultrasound imaging system is challenging, as the target region may be too deep due to a thick fat layer. Moreover, a high penetration depth with high resolution is demanded to visualize a fetus in early stage pregnancy. Using large aperture transducers could

be a solution, but this increases the cost and significantly reduces the flexibility for different situations and procedures. There are also some cases for which large aperture probes cannot be used such as surgical interventions. Therefore, we investigate an approach that improves ultrasound image quality without changing the size of the ultrasound array transducer.

Our innovative approach is to expand the synthetic aperture size beyond that of conventional SA by utilizing tracking technology, which we call synthetic tracked aperture ultrasound (STRATUS) imaging [Fig. 6.1]. The tracking information is used to identify the orientation and the position of the ultrasound image, and an adaptive SA beamforming algorithm merges multiple sub-apertures from different poses of an ultrasound transducer. In other words, we virtually generate a wider coherent aperture to form an ultrasound image for a fixed region of interest. The ultrasound image quality improves, in that the aperture size expansion reduces the F-number. We conducted preliminary experiments and demonstrated the effect of aperture size in previous work [49, 50]. Considering the practical implementation, tracking inaccuracy and ultrasound calibration are causes of image degradation. Therefore, this chapter extends the previous work by providing a simulation to evaluate the effect of these errors on image quality, to determine the relationship between the accuracy of the tracking device and ultrasound calibration, and to compare simulation and experimental results.

This chapter is structured as follow. We first introduce the background and con-

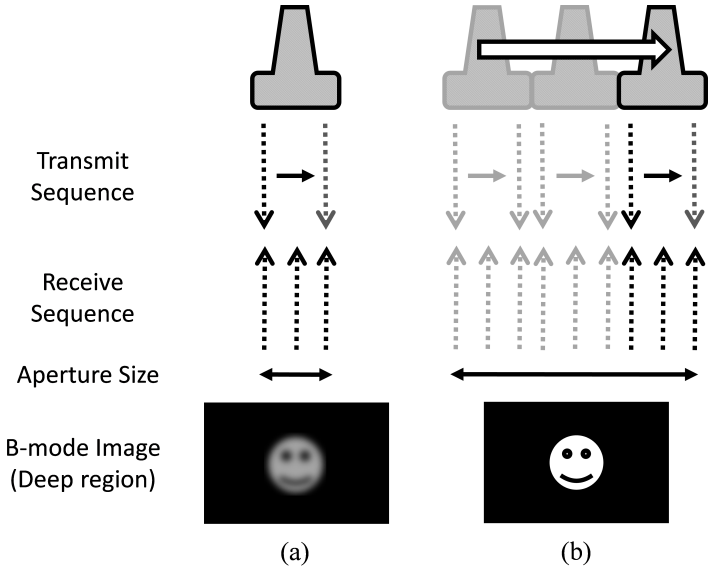

Figure 6.1: Synthetic tracked aperture ultrasound (STRATUS) imaging compared to conventional synthetic aperture ultrasound imaging. (a) Synthetic aperture ultrasound imaging with a single pose, and (b) STRATUS imaging with multiple poses.

cept of STRATUS imaging. Then, we demonstrate the feasibility of STRATUS imaging through simulations and experiments based on a particular configuration utilizing a 6 degree-of-freedom (DOF) robot arm. In the simulation, the effect that tracking accuracy and ultrasound calibration has on the ultrasound image quality is evaluated. We also conducted experiments using a 6 DOF robot arm to validate the image quality improvement due to aperture extension. Finally, we compare experimental results to simulation results, and discuss suitable tracking systems and configurations for this approach.

6.2 Contributions

The main contributions of this chapter are the following:

- Introduction of a synthetic tracked aperture ultrasound imaging system integrating tracking technique and ultrasound beamforming
- Proof of concept for STRATUS imaging through simulation and experiment
- Extensive simulation analysis evaluating the effect of mechanical error sources

6.3 Approach

6.3.1 Synthetic Aperture Imaging

In conventional clinical ultrasound systems, a fixed number of transmission and receiving elements is used to generate an A-line, and by sequentially acquiring multiple A-lines, a B-mode image is formed. The lateral resolution is determined by the number of elements used to build an A-line. On the other hand, in synthetic aperture, signals transmitted from a single source will be received by all of the elements of the ultrasound transducer. A reconstructed image from a single element transmission has a low resolution because transmission focusing is not applied. These low-resolution images are considered as intermediate reconstructed images. Accumulating low-resolution images from different transmission elements has the effect of

focusing transmission waves, and a higher resolution image can be obtained. When an image point $\vec{r_F}$ is reconstructed, the delay function applied can be expressed as:

$$t(\vec{r_F}) = \frac{1}{c}(|\vec{r_T}| + |\vec{r_R}|), \tag{6.1}$$

where $\vec{r_T}$ is the distance from the transmission element to the focusing point, $\vec{r_R}$ is the distance from the receiving element to the focusing point, and c is the speed of sound. Therefore, the focused signal in two-dimensional image $y_F(\vec{r_F})$ is

$$y_F(\vec{r_F}) = \sum_{j=1}^{N} \sum_{i=1}^{M} y_R(t(\vec{r_F}), i, j), \tag{6.2}$$

where y_R is the received signal, and i and j are the transmission and receive line numbers, respectively. M is the number of emissions, and N is the number of elements that receive the signal. Conventional ultrasound beamformers can only focus a single focus depth for each transmission, so it is practically impossible to transmit focus at every pixel of an image. A synthetic aperture algorithm, however, emulates transmit focus at every single location of an image, so that a dynamic focus can be applied to both transmit and receive. Hence, a significant improvement in resolution can be expected relative to the aperture size used to construct an image. In the case of STRATUS imaging, we further extend the algorithm by changing the locations of the transmission and receiving elements.

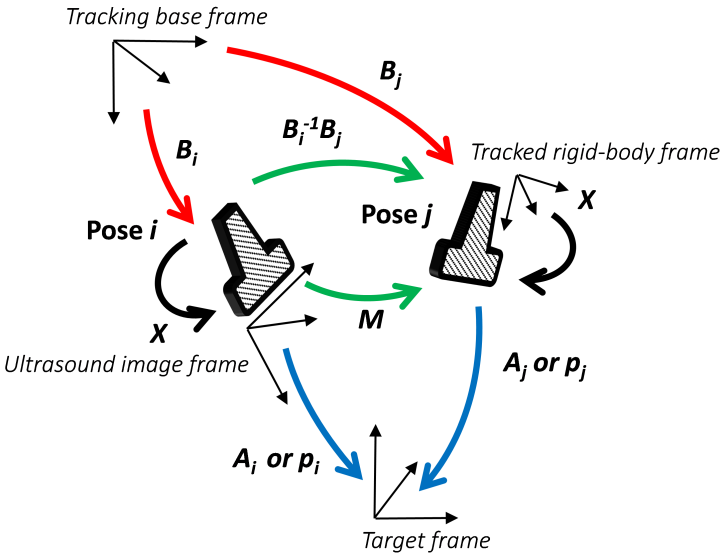

Figure 6.2: The coordinate systems involved in synthetic tracked aperture ultrasound (STRATUS) imaging.

6.3.2 Synthetic Tracked Aperture Ultrasound Imaging

The background of ultrasound image tracking using tracking systems are summarized in Appendix B.1. A rigid-body transformation between two coordinate systems is defined as:

$$F = \begin{bmatrix} R & t \\ 0 & 1 \end{bmatrix} \tag{6.3}$$

where R is a rotation matrix, and t is a translation vector. Figure 6.2 shows the coordinate systems involved in STRATUS imaging. The transformation from the tracking base frame to its tracked marker frame is defined as B, the transformation from the tracked marker frame to the ultrasound image frame is defined as X, and

the transformation from the ultrasound image frame to the imaging target frame is defined as A. When the target is a single point, p is used to describe the point location in the ultrasound image. The motion applied to the ultrasound probe, the relative transformation between two poses from the ultrasound image frame, can be expressed as:

$$M = X^{-1}B_i^{-1}B_jX, \tag{6.4}$$

where B_i and B_j correspond to two poses of the tracked marker. To introduce the motion M, the new probe pose is determined from its original pose. When the original rigid body transformation is B_i, a new pose B_j can be expressed as:

$$B_j = B_iXMX^{-1}. \tag{6.5}$$

In the reconstruction process, data collected at each pose is projected back into the original ultrasound image frame and summed up.

6.3.3 Implementation Strategies

Improving ultrasound image quality by tracking the ultrasound transducer is the fundamental goal of STRATUS imaging. Here, we discuss potential combinations of tracking techniques and scanning strategies that can be used under STRATUS framework. Scanning scenarios can be mainly divided into two categories: freehand scanning, and robotic scanning. Freehand scanning indicates that a physician controls and moves the ultrasound probe, while a tracker provides accurate pose information

to help coherently synthesize information from multiple poses. Robotic scanning involves more specific strategies that involve the physical input from a mechanical actuator to move and follow a certain trajectory.

In freehand scanning, the physician is allowed to scan the ultrasound probe as usual without receiving any direct physical feedback during tracking [Fig. 6.3(a)], and two sub-modes are considered. The first mode is the blind scanning mode. In this mode, the tracker does not provide any feedback to the physician during data acquisition. After determining the initial pose, its position and orientation are recorded through the tracking device. This geometry is used as the base image frame during SA reconstruction. Then, the ultrasound transducer is moved by the physician freehand, while the tracking information and channel data for each pose are recorded simultaneously. The fusion of image information from multiple poses can be done by selecting poses that extend the coherent aperture. The second mode is the guided scanning mode. In this case, the physician receives a real-time feedback from sensor during the scanning. After the initial pose is set, an ideal trajectory to enhance image quality can be calculated automatically. While the physician moves the probe following the guidance, the tracking device provides the real-time feedback indicating the compatibility of the actual trajectory and the computed ideal trajectory. The data will be recorded when the pose lies on the desired trajectory. Once all of the required data is collected, the adaptive synthetic aperture beamformer can be applied to the ultrasound data utilizing its associated pose information.

In robotic scanning, a robot arm enables advanced data collection strategies [Fig. 6.3(b)]. Since the robot arm can act as a mechanical tracker, the aforementioned freehand scanning is also applicable to this configuration. Two additional modes are described here. First, the co-pilot mode is a mode where scanning is done by a physician and the robot system cooperatively. In this mode, we utilize virtual fixtures, a software construct designed to prevent humans from causing an accident due to human error [51], by rejecting undesirable inputs or guiding the physician towards the ideal scanning trajectory. After setting the initial pose, a trajectory to extend the aperture is computed. A virtual fixture is used to lead the physician to move along the trajectory, while some haptic feedback discourages motion away from the computed path. The benefit of the co-pilot mode is that it is possible to follow the ideal trajectory more closely than freehand scanning. At the same time, as the probe remains under the physicians control, it is safer than the autonomous scanning approach. The auto-pilot or autonomous mode is one where the robot itself moves the ultrasound probe to its destination without requiring input from the physician. Therefore, the scan can be faster and more precise, minimizing motion artifacts. Naturally, safety becomes a bigger concern in this case.

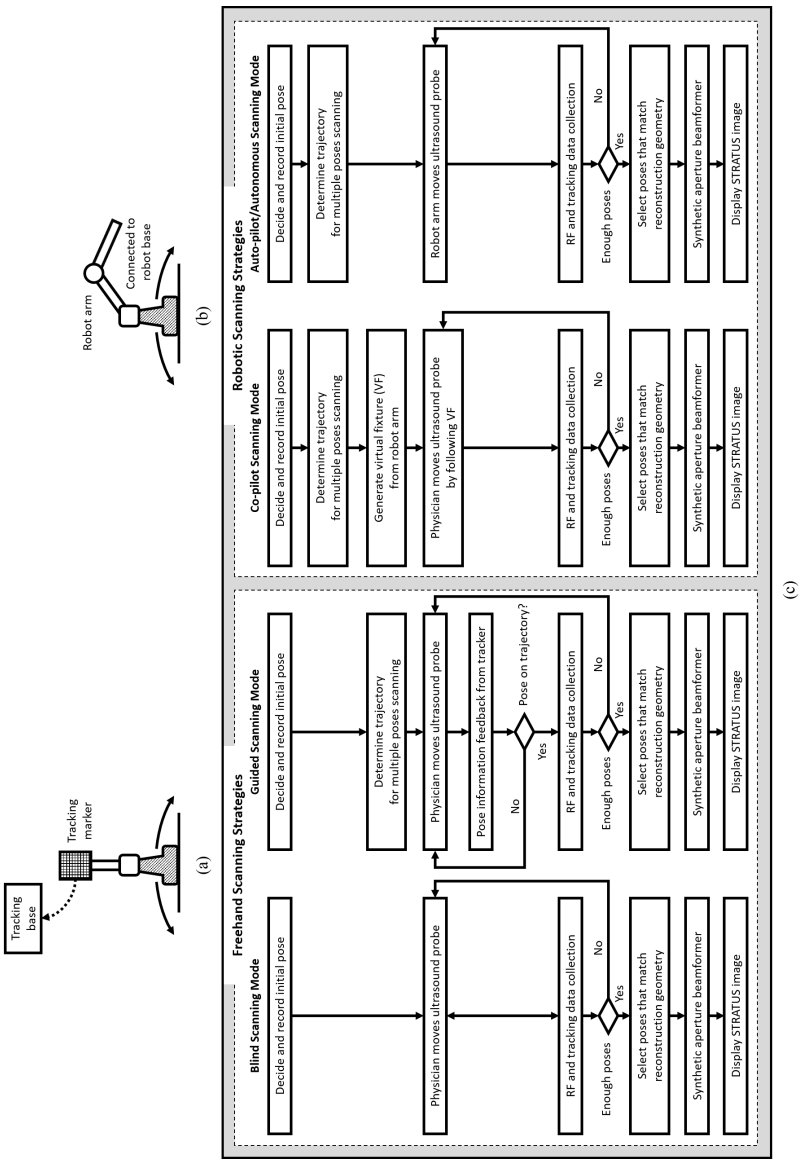

Figure 6.3: Scanning strategies: (a) freehand scanning, and (b) robotic scanning. (c) Diagrams visualizing STRATUS image acquisition and formation under different scanning approaches.

6.4 Materials and Methods

6.4.1 Robot Motion Generation in Pure-translation Scenario

In this chapter, a robot arm is used as the tracking system to track the pose of the ultrasound transducer rigidly attached to its end-effector. The advantage of robotic tracking is that the tracking accuracy is higher than other tracking devices because of its direct physical connections. By sweeping the ultrasound transducer using the robotic arm, multiple images from multiple poses can be acquired. When only translational motion is applied, the rotation matrix can be regarded as an identity matrix, and the equation to determine next pose from Equation 6.5 becomes:

$$
\begin{aligned}
B_i &= B_j X \begin{bmatrix} I & t_M \\ 0 & 1 \end{bmatrix} X^{-1} \\
&= \begin{bmatrix} R_{B_j} & t_{B_j} \\ 0 & 1 \end{bmatrix} \begin{bmatrix} R_X & t_X \\ 0 & 1 \end{bmatrix} \begin{bmatrix} I & t_M \\ 0 & 1 \end{bmatrix} \begin{bmatrix} R_X^{-1} & -R_X^{-1} t_X \\ 0 & 1 \end{bmatrix} \\
&= \begin{bmatrix} R_{B_j} & R_{B_j} R_X t_M + t_{B_j} \\ 0 & 1 \end{bmatrix},
\end{aligned}
\tag{6.6}
$$

Equation 6.6 indicates that only the rotational components of X are required to determine the pose in translation-only scenarios, and the translational error term in

X has no effect. This property is useful in the practical situation, because it reduces the accuracy requirement for ultrasound calibration, or the rotational components can be prioritized during the calibration process. Accordingly, the translation-only scenarios is the focus as an initial system implementation.

6.4.2 Simulation

From a practical point of view, marker tracking inaccuracy and ultrasound calibration are the two major error sources. Thus, it is necessary to understand how these uncertainties affect the ultrasound image quality in STRATUS imaging. We conducted an extensive simulation to evaluate the overall performance under varying levels of both tracking and calibration errors.

The simulations were conducted using Field II software, which was used within MATLAB (The MathWorks Inc., Natick, MA) [14]. To produce simulation data, a 64-element linear transducer array with a pitch size of 0.32 mm was designed for both transmission and receiving, which corresponds to a 20.48 mm array transducer. A single element was transmitted sequentially throughout the ultrasound array, and for each element transmission, each of the 64 elements were used to receive. The adaptive delay function was applied on each transmit data based on Equation 6.2 for synthetic aperture beamforming. Under these conditions, a single pose will result in 64 lines of received signals. The probe pose was moved five times with a 32-line overlap with each neighboring pose, corresponding to a total of 192 lines. After setting the center pose,

the two poses to the left and to the right, respectively, were calculated by taking into account their relative motion between them and the center pose. The transmission center frequency was set to 2 MHz, and the sampling frequency was set to 40 MHz based on the following experimental setup. A single point target was placed at a depth of 100 mm.

6.4.3 Experiment Implementation

The experimental setup is shown in Fig. 6.4. A 6 DOF robot arm (UR5, Universal Robot) was used to move the transducer, and pre-beamformed RF signals were collected from the clinical ultrasound machine (Sonix Touch, Ultrasonix Inc.) using a Sonix DAQ device. A 20.48 mm width phased array transducer (P4-2, ATL) with 64 elements was prepared. A 2 MHz center frequency was transmitted, and received signals were collected at a 40 MHz sampling frequency. One dimensional (1-D) translational motions of 10.24 mm displacement were applied for each step. A line phantom was used and a general ultrasound phantom (84-317, Nuclear Associates) with wire targets and anechoic regions was used as the imaging target to evaluate the point spread function. During the procedure, each pose of the robot end-effector was recorded on the PC. At the same time, the clinical ultrasound systems transmitted an acoustic wave from each element sequentially. The same transmission sequences applied in the simulation were used to generate probe motion. The channel data is collected on the DAQ device, and transferred to the PC.

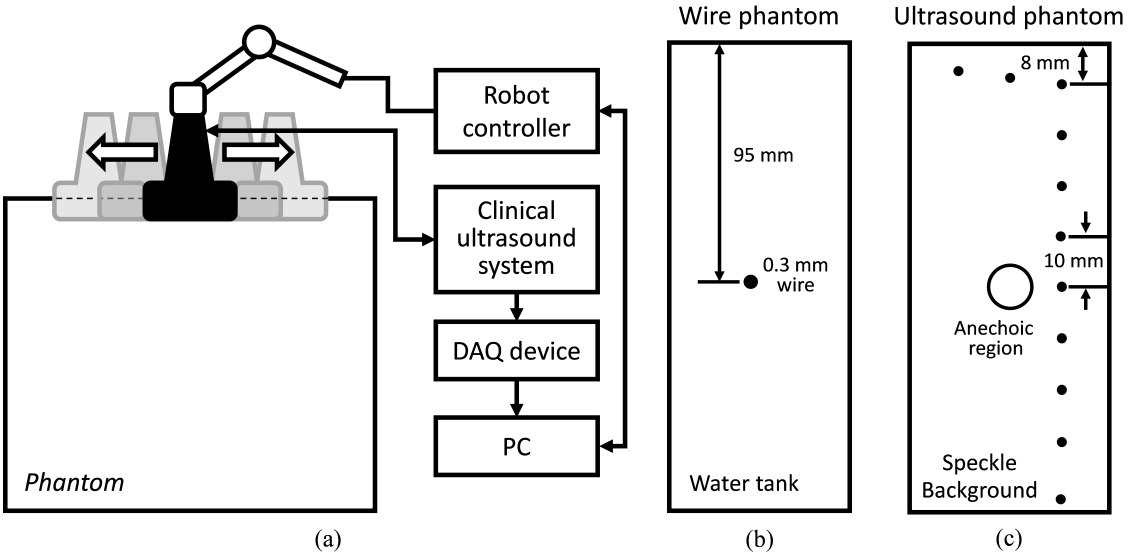

Figure 6.4: Experimental setup for synthetic tracked aperture ultrasound (STRATUS) imaging. (a) Robot control and ultrasound data acquisition system. (b) Wire phantom design. (c) General ultrasound phantom design.

6.4.4 Ultrasound Calibration Using Active Echo Phantom

We used a point-based calibration method, in which an active-echo (AE) element was treated as the point target [52, 53]. The AE element will be apparent in the B-mode image as a point, with the assumption that the point is located in the ultrasound image mid-plane. A set of segmented points is used as the information of the AE location in ultrasound image coordinates. The active-echo element is fabricated from a piezoelectric element, with functionalities to convert the received acoustic wave to electrical signals and simultaneously transmit an acoustic pulse feedback. The amplitude of the converted electrical signals corresponds to the strength of the

received acoustic pulse, which is maximized at the mid-plane of the ultrasound beam. Ideally, the generated ultrasound beam is infinitesimally thin, but in reality the ultrasound beam has some elevational thickness. This is a typical source of error in ultrasound calibration where the segmented point is often assumed to be located in-plane. Therefore, the AE element helps in positioning the point phantom with respect to the ultrasound image such that this assumption is less erroneous. The AE phantom is considered to be more accurate than cross wire, which is one of the most commonly used phantoms for ultrasound calibration [54–57].

The unknown transformation X is solved through the following equation [58]:

$$\underset{X \in \mathrm{SE}(3)}{\arg\min} |B_i X p_i - B_j X p_j|, \tag{6.7}$$

where the tracker transformation B is recorded from the robot encoders. We collected 100 poses by moving the robot arm to provide unique rotations and translations; concurrent tracking information and ultrasound channel data were recorded. The SA beamformer is used to reconstruct the received channel data for point segmentation [59]. To quantify the performance of ultrasound calibration, point reconstruction precision (RP) is used. RP is a widely used metric to evaluate the performance of ultrasound calibration. When a point phantom is scanned from different poses, the distribution of the reconstructed point in the tracking base frame, BXp, is expected to be a point cloud. The reconstruction precision is quantifying the size of the point

cloud by showing the norm of standard deviation.

$$\sigma_{RP} = \| \frac{1}{N} \sum_{i=1}^{N} (B_i X p_i - \overline{BXp})^2 \|_2, \tag{6.8}$$

where N is the number of poses, and $\overline{BXp}$ is the mean of $B_i X p_i$ for every i.

As a result, 89 out of 100 data points were selected for calibration and evaluation, while 11 data points were removed due to low image quality and segmentation difficulty. Accordingly, 60 points are randomly chosen for calculating the unknown transformation X, and the remaining 29 points were used for evaluating reconstruction precision (RP). This random selection was repeated 20 times. The mean of the computed reconstruction precision was 1.33 mm with a standard deviation of 0.11 mm. The minimum was 1.15 mm, and the maximum was 1.60 mm.

6.4.5 Image Quality Assessment Metrics

In simulation, to quantitatively evaluate the resolution and blurring of images due to errors, the size of the point spread function was measured by counting the number of pixels over a certain threshold. The threshold was set to -25 dB. The pixel count result in single pose was set as the baseline, and the ratio compared to the baseline case was used as the metric to express the quality of the image. To be precise, the pixel count ratio ($R_{\text{PixelCount}}$) is formulated as

$$R_{\text{PixelCount}} = \frac{\text{PixelCount}_{Single}}{\text{PixelCount}_{Multi}}. \tag{6.9}$$

The ratio higher than 1 indicates better image quality compared to the single pose case. The pixel count was used instead of the full width at a half maximum (FWHM), because FWHM is optimized to quantify one-dimensional resolution, but not good at representing two-dimensional effects. However, the blurring effect due to errors occurs in two dimensions, and FWHM is insufficient in quantifying the effect. Pixel count, on the other hand, can characterize the diffusion of the point spread function, and this is a more representative metric for our analysis.

For experiment results evaluation, in addition to pixel count metric, the classic FWHM is also used when a point spread function is well reconstructed. For general ultrasound phantom, the contrast-to-noise ratio (CNR) of the anechoic region to its surrounding area is calculated. The CNR is defined as

$$\text{CNR} = \frac{|\mu_i - \mu_o|}{\sqrt{\sigma_i^2 + \sigma_o^2}}, \tag{6.10}$$

where μ_i and μ_o are the means of the signal inside and outside of the region respectively, and σ_i and σ_o represent the standard deviation of the signal inside and outside of the region respectively.

6.5 Results

6.5.1 Simulated Point Spread Function

Example results of STRATUS imaging without introducing any error are shown in Fig. 6.5(a). To assess the effect of tracking error, we added error matrix in B and X. Now the ideal motion M becomes,

$$\hat{M} = (X\Delta X)^{-1}(B_i\Delta B_i)^{-1}B_j\Delta B_j X\Delta X, \tag{6.11}$$

where ΔX is the error in X, which is constant for multiple poses, while the error in B, ΔB_i and ΔB_j varies for each pose. An example of the simulated result from five poses with error is shown in Fig. 6.5(b). The received data of five poses were generated similarly as the case with no error except that $\hat{M}$ is used instead of M. The translational error in X was not considered because it does not have an effect on STRATUS image formulation from Equation 6.6.

Then, the image quality metric was evaluated as a function of precision error in B and rotational error in X, which are the two main errors affecting STRATUS image quality. We considered nine variables: rotational and translational errors in B, and rotational errors in X. For each dimension, the step was 0.1 mm or degree for the translation and rotation components, respectively. To display a three-dimensional matrix, both dimensions of rotation and translational errors in B were compressed to a single precision dimension using the relationship map shown in Appendix B.2. The

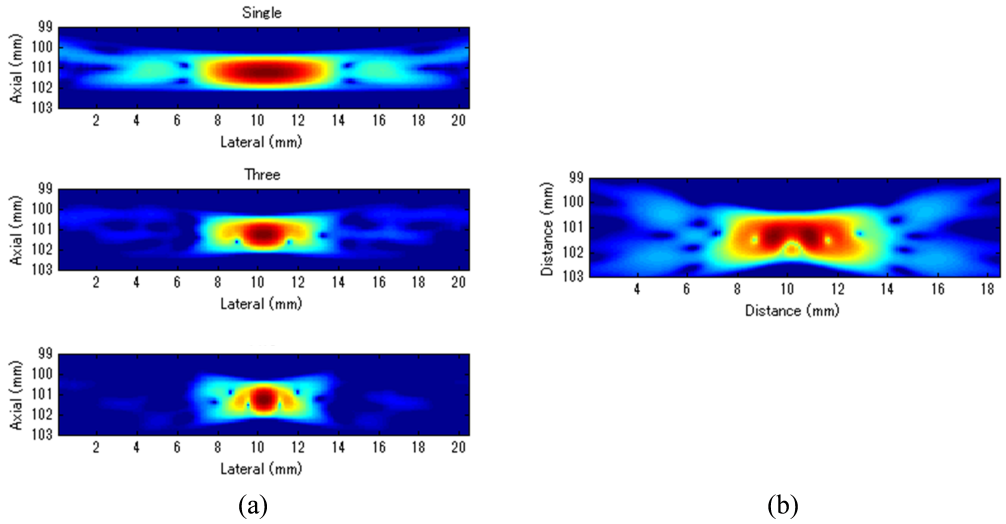

Figure 6.5: (a) Simulated point source by utilizing single pose, three poses, and five poses. (b) Simulated point source from five poses with image tracking error. Rotational error in X was 0.7 degree, and rotational and translational error in B was 0.1 degree and 0.1 mm, respectively.

precisions range in B is set to vary from 0 to 1 mm, while the rotational errors range in X varied from 0 to 2 degrees. For each value in the precisions range, all possible corresponding rotational and translational components, according to the distribution map shown in Fig. Appendix B.1, were taken into consideration, and their corresponding simulation image quality values were averaged. As mentioned earlier, the rotational error dimension shown in Fig. 6.6 represents the norm of the rotational error components. Thus, different rotational vectors can share the same norm value. Similarly, different translational vectors can share the same norm. To consider the variation of vectors, we run the simulation algorithm and acquire data from 18 independent trials with varying rotational and translational error vectors while maintaining the same

corresponding norm values. As a result, Fig. 6.6 shows the mean, the worst-case, and the best-case scenarios of this image-quality analysis. The best-case scenario means that the highest value in each matrix is shown through 18 trials, and the worst-case scenario means that the lowest value is shown. The raw image quality metric is shown in Fig. 6.6(a), while Fig. 6.6(b) is rescaled to only show values larger than 1, which corresponds to the image quality of the single pose case. Any color other than the dark blue can be regarded as an image quality improvement compared to the single pose case. The value for each trial has a variation, and it indicates that the same magnitude of X and B can result in different image quality. The accumulation of multiple randomized errors in the process to simulating images from five poses can be one of the reasons to explain this phenomenon. However, a more important factor is that each Euler angle in the rotational error in X has a different contribution to image quality. Axial direction misalignment between multiple poses is the most influential factor, and the rotation in elevation axis is the dominant component in causing misalignment between multiple poses in the axial direction. Therefore, the image quality can be degraded when the error in the elevational axis of rotation is significant even if the overall rotational error in X is small. The error in X is more tolerant than the error in B, because the error in X is constant for five poses, while the error in B varies for each pose. Nevertheless, it does not mean that the error in X is not important compared to that in B because the rotational error in X depends on the performance of ultrasound calibration that has room for improvement, while

the error in B is a predefined factor based on what tracking system is used.

The best-case scenario result is considered as the necessary condition of the STRATUS imaging. In this case, image quality improvement can be expected when an appropriate X is chosen based on a task-oriented evaluation, in that not all X is useful. On the contrary, the worst-case scenario can be regarded as the sufficient condition. If this condition is satisfied, the image quality can be improved for any rotational error in X, and no additional task-based evaluation of X is required. Nevertheless, this image quality evaluation result demonstrates that a supreme ultrasound calibration is desired to get an accurate X. In addition, the error in X is closely related to the error in B because ultrasound calibration depends on the tracking accuracy B. The error propagation relationship between them is analyzed in more detail in the discussion section.

6.5.2 Experimental Phantom Validation

Figure 6.7 depicts experimental results for the line phantom using two different computed calibration transformation Xs, in which different combinations of poses were used to compute each X. The results of a single pose SA image and a STRATUS image from five poses were compared. In trial 1, the image quality improvement based on the ratio of pixel counts was 1.84. FWHM of the point spread function for the cases using a single pose and five poses were 2.40 mm and 0.87 mm, respectively, and the lateral resolution was improved by a factor of 2.76. The result indicates that the

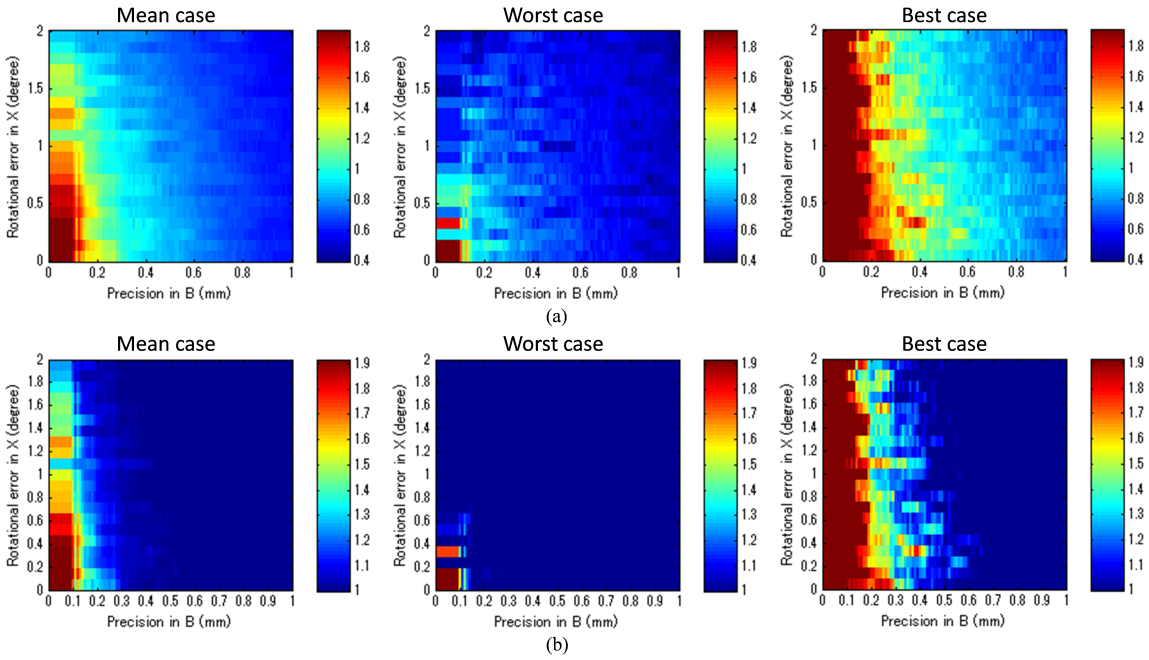

Figure 6.6: Simulation results of image quality evaluation. (a) Quality of images of proposed method with different level of uncertainty in X and B. (b) As a normalized result, the pixel count for single pose was taken as the maximum value to show that the area the image quality did not improve.

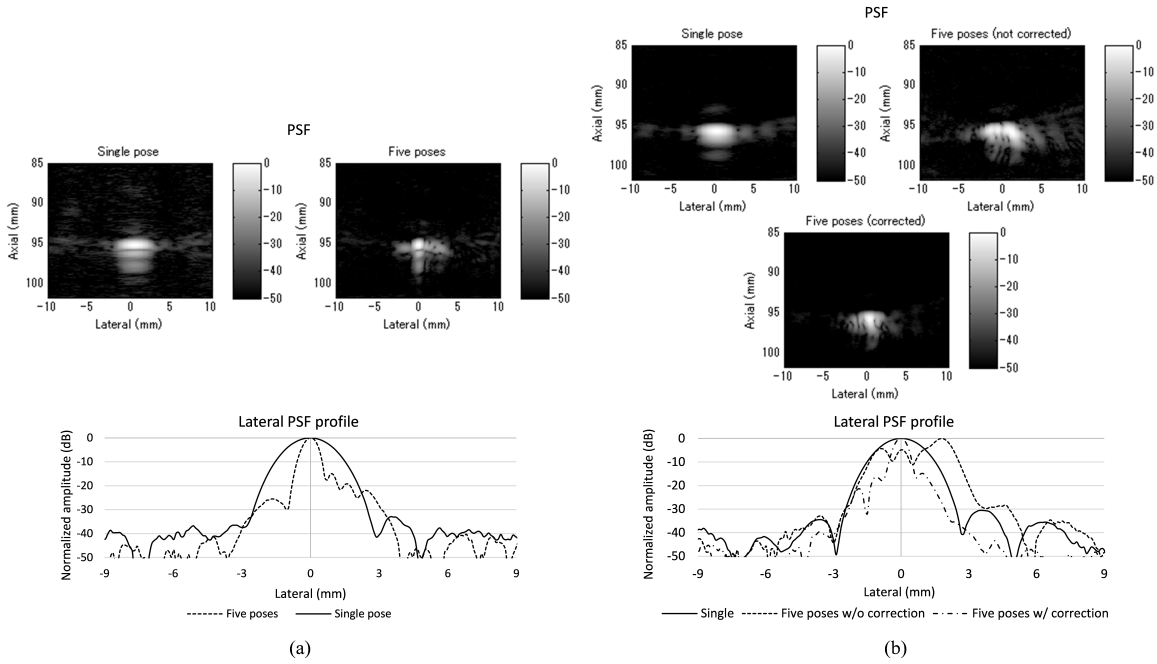

Figure 6.7: A line phantom was imaged using two different calibrated transformation. When Xs was close to the true transformation between the robot end effector to the image, the effect of aperture extension was clearly observable (a, trial 1). However, if inappropriate X was chosen, the merged image was blurred, and that can be compensated by shifting each pose based on the amount of error in rotation (b, trial 2).

X used in trial 1 was close to the true X. In trial 2, the point spread function is blurred because of the displacement of each pose. The rotational error of X induces axial and lateral displacement for each pose, and axial displacement was especially sensitive. When 533 μm and 55 μm shift was applied in the lateral and axial directions respectively, the blurring effect could be compensated. Since the compensation was linear between multiple poses, the error attributed to the inaccuracy of X can be compensated.

In addition to the line phantom, a general ultrasound phantom was used as the

imaging target. Wire targets were located at 10 mm depth intervals, and the anechoic region was located at 50 mm [Fig. 6.8]. When we compared the resulting image between the case with single pose and with three poses, we observed that the reconstructed images of the wire targets were clearly improved. This tendency could be seen over the entire structure, and the effect is more apparent in the deep regions. In Fig. 6.8(b), the anechoic region is magnified. It could be confirmed that the speckle size of the image reconstructed with 5 poses was reduced the lateral direction, and the center region was darker than the single pose result. The CNR of the single pose result was 5.90, while that of three poses was 6.59; this is a 12 % improvement due to aperture extension.

6.6 Discussion

6.6.1 Comparison of Experiment to Simulation

We used a robot arm UR5 with a translational accuracy of approximately 0.1 mm. Tracking accuracy is the metric commonly used to express the accuracy of tracking methods, but it only includes the translational components of error, although both rotation and translation error need to be considered in the analysis. Since the rotational accuracy is not reported, we estimated the rotational error from the translational error by considering that a rotational motion along a remote center generates a translational motion. Assuming the robot end effector is located 20-60

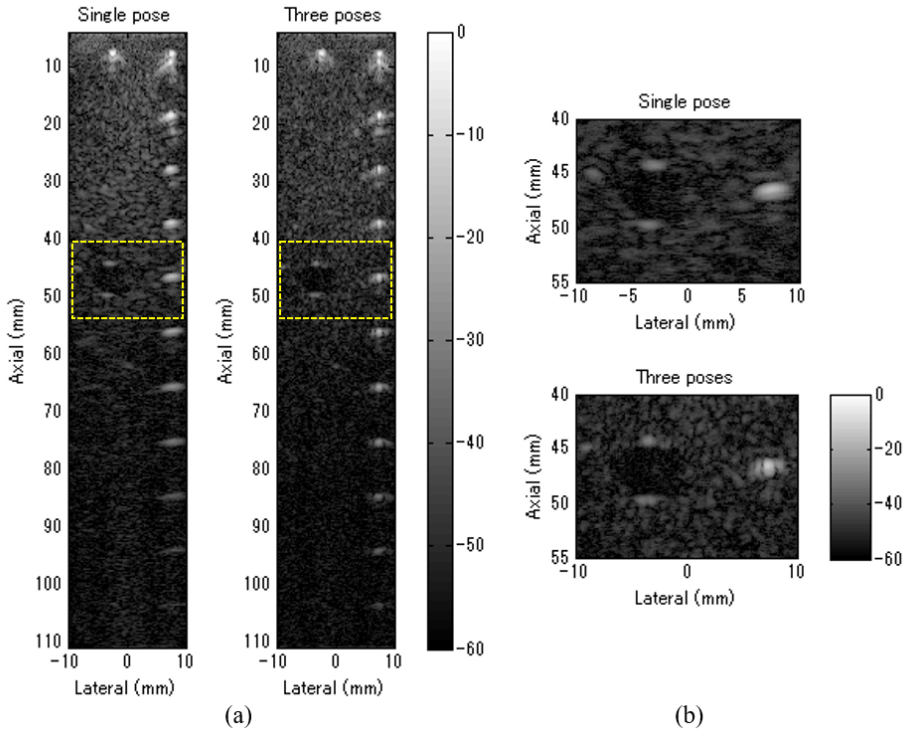

Figure 6.8: General ultrasound phantom was imaged. (a) The result from a single pose and three poses of the entire structure of the phantom is shown. (b) The anechoic region is magnified.

cm away from the centroid of the rotation of a joint, the estimated corresponding rotational error became in the range of 0.029 to 0.095 degree. This number and the translational accuracy were used to compute the precision in B of the system in Fig. 6.9(a). As a result, the precision in B was estimated to be in the range of 0.17 mm to 0.43 mm. Given this estimated precision number, the rotational error in X is shown in Fig. 6.9(b), when the segmentation error in the range of 1 mm to 2 mm is considered. The estimated segmentation error was derived from error propagation analysis shown in Appendix B.3. Accordingly, the X has to reside in the region drawn, and the best possible error in X was 0.31 degrees, while the worst case was 0.67 degrees. Now the experiment result and the simulated quality evaluation in Fig. 6.6 could be compared. For the experimental result in trial 1, the best X case was chosen, while multiple Xs based on different combinations of poses in ultrasound calibration were computed. Thus, the graph of the best-case in the image quality evaluation simulation was chosen for comparison. In the simulation result, the best possible image quality improvement was 1.75 and the least improvement was 1.19 under the same conditions as the experiment. We computed the pixel count for the experimental result in trial 1 on a wire phantom, the image quality improvement compared to the value of single pose experiment result was 1.84. This number is close to that seen in the simulation.

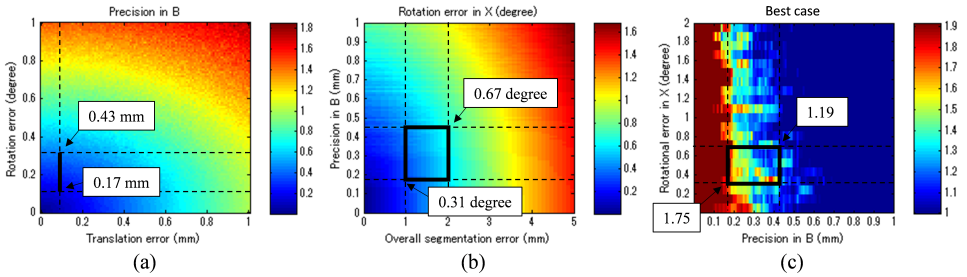

Figure 6.9: Evaluation of experimental results based on simulation. (a) Analysis of precision in B in UR5. (b) Analysis of a possible range of rotational error in X, (c) the possible image quality improvement in the best case.

6.6.2 Error Sources Affecting STRATUS Imaging

STRATUS imaging is very sensitive to the registration error between multiple poses, because the acceptable range of error in the beamforming is smaller than the transmission acoustic wavelength. Thus, compared to conventional synthetic aperture, more error sources should be considered and analyzed. Errors in tracking systems and ultrasound calibration can be regarded as the static error that is independent from the imaging subject, while motion artifacts, tissue deformation, or tissue aberration [50] are regarded as the dynamic error strongly depends on the subject or the operation conditions. The static error could be reduced by improving tracking systems and ultrasound calibration as discussed in simulation. On the other hand, the dynamic error is more difficult to handle, but should be overcome by optimizing the scanning plan and developing adaptive beamforming algorithms. Investigation on both the static and the dynamic error is essential to improve the performance of STRATUS imaging.

In particular, the effect of tissue deformation introduced by the ultrasound probe could be overcome for the following reasons. First, the primary imaging target of this technique is deep tissue. According to Buijs's work [60], it is demonstrated in simulation and experiment that the force applied on the surface will not be equally distributed in the tissue, but it will cause most of its compression on the surface, and the compression or tissue deformation becomes less as the depth increases. In addition, the compressibility of different tissues depends on their Youngs modulus, and it is known that the near field tissue, which is occupied by fat, has a much higher compressibility compared to the deep field tissue of muscle or internal organs. Second, the tissue deformation that matters for this technique is not the absolute amount of tissue deformation, but the relative tissue deformation between neighboring poses. When a robotic arm with force sensing functionality is used, we can measure the force applied to the tissue, and control the robot arm to keep the same amount of force throughout the scan [42]. In other words, the relative tissue deformation could be even smaller by keeping the force applied on the tissue to be the same. Third, one of the purposes of conducting general ultrasound phantom experiment is to observe the effect of clinically realistic errors including tissue deformation. The general ultrasound phantom mimics soft-tissue properties of the human body, and tissue deformation should happen when the probe directly touched the phantom surface. However, as a result, the tissue deformation effect was not significant to cause negative effect on the synthesized image.

6.6.3 Effect of Tracking Systems and Ultrasound Calibrations

Figure 6.10 merged Figs. 6.6, B.1, and B.2 to compare tracking accuracy (precision error in B) versus the ultrasound calibration performance in terms of segmentation error. The number in each segmentation error metric was estimated by computing the corresponding rotational error in X through Fig. B.2. Since the accuracy of X is closely related to B, Fig. 6.6 contains certain regions that are unrealistic in reality. To show the trend with different parameters, the precision error in B was taken in 0.2 mm bins, and the average value in each bin is shown. The robot arm used in the experiment (UR5) should be considered as a system with precision in the range of 0.17 mm to 0.43 mm. If better tracking systems are used, the performance of the ultrasound calibration as well as the STRATUS image quality will improve. The segmentation error must always be smaller than the worst case result if we wish for the result to always be an improvement in image quality. The best-case result in Fig. 6.10 indicates the acceptable limit for the system. The plots show that a precision error in B of 0.41 mm to 0.60 mm is the limit. In this range, the segmentation error plays a major role in determining if the system is acceptable or not; however, we can see a trend that the effect of the segmentation is less compared to the worst-case and mean-case.

Two approaches can be considered to improve ultrasound calibration: reducing the

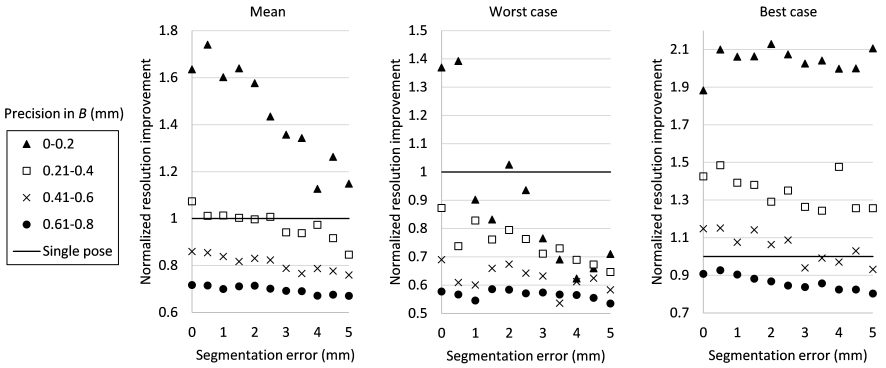

Figure 6.10: The image quality corresponding to precision in B and segmentation error. The bold line represents the line of image quality for a single pose case.

segmentation error and the covariance of X. The first approach is related to using a better calibration phantom or imaging system. We also can improve the segmentation algorithm through accurate wavefront detection or reconstructed point segmentation. The second approach is to improve the optimization algorithm to solve X. Optimizing X solves a complicated function, which can easily result in local minima but not the global minimum. Therefore, if the optimization algorithm is able to decrease the variance of the computed Xs, higher image quality improvement can be expected even in the worst case. In addition, the compensation of the segmentation error can also be expected.

6.7 Conclusion

We have proposed a novel method to extend the aperture size during ultrasound image acquisitionnamed synthetic tracked aperture ultrasound (STRATUS) imag-

ingby sweeping the ultrasound array transducer while tracking its orientation and location, and combining this information into a synthetic aperture beamformer. To support our conclusions, we estimated the effects of overall tracking errors involved in the system on final beamformed image quality through simulation. We also demonstrated the feasibility of the system by moving the ultrasound probe with a robot arm, and showed the lateral resolution improvement through a line phantom, and CNR improvement through a cystic region in a general ultrasound phantom.

A pure translational motion in the focus of this chapter, and this motion can be a basic scanning strategy, as it can be applied to almost all planar surfaces. Another advantage of lateral-direction scanning is that only the rotational component of X will be used, so the error in the translational component can be neglected. This property helps to reduce the possible errors between different poses. Motion that includes rotation will be useful in a sense that if the target region is known, more coherent information can be acquired. Each element has its angular sensitivity, and the element far from the region of interest has limited sensitivity to receive signals from the target region. If the motions include rotations to make the transducer elements face the target region, the signals will be more coherent for beamforming. Practically, the opportunity to scan the target with a remote center of motion is limited except cases where the tissue surface is a round shape. Hence, the combination of translational motion with rotation motion should be implemented as a realistic trajectory.

Chapter 7

Synthetic Tracked Aperture Ultrasound Imaging with Virtual Fixture Control and Motion Compensation

This chapter has been published as: *H. K. Zhang, Rodolfo Finocchi, Kalyna Apkarian, E. M. Boctor, "Co-Robotic Synthetic Tracked Aperture Ultrasound Imag-ing with Cross-Correlation Based Dynamic Error Compen-sation and Virtual Fixture Control", in Proceedings of IEEE International Ultrasonics Symposium (IUS), 2016*, and *H. K. Zhang, F. Aalamifar, G. E. Trahey, E. M. Boctor, "In vivo visualization of robotically implemented Synthetic Tracked Aperture Ultrasound (STRATUS) imag-*

ing system using curvilinear array", in Proceedings of SPIE Medical Imaging, 9790, 97901X, 2016.

I was responsible for the project design, system integration, data collection, analysis and writing. Rodolfo Finocchi and Kalyna Apkarian contributed on implementing virtual fixture control. Dr. Emad M. Boctor supervised the project.

7.1 Introduction

Ultrasound imaging has been widely used in many medical applications due to its low cost and real-time, safe, and convenient properties. The remaining challenge of medical ultrasound is its limited field-of-view (FOV) and the resolution in deep regions, which highly depends on the lateral width of the ultrasound probe. Although a wider aperture size can achieve higher spatial resolution, conventional ultrasound beamforming only utilizes limited number of elements during sequential line scanning. Synthetic aperture is a technique that fully utilizes a wide aperture to both transmit and receive focusing [46]. By summing signals from different transmit sources, a high resolution image can be generated assuming the transmit focus is applied at all depths. The limitation of synthetic aperture is that the maximum available aperture size is determined by the physical size of the ultrasound probe. Thus, it is challenging to achieve a high resolution image for any target located in a deep region, such as in an obese patient. Using a wide aperture probe could be a solution, but it would make

the probe bulky and less flexible to use with different subjects who have unique skin surfaces.

Although three dimensional image registration techniques such as mosaicing [61] could help accomplish FOV extension, it is not possible to accurately extract 6 degree-of-freedom pose motion from the noisy ultrasound data. Ultrasound mosaicing only uses B-mode images, and it does not help improve image resolution in deep tissue. Ultrasound tracking could be a potential aid to address this problem. Throughout history, ultrasound imaging has been widely integrated with tracking or robotic systems in medical procedures for tool tracking and image guidance. A robotic arm, in particular, is a mechanical rigid-body which can hold and manipulate objects in three dimensional space. The robotic arm has been used to assist in ultrasound imaging [31] such as for teleoperated procedures [62] or with surgical intervention involving multiple robotic arms [63]. In the previous chapter [43, 50], the feasibility of improving ultrasound image quality through the robotic aperture extension under specific pre-defined robotic motion has been studied.

We introduce a co-robotic synthetic tracked aperture ultrasound (STRATUS) imaging system to address the aperture limitation problem by utilizing robotic tracking, and also to allow the sonographer to actively manipulate the ultrasound probe in semi-freehand mode. While the ultrasound probe is moved, the pose is tracked in real-time, and data from each pose can be synthesized to construct a high resolution image. A co-operative system, the robotic arm moves only when a force is applied on

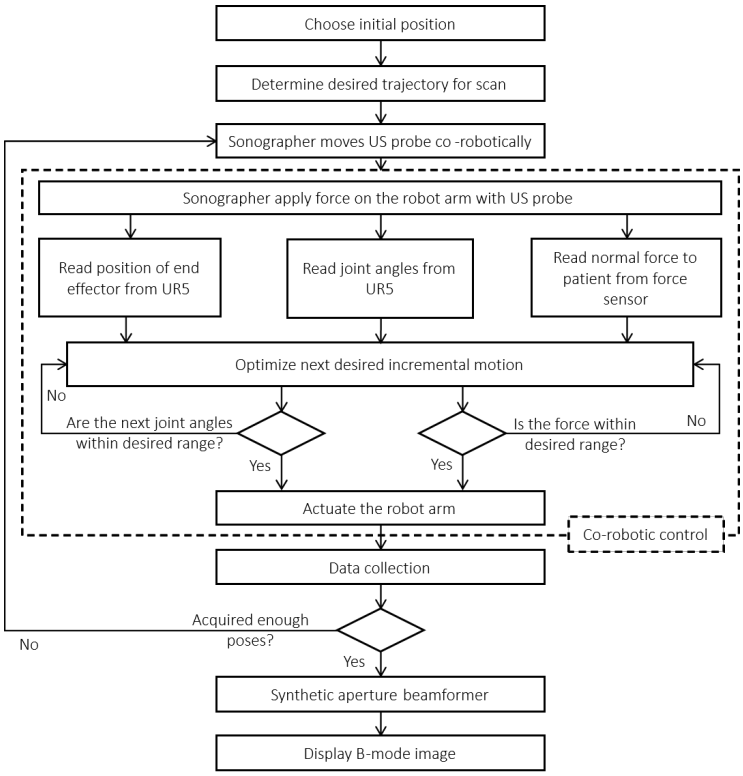

Figure 7.1: The system diagram and the workflow of co-robotic STRATUS imaging system.

the probe, which provides a safer operation compared to autonomous robot motion, and has a potential to draw a patient specific trajectory. The implementation of virtual fixtures allows for constrained motion along the desired trajectory, guiding the sonographer to scan the correct area and nowhere else.

Practical concerns of the STRATUS imaging system are the image distortions due to various error sources. Static errors include the calibration and tracking inaccuracy, which do not depend on the imaging target. The effect of those errors has been analyzed in our previous work [43]. In addition, even if static errors are negligible, dynamic errors from tissue motion or tissue aberration could have a negative impact

on the STRATUS images. Therefore, we also introduce an algorithm to mitigate the potential dynamic errors between different scanning poses by computing subtle image shifts through cross-correlation.

7.2 Contributions

The main contributions of this chapter are the following:

- Implementation of virtual fixture control on STRATUS imaging
- Development and validation of cross-correlation based motion compensation for STRATUS imaging
- Validation of STRATUS imaging with *in vivo* subjects

7.3 Methods

7.3.1 Synthetic Tracked Aperture Ultrasound Imaging

STRATUS imaging is based on the principle of synthetic aperture, in which low resolution images from multiple sub-apertures are used to construct a high resolution image with large aperture information. The ultrasound image tracking is based on

the computation of a rigid-body transformation chain. The transformation from the tracking base frame to the tracking marker (robot end-effector in the case of robotic tracking) frame is defined as B, and the ultrasound calibration transformation from the tracking marker to the ultrasound image frame is defined as X, which is obtained through a pre-operational task called ultrasound calibration. In the synthetic aperture process, the data collected from each pose will be transformed to a uniform base coordinate system. The location vector of the i-th pose frame from the base image coordinate system can be expressed as

$$p_b = X^{-1} B_b^{-1} B_i X p_i, \tag{7.1}$$

where p_i is the location vector of the pose i. The tracking transformation for the base image coordinate system and for the i-th pose are expressed as B_b and B_i, respectively. The received pre-envelope detected radio frequency (RF) signals are summed up as

$$RF_b(p_b) = \sum_{i=1}^{N} RF_i(X^{-1} B_b^{-1} B_i X p_i), \tag{7.2}$$

where RF_i is the received RF signals in the i-th pose, and RF_u is the RF signals for the final reconstructed data. The post-beamforming processes such as envelope detection and scan conversion are applied on the beamformed RF data, and the STRATUS image is displayed in B-mode.

7.3.2 Curvilinear Array

The requirement of STRATUS imaging is to capture a coherent region on the received signals from each pose. Thus, the capture angle range for each pose becomes crucial. The angle sensitivity of the ultrasound transducer element is defined by the shape and the size of the element. Linear array transducer has a higher sensitivity to the target that exists right below the probe surface, in that the elements form a straight line along with the body surface. Although a remote center of motion along a point at certain depth is effective to keep a coherent region throughout the scanning, those motions are not always available because of the non-uniform surface of the body.

Curvilinear array has a shape that elements are placed to the diverging direction, so that it has a wide capture angle range. Thus, more variety of motions can be applied compared to the linear array. Moreover, the curvilinear array is designed for abdominal region, and it has low center frequency transmission capability. These characteristics enable to build more patient dependent motion and scanning trajectory plan.

7.3.3 Co-Robotic Control with Virtual Fixtures

In order to ensure that the sonographer is in full control of the ultrasound probe while it moves along the desired trajectories, a constrained optimization approach

was taken to formulate the control scheme of the robotic arm. The system diagram and the workflow of the co-robotic STRATUS imaging system is summarized in Fig. 7.1. This co-robotic approach enables the sonographer to comfortably scan along the trajectory without allowing significant deviation that might affect the image quality. A 6 degree-of-freedom (DOF) force sensor is used to measure the force and torque applied by the user while manipulating the probe. The measurements from the force sensor are then translated into robot joint velocity commands, allowing for compliance or admittance control of the robot. The relationship between the forces exerted by the clinician, f, against the robot end effector velocities $\dot{x}_{des}$, when manipulating the ultrasound probe takes the form

$$\dot{x}_{des} = K \cdot f, \tag{7.3}$$

where K is a diagonal coefficient matrix that scales the input force to an appropriate end effector velocity in Cartesian coordinates. From this end effector velocity vector, $\dot{x}_{des}$, the corresponding joint angular velocities, $\dot{q}$, are calculated using the well-known equation

$$\dot{x} - \dot{x}_{des} = J\dot{q} \rightarrow \dot{q} = J^{-1}(\dot{x} - \dot{x}_{des}), \tag{7.4}$$

where $\dot{x}_{des}$ is the desired robot end effector velocities in Cartesian space, and J is the robot Jacobian matrix, the time derivative of the robot kinematic equations. As seen on the right-hand side of this equation, the inverse of the Jacobian must be calculated to determine the joint velocities. However, in certain configurations of the robot, referred to as singular configurations, this matrix cannot be inverted, causing

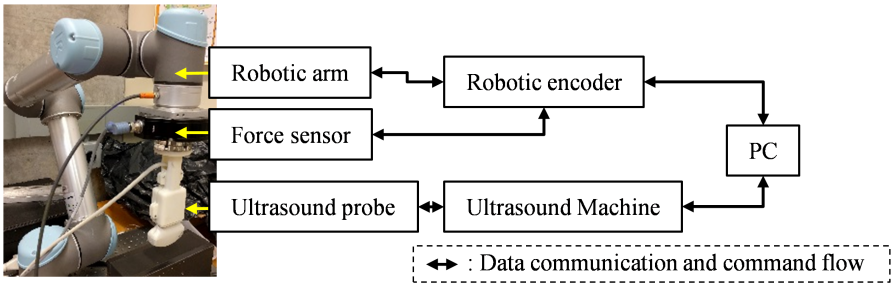

Figure 7.2: Co-robotic STRATUS system diagram.

this method to fail. To avoid these cases, an optimization method can be employed instead, resulting in the formulation

$$\dot{q} = \arg\min_{q} ||W(\dot{x} - \dot{x}_{des})||, \tag{7.5}$$

where the joint velocity vector that minimizes the objective function is calculated.

This optimization equation can be further constrained to restrict or require certain behaviors of the robot, as in [42]. A general form of the constraints is given as

$$H\dot{x} \geq \vec{h}, \tag{7.6}$$

The desired behavior of the system is used to define the linearized subject functions H, the constraint coefficient matrix and h, the constraint vector. The joint velocities were limited to ± 0.5 radians/sec and the probes linear translation was restricted to a linear path with a permitted margin of error of ± 0.5 mm in any direction not on this line.

7.3.3.1 Stay on Line

A basic constraint that can be appropriate for ultrasound imaging is to move along a reference line in 3D, which can allow the STRATUS algorithm to receive the most relevant series of images. Given a line $L(s) = \vec{L_0} + \hat{l} \cdot s$, where $\vec{L_0}$ is a point on the line and $\hat{l}$ is the unit vector indicating the direction of the line. While the virtual fixture is active, the system must correct any offset from its current position to the closest point on line, and each increment motion must be along or close to the line. If we name $\vec{\delta_p}$ as the perpendicular vector from the tool tip to the line, it can be determined by

$$\vec{\delta_p} = \vec{x_p} - \vec{P_{cl}}, \tag{7.7}$$

where $\vec{x_p}$ is the tool position, and $\vec{P_{ct}}$ is the closest point on plane.

To perform this computation, a rotation matrix that transforms the plane to the world coordinate frame is needed. To determine R_3, we use the following equations:

$$R_3 = [\widehat{v_1}\widehat{v_2}\hat{l}];\ \widehat{v_1} = \frac{\hat{l} \times \hat{l'}}{||\hat{l} \times \hat{l'}||};\ \widehat{v_2} = \frac{\widehat{v_1} \times \hat{l}}{||\widehat{v_1} \times \hat{l}||}; \tag{7.8}$$

where $\hat{l'}$ is an arbitrary vector which is not aligned with $\hat{l}$.

We can approcimate the circle of radius $\vec{\epsilon_1}$, around the line by considering a polygon with n vertices centered at origin, and we have:

$$[R_3[c_{\alpha i}, s_{\alpha i}, 0]^t, 0, 0, 0] \cdot (\vec{\delta} + \Delta\vec{x}) \leq \vec{\epsilon_1}, i = 1, ..., n \tag{7.9}$$

and we can set H and h as:

$$H = \begin{bmatrix} -R_3[c_{\alpha i}, s_{\alpha i}, 0]^t & 0 & 0 & 0 \\ & & ... & \\ R_3[c_{\alpha n}, s_{\alpha n}, 0]^t & 0 & 0 & 0 \end{bmatrix}, h = \begin{bmatrix} -\epsilon_1 \\ -\epsilon_1 \\ -\epsilon_1 \end{bmatrix} - H\vec{\delta}. \tag{7.10}$$

A high value of n means the geometry of the virtual constraint will be closer to the desired shape, but will require a longer computation time.

7.3.3.2 Maintain A Direction

The second virtual fixture, maintaining a direction, is also crucial for the functionality of STRATUS, it requires the tool orientation being close to zeros after each incremental motion. The constraint can be expressed as:

$$||\vec{\delta_r} - \Delta\vec{x_r}|| \leq \epsilon_2, \tag{7.11}$$

where ϵ_2 is a small positive number for allowable error, the subscript r indicates the rotation components. The matrix form of the linear constraints are then

$$H = \begin{bmatrix} 0 & 0 & 0 & c_{\alpha i}c_{\beta i} & c_{\alpha i}c_{\beta i} & s_{\alpha i} \\ & & & ... & & \\ 0 & 0 & 0 & c_{\alpha i}c_{\beta i} & c_{\alpha i}c_{\beta i} & s_{\alpha i} \end{bmatrix}, h = \begin{bmatrix} -\epsilon_1 \\ -\epsilon_1 \\ -\epsilon_1 \end{bmatrix} - H\vec{\delta}. \tag{7.12}$$

7.3.3.3 Plane Related Constraints

In some scenarios, the tool tip must not penetrate a plane or be confined in a given plane. The closest point on plane can be calculated using:

$$\vec{\delta_p} = \vec{x_p} - \vec{P_{cl}}, \tag{7.13}$$

the geometry constrain is then:

$$\vec{d^t} \cdot (\vec{\delta_p} + \Delta\vec{x_p}) \geq 0, \tag{7.14}$$

where $\vec{d^t}$ tis the unit normal direction of the plane and points to the free half space. To confine the tool on the plane, an additional constrain can be added:

$$\vec{d^t} \cdot (\vec{\delta_p} + \Delta\vec{x_p}) \leq 0, \tag{7.15}$$

where ϵ_3 is a small positive number that defines the error tolerance. Combining the two constrains, the constraints matrices then can then be written as:

$$H = \begin{bmatrix} \vec{d^t} & 0 & 0 & 0 \\ -\vec{d^t} & 0 & 0 & 0 \end{bmatrix}, h = \begin{bmatrix} 0 \\ -\epsilon_3 \end{bmatrix} - H\vec{\delta}. \tag{7.16}$$

7.3.4 Cross-Correlation Based Dynamic Error Compensation

Though the ultrasound image should be accurately tracked by the robot end-effector, there are multiple error sources involved in the system as discussed in the

introduction. To compensate the dynamic error, an error compensation method based on cross-correlation is introduced to correct the spatial inconsistency introduced in the axial axis for different scanning poses.

During the process of reconstructing each pixel in the STRATUS image, a kernel window surrounding the pixel is chosen. We compare this window with the data from neighboring poses across the image. For each axial sample t in the pose i, the error in the neighboring pose $i+1$ in the axial axis, Δt_i, can be found through the cross-correlation as,

$$\max_{\Delta t_i} \frac{\sum_{i=1}^{N-1} s_i(t) s_{i+1}(t+\Delta t_i)}{\sqrt{\sum_{i=1}^{N-1} s_i(t)} \sqrt{\sum_{i=1}^{N-1} s_{i+1}(t+\Delta t_i)}}, \tag{7.17}$$

where s_i, and s_{i+1} are the two dimensional kernel windows of the RF data for the pose i and $i+1$. The detected error shift Δt_i is compensated during the summation process, and the new STRATUS image is formed by using the delay function to mitigate its dynamic errors.

7.3.5 Experimental Setup

7.3.5.1 Virtual Fixture Evaluation

The goal of the experiment was to test the feasibility of co-robotic STRATUS system using a 6 degree-of-freedom robotic arm (UR5, Universal Robot). In this demonstration, we defined an in-plane translational virtual fixture, and the ultra-

sound probe was only allowed to move along the path. The forces exerted on the ultrasound probe by the user are measured by a 6-axis force/torque (F/T) sensor (FT150, Robotiq). The FT150 connects directly to the robots controller. It has an outside diameter of 12 mm, a 100 Hz data output rate, a linear force measuring range of ± 150 N and a torsional measuring range of ± 15 Nm. The FT150 was rigidly attached to the robot tooltip and the ultrasound probe was attached to the sensors tool interface. The calibration transformation X is initially obtained from the design of the probe attachment, and then refined by translationally scanning a wire phantom until the optimal X is found. A convex probe with 128 elements (C5-2 Convex, Ultrasonix) was used as the ultrasound probe, and the center frequency was set to 2 MHz. The data was collected by a clinical ultrasound scanner (Sonix CEP, Ultrasonix), which has real-time pre-envelope detected RF data collection capability. The recorded RF data is transferred to a workstation through the MUSiiC RF server [8] at 6 fps. Multipurpose tissue/cyst ultrasound phantoms (84-317, Nuclear Associates) containing point targets as well as anechoic and hyperechoic regions were used for the imaging targets.

7.3.5.2 *In Vivo* Experiment

The goal of the experiment is to visualize the in vivo target with robotically implemented STRATUS system. A similar experimental preparation was made as the virtual fixture evaluation except the force sensor and cooperative control was

not used. The human forearm is scanned in two conditions. At the first setup, the forearm is submerged in a water tank at 8-12 cm depth, and the robotic arm motion is applied without having a direct contact to the body. We set a 6 cm translational motion based on an initial scan of the wire phantom, and the same motion trajectory was applied to the human forearm target assuming the motion using the robotic arm is repeatable. The initial pose for scanning could be arbitrarily defined. At the second setup, the probe directly touched the forearm while the same 6 cm translation motion was applied.

For quantitative evaluation, the full width at the half maximum (FWHM) was used to measure the lateral width of the wire phantom. For *in vivo* targets, the contrast ratio of anechoic region versus echoic region was calculated.

7.4 Results and Discussion

7.4.1 STRATUS Images with Virtual Fixture

Before scanning the imaging phantom, the robotic tracking with and without virtual fixture control was evaluated (Fig. 7.3). The automatic scanning was performed by inputting a constant velocity for the translational motion, and in the other case, the ultrasound probe was moved manually with the virtual fixture constrained trajectory on the same line. The raw robotic tracking data of three axes corresponding for 60 poses under a translational motion is shown in Fig. 7.3(a). Since the raw data

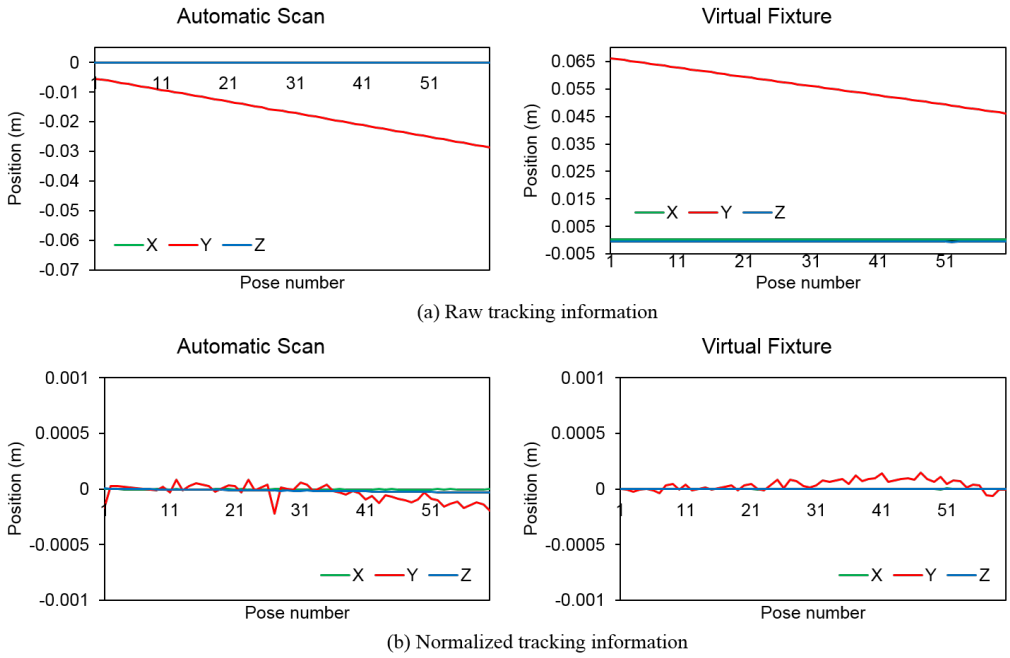

Figure 7.3: Robotic tracking under virtual fixture control compared with automatic scanning. (a) The raw robotic tracking information with and without virtual fixture control, and (b) The robotic tracking information normalizing slope and intersect to cut the effect of velocity difference.

were difficult to compare with and without virtual fixture cases because the velocity of virtual fixture is not easily controllable and varied, the results normalizing slope and intercept are shown in Fig. 7.3(b). The quantified standard deviation of each axis was 0.002, 0.072, and 0.010 mm under automatic scanning, and 0.002, 0.047, and 0.001 mm under virtual fixture control. These errors were sub-hundred micrometer, and this result indicates that a stable scanning is possible with the virtual fixture control, and it does not affect on synthetic aperture beamforming.

Figure 7.4(a) shows the single pose ultrasound image acquired by scanning the general ultrasound phantom. The center region of the image shows a brighter contrast

compared to lateral regions because the convex probe could not have full contact with the flat phantom surface.

For STRATUS imaging, a data set from 105 poses was collected under virtual fixture control. STRATUS image formation was applied on the data, while the specific aperture size range was set to synthesize each line on the STRATUS image. In other words, the average intensity of the data captured within the assigned motion range was plotted for each line reconstruction. Figures 7.4(b-c) show the result using the synthesizing aperture ranges of 10 mm and 60 mm. By integrating the information from all poses, the FOV of the image expanded by 131 mm, and it enabled us to visualize features that were not visible in the single pose image. The resolution of the point targets improved as the aperture size increased, and the contrast of the anechoic region became more obvious. The image quality measurement result of Fig. 7.4 is summarized in Table 7.1. The full width at half maximum (FWHM) was used to quantify the resolution, and contrast and signal-to-noise ratio (SNR) were used to show the overall image quality. However, the resolution of point targets aligned around 85 mm depth did not improve well because of the error introduced by motion artifacts, ultrasound calibration, or tracking inaccuracy.

7.4.2 Dynamic Error Compensation

Using the same data used in the previous section, the dynamic error compensation shows a substantial image quality improvement when comparing the STRATUS image

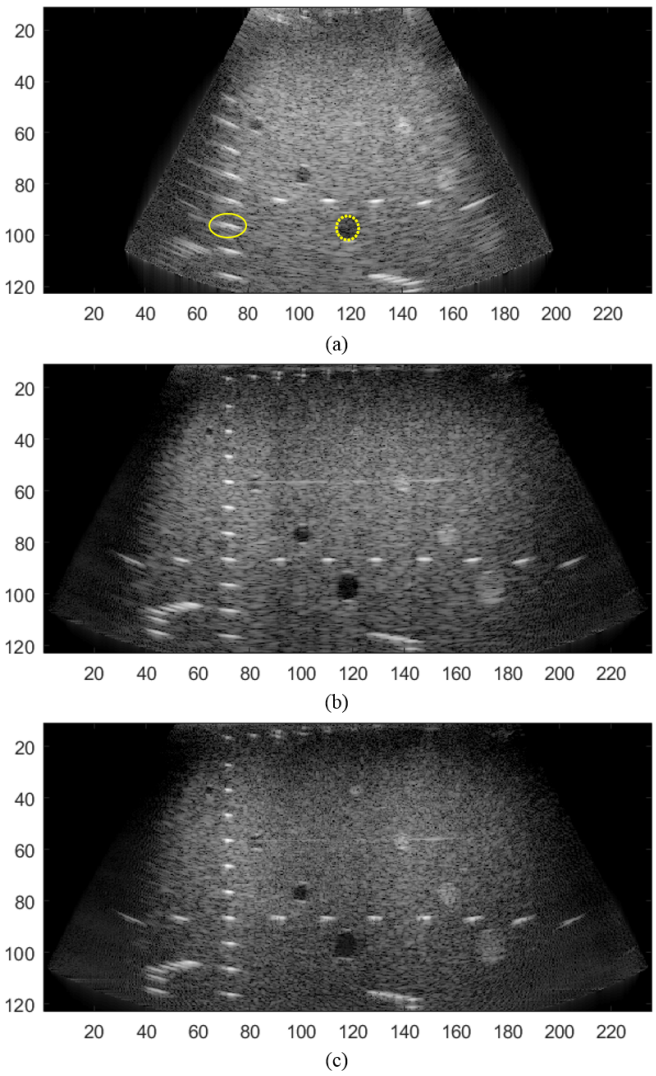

Figure 7.4: (a) Single pose B-mode ultrasound image. (b-c) STRATUS images synthesized the range of 10 mm (b) and 60 mm (c) motion data. The yellow solid circle region was used for FWHM and SNR measurement, and the dot circle region was used for contrast measurement.

Table 7.1: Quantitative analysis on ultrasound images.

	Single pose	STRATUS	
		10mm	60mm
FWHM(mm)	3.87	3.96	2.37
Contrast(dB)	-7.14	-13.24	-10.67
SNR(dB)	25.01	27.20	29.35

to conventional single pose image (Fig. 7.5). The FWHM of a point target located at a depth of around 85 mm (second point from left) was 3.13 mm and 2.78 mm, before and after applying the STRATUS algorithm, respectively. The dynamic error compensation further reduced the FWHM to 1.15 mm. For SNR, the STRATUS image improved from 28.96 dB to 30.27 dB even before applying the dynamic error correction. The SNR of the error corrected image was 33.17 dB.

7.4.3 *In Vivo* Evaluation Results

Given the established system, the system performance was evaluated by scanning a human forearm with two setups. For the first setup, a human forearm under the water tank was scanned in the direction perpendicular to the forearm axis [Fig. 7.6]. The speckle pattern got smaller as the aperture size extends, and the boundary of the forearm and its inner structure got clearer compared to the single pose image.

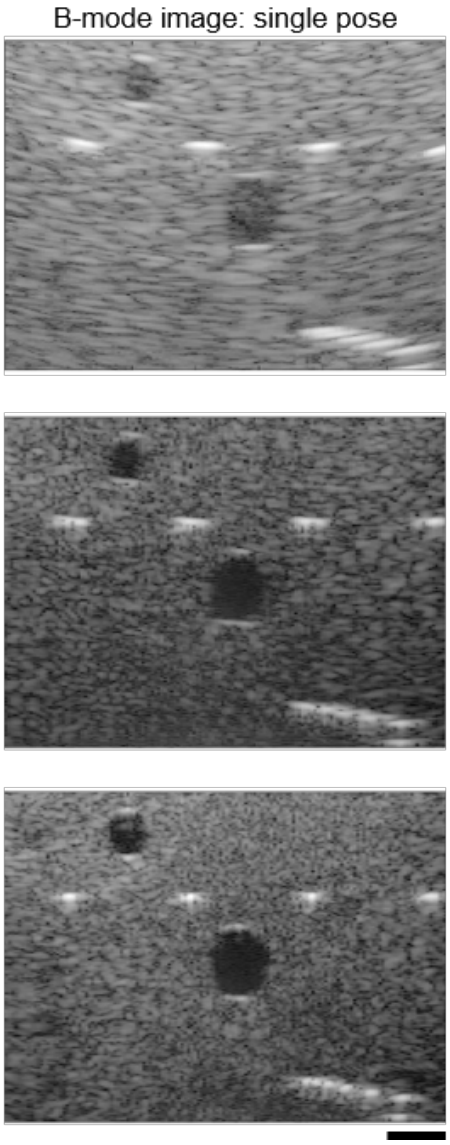

Figure 7.5: STRATUS imaging results with and without dynamic error compensation, compared to conventional B-mode image. Scale bar represents 10 mm.

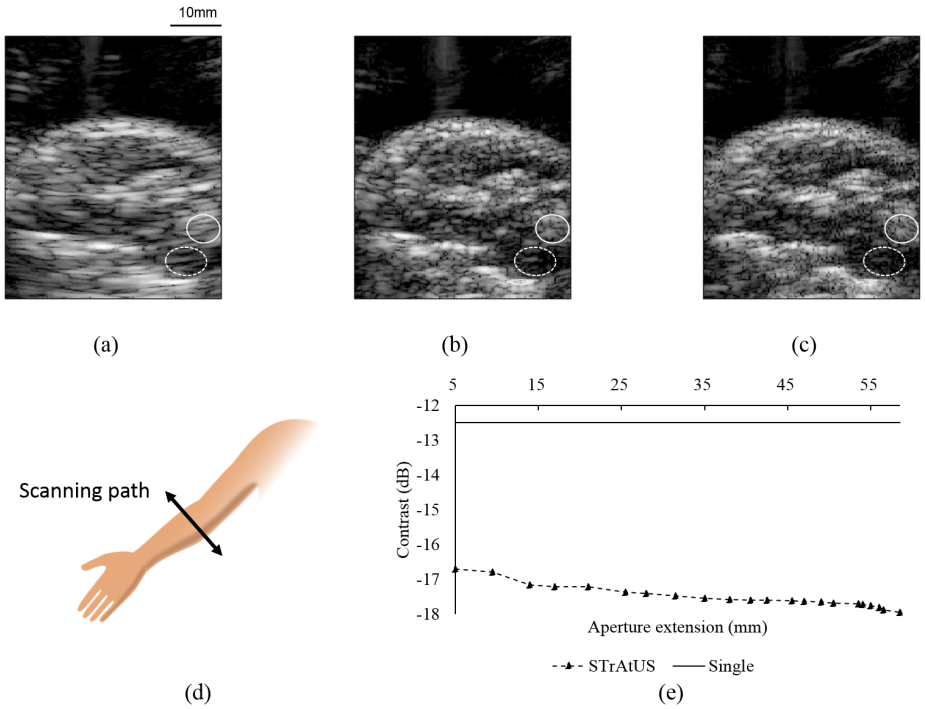

Figure 7.6: The reconstructed image of the human forearm under the water tank. (a) Single pose result represents conventional ultrasound image, (b) the STRATUS imaging result using 10 poses data corresponding to 19.5 mm motion, and (c) the STRATUS imaging result using 20 poses data corresponding to 36 mm motion. (d) Illustration of the scanning path. (e) Contrast comparison between single pose case and multiple poses case are shown. The solid line circle and the dot line circle in the image was regarded as the target region and the background region, respectively.

The image quality improvement of the forearm in the deep region demonstrate the feasibility that the same improvement is expected in the abdominal region of the body. The solid line circle and the dot line circle in the image was regarded as the target region and the background region, respectively. The contrast at the single pose was -12.49 dB, and that of STRATUS imaging was from -16.70 dB to -18.00 dB as the aperture size increases.

For the second setup, the ultrasound probe directly scanned a human forearm along with the forearm axis [Fig. 7.7]. The boundary of muscle structures became obvious corresponding to the aperture extension. Moreover, the field of view of STRATUS imaging became wider than that of single pose. The contrast of the image was analyzed in the same way as the first setup. The contrast at the single pose was -11.73 dB, and that of STRATUS imaging was from -13.95 dB to -21.77 dB as the aperture size increases.

In this study, the static errors were minimized through calibration refinement using a wire phantom. The first setup with water tank is to evaluate the scanning target located at deep region. The motion artifacts from the forearm was minimal when there is no direct contact with the probe. On the contrary, the second setup directly scanning the forearm using the probe is to test the probe misalignments due to the force from the contact. In addition, the field of view extension could be confirmed in this study. Image quality improvement was observed in the near region, but scanning abdominal regions is desired to further evaluate this criteria. To improve the current setup, the frame rate of ultrasound RF data acquisition should be increased to enable faster scanning motion.

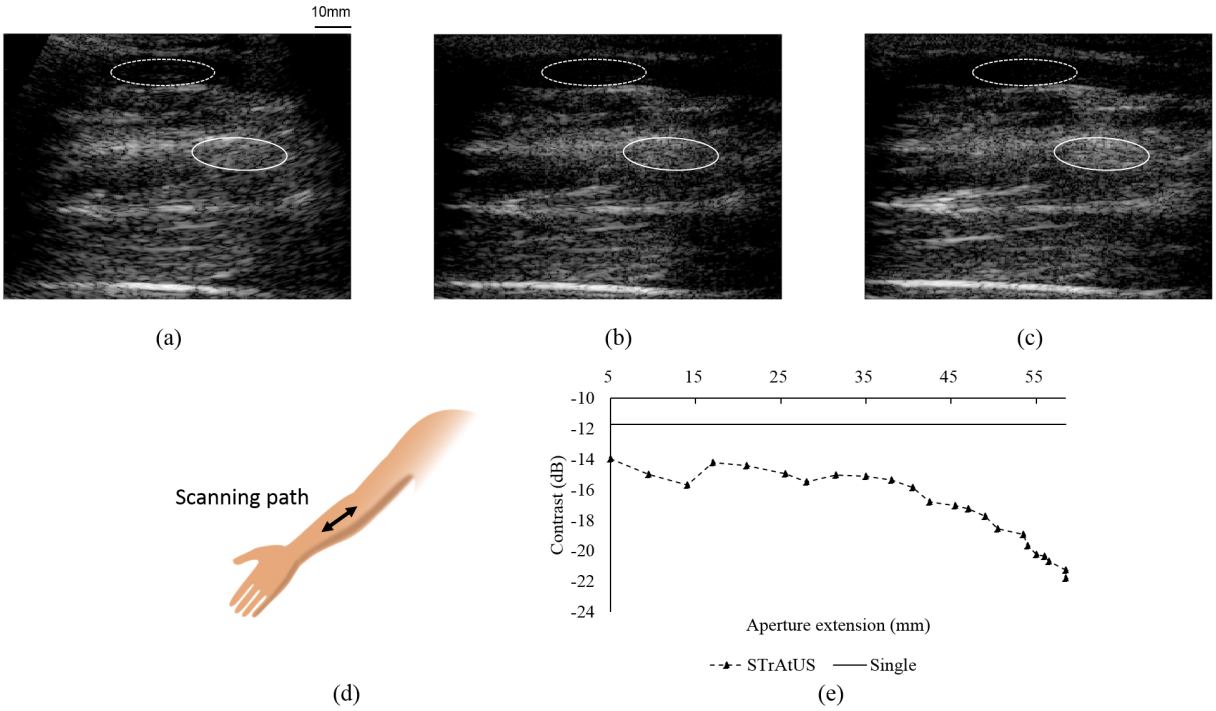

Figure 7.7: The reconstructed image of the human forearm with the probe touched. (a) Single pose result represents conventional ultrasound image, (b) the STRATUS imaging result using 10 poses data corresponding to 19.5 mm motion, and (c) the STRATUS imaging result using 20 poses data corresponding to 36 mm motion. (d) Illustration of the scanning path. (e) Contrast comparison between single pose case and multiple poses case are shown. The solid line circle and the dot line circle in the image was regarded as the target region and the background region, respectively.

7.5 Conclusion

We demonstrated an image quality improvement over conventional ultrasound under virtual fixture control in a general ultrasound phantom. The experiment results show that multiple image quality factors such as resolution, contrast, and SNR improved with STRATUS imaging. In addition, we demonstrated that dynamic error compensation could further improve image quality. *In vivo* experiment was performed to validate the clinical applicability. Co-robotic ultrasound imaging approaches could change the paradigm of ultrasound imaging by providing high resolution deep tissue imaging and human/robot cooperative diagnostic capabilities.

Chapter 8

Three-dimensional Synthetic Tracked Aperture Ultrasound Imaging

This chapter has been published as: *H. K. Zhang, T. Y. Fang, R. Finocchi, E. M. Boctor, "High Resolution Three-Dimensional Robotic Synthetic Tracked Aperture Ultrasound Imaging: Feasibility Study, in SPIE Medical Imaging, 2017.*

I was responsible for the project design, system integration, data collection, analysis and writing. Rodolfo Finocchi and Ting-Yun (Angel) Fang contributed on robot arm control. Dr. Emad M. Boctor supervised the project.

8.1 Introduction

Three dimensional (3D) ultrasound imaging is becoming a standard mode for medical ultrasound diagnoses such as fetus status observation [64,65] or image guided interventions [66]. Real-time 3D ultrasound provides intuitive anatomical information by showing whole structure compared to a single slice B-mode image. Therefore, 3D ultrasound allows for imaging any cross section in the same way as X-ray Computed Tomography (CT), so that users can extract the desired slice for examination without needing to find the optimal scanning angle. This feature reduces the ultrasound scanning time, and makes ultrasound a more accessible, and reliable diagnostic tool. Following the trend of 3D ultrasound, recently, automated breast scanning systems have been introduced, which are capable of scanning a wide region of breast automatically without requiring sonographers to manually search the scanning regions [67,68].

Existing 3D ultrasound imaging systems are mostly either using a two dimensional matrix array or mechanically scanning a one dimensional array in the elevational direction. Although the former approach is capable of real-time imaging without any mechanical volume scanning, it requires expensive and sophisticated hardware, and is still not widely available in clinics. The latter approach is more available, but has several limitations: 1. To shape the beam in-plane, only a single focal point is possible through the focus lens. Thus, the image resolution in the elevational axis is worse as the distance to the focal point increases; 2. The volume size of 3D ultrasound is predetermined by the scanning field of the 3D probe. Thus, this system has a limited

field-of-view.

To overcome these two limitations, we propose to integrate robotic tracking into synthetic aperture beamforming approach. While the ultrasound probe is moved by a robotic arm, each probe position is tracked and can be used to form a wide volume data as there is no physical barrier that restricts scanning in the elevation direction. At the same time, synthetic aperture beamforming provides a dynamic focusing at all depths. To synthesize the elevational aperture information, the single focal point provided by the acoustic lens is regarded as the virtual element, and forward and backward delay-and-sum are applied to the radio-frequency (RF) data collected through the volume.

In this feasibility study, we built the 3D synthetic tracked aperture ultrasound imaging system using a 6 degree-of-freedom robotic arm. A 3D volume is collected by scanning a translation trajectory in the elevation direction. A general ultrasound phantom is scanned as the imaging target, in which wire targets at different depths were used to evaluate its elevational resolution. Furthermore, in addition to B-mode slices, we implemented a 3D visualization algorithm that enable to display 3D data in any angle through volume projection.

8.2 Contributions

The main contributions of this chapter are the following:

- Establishment of elevational synthetic aperture focusing algorithm with robotically tracked ultrasound system
- Development and validation of 3D STRATUS imaging

8.3 Methods

8.3.1 Synthetic Tracked Aperture Ultrasound Imaging in Elevation Direction

To integrate tracking information with elevational synthetic aperture focusing, we implemented our Synthetic TRacked AperTure UltraSound (STRATUS) imaging system that integrates two concepts: Mechanical pose tracking and elevational synthetic aperture beamforming [43, 44, 69–71]. A robotic arm provides the transformation, B, from the robot base to the end-effector coordinate. To track the ultrasound image for all rotations and translations, the tracking device coordinate frame B and the following calibration transformation X should be known (Fig. 8.1). A robotic arm is used as a mechanical tracker as well as an actuator. The calibration transformation X can be obtained through ultrasound calibration, which is a separate procedure from the actual 3D data acquisition [52]. When the probe is moved in the in-plane direction, the field-of-view of a B-mode image will expand, and when the motion is in elevation direction, this lead to extend the imaging dimensionality from two dimension to three

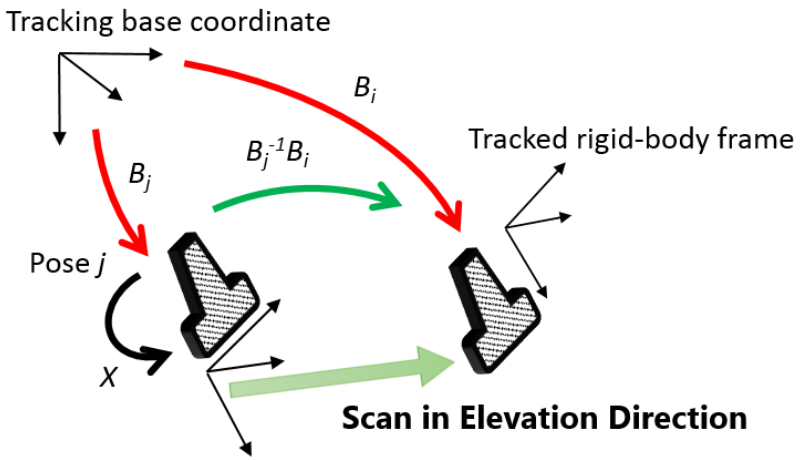

Figure 8.1: The coordinate systems involved in STRATUS imaging system. The transformations associated with pose i and j are shown.

dimension 3D. The obtained two dimensional scanning data (RF) from each pose can be rearranged in 3D space by registering ultrasound data positions into the world frame using the BX transformation.

This rearranged 3D volume, however, has a limited elevational resolution because of the ultrasound beam thickness in the elevation axis. There is a single focal point provided by the acoustic lens, and the near field or far field from the focal point will be defocused. To apply the synthetic aperture concept here, this single focal point is regarded as the virtual element, and multiple aperture windows from elevational slices are dynamically re-beamformed in the elevation direction [43, 68]. Assuming r_F is the reconstruction depth and z_F is the focal point, the time-of-flight (TOF) considered in this adaptive beamformer is:

$$t(r'_f) = \frac{2|r'|}{c}, \tag{8.1}$$

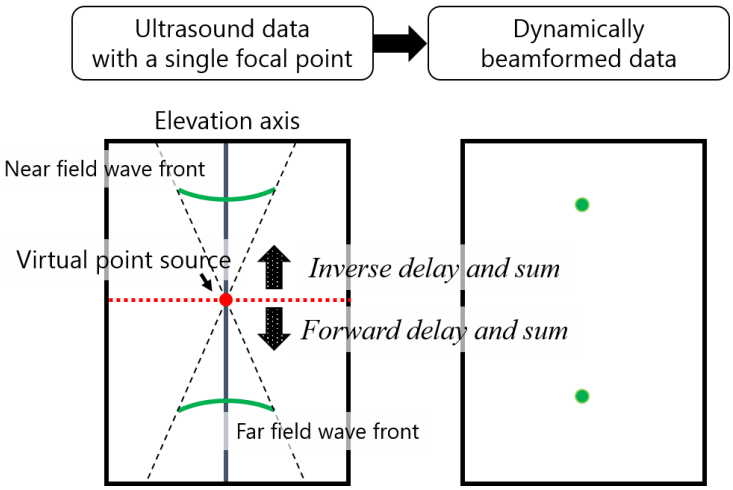

Figure 8.2: The illustration of synthetic aperture focusing on elevational axis. Inverse and forward delay-and-sum algorithm was applied from the single focal point regarded as virtual element.

where,

$$|r'| = \sqrt{(x)^2 + (z - z_F)^2}, \tag{8.2}$$

$r'_F = r_F - z_F$; x and z is the lateral and axial components of the geometrical vector r, respectively. The dynamic receive delay focusing will be applied in the positive axial direction when $z \geq z_F$, and a negative dynamic focusing delay will be applied when $z < z_F$.

8.3.2 Three-Dimensional Visualization

Although conventional B-mode image displays serve a standard visualization approach for ultrasound slices, with 3D volume data, a more adaptive visualization approach is desired for intuitive perception. In this paper, we project the model matrix onto planes viewed from several different angles, the same as the conversion

method used between X-ray and X-ray CT. By constructing images viewed from specific angles, it can give us an intuitive sense of what the 3D matrix looks like in space. To construct the images, firstly, we perform a rigid transformation to the 3D matrix, where the rotation is defined by the Euler ZYX Convention. After the transformation, we can get the transformed 3D matrix seen in the world frame. To rotate the matrix, each point position is multiplied by the homogenous transformation matrix as shown in the following equation:

$$P = \begin{bmatrix} x \\ y \\ z \\ 1 \end{bmatrix} = \begin{bmatrix} R_{zyx} & 0 \\ 0 & 1 \end{bmatrix} \begin{bmatrix} x' \\ y' \\ z' \\ 1 \end{bmatrix} = \begin{bmatrix} R_{zyx} & 0 \\ 0 & 1 \end{bmatrix} P', \tag{8.3}$$

where, P is the position w.r.t the world frame, and P is the position w.r.t the model frame. After rotation, the model matrix is translated to the first quadrant w.r.t the world frame; thus, the points set would be adjusted to positive values and have a minimum of 0.

Then, we project the new 3D matrix to the $x - y$ plane with respect to the world frame (Fig. 8.3(a)). Due to the discrepancy of the model matrix data, the new location of each point mostly lays between two integers after the transformation. In this case, an interpolation method should be taken into account. At (x, y) coordinate on the new projected image, a straight line normal is drawn to the projection surface, and any point in the rotated matrix that has a distance (d_i) within 0.5 to the normal

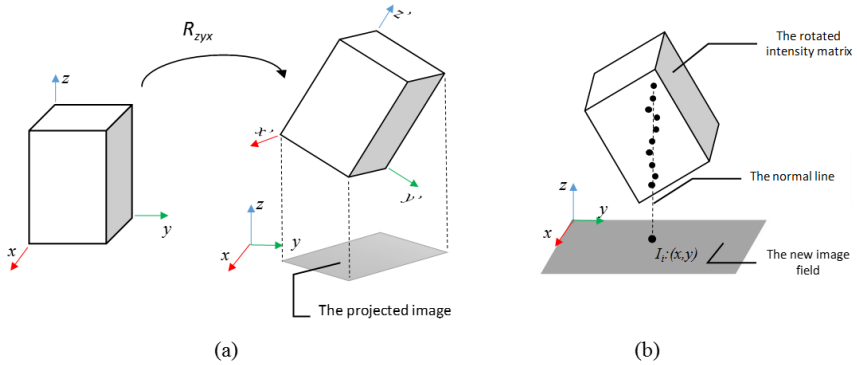

Figure 8.3: The methodology of visualizing 3D ultrasound volume. (a) Transforming 3D volume with a desired rotation. (b) Projecting the 3D volume into 2D x-y plane with respect to the world frame.

line would be considered and multiply by $(0.5 - d_i)$ as a weighting number (Fig. 8.3(b)). By summing all the weighted intensity and dividing by the total weight, the intensity (I_i) at (x, y) can be calculated.

$$\text{Intensity} : (x, y) = \frac{\sum_i (I_i \cdot (0.5 - d_i))}{\sum_i (0.5 - d_i)}, \tag{8.4}$$

where, I_i is the intensity of ith point, and d_i is the distance between the ith point and the normal line.

8.3.3 Experimental Setup

Given the approach described earlier, the goal of the experiment is to visualize structures in the elevation plane with the robotically implemented STRATUS system [44]. Although this system equips the cooperative control mode by utilizing a combined force sensor setup, this is not used here to focus on evaluating the image performance under a controlled scan. We set an elevation translational motion that

was provided by a 6 degree-of-freedom robotic arm (UR5, Universal Robot). A convex probe with 128 elements (C5-2 Convex, Ultrasonix) was used as the ultrasound probe, and the center frequency was set to 2 MHz. The data was collected by a clinical ultrasound scanner (Sonix CEP, Ultrasonix), which has real-time pre-envelope detected RF data collection capability. The recorded RF data were transferred to a workstation through an RF server [8]. The robot motion speed was set to 3.6 mm per second, and the RF data was collected at 6 fps during the motion. To control the motion, the tracking data were collected from a robot controller linked to the workstation. The transformation X was initially obtained from the CAD model design of the attachment connecting the probe and the robotic arm; then we refined the transformation based on a task oriented evaluation. As the scanning object, a general ultrasound phantom (84-317, Nuclear Associates) with point targets and anechoic regions is used.

8.4 Results

For one set of elevational sweeping, the motion trajectory recorded by the robotic arm with respect to the ultrasound image coordinate is shown in Fig. 8.5. The motion in the lateral and axial directions was almost zero, while the position in the elevation direction was moved with a constant velocity as predefined.

The elevational view of the phantom is shown in Fig. 8.6(a). Without elevational

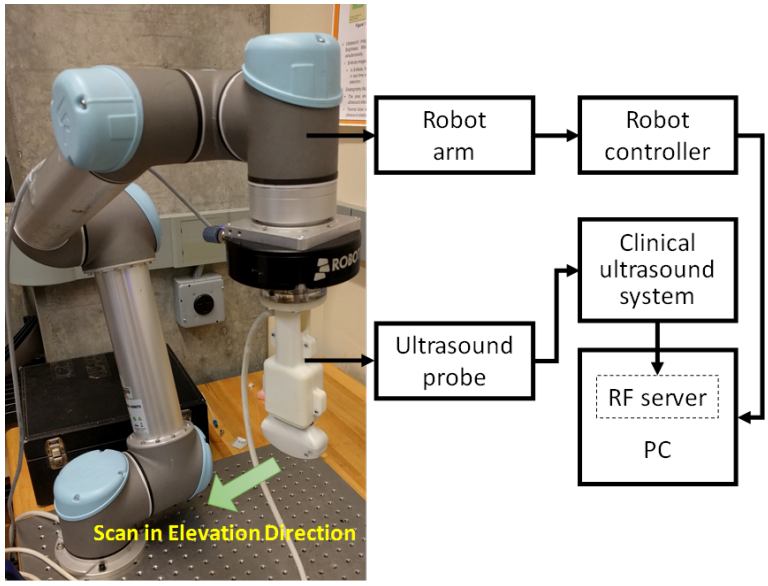

Figure 8.4: The experiment setup. A pure translational motion in the elevation direction is assigned. The ultrasound data at each tracking timing has been recorded through a clinical ultrasound machine.

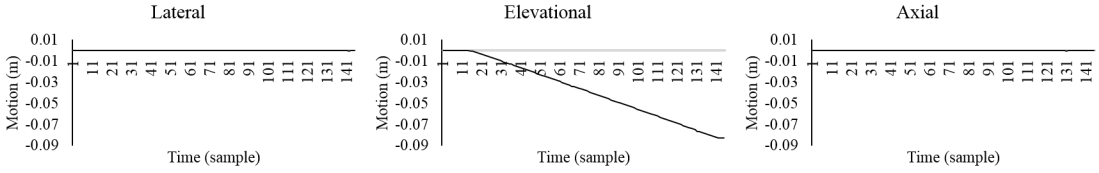

Figure 8.5: The tracked motion from the robotic arm on ultrasound image coordinate for three axes.

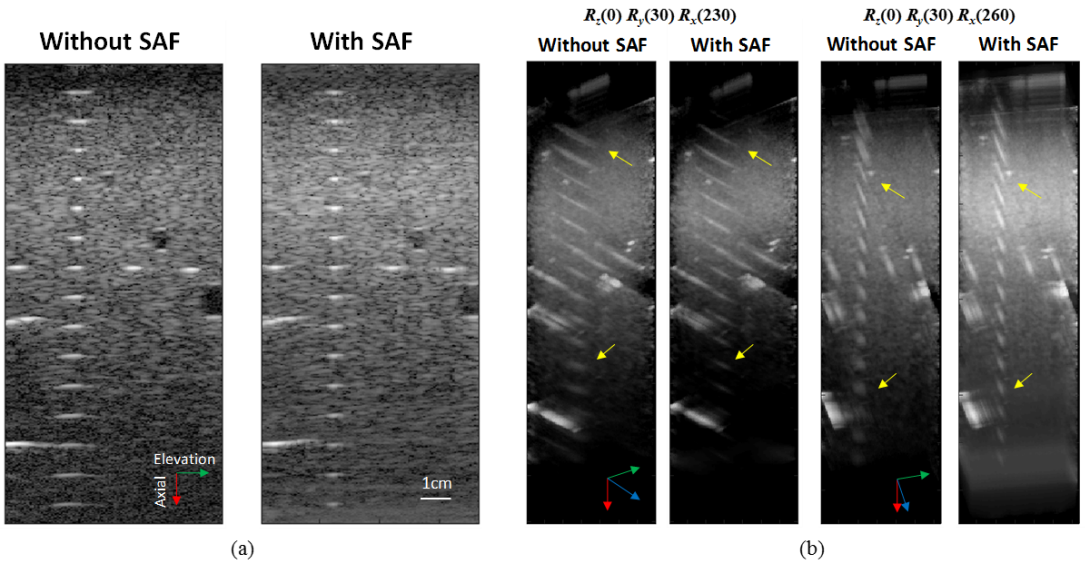

Figure 8.6: Elevational plan (a) and (b) 3D visualization results in conventional B-mode (left), and STRATUS imaging (right), comparing with and without synthetic aperture focusing (SAF).

synthetic aperture, the point target was well focused around the 48.5 mm depth, but is gradually defocused as the distance to the focused target point increases. However, with synthetic aperture focusing, a dynamic focusing is applied so that the focus can be applied for all depths. The full width at half maximum of the point target located at 20 mm and 110 mm depths improved from 4.83 mm to 1.90 mm, and from 6.03 mm to 2.82 mm, respectively. Figure 8.6(b) shows the projected 3D volume with a rotation of 30 degrees in the y axis, and 230 degrees and 260 degree in the x axis, respectively ($R_{zyx} = R_z(0) \cdot R_y(30) \cdot R_x(230)$ and $R_{zyx} = R_z(0) \cdot R_y(30) \cdot R_x(260)$). The wire structures have better resolution, as highlighted by the yellow arrows.

8.5 Discussion and Conclusions

We have proposed a novel robotic ultrasound approach to enable high elevational resolution 3D ultrasound imaging. A critical limitation on conventional B-mode ultrasound imaging is that sonographers are required to search around the region until finding an optimal angle. An automatic ultrasound scanning system could be a solution for that in a sense that a wide region in 3D can be captured, and any angle slices can be recovered offline. Our approach could further generalize to 3D scanning without any constraints on the scanning field due to a large dexterity and workspace enabled by a 6 DOF robotic arm.

An one dimensional array transducer is optimized to obtain a plane beam slice, so that the only focus on the elevation axis is a fixed focusing at both transmit and receive. With synthetic aperture focusing, dynamic focusing can be applied in the elevation axis and it is possible to maximize the resolution on the axis. For 3D ultrasound imaging, having a high resolution in all axes is desired to allow the user to select any angle slice for the diagnosis. The proposed algorithm could bridge the elevational resolution to be comparable to the resolution in other axes, and this enables the idealistic 3D imaging.

This chapter serves as the proof of concept of robotically enabled 3D ultrasound imaging by demonstrating the resolution enhancement in phantom experiments. For future direction, the force sensing element can be combined to incorporate cooperative robot control with virtual fixtures, and be validated on *ex vivo* and *in vivo* subjects.

Chapter 9

Photoacoustic Synthetic Tracked Aperture Imaging and Application on Transrectal Ultrasound Probe

This chapter has been published as: *H. K. Zhang, F. Aalamifar, H-J Kang, E. M. Boctor, "Feasibility Study of Robotically Tracked Photoacoustic Computed Tomography, in Proceedings of SPIE Medical Imaging, 2015* and *H. K. Zhang, A. Cheng, E. M. Boctor, "Three-dimensional Photoacoustic Imaging Using Robotically Tracked Transrectal Ultrasound Probe with Elevational Synthetic Aperture Focusing", in Proceedings of CLEO, 2016.*

I was responsible for the project design, system integration, data collection, analysis and writing. Alexis Cheng and Fereshteh Aalamifar provided technical supports.

Dr. Emad M. Boctor supervised the project.

9.1 Introduction

Photoacoustic imaging (PA) is becoming a promising imaging modality for pre-clinical and clinical applications by providing both functional information and depth information. In particular, PA computed tomography (PACT) aims to visualize the tomographic image of PA source distribution by scanning the surface of the target structure with an ultrasound transducer [72]. Circular scanning geometry is generally used to acquire wide range of scanning angle, which enables high spatial resolution compared to linear scanning, and ideally full 360 degree scan is necessary to reconstruct the entire target. Placing transducers around the subject or rotating the subject with fixing transducer position are two major approaches to scan in circular arc trajectory [73, 74]. Circular array transducer enable a stable and fast scan because for a single laser emission, it is possible to receive signals from full range simultaneously and the reconstruction can be applied on it. Rotating the subject is a simpler setup, and only a single element transducer and rotation station are required. However, both are not flexible and have their drawbacks. For example, dedicated customized setup requires to allocate ultrasound transducers in a round shape, and since transducer has to be fixed, once the geometry is fixed, there is no flexibility to modify scanning diameter based on the size or shape of the subject. For the case

of rotating the subject, motions of the rotating object easily causes motion artifacts, and it is not practical to rotate large scale targets such as human subjects. Therefore, there is a huge demand for a simple and flexible scanning system for PACT. An array transducer is used as a flexible scanning system for PA tomography, but the problem is its limited view and incomplete reconstruction.

To resolve the problem, we propose a scanning method based on robotic tracking. A robot arm is used to hold an ultrasound transducer, and the motion of the transducer will be regarded as its scanning path. Any trajectory can be created by moving the transducer to multiple positions. Received data from multiple poses can be accumulated simultaneously and put them into tomographic reconstruction algorithm. Therefore, the PACT wont be restricted by the small target, and more large scale target such as human also can be considered as the imaging object. There are a variety of trajectories to scan the target in this approach, and in this chapter, we focus on an in-plane remote center rotational motion.

For translational application, this concept was adapted on transrectal ultrasound (TRUS). TRUS imaging has been a standard approach to localize prostate and seeds for brachytherapy treatment [75]. In addition, PA imaging has the potential to assist the intraoperative treatment planning due to its high sensitivity for brachytherapy seeds [15]. Yet, finding seeds located in three-dimensional space using two-dimensional image planes is challenging, and the technique requires a rich experience on ultrasound scanning. Three-dimensional PA imaging could be a solution by visualizing all seeds

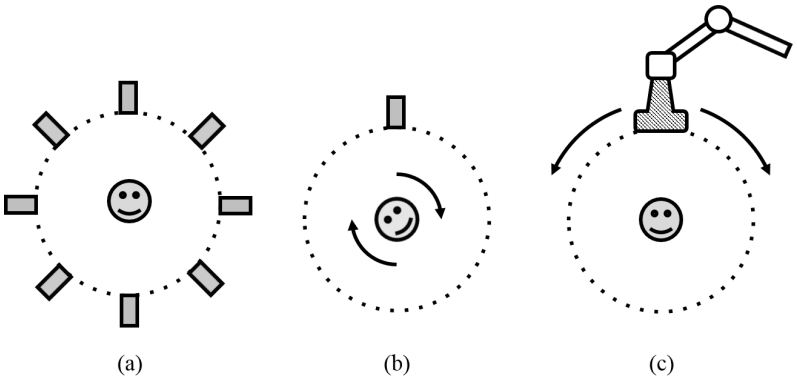

Figure 9.1: Three ways to scan in circular geometry. (a) Placing transducers around the contrast agent, (b) rotating the target, and (c) moving ultrasound transducer around the target using a robot arm.

at once.

Some TRUS probes possess two scanning arrays; one is linear and the other is curvilinear. Rotating the probe for the lateral axis of the linear array could generate three-dimensional volume information. However, the resolution in elevational dimension is low if the region of interest is away from the single focal point generated by acoustic lens. We utilized a 6 degree-of-freedom robot arm to apply a rotational motion to construct a three-dimensional PA image. Elevational synthetic aperture focusing was used to dynamically beamform signals [76].

9.2 Contributions

The main contributions of this chapter are the following:

- Extension of synthetic tracked aperture imaging on photoacoustic computed tomography (PACT)

- Demonstration of photoacoustic synthetic tracked aperture imaging using transrectal ultrasound probe

9.3 Methods

9.3.1 Photoacoustic Computed Tomography Reconstruction and Synthetic Aperture Focusing

There are various PA reconstruction algorithms proposed based on time-domain, Fourier domain, or model based approaches. Here, time-domain delay and sum based reconstruction algorithm is considered. Received PA signals contain shape information of the contrast agent as well as the distance from the target to the receive elements. Back projection algorithm works by recovering the information of the original structure by putting signals for each receive elements back to the source of the signal. The initial pressure $p_0(\vec{r})$ in the time domain can be expressed as follows:

$$p_0(\vec{r}) = \int_{\Omega} b\left(r_0, t = \frac{|\vec{r} - \vec{r_0}|}{c}\right) \frac{d\Omega_0}{\Omega_0}, \tag{9.1}$$

where Ω_0 represents the solid angle subtended by the measurement surface S_0 with respect to the reconstruction point $\vec{r}$ and $\Omega_0 = 2\pi$ for planar geometry. $b(r_0, t)$ is the back projection term, and The received acoustic pressure $p(\vec{r_0}, t)$ at position $\vec{r_0}$ and

time t is directly inserted in this paper. c is the speed of sound, and $d\Omega_0$ is the solid angle subtended by the detection element with respect to $\vec{r}$.

Similar to computed tomography reconstruction, synthetic aperture focusing could be also used to beamform the limited angle information.

9.3.2 Robotically Tracked photoacoustic Imaging

As mentioned in introduction, an ultrasound transducer hold by a robotic arm is swept around the surface. To enable this motion, ultrasound calibration is necessary to identify rotational and translational relationship between ultrasound image and robot end-effector. This rigid-body transformation is used to transform the coordinate system of robot base and ultrasound image, and it is possible to calculate the motion which is applied in robot controller to generate a designated motion in ultrasound image coordinate. A base ultrasound image coordinate is defined and the position of transducer is controlled based on the base. Positional information is assigned to each pose and each single element, and that information will be used to reconstruct a tomographic image.

At the same time, it is necessary to recognize that there are several uncertain factors involved in the system: 1) the movement accuracy of the robotic tracking system, and 2) the precision of ultrasound calibration which affects the transformation from robot end effector to the ultrasound coordinate system. These uncertainties reduce the continuity and prevent a perfect reconstruction when pre-beamformed

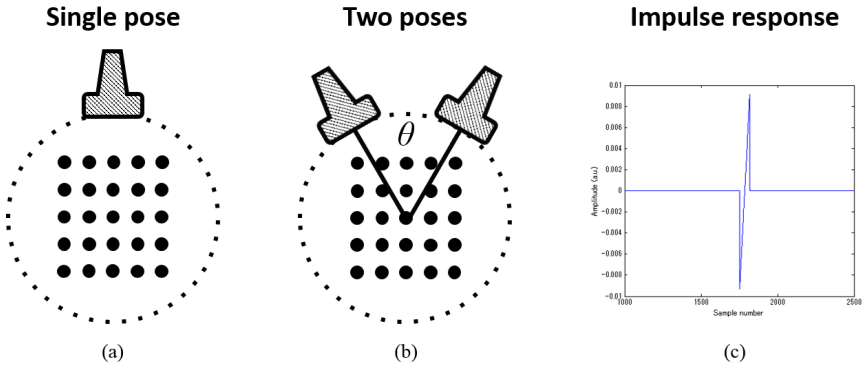

Figure 9.2: Concept of 3D PA image utilizing robotically tracked transrectal ultrasound probe. (a) Picture of setup. (b) Virtual element could be formed for each elevation line scan, and a collection of rotation scan earns a virtual probe surface. Forward and inverse dynamic receive focusing (DRF) is applied based on virtual elements location. (c) Conventional single slice elevational beam width. The target is defocused if it is away from the focal point. (d) New elevational beam with synthetic aperture focusing.

data from multiple poses are combined. Therefore, it is necessary to know the effect of the uncertainty in the reconstruction process.

9.3.3 Robotically tracked Transrectal Photoacoustic Imaging

As a particular case using tracked TRUS imaging, we used synthetic aperture focusing. A focal point generated by acoustic lens was assumed as a virtual element, and a new virtual elements surface could be formed [Fig. 9.2(b)] [43]. Forward and inverse delay-and-sum beamforming was applied originating from these virtual elements [Fig. 9.2(d)].

9.3.4 Simulation Setup

To validate the benefit of robotic aperture extension, numerical phantom simulation studies were conducted. As the base condition, a 128 elements ultrasound transducer with 0.47 mm pitch was used and it is assumed to be attached into a robot arm. The reconstructed result using the data from this transducer at only one position was regarded as the result of conventional PACT (Fig. 9.3(a)). On the contrary, it was assumed in two poses case that the transducer was placed two positions, in other words, it was moved from the first position to the other location (Fig. 9.3(b)). The angle between two poses was varied from 10 to 120 degree while the distance from the contrast agent was kept. The PA signals were collected twice at each position corresponding to two laser irradiation. A final image was generated utilizing these data. As the reason to choose this configuration, it was suitable to demonstrate the effect only comes from angle increase without increasing the number of receiving poses.

A set of 25 contrast agents was placed at the center with the diameter of 2 mm, each of them was separated by 10 mm in lateral and axial direction. The distance of the remote center from transducers was 50 mm. An N-shape impulse response was generated as the PA signal (Fig. 2(c)) [77].

$$\hat{t} = \frac{v_s}{a}\left(t - \frac{r-a}{v_s}\right), \tag{9.2}$$

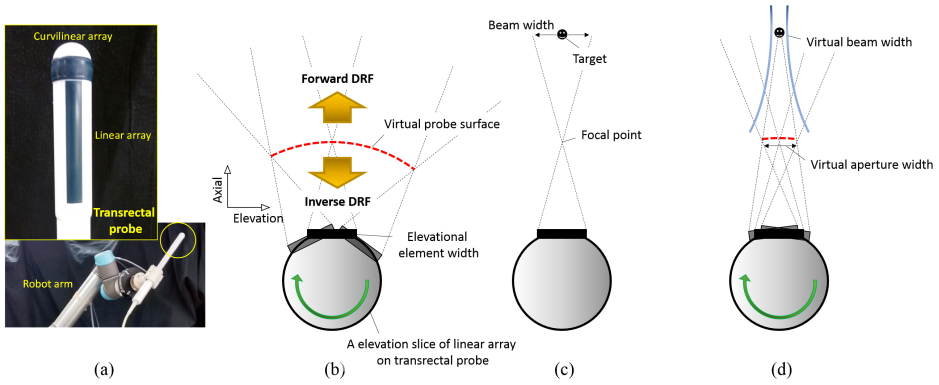

Figure 9.3: Concept of 3D PA image utilizing robotically tracked transrectal ultrasound probe. (a) Picture of setup. (b) Virtual element could be formed for each elevation line scan, and a collection of rotation scan earns a virtual probe surface. Forward and inverse dynamic receive focusing (DRF) is applied based on virtual elements location. (c) Conventional single slice elevational beam width. The target is defocused if it is away from the focal point. (d) New elevational beam with synthetic aperture focusing.

$$p(r,t) = \begin{cases} \frac{C v_s^2 a}{r}(1-\hat{t}) & \text{for } 0 < \hat{t} < 2 \\ 0 & \text{otherwise} \end{cases} \tag{9.3}$$

where v_s is the sound speed, r is the radius coordinate, a is the radius of a uniformly irradiated sphere, and C is a constant to normalize the amplitude. Back projection algorithm based on the equation 1 was used in reconstruction. Hilbert transform was applied to reconstructed data. The speed of sound of 1500 m/s was used and, and the sampling frequency was 40 MHz. For display, the region around the target was cut.

In addition, the effect of tracking error in robotic arm is considered. To simulate possible uncertainty caused by robotic accuracy of motion as well as imperfect ultrasound calibration, the displacement with a certain magnitude was added in axial and

lateral direction toward the right pose data. The rotational uncertainty was negligible in this case, because relative rotation between two poses should be accurate enough when only one transducer was used.

9.3.5 Experiment Setup

We conducted an experiment to validate the proposed approach. A UR5 robot (Universal Robot) is used as the robot arm, and a 6 cm linear array transducer was attached on the robot arm (L14-5W/60 Linear, Ultrasonix). The transducer has 128 elements with 0.47 mm pitch. 532 nm YAG laser was irradiated through an optical fiber to a black plastisol phantom, and the PA signal was generated from the irradiated spot. The probe was rotated in plane rotation with remote center of motion with 80 mm radius. The raw channel data was collected by DAQ device, and beamforming and consecutive data processing were operated in PC. As preoperative ultrasound calibration, a point based algorithm utilizing active-echo phantom was used [52, 53]. The reconstruction precision of the calibration was 1.5 mm.

Three-dimensional PA imaging system is built by rotating a linear array (BPL9-5/55) on a TRUS probe for 31 degrees using a 6 degree-of-freedom robot arm (UR5, Universal Robot) [Fig. 9.2(a)]. The 1064 nm laser pulse was irradiated in 10 Hz using a Nd:YAG laser (Quantel, Bozeman, Montata), and the received channel data was saved using a data acquisition unit (SonixDAQ, Ultrasonix). A focused light was shined to a black inked plastisol gel to form a PA point target.

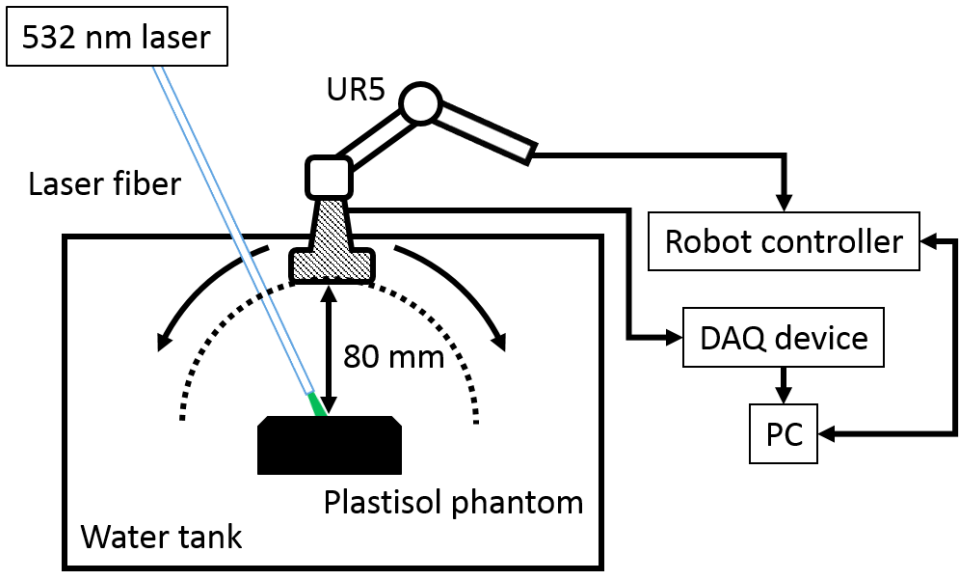

Figure 9.4: Experimental setup.

9.4 Results

9.4.1 Rotational Angle Effect on Photoacoustic Computed Tomography

Figure 9.5 depicts the reconstructed result for single pose case and two poses case (60 degree). In the single pose result, it could be seen that the shape of the target was extended in lateral direction, which was due to the limited aperture size. This result indicates the necessity to expand aperture for this depth. For the same aperture size, the image resolution depends on the target depth. It could be seen that the image resolution is better in the near region and it gets as the target depth increases. The

aperture size is more significant in PA imaging compared to ultrasound, because only receive focusing is available in PA imaging, while both transmit and receive focusing can be applied in ultrasound. When two poses data were used to reconstruct an image, the lateral size of the target clearly became close to its original round shape due to aperture extension.

In Figure 9.6, the zoomed sphere point targets with different rotation angles are shown. As the rotation between two poses increases, the target shape got close to the round shape. When the angle over the 60 degree, the artifact in axial direction started to be appeared. The axial resolution also became worse compared to the 10 degree case. This effect increased more as the rotation angle between two poses increased. This is because that the rotation angle between two poses became too large that the aperture in between two poses was lacking. The artifact will be disappeared if consecutive apertures between two poses were kept. The lateral resolution of the target was evaluated as full with at half maximum (FWHM) (Figure 9.7). One pixel represents 0.2 mm, the FWHM gradually got close to the target diameter 2 mm corresponding to the increase of rotational angle.

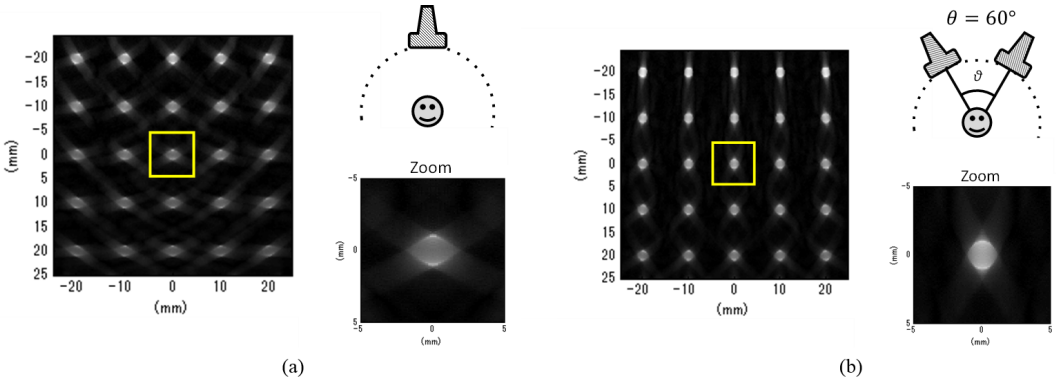

Figure 9.5: Simulation results of (a) single pose and (b) two poses with 60 degree rotation. The center region is zoomed in the bottom right image.

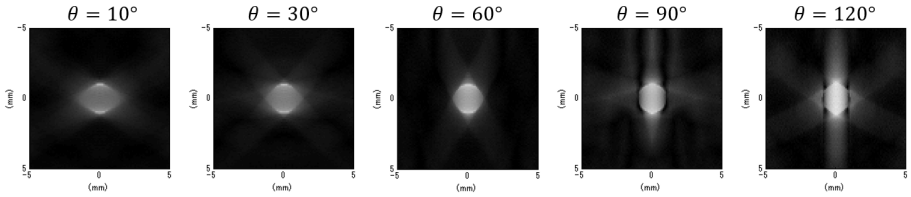

Figure 9.6: Zoomed sphere target around 50 mm depth with different rotation angles.

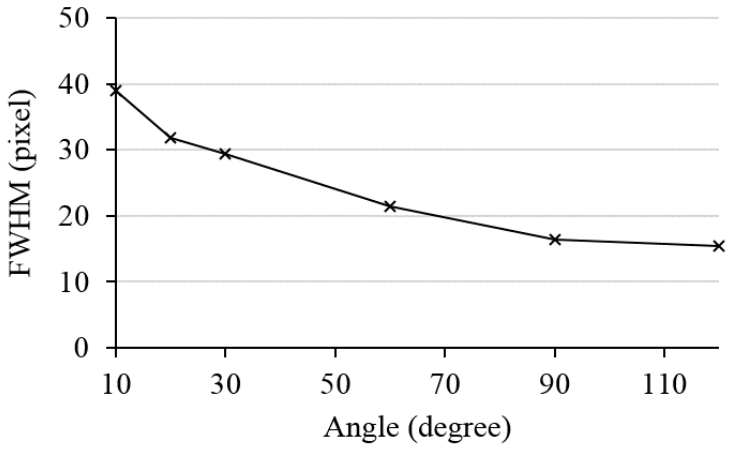

Figure 9.7: Full with at half maximum of the center sphere target.

9.4.2 Effect of Tracking Error on Photoacoustic Computed Tomography

The reconstructed result with tracking error is shown in Fig. 9.8. The left top image is the ground truth, and it shows the result without applying any uncertainty. When the error is applied, one of the two pose is applied a translational error in lateral and axial direction with the designated amount. The reconstructed target in the result with tracking uncertainty was corrupted compared to the ground truth, and the effect increased corresponding to the magnitude of error. When the error in lateral direction is focused, the round shape was still kept until 0.45 mm error, but in 0.9 mm, it is hard to tell this is a round shape. In axial direction, the result with 0.5 mm error caused artifacts on the top and bottom of the target. From the result, the error in axial direction was more significant than that in lateral direction when the similar amount of error was applied. This is attributed to the fact that the axial direction is the direction that RF signal transfers. When the full directional scan is considered, the effect should be equivalent in lateral and axial. Therefore, it can be expected that when the rotation angle between multiple poses are huge, the effect in lateral and axial will be closer. The number shown in the corner of the image is the FWHM. The FWHM increased as the error increased.

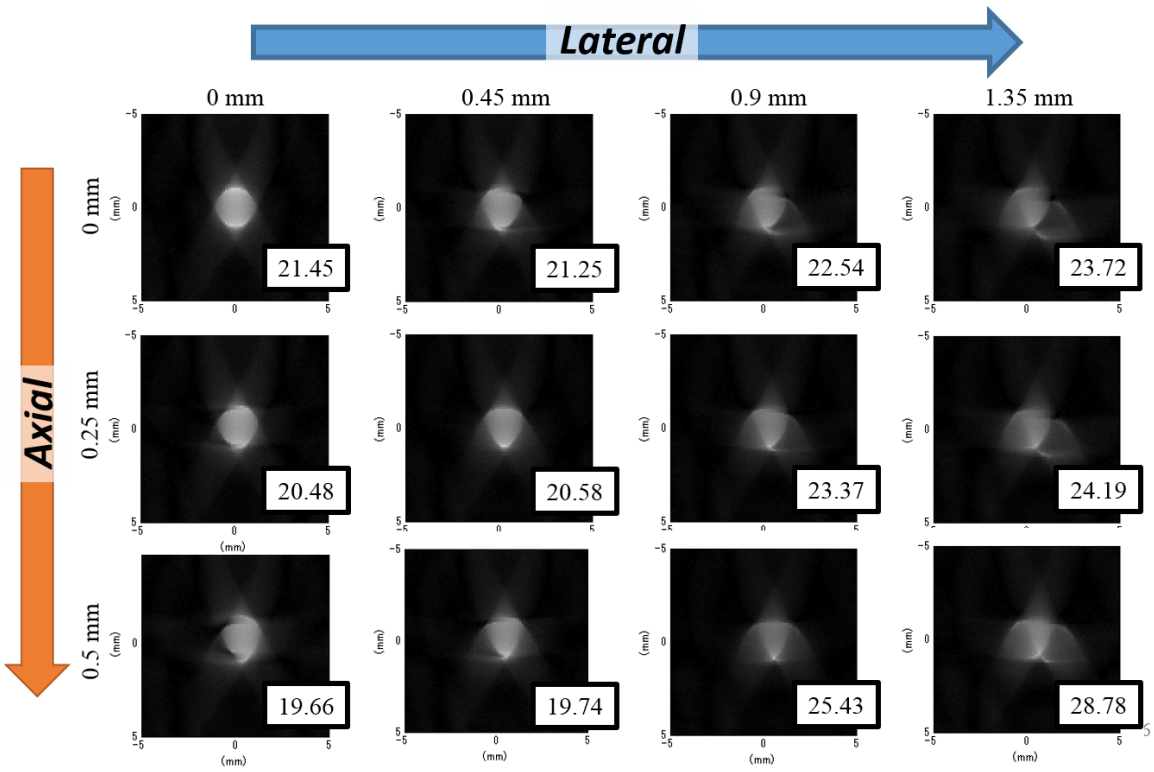

Figure 9.8: The effect of error in lateral and axial direction. The measured FWHM is shown in the right bottom corner.

9.4.3 Experiment Result of Photoacoustic Computed Tomography

The experimental result is shown in Figure 9.9. In Figure 9.9(a), the result of single pose is shown in the left and three poses with 20 degree as total rotation angle is shown in the right. The beamforming artifact appeared in the single pose result is reduced in the three poses result. The error existed between three poses was 3.7 mm, and it was manually compensated. The cause of error could be the inaccuracy of ultrasound calibration. The lateral profile of the target is shown in Fig. 9.9(b). The CNR improvement of 8 % was confirmed. In the single pose result, the side lobe was visible because of limited aperture, but that is reduced for multiple poses result due to compounding. No lateral resolution improvement was seen, because that when the light was shined into the phantom, the spot was not small enough, so that the original target shape was extended laterally. And the rotation angle was also not large enough to make the lateral resolution improvement be clearly seen.

9.4.4 Experimental Result of Transrectal Photoacoustic Imaging

Figure 9.10 shows elevation and lateral slices cutting through three-dimensional PA volume based on PA point target location. The elevational resolution of the target

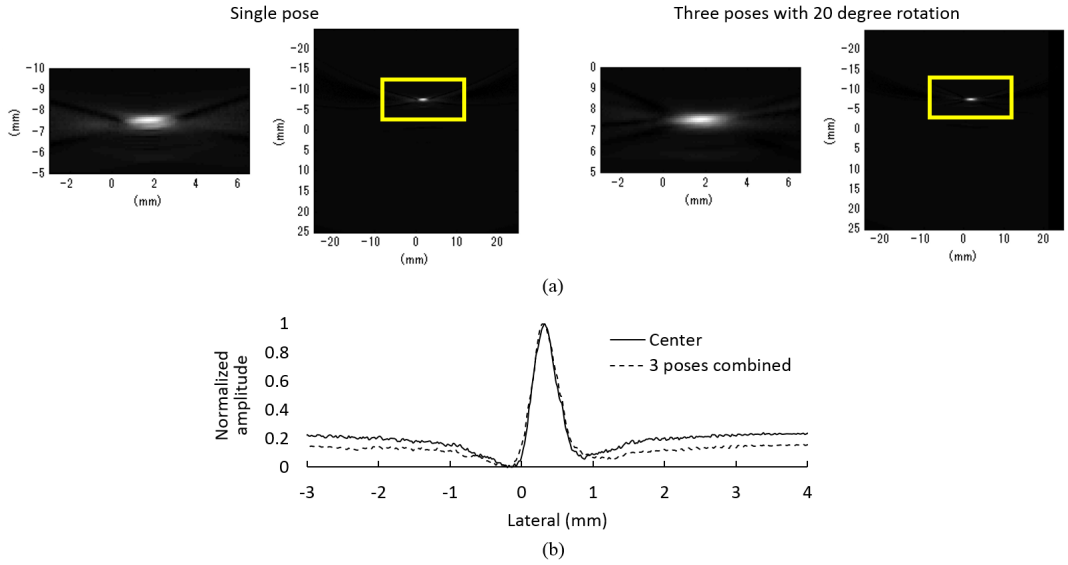

Figure 9.9: The experimental result. (a) Reconstructed image of single pose and three poses with consecutive 10 degree rotation angle, and (b) the profile of the center pose and three poses combined result.

was improved from 1.55 mm to 1.06 mm in full width at half maximum (FWHM). To assess the potential benefit of signal-to-noise ratio (SNR) improvement, -6 dB Gaussian noise was added to background to reproduce a low SNR condition. As a result, the PA target was more visible in both lateral and elevation planes by applying elevational synthetic aperture focusing, and SNR improvement of 4.10 dB and 4.64 dB was measured at lateral and elevation plane, respectively.

9.5 Discussion and Conclusions

In this chapter, we proposed a robotic approach to enable PA computed tomography. Simulation studies were conducted to validate the method, and a lateral

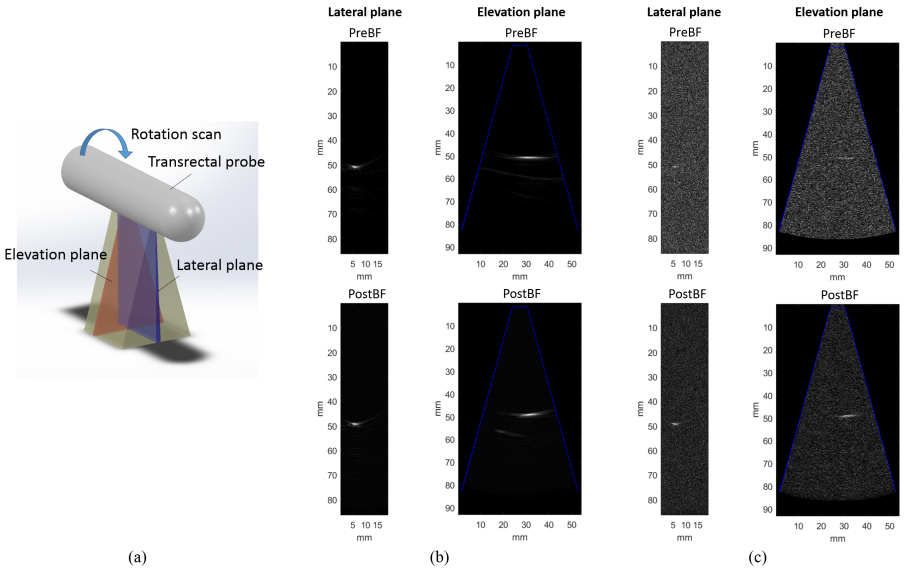

Figure 9.10: Experiment results. (a) Both lateral and elevation plane were cut from the PA point location. The elevation plane after scan conversion is shown. (b) PA images before and after elevation synthetic aperture focusing. (c) PA images with -6dB background noise.

resolution of the image could be seen. The tracking error of robot and ultrasound calibration degraded the shape of the target and FWHM. An experiment was conducted to demonstrate the feasibility of the system. The result indicates that the ultrasound calibration is required to the system, and the robotically tracked PACT has a huge potential to be a new scanning strategy.

FWHM is the matrix expected to evaluate the image quality, and the number becomes large when the error is large. However, it is not necessarily agree with the visual effect of the target. For instance in Fig. 9.8, the left bottom image with 0.5 mm axial error shows the best FWHM, but the image was distorted around the boundary of the round shape. This indicates that other matrix such as pixel count with certain

amplitude threshold should be considered as alternative parameter to judge the image quality. This paper discussed the effect of error corresponding in each lateral and axial direction, and this means that the overall error should be limited in the range. As the next step, further simulation analysis describe the effect of tracking inaccuracy is considered. Moreover, the simulation indicates that a super accurate calibration is necessary, so we will work on developing better ultrasound calibration to enhance the quality of practical implementation.

Further, we experimentally demonstrated the three-dimensional PA imaging system based on robotically induced rotational motion using a linear array on a TRUS probe. The proposed system improved the PA image quality in terms of elevational resolution and SNR. The PA volume acquisition could ease brachytherapy seeds visualization and make the operation more user independent.

Chapter 10

Ultrasound Calibration Using A Phantom with Multiple Active Points

I was responsible for the project design, theory solidification, simulation, data collection, analysis and writing. Alexis Cheng contributed in theoretical development. Younsu Kim helped experimental data colloection. Dr. Gregory S. Chirikjian and Dr. Emad M. Boctor supervised the project.

10.1 Introduction

Ultrasound (US) imaging has been widely used as a medical diagnostic tool and for image guidance during surgical interventions. The tracking information of ultrasound images substantially expands the applications, and it is an active area of research to use the tracking information for assisting image-guided interventions [78, 79], constructing 3-D volumes [61], or even improving ultrasound image quality [43, 50]. Various tracking systems could be used as the tracker to track US images, and for any tracking system, in principle, an additional task is required to compute the transformation bridging the tracker frame to the ultrasound image frame. Ultrasound calibration is a pre-operative process to compute this unknown transformation between these two different coordinate systems [80]. Once calibration is complete, the set of ultrasound images and tracking information can be associated together through the recovered transformation. Therefore, the performance of the application depends on the accuracy of ultrasound calibration.

In general, calibration phantoms are used to carry out ultrasound calibration [80]. Many of ultrasound calibration phantoms have been proposed, and these phantoms can be categorized into two: point-based phantoms and structural phantoms. Point-based phantoms are made by stylus [81] or a cross-wire [54, 82] representing a single or multiple points in three-dimensional (3D) space. For one-dimensional (1D) array US probe case, an ultrasound image slice can determine its 3D position by assuming the point is in the ultrasound image plane, and the elevational axis component is

Table 10.1: General characteristics of ultrasound calibration phantoms.

Phantom	Point-based	Structure (Line/Wall) based
Segmentation automation	Hard	Easy
Data collection time	Time-consuming	Fast
Elevation accuracy	High	Low
Available information	Position	Rotation and position

zero. Structures such as line- or wall- based phantoms, on the other hand, have its pre-determined structure, and the segmented feature(s) from an ultrasound image is registered back to the model structure to recover the ultrasound image pose with respect to the phantom [83]. Point-based phantoms are generally more accurate compared to structural phantoms because it does not require a registration process, but takes a longer time to collect data because of its requirement to align the ultrasound plane with the point. Moreover, calibration using point-based phantoms is hard to be automated due to the mid-plane alignment process with respect to the point, while structural phantoms are flexible and easy to implement automation by segmenting lines or features.

Another point of view of ultrasound calibration is its mathematical perspective. The equation available to compute depends on the accessible information; for example, point-based phantoms only provide positional information of the phantom, while structural phantoms provide both orientation and position. Having the full pose

information from structural phantoms has a benefit to be able to formulate a closed-form solution, and a fast computation is available by avoiding solving an optimization problem.

The goal of the work is to present a phantom design and the associated algorithm enabling a fast and accurate US calibration. A point-based phantom is considered as the base design because of the superior elevational position detection capability compared to the structural phantoms. Still, the limitation of the point-based phantoms to have supreme calibration accuracy is its localization accuracy in the elevation dimension determined by US beam thickness. To address this challenge, Guo et al. has proposed using an active echo (AE) phantom approach to precisely find the mid-plane of the ultrasound beam [52,84]. AE phantom is made by a single PZT point, which receive a US beam from the probe, then instantly transmit back an echo. The strength of the echo depends on the distance and angle of the US beam, so that the maximum echo received by the probe indicates that the probe is perfectly aligned with the PZT element in the hundreds micron accuracy. However, repeating mid-plane search for each pose is time-consuming and requires a cumbersome system, that AE requires a specialized signal processing system on board which is not easily accessible. Here, we propose a new phantom design using multiple active point (MAP) sources that can drastically simplify the process of mid-plane detection to speed up the calibration, and has improved calibration accuracy as well. Compared to AE, active phantom only requires a synchronized transmission board, and multiple points enable a closed-form

solution which is not possible in AE, which is the single point.

This chapter is structured as follow. We first introduce the theory behind ultrasound calibration and the algorithm for the proposed phantom. Then, we present the simulation and experiment setup to analyze the performance of the method. After that, the results of numerical simulation and experiment are shown. Finally, we discuss the limitation and potential applications of the method.

10.2 Contributions

The main contributions of this chapter are the following:

- Minimization of mid-plane search process for point based ultrasound calibration
- Development of mathematical framework of solving $AX = XB$ formulation using point-based phantom
- Theoretical derivation of multiple active points phantom based ultrasound calibration using invarients
- Evaluation of the concept through simulation and phamtom experiment

10.3 Theory

10.3.1 Solving Ultrasound Calibration Problem

The ultrasound calibration is the process solving for the rigid-body transformation from the ultrasound image frame to the tracking sensor frame, X. Various calibration phantom designs have been proposed, and there are corresponding formulations, for which $BX^{-1}p$ and $AX = XB$ are the two most common formulations, where $A, X, B \in SE(3)$, $p \in R^3$ and $SE(3)$ denotes the 3D homogeneous transformation.

The $BX^{-1}p$ formulation is used for point-based phantoms (Fig. 10.1(a) illustrates an example of the point-based phantom coordinates). A single or multiple point-like fiducials are scanned with a tracked ultrasound probe with a marker attached from multiple poses with different orientations and positions. B is the homogenous transformation from the tracking base to the sensor marker, and can be obtained from the sensor reading. p is the physical point location within the ultrasound image frame, segmented from the ultrasound image. Though 3D position is known in 2D array probe, 1D array assumes the elevation axis to be zero, when the point is perfectly aligned to be the mid-plane. For all combinations of B_i and B_j,

$$B_i X^{-1} p_i = B_j X^{-1} p_j, \tag{10.1}$$

has to be satisfied, relying on the assumption that the point phantom from the tracking base frame is constant and fixed. At least three independent poses are required

to find the unique solution of X.

$AX = XB$ is another formulation solving this sensor calibration problem (Fig. 10.1(b) illustrates an example of $AX = XB$ framework). For all combinations of pose i and j,

$$A^{ij}X = XB^{ij}, \tag{10.2}$$

stands, where A^{ij} represents the relative rigid body transformation between the poses A_i and A_j, as $A^{ij} = {A^{-1}}_i A_j$. Similarly, B^{ij} is the transformation between B_i and B_j, as $B^{ij} = B_i^{-1} B_j$. Subscript As such as A_i and A_j are the transformations from the ultrasound image frame to the phantom base frame for pose i and j, and subscript Bs are the tracking transformation as used in the $BX^{-1}p$ formulation. $AX = XB$ formulation have a closed form solution, which means that it does not require to solve an optimization problem [85, 86], and this can reduce the computation time. Additionally, a method using pose covariance can be used to solve for the $AX = XB$ formulation without knowing the temporal correspondence between subscripts As and Bs [87].

Practically, BXp formulation could compute a better X. Acquiring the full transformation A requires a dedicated structure phantom such as a line or a wall. However, instead of avoiding the time-consuming mid-plane search process compared to point-based phantoms, it is typically challenging to provide accurate segmentation with these structural phantoms due to beam thickness and US insonification angle.

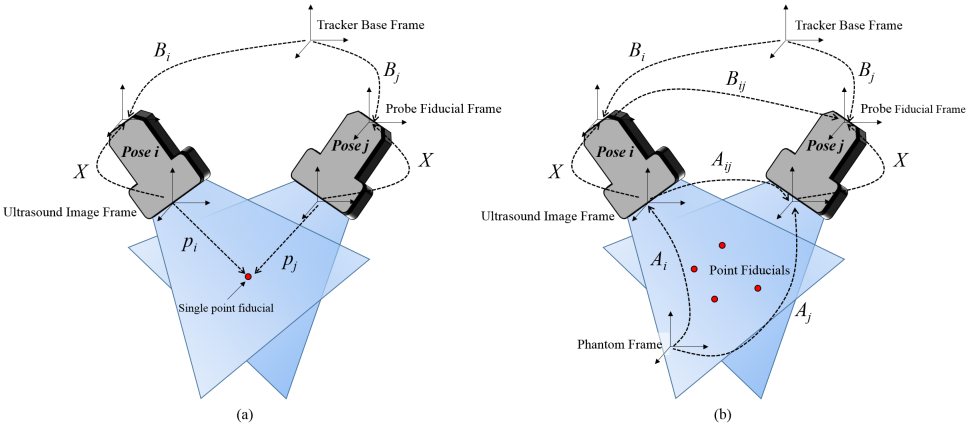

Figure 10.1: Illustration of multiple active-point phantom concept. (a) The conventional single point target phantom, and BXp framework. (b) The proposed multiple active-point phantom, and associated $AX = XB$ framework.

10.3.2 Ultrasound Calibration Using Multi Active-Point Phantom

Active point target is defined as the point fiducial that itself has the capability of transmitting acoustic wave. It is contrasting with general calibration phantoms, in which phantoms are passive all the time, and the signal appearance relies on the ultrasound excitation from the ultrasound probe. Guo at al. [52] integrated a piezoelectric element into a needle tip to fabricate an active target. With the synchronized transmission with respect to the line trigger, the signals can reach the ultrasound probe even if the point position is not in-plane. The geometrical distance from the probe to the active point can be estimated based on the time-of-flight (TOF) of the transmitted wave. Therefore, the active point phantom can eliminate the mid-plane search process, and enable to distribute multiple active points in the 3D space.

Traditionally, only BXp formulation was available using the point-based phantom because the rotational relationship between the ultrasound image and a point is not accessible. Our multiple active-point phantom enables $AX = XB$ formulation by recovering both rotation and translation from the geometrical relations of multiple points on the phantom.

The concept of the multiple active-point phantom is illustrated in Fig. 10.1(b). If the three-dimensional (3D) position of the point target is accessible with a 3D ultrasound system such as two-dimensional (2D) array, the 3D location of each point target on the phantom can be segmented, and the point cloud registration can be used to recover the transformation A [88], relating two point clouds between the phantom model frame and the ultrasound image frame through the formulation as

$$A = \arg\min \sum_i ||Ap_{US} - p_{MAP}||^2, \tag{10.3}$$

where p_{US} is the point position from the ultrasound image frame, and p_{MAP} is the position from the phantom model frame. Although conventional point targets are available with the 3D ultrasound system, active-point phantom provides background free signals, and does not suffer from the imaging artifacts such as reverberation or the surrounding environment.

Considering the one-dimensional linear array probe case, three-dimensionally located active point target signals appear as 2D information in the raw channel data. When x, y, and z axis are defined as lateral, axial, and elevation dimension from the ultrasound image coordinate, the x axis of the point is the lateral position, and the

norm of y and z axes is its time-of-flight as

$$p_{US} = \begin{bmatrix} x \\ y \\ z \end{bmatrix} = \begin{bmatrix} x \\ \sqrt{D^2 - e^2} \\ e \end{bmatrix}, \tag{10.4}$$

where e is the unknown elevational component. D is the distance from the target to the receiver based on the earliest time of arrival signal in the received channel data. When this p_{US} is used to solve for A together with the unknown e for each pose, the Equation 10.3 would output A^* with 1DOF unknown rotation as,

$$A = A^* \cdot \Delta A, \tag{10.5}$$

$$\Delta A = \begin{bmatrix} \Delta R & 0 \\ 0 & 1 \end{bmatrix}, \text{axis} - \text{angle}(\Delta R) = \begin{bmatrix} r \\ 0 \\ 0 \end{bmatrix}, \tag{10.6}$$

where A is the true A, and the recovered A^* containing unknown 1 DOF rotation r in the x-axis of the ultrasound image coordinate. The Equation 10.3 including unknown e has solutions for different r, thus it is not possible to solve for A without knowing e. The $AX = XB$ formulation with one unknown DOF in rotation is formulated as,

$$(A_i^{-1} A_j) X = X B^{ij}, \tag{10.7}$$

and Equation 10.5 gives

$$(\Delta A_i^{-1} A_i^{*-1} A_j^* \Delta A_j) X = X B^{ij}, \tag{10.8}$$

Equation 10.8 has eight unknown parameters: six unknown in X, and two from ΔA_j and ΔA_j. Thereby, the solution of Equation 10.8 using multiple poses is X^* as

$$X = \Delta X X^*, \tag{10.9}$$

where X is one DOF rotation (Proof is shown in Appendix C.1).

Although X cannot be solved with A with one DOF rotation, if at least one pose of A is fully known, every other unknown A can be recovered using the Euclidean-Group invariants. From screw theory, the homogenous transformation can be written as

$$H = \begin{bmatrix} e^{\theta N} & (I_3 - e^{\theta N})p + dn \\ 0^T & 1 \end{bmatrix}, \tag{10.10}$$

where $e^{\theta N}$ is the matrix exponential on θN, I_n is the n by n identity matrix, and θ is the angle of rotation. In addition,

$$N = \begin{bmatrix} 0 & -n_3 & n_2 \\ n_3 & 0 & -n_1 \\ -n_2 & n_1 & 0 \end{bmatrix}, \tag{10.11}$$

where $n = [n_1, n_2, n_3]^T \in R^3$ denotes the unit vector representing the axis of rotation, and $p \cdot n = 0$. θ, d, n, p are known as the Plcker coordinates of the screw motion. Here, we introduce the invariants θ and d, defined as

$$\theta = \arccos\left(\frac{tr(R) - 1}{2}\right), \tag{10.12}$$

$$d = t \cdot n, \tag{10.13}$$

where R and t are rotation and translation vector of the matrix. It is known in the $AX = XB$ formulation, two invariant relations

$$\theta_A = \theta_B, \text{and } d_A = d_B \tag{10.14}$$

should be satisfied.

In the MAP phantom, the full A can be recovered by making ultrasound beam in-plane to one of the point targets. Using invariants θ and d, and one complete A, all ΔA can be recovered by minimizing the following function:

$$\min_{\Delta A} \sum_{i=1} M(||f_\theta(\Delta A_i^{-1} A^{*i,j+1} \Delta A_{i+1}) - f_\theta(B^{i,j+1})|| + ||f_d(\Delta A_i^{-1} A^{*i,j+1} \Delta A_{i+1}) - f_d(B^{i,j+1})||) \quad \text{s.t.} \Delta A_k = C_k, \tag{10.15}$$

where C_k is the known rotation components by aligning a point to the ultrasound plane for pose k. Two functions $f_\theta(H)$ and $f_d(H)$ are defined as the function to output θ and d by inputting the transformation H. Once all A's are known, X can be recovered by solving $AX = XB$ problem.

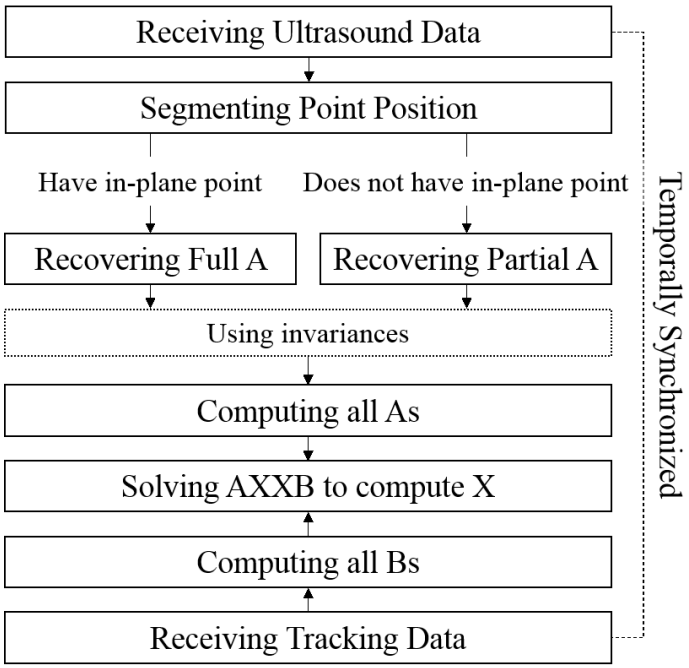

Figure 10.2: Diagram showing ultrasound calibration procedures using multiple active-point phantom.

10.4 Methods

10.4.1 Calibration Workflow

The ultrasound calibration steps using the MAP phantom are summarized in Fig. 10.2. For the data collection, the active points are placed as illustrated in Fig. 10.1(b), and the transmitted signals were received by the ultrasound transducer. The phantom should consist of more than three points, and the relative location of these points should be known prior to usage. The received raw ultrasound data was saved using the channel data acquisition system. The tracking device is attached to the probe, and the tracking sensor information was recorded corresponding to the

ultrasound data acquisition timing. Those two sets of data were used to generate A and B, respectively, and finally used to reconstruct X.

The data processing was initiated by acquiring the active point location in the ultrasound data. Although the elevational component is not accessible, the lateral and axial components of the active point can be segmented from the earliest time of arrival point. The lateral position is known by taking into account the probe pitch, and the axial position is calculated from time to distance based on

$$D = \tau \cdot SoS, \tag{10.16}$$

where τ denotes the temporal length from the probe to the active point, and SoS is the speed of sound. The obtained two DOF point information and the phantom point distribution were used to recover partial A (Eq. 10.5) using Equation 10.3. If one of the points is located in-plane for the ultrasound plane, the elevational component can be assumed to be zero. Thus, a full A can be recovered with this in-plane data set by setting as a constraint during the optimization in Equation 10.3. By relying on the earliest time-of-flight, only single point would be segmented as the axial component, but there is an alternative approach using the entire waveform to recover A as described in Appendix C.2.

From given the partial As including at least one full A and Bs (obtained by the tracker), the full As are recovered using the invariants. Equation 10.15 derives the one DOF unknown component in the partial A, and the full A can be found as $A_i \Delta A_i$. Once corresponding As and Bs are recovered, the unknown transformation X can be

solved with various solvers including optimization free closed-form solution [9-11].

10.4.2 Simulation

Geometrical simulation was conducted to test the calibration performance under the presence of different sources of error. For the BXp simulation, a single point target was set as the phantom, and a 128 elements linear array transducer was used as receiver. To simulate the in-plane scanning where the ultrasound beam is across the point target, the elevational component of the point position was set to zero. For the $AX = XB$ simulation, multiple points were set instead of the single point, while other setups were kept to be the same. 80 poses were simulated and half of them were used for calibration, and the rest were used for evaluation.

10.4.3 Experimental Implementation

An active element is used to transmit ultrasound signals and these signals were received by DAQ device to collect channel data. Transrectal probe is used as an ultrasound probe, and the linear array part is used for calibration. The curvilinear part of the probe is used to obtain another set of locational information which could be used to localize 3D location of the active element position. In this experimental evaluation, we used UR5 (Universal Robot) as the mechanical tracker. Instead of placing multiple active elements, we moved the robotic arm in the translational motion

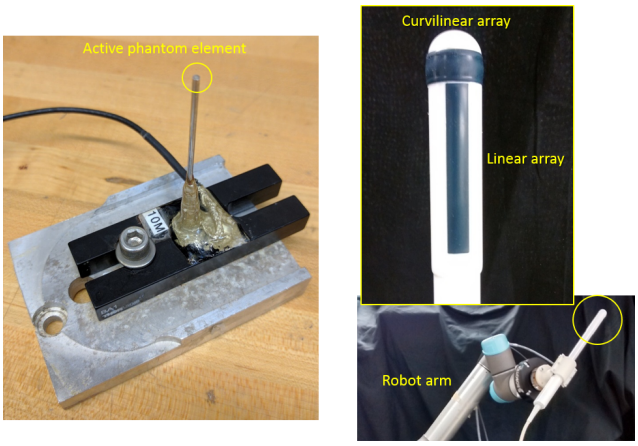

Figure 10.3: Experimental setup. (a) Active point phantom, (b) Transrectal probe mounted on the robotic arm.

from the robotic base frame to emulate multiple point sources (Fig. 10.4(a)). The robot arm is moved 125 positions corresponding to 125 unique poses for calibration. For each of the poses, the robot arm is applied five translational motions from the robot base coordinate to imitate a multiple active elements phantom is used. Five position data is treated as the data received from a fixed pose while the active elements position is changed.

10.4.4 Evaluation Methods

The evaluation of the calibration is done based on accuracy and precision. The accuracy is the most direct metric showing the error distance comparing the recovered point location and the true location for the same target, as

$$\sigma_{Accu} = \left\| \frac{1}{N} \sum_{i=1}^{N} (B_i X p_i - c) \right\|_2, \tag{10.17}$$

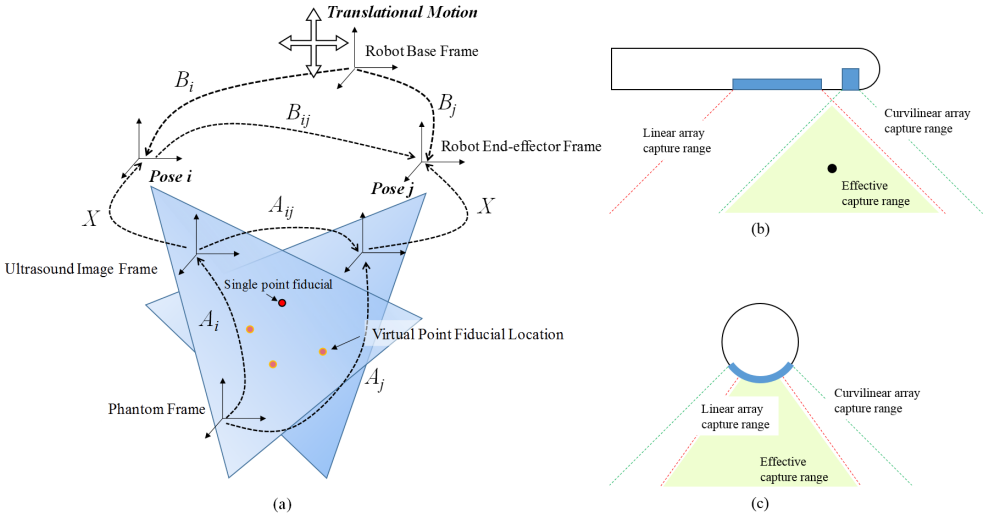

Figure 10.4: The experimental design and the scanning field in the transrectal probe.

where c is the ground true target point from the tracking base frame. The precision is the metric defined by

$$\sigma_{RP} = \left\| \sqrt{\frac{1}{N}\sum_{i=1}^{N}(B_i X p_i - \overline{BXp})^2} \right\|_2, \tag{10.18}$$

where $\overline{BXp}$ is the mean of $B_i X p_i$ for all i. Ideally, if no error exists, the true X would make all $B_i X p_i$ converge into a single point. When error exist, $B_i X p_i$ for all i will form a point cloud instead of a single point, and the size of the point cloud is expressed as the validity of X.

Although the accuracy is more reliable metric to evaluate X, the experimental analysis was based on precision because the ground truth point location c is not accessible. Instead, the simulation evaluated both metrics of accuracy and precision to compare their relevancy.

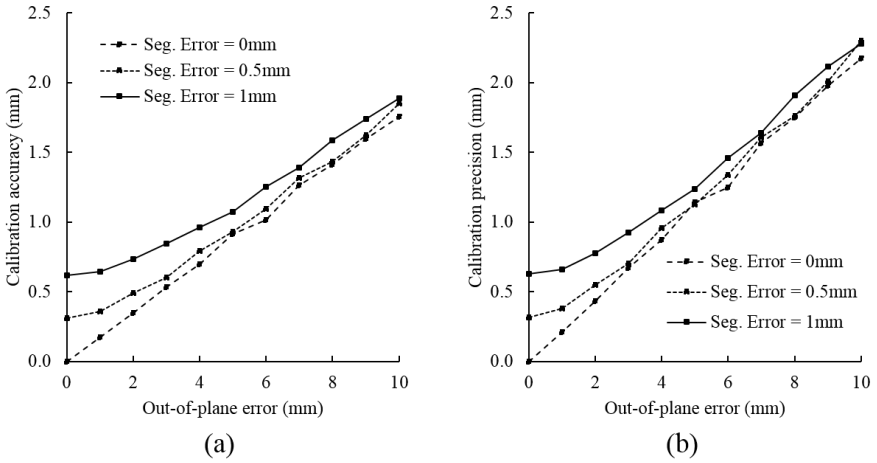

Figure 10.5: Calibration error of BXp in (a) accuracy and (b) precision for corresponding segmentation and elevational error.

10.5 Results

10.5.1 Geometrical Simulation

The first simulation is to evaluate the error tolerance of conventional BXp formulation. Assuming a point target is scanned by the 1D array ultrasound probe, the out-of-plane error and the segmentation error was injected. The result is shown in Fig. 10.5.

The out-of-plane error increases the calibration error linearly and the 10 mm error will result in around 2 to 2.5 mm range. Segmentation error provides a significant effect of calibration error compared to the out-of-plane error especially when the out-of-plane error is small. When out-of-plane error is huge, the effect will be relatively weaker because the error will be embedded into the out-of-plane error. The calibration

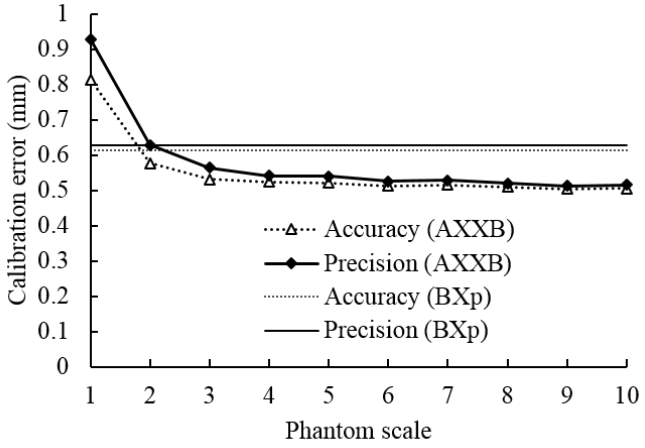

Figure 10.6: Calibration error of $AXXB$ for different size of point phantom.

accuracy and precision metrics shows a close value, and it indicates the validity of precision as the metric to evaluate the experimental results. However, it should be noted that the experimental precision also includes the error in tracking B, while it is not taken into account in this simulation.

Next, the BXp formulation is compared with the $AX = XB$ formulation (Fig. 10.6). In this simulation, it is assumed that the 3D position of the multiple point targets is known and A is recovered from that. The segmentation error was set to 1 mm and the error will add the uncertainly on the point location detection, and size of the $AX = XB$ multiple points phantom was changed from 1 to 10. The out-of-plane error for BXp is not considered. The same evaluation was repeated 200 times and the average case is shown in the Fig. 10.6. For both BXp and $AX = XB$, the segmentation error of 1 mm was added. The result shows that although the

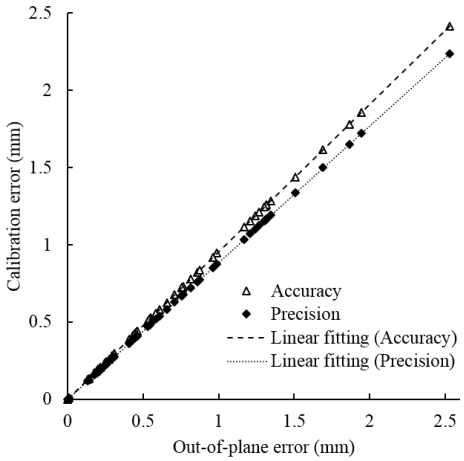

Figure 10.7: The effect of out-of-plane error on the calibration error.

calibration performance of BXp is fixed, $AX = XB$ formulation has a potential to outweigh that of BXp when certain phantom design is taken. In this case, the size of the phantom was shown as the factor to improve the calibration.

Figure 10.7 shows the result when different out-of-plane error is applied. Only single pose information is used, and the rest is only using the absolute distance from the probe depth parameter. The calibration error is proportional to the out-of-plane error. It is seen the proposed method is very sensitive to the out-of-plane error. The single pose effect will be accumulated to the entire accuracy while if out-of-plane error exists for all poses, the result becomes small because the error will be randomly distributed. In this plot, the phantom size scale was varied from 1 to 10, but it did not change the calibration error.

Tables 10.2 and 10.3 are results of calibration accuracy and precision when segmen-

Table 10.2: 1D probe calibration accuracy using multi active point phantom.

Unit: mm				Out-of-plane error		
				0 mm	0.5 mm	1 mm
Phantom size scale	1-5	Segmentation error (SD)	0.5 mm	0.36±0.06	0.58±0.21	1.00±0.29
			1 mm	1.16±0.92	1.04±0.33	1.23±0.72
	6-10	Segmentation error (SD)	0.5 mm	0.34±0.03	0.51±0.08	0.95±0.18
			1 mm	0.64±0.06	0.79±0.07	1.11±0.08

Table 10.3: 1D probe calibration precision using multi active point phantom.

Unit: mm				Elevation error		
				0 mm	0.5 mm	1 mm
Phantom size scale	1-5	Segmentation error (SD)	0.5 mm	0.33±0.04	0.53±0.18	0.93±0.26
			1 mm	1.06±0.82	0.98±0.32	1.13±0.66
	6-10	Segmentation error (SD)	0.5 mm	0.31±0.02	0.46±0.07	0.89±0.05
			1 mm	0.60±0.06	0.72±0.07	1.00±0.08

tation error as well as calibration error exists. Sub-millimeter accuracy was achieved when the segmentation error smaller than 1 mm and the phantom size is certainly large. In this case, out-of-plane error should be restricted by 0.5mm. The reason why the segmentation error effect was stronger compared to 3D $AX = XB$, is that the single pose used to determine all the rest As and the error will be accumulated during other poses recoveries.

10.5.2 Experimental Results

The experimental results based on 3D segmentation using both linear and curvilinear array are summarized in the table 10.3. For total five point targets, when each of four points were used in calibration BXp, the internal precision shows the reconstruction precision on the same point, but the poses not used for the calibration. For the same number of poses, the external c shows the reconstruction precision when the fifth point was used for the evaluation. In $AX = XB$, four points were used to calibrate, and the same set of point targets as BXp was used to compute the reconstruction precision. This indicates that BXp is going to recover particular point, but it does not provide a better estimate for the point not chosen.

For 1D array calibration, the intermediate step of A recover is shown in Fig. 10.8. This is comparing the A between the recovered As using the 1D array and the As from two array ground truth data. The relative matrix is taken and the rotation component is opened to the Euler angle representation. Before the 1DOF recovery using the invariants, the 1DOF unknown error is distributed in the rotation around the x axis, but after the invariants compensation, the error was drastically reduced.

Using the recovered A, the final performance of $AX = XB$ formulation was 1 mm with the internal c and 0.93 mm for the external c. This result was worse compared to the two probes calibration, because the one mid-plane information could affect all other poses, and also there is no minimization effect by taking multiple data as included in the two-array calibration. Interestingly, the calibration using

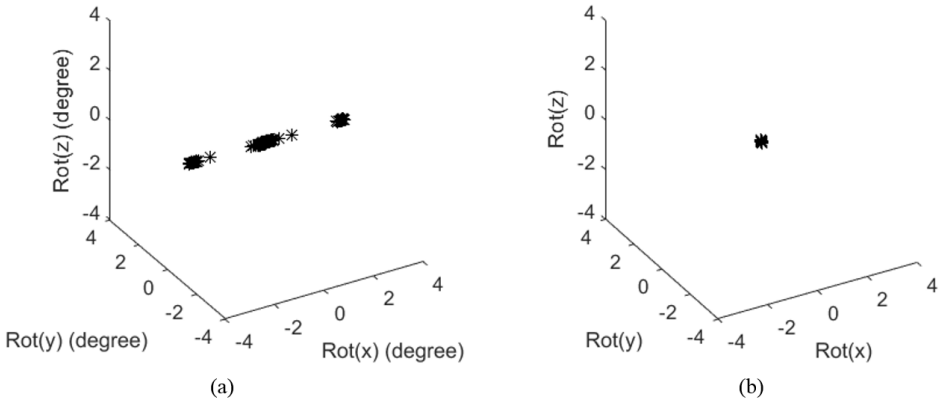

Figure 10.8: Before (a) and after (b) recovering the unknown rotation.

the translational component of the recovered A provided the better X. This could be because the BXt is using the global optimization, which is searching the X to minimize the translational single point recover, and this is closer to the process of calculating the reconstruction precision.

10.6 Discussion and Conclusions

We have proposed a new ultrasound calibration concept utilizing MAP phantom, and demonstrated its feasibility thought theory, simulation, and experiment.

In simulation, both accuracy and precision were used as the metric to show the calibration performance. And, it is shown that both metrics show a similar value. It indicates that the precision could be a good indicator of calibration without knowing the true accuracy. is similar from simulation.

For $AX = XB$ formulation, the phantom size is very crucial for its effect. Bigger phantom could provide a reliable A, which eventually could be used to solve for a better X. Conventional phantom design is limited because in-plane has to be considered. Especially point base phantom is strongly restricted to scan the point. The proposed one has wider freedom in the phantom design. If phantom will be fabricated, then the bigger size can be chosen. If the phantom is based from the multiple virtual points through applying static motion as shown in this paper, the phantom design such as the number of points or the size of the phantom could be more flexible.

The calibration phantom selection could be done based on needs, available equipment, and particular applications. If millimeters calibration accuracy is acceptable, the mid-plane error could be trivial. Then, the rapid phantom design such as structural phantom does not require the mid-plane search can be chosen. If the goal is to achieve sub-millimeter accuracy, then the calibration methods including the mid-plane error mitigation should be used. The point based calibration such as active echo system would be ideal in this case. The multiple calibration possesses both advantage in one system. This phantom design not only can minimize the mid-plane detection, but also can neglect the mid-plane problem.

The limitation on the phantom design is the complexity of the equipment preparation. This phantom design requires at least an active element transmission system if the translational motion can be applied to the phantom through a mechanical arm

as UR5. Or, simply building multiple active elements phantom could be a direct solution. Transrectal probe has two arrays placed in the 2D space, so could be used as the phantom itself.

Chapter 11

Single Element Synthetic Tracked Aperture Ultrasound Imaging

This chapter has been published as: *H. K. Zhang, M. Lin, Y. Kim, N. Patel, A. Moghekar, N. Durr, E. M. Boctor, Toward Dynamic Lumbar Punctures Guidance Based on Single Element Synthetic Tracked Aperture Ultrasound Imaging, in SPIE Medical Imaging, 2017.*

I was responsible for the project design, system integration, data collection, analysis and writing. Younsu Kim, Melissa Lin, Mateo Paredes, and Karun Kannan assisted on designing and building the prototype, and performing the experiments. Dr. Abhey Moghekar, Dr. Nicholas Durr, and Dr. Emad M. Boctor supervised the project.

11.1 Introduction

Lumbar punctures (LPs) are performed to collect cerebrospinal fluid (CSF), an important bodily fluid needed to diagnose a variety of central nervous system disorders or conditions, including life threatening ones like encephalitis or meningitis, where a diagnosis delay of even a few hours can be catastrophic [89]. The current standard of care utilizes anatomical landmarks to locate the L3-L5 intervertebral space; a needle must be advanced through several tissue layers, between the vertebrae and into the subarachnoid space without hitting other obstacles (e.g. blood vessels or bone) along the way. Most LPs are performed blindly without the assistance of imaging or guidance mechanisms. More than 400,000 LPs are performed annually, but nearly 23.3 % end in failure due to the myriad of challenges [90,91]. These failures lead to misdiagnoses, treatment delays, and subsequent unnecessary and dangerous procedures [92–94]. Obese patients with excess adipose tissue between skin and target structures suffer a significantly increased probability of LP failure [92], and the rate of overall complications as a result of LPs almost doubles in obese patients to nearly 50 % [95–97].

The conventional image guidance used when a physician is unable to collect CSF with a blind entry is fluoroscopy. While fluoroscopy is accurate, it cannot be used on all patients, such as pregnant women, and it is expensive due to the required equipment. It also delays diagnosis because it is usually scheduled for the following day, and it exposes the patients and physicians to high levels of radiation for the entire

duration of the procedure. There are several emerging imaging approaches to further improve LPs. A majority of these solutions tackle this issue by improving upon existing imaging technology through introducing tracking methods [98–103]. For example, one solution introduced EM tracking to both the needle and the ultrasound transducer, which resulted in a significantly improved success rate in facet joint injections [98]. However, this technology introduces additional systems to the clinic, which can discourage adoption. Another proposed solution is a guidance system that incorporates ultrasound tracking of the needle coupled with patient specific geometries and augmented reality to enable the accurate placement of anesthetic nerve blocks [99]. This approach again forces the physician to familiarize his/herself with both the tracking system and augmented reality. Some of the solutions described above have been brought to market. The eZono [104], eZGuide magnetizes the needle to take advantage of the Hall effect to track the needle in the body. This solution, however, does not provide adequate resolution and sensitive tracking at greater depths. Moreover, physicians have to acquire this system and adapt it in their clinical workflow. Another example is the ClearGuide One, which utilizes a combination of CT and US to calculate optimal needle trajectory [105]. A common trait among these existing solutions is the introduction of additional equipment into the procedure creating substantial disruption to existing workflow, which in turn leads to lower adoption rate.

Alternatively, integrating an ultrasound element directly with the epidural needle is an approach combining the guiding and procedural tools into one, and several

studies have investigated an ultrasound needle for A-line sensing [106, 107]. The advantage of this approach is the sensor forward direction has already been aligned to the actual needle insertion direction. Although, no additional interpolation or registration process is needed, the limitation is that utilizing A-mode line alone to guide a goal located several centimeters away is not realistic.

The proposed system extends this ultrasound needle approach by introducing an imaging component to allow for visualization of tissues in LP procedures to eliminate failed or traumatic attempts and iatrogenic complications in obese patients. We propose a simple and direct needle insertion platform that dynamically tracks needle position, enabling image formation from sweeping a single ultrasound element at the needle tip. The needle-shape ultrasound transducer can not only sense the distance between the tip and a potential obstacle such as bone, but also visually locate the structures by combining transducer location tracking and back projection based synthetic aperture (SA) beamforming algorithm. For dynamic image guidance, the angle of the needle relative to the holster is measured, and back projection based synthetic tracked aperture imaging algorithm is applied on the received US data to produce high resolution images. In a typical use-case, the physician would insert the needle into the patient subcutaneous fat layer and sweep the needle in an arc within the adipose tissue to acquire an image of the tissue in front of the needle. This image can then be used to guide and alter the trajectory of the needle to avoid peripheral bone structures and access the correct target. Importantly, we propose that the ultrasound

scanning is performed to guide the introducer to the correct location and that the actual LP be performed by removing the ultrasound needle and inserting Quincke needle through the same introducer.

This chapter serves the proof-of-concept of this technology through simulation and phantom experiments. In simulation, the point targets were imaged for the resolution evaluation, and the tolerances toward various errors have been evaluated. For the experiment, metal wires phantom mimicking bone structures and human spine bone phantom were imaged with the controlled motion and freehand scanning. Finally, we discuss the uniqueness, benefits, and limitations of our approach compared to other image-guided procedures.

11.2 Contributions

The main contributions of this chapter are the followings:

- Development and validation of single element based synthetic tracked aperture imaging
- Development of registration-free lumbar puncture guidance using single element ultrasound imaging

11.3 Approach

11.3.1 Single Element Ultrasound Sensing and Imaging

The conceptual design of the proposed single element ultrasound imaging system is shown in Fig. 11.1(a). The technology consists of two subsystems: the needle-shape ultrasound probe, and the ultrasound element tracking system, which consists of the holster and encoders. An insert that can fit inside a Quincke needle, the spinal insertion needle, is included in the system. The insert contains a PZT element embedded at the tip, with a magnet wire backing material. The needle is fabricated using a stainless steel tube with a magnet wire threaded through, with one end of the magnet wire connected to the PZT element and the other end soldered to a coaxial cable with a BNC connector. An angular encoder was used to track the 1-DOF rotational motion. The needle itself provides an A-lines in real-time to the user, so that the strong contrast from the bone could be used as a warning to prevent the needle from collision. An ultrasound image of a slice of the scanning trajectory can be formed during the procedure, which can aid in determining the direction the needle should proceed.

The workflow for conventional blind insertion can be summarized as finding insertion, actual insertion, forward motion of the needle penetrating the subarachnoid

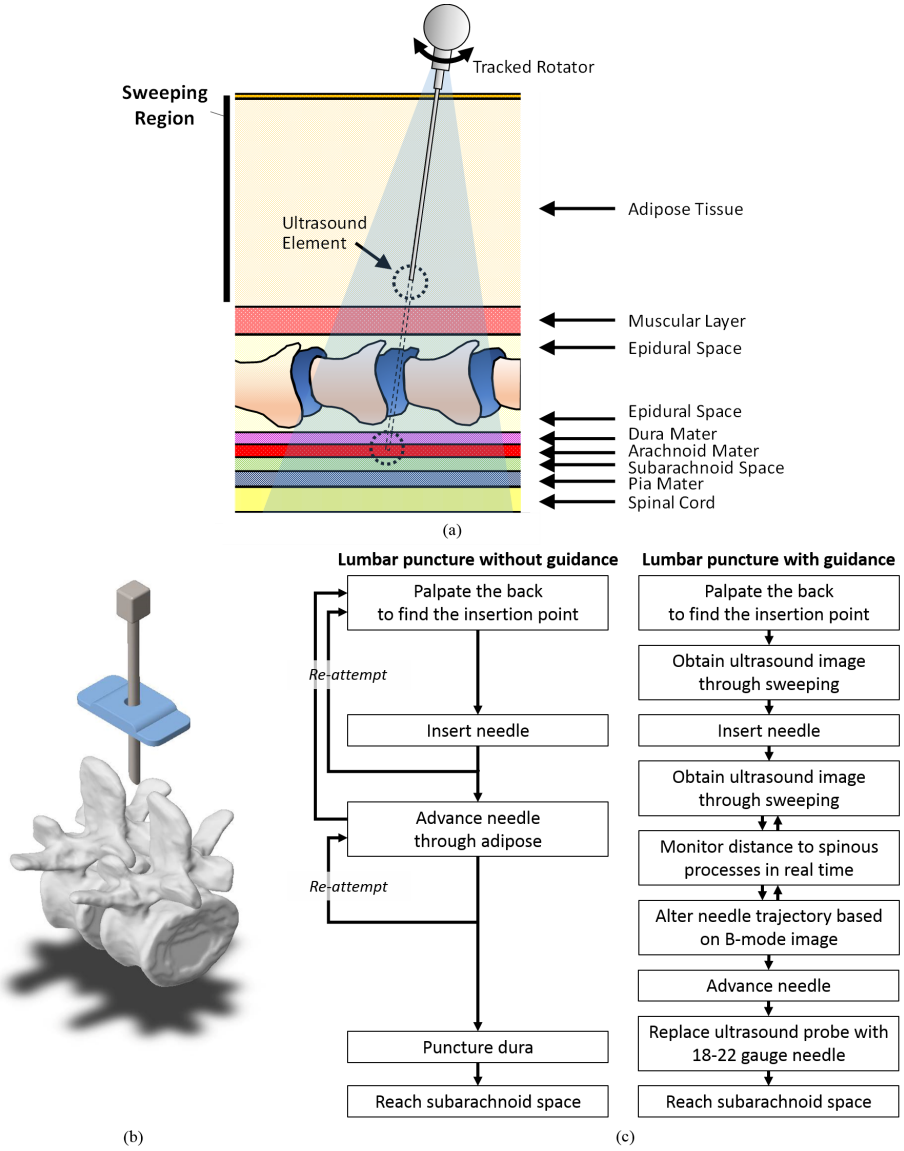

Figure 11.1: The concept of single element ultrasound sensing and imaging system for dynamic lumbar puncture guidance. (a) The layers of tissue from skin to spinal cord. Conventional LPs require advancing a needle through a small target window that is difficult to identify in obese patients. (b) the illustration of the needle-based single element ultrasound imager. The blue piece of the attachment will guide the location of the ultrasound element. (c) The workflow diagram of the blind needle insertion, compared with the proposed procedure with dynamic ultrasound guidance. The proposed workflow reduces re-attempts that could be necessary in conventional workflow without guidance. Note that the needle sweep occurs only up to subsurface adipose tissue.

space, and CSF collection. In our proposed workflow, our image/sensing guidance can take place at the step prior to the needle penetrating subsurface fat tissue. First, the physician palpates the patient's back, as in the current standard of care. Ultrasound images can be collected as need for finding the insertion position. Once the initial entry point has been determined, the tracking holster is placed on the back of the patient at the determined location. When the holster is secured, the physician threads the needle through the holster into the patient. To generate an image, the physician sweeps the needle in an arc, a motion similar to one that is already needed in navigating the needle for a no-guidance procedure. Tissue damage is not a concern because the adipose and connective tissues surrounding the spine are soft and simply move out of the way of the needle while sweeping. This sweeping motion allows our system to collect data from both the needle probe and the tracking holster, and the angle range of 10-30 degrees are expected depends on the target window size and the needle insertion depth while in adipose tissue. As the algorithm processes this data, the image is updated on the screen for the physician to use in real-time. The physician is then able to sweep again at a deeper layer to produce another image. It is important to note that these sweeping motions are routinely performed by physicians in LPs. During the needle insertion beyond adipose tissue, the distance from bone to the needle can be updated in real-time through sensing. The needle will not be swept close to the target or in the subarachnoid space after dural puncture. Before puncturing the dura, the ultrasound element insert can be pulled out and a small

biopsy needle (22G or higher gauge) threaded in to puncture the dura for CSF collection, creating a small hole in the dura and minimizing the possibility of iatrogenic complications arising. In this way, it is possible to safely perform a LP while avoiding structures along the way to the subarachnoid space.

11.3.2 Back Projection Based Synthetic Aperture Reconstruction

Synthetic aperture focusing is a technique of merging small sub-aperture information into a coherent wide aperture to reconstructing a resolution-enhanced B-mode image. This concept is applicable to a virtual ultrasound array, which is formed by combining multiple A-line data and ultrasound element tracking information [43, 44, 46, 50]. The needle can rotate with one tracked degree-of-freedom (DOF), producing a scan of a curvilinear region. In conventional delay-and-sum based synthetic aperture focusing, multiple re-acquired A-line data are used to beamform a line, and a B-mode image is formed by repeating this process. However, this method does not allow real-time updating of the image based on newly acquired A-line data from continuously changing ultrasound element positions as the needle pivots. Therefore, a back-projection approach is applied here by projecting each collected radio-frequency (RF) A-line data back to a pre-defined 2D field for real-time visualization. The rela-

tionship between pre and post reconstruction can be formulated as

$$y_{bf}(m,n) = \sum_{e} y_{bf_e}(m,n,e), \tag{11.1}$$

$$y_{bf_e}(m,n,e) = y_{pre}(d,e), \tag{11.2}$$

where y_{bf} is the final reconstructed RF data, y_{bf_e} is the reconstructed RF data from single position, and y_{pre} is the received raw RF data. m, n are the pixel information of the lateral and axial direction, respectively. The distance in the pre-beamformed data is d, and the element number is e. The received signal distance is related to the actual image geometry from

$$d^2 = m^2 + n^2. \tag{11.3}$$

For each element position, this back projection is repeated. Figure 11.2 presents the back projection process by adding the number of angles for reconstruction. From the very left, a single element back projection is shown. As the number of poses increases, the focusing effect becomes gradually stronger, which makes the point target size smaller. For all intermediate or final B-mode image display, envelope detection and scan conversion are applied on the beamformed data.

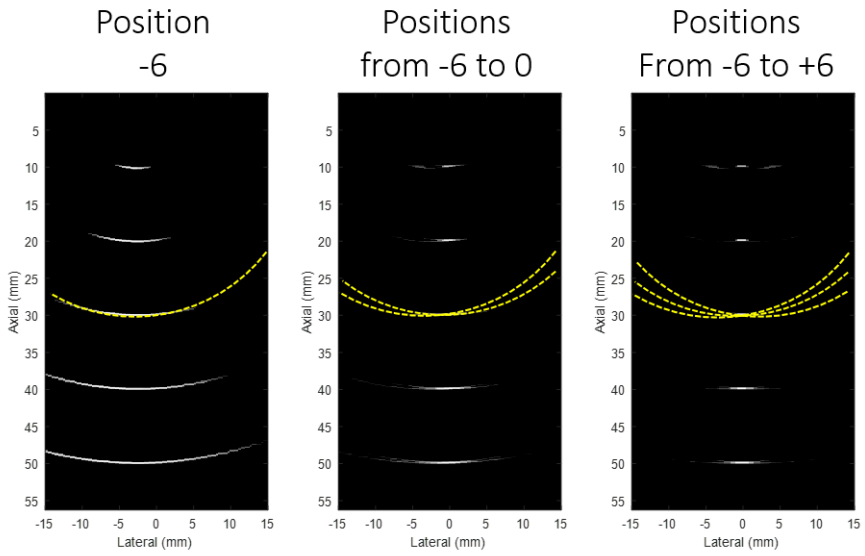

Figure 11.2: The back projection reconstruction process corresponding poses. Left: A position -6 degree from the center pose was back-projected. Middle: Position in the range from -6 degree to the 0 degree position were back-projected and summed. Right: Positions in the range from -6 degree to +6 degree position were back-projected and summed. The yellow line represents the back projection geometrical loci of the point at 30 mm depth point target.

11.4 Methods

11.4.1 Simulation

Simulations were performed to validate image reconstruction and analyze the effect of needle localization errors on image. Five target points were simulated from 10-mm to 50-mm with 10-mm intervals. Assuming a single element ultrasound transmit and receiver, the rotation radius from the rotation axis to the element was 40 mm. The center frequency of the point target was set to 4 MHz, and the data was sampled in 40 MHz. The image was reconstructed with the back projection based synthetic aperture algorithm. The simulated virtual scan collected 128 poses with 0.46 degree pitch. Two types of tracking errors, rotation tracking error, and rotation radius error, were considered for the error tolerance analysis. The full-width at half maximum (FWHM) was the metric to represent the point target size and the lateral resolution.

11.4.2 Experimental Implementation

11.4.2.1 Needle with PZT Element Fabrication

As described in section 11.3.1, the needle-shape ultrasound transducer is based on the PZT-5H element placed on the tip of the wire inserted in a 14G Quincke needle. The center frequency of the PZT element was 10 MHz. The element is placed at the tip of a wire which is threaded through a stainless steel tube; itis attached on end of

the tube, with an electrode conductively adhered to the wire and the other electrode to the steel tube. The thickness of the wire is analogous to the element diameter, so the wire has the effect of a backing layer. The other end of the wire and tube are connected to a coaxial cable with a BNC connector so that the needle can be connected to sampling devices.

11.4.2.2 Ultrasound Tracking

The proposed imaging approach is based on the accurate tracking of the element location informed by a 12-bit absolute magnetic angular encoder (AEAT-6012). The fabricated single element transducer is mounted on a holster with a rotation encoder to read the precise rotational position [108]. The encoder can provide absolute angle detection with a resolution of 0.0879; it has no upper speed limit, though there will be fewer samples per revolution as the speed increases. The encoder is connected to an encoder-to-tube adapter, which allows the pivot angle of the needle to directly correspond to the angle of read by the encoder. The current design incorporates an Arduino UNO which collects the encoder angle. The distance from the needle tip to the rotation pivot point was 36 mm. This translation from the pivot point directs the ultrasound element tracking together with rotation information.

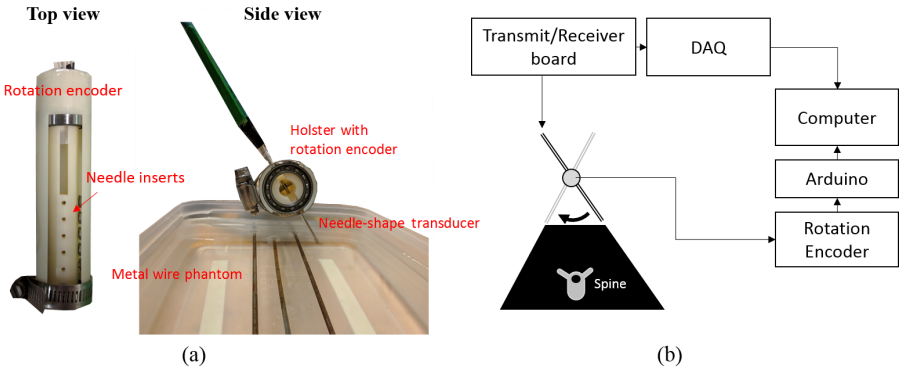

Figure 11.3: Experimental setup. (a) The pictures of the needle transducer mounted on the holster and the metal wire phantom design. (b) Diagram of hardware integration for the single element ultrasound system.

11.4.2.3 Data Collection

The transmission was triggered by a function generator, and received ultrasound and the trigger signals are captured by an oscilloscope or data acquisition system (US-Key, Lecoeur Electronique). In this validation experiment, we firstly scanned with a known trajectory. The top of the needle was attached to a Cartesian stage which was used to precisely rotate the needle and set its position, allowing it to hold steady at each incremental angle step. The RF data was collected nine times at each position, and we used the averaged RF line at each position for synthetic image formation. For the freehand scanning, the needle was moved freely along the rotation, and data for 500 positions for ultrasound and rotation tracking were collected. The encoder and ultrasound reception was synchronized through MATLAB software. The tracking data and the ultrasound data are transferred to a PC for data processing.

11.5 Results

11.5.1 Simulation Results

The result of the simulated point targets is shown in Fig. 11.4. For the ground truth data without any error, well reconstructed point targets could be confirmed. However, two types of error sources introduced image deformation. The first type of error was axial uncertainty simulating incorrect rotation radius; this error could be introduced by tissue motion artifacts or the motion of the holster itself. The second type of error was the rotation reading error. This false reading occurs when the rotation reading has an error or the recording was faster than the actual motion. As shown in Figs. 11.4(b-c), the image quality was drastically worse compared to the ground truth case with no error.

Next, the tolerance of the system to these errors was quantitatively evaluated by varying the magnitude of the error. Fig. 11.5 shows the amount of image deformation for certain error conditions through the metric of FWHM. The error magnitude in the figure represents the standard deviation of the randomized shift applied on the ground truth data. For the axial motion, FWHM was stable until 0.04 mm, but start degrading after introducing 0.05 mm error. For the error in rotational angle, FWHM was acceptable until 1 degree, but gradually degraded as the error magnitude increased. If the potential magnitude of error is predictable, it is necessary either to sweep the same region several times or to sample angles in smaller steps to average

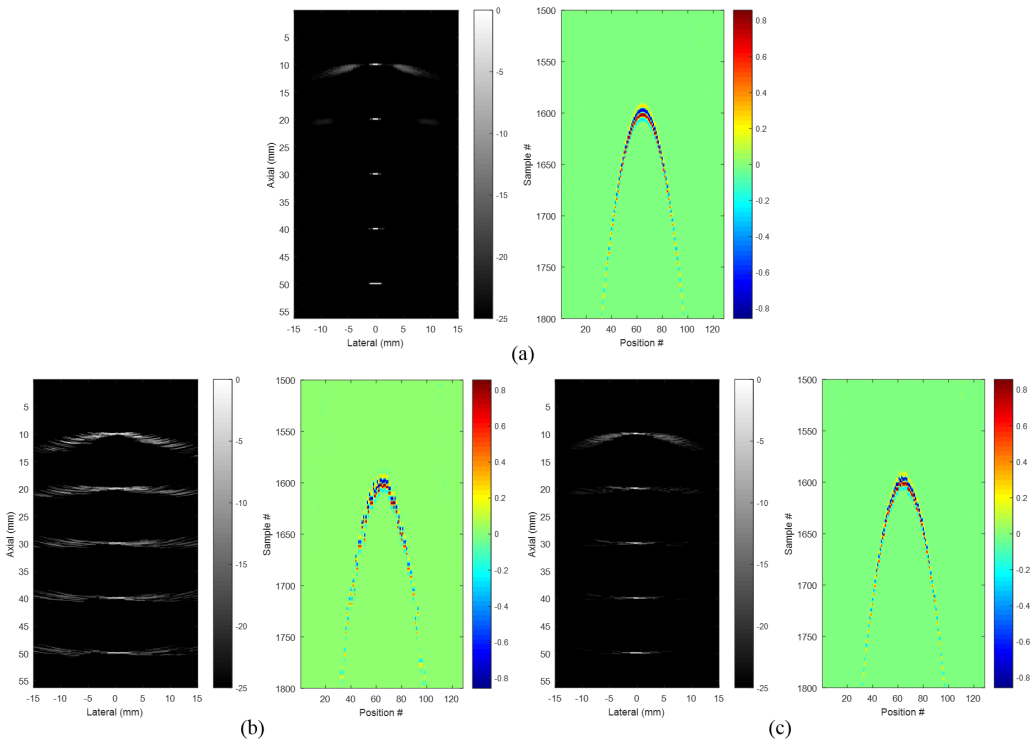

Figure 11.4: Simulated point targets and corresponding received RF data of a point at 30 mm depth. (a) ground truth image with no error. (b) The result with error in the axial axis, and (c) the result with error in the rotation axis.

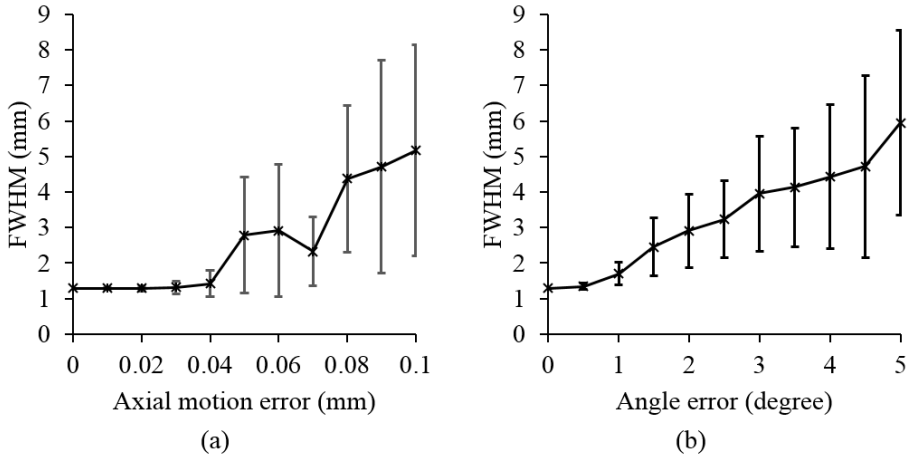

Figure 11.5: The full-width at the half maximum (FWHM) of the point targets for different error sources. (a) The resolution in the presence of error in axial direction for each receive line. (b) The resolution in the presence of error in rotational angle tracking.

out the error. Sweeping in the lower speed is another solution to minimize scanning angle pitch, but slow sweeping has more rooms to contain errors due to breathing or body motion.

11.5.2 Needle Sensing Evaluation

Figure 11.6 shows the sensitivity of the depth detection, and the accuracy of the rotation encoder. The depth detection result is shown in Fig. 11.6(a), showing that the ultrasound needle could accurately sense the depth information. The needle depth sensing itself could be used as a real-time guidance tool, by indicating how deep the needle could go before hitting the high contrast region. This could work well, given that in our case, the largest structures are bone. The accuracy of the encoder was

assessed experimentally prior to implementing in our system. The needle was placed vertically and incrementally rotated such that, at each new angle position, the new angular reading from the encoder and the horizontal displacement of the tip of the needle were recorded. With the horizontal displacement of the needle tip (x) and the known length of the arc radius (r), the actual angle can be calculated with this simple trigonometric equation:

$$\theta = \tan^{-1}\frac{x}{r}. \tag{11.4}$$

This was compared to the angle found with the encoder to find the error, and a linear trend was observed as seen in Fig. 11.6(b). The angle sensitivity of the needle was 11.44 degrees where -6 dB signal strength was reached. These two pieces of information indicate that the sensing system is sufficient to produce images with minimal distortion as indicated by motion from tissue or sensors.

11.5.3 Single Element Ultrasound Imaging with Controlled Scan

Experimental results using our prototype imager are shown in Fig. 11.7 and Fig. 11.8. For a controlled scan, the needle position was fixed at each angle, and swept in 1 degree step. Figure 11.7(a) shows the reconstructed images before and after applying synthetic aperture focusing (SAF). The signals from point targets did not appear across a wide range of line data, because the needle has inherent high angular

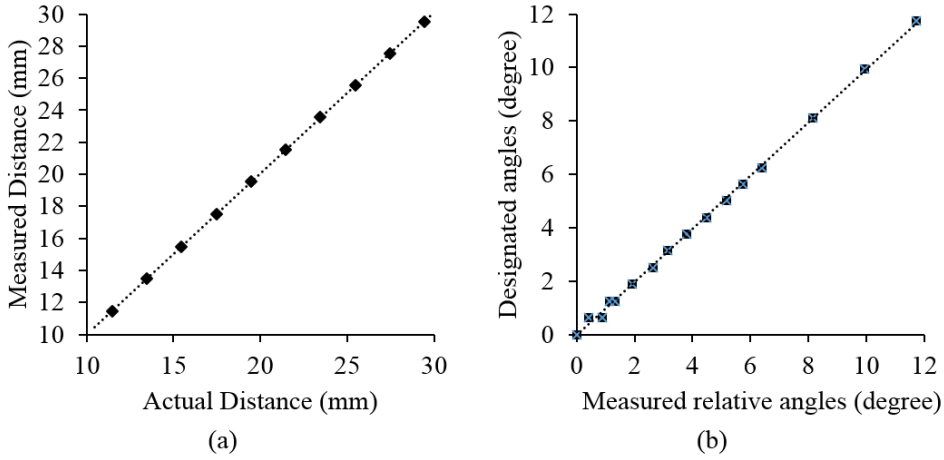

Figure 11.6: The evaluation results of the needle (a) and the rotation encoder (b). (a) The distance from the needle reading was compared to the designated motion distance, and (b) the angle measurement for the encoder was compared to the actual angle. The correlation function for both the depth sensing and rotation encoder sensing was higher than 99.99 and 99.94, respectively.

sensitivity. The beamformed image shows a clear resolution improvement for both targets, but the targets contrasts were slightly deteriorated because of the strong background noise and off-axis summation from tracking errors. The beamforming side lobes appeared in the near field, which could be attributed to incoherency of the data due to the tracking inaccuracy. The FWHM of the shallower wire improved from 3.53 mm to 1.94 mm through SAF, and that of the deeper wire improved from 6.36 mm to 2.51 mm.

After testing on the point target phantom, the real spine bone phantom was scanned to test a more practical scenario. Figure 11.8 shows the spine image in the slice crossing the vertebrae horizontally. While two edges of the bone were observed, the center region captures the bone in the middle, signifying that this point should be

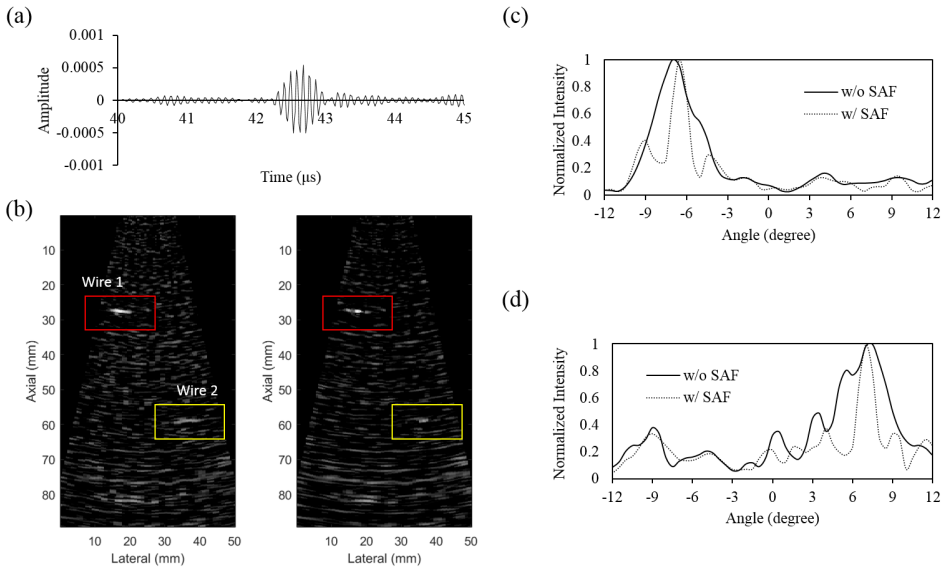

Figure 11.7: The imaging result of the metal wire phantom. (a) The B-mode image of pre- and post-beamforming. The angle axis profiles of two metal wire targets are shown in (b) and (c), corresponding to wire 1 and 2, respectively. For each profile, the results before and after applying synthetic aperture reconstruction are compared.

avoided for insertion. The contrast is not strong in the center region due to the angled reflection from the bone. When the needle angle and the target are perpendicular, the signal will reflect mostly to the receiver but if there is an angle, the reflection will be weaker than the perpendicular position.

11.5.4 Single Element Ultrasound Imaging with Free-hand Scan

After confirming the validity of the controlled scan, we tested the feasibility of free hand scanning with the wire phantom. Continuous 500 positions were recorded by sweeping the needle back and forth, and at the same time, the rotation angle was

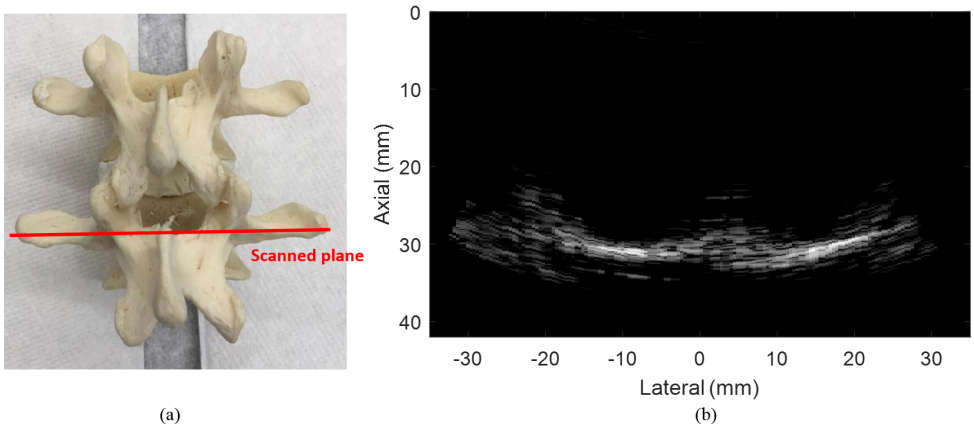

Figure 11.8: (a) The spine phantom picture and the scanned plane. (b) The ultrasound image of the spine phantom. The contrast from the center region indicates that the needle cannot go through without changing the insertion orientation.

collected by the encoder. The angular range of the scanning was 61 degrees. The result captures the three wire targets, and the size and position match the original phantom design. Comparing the reconstructed point size of the very left wire, the FWHM improved from 2.08 mm to 0.95 mm through synthetic aperture beamforming.

11.6 Discussion and Conclusions

The current standard of care for LPs introduces a wide range of iatrogenic complications and places a heavy financial burden on the patient, physician, and healthcare system overall. The proposed imaging system incorporates an ultrasound element at the tip of the needle to allow for high resolution imaging at any depth the needle can be inserted. The needle probe bypasses the attenuation from adipose tissue and

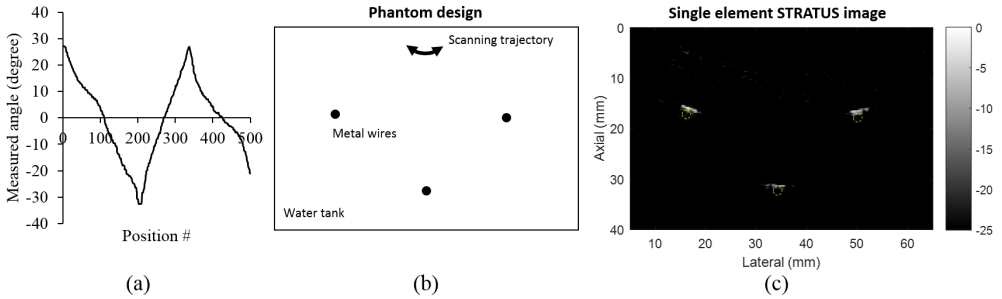

Figure 11.9: The freehand scanning result of single element ultrasound imaging system. (a) The measured angle for 500 needle positions. (b) The metal wire phantom design, and (c) the ultrasound image from the data of 500 positions corresponding to 61 degrees sweeping.

skin that plagues traditional topical ultrasound approaches. By providing the physician with visualization of the bone structure ahead, and facilitating accurate midline placement, the needle will pass through a plane known to be devoid of significant blood vessels and nerves [109]. The simulation validation and experiments using our prototype successfully demonstrate the potential of the tool for LPs guidance.

Compared to other imaging systems, there are clear advantages. Unlike other ultrasound guidance systems, the proposed system is an independent imager that does not require any registration process which could introduce additional needle tracking inaccuracy. The real-time sensing of information is the most direct and informative way to prevent undesired contact between the needle and bone. As the image plane is kept in the needle frame, there is no out-of-plane error that could be introduced due to ultrasound beam thickness in the conventional ultrasound probe based guidance. The system also requires minimal electrical components, making it more cost effective.

Another unique aspect of the system is the fact that the proposed system could update the sensing/imaging at any intermediate insertion depth in real-time, while conventional guidance must rely on information gathered prior to entry such as preoperative CT or ultrasound-to-tool calibration. This up-to-date information is not only more reliable, but also enables higher resolution especially as the needle approaches the real target. Conventional ultrasound could have a limited imaging depth depending on the object and frequency used. Thus the proposed system can provide clearer and more precise information for guidance.

Regarding the limitation of the system in practical implementations, the tissue layer could cause signal attenuation that lowers the intensity from the bone surface. Therefore, a more sensitive receiver circuit and needle are desired. SNR can be improved by electrical impedance matching between the sampling circuit and needle. Another solution is to use a PZT element with lower center frequency, which can lower the requirement for the error because the wavelength also becomes low. This will also help reduce beamforming artifacts because the wavelength of signals becomes longer. Additionally, signal processing or a more adaptive beamforming algorithm could also help to counter this concern. The tracking accuracy due to motion artifacts are considered as another problem. There is some inevitable error from the mis-synchronization between the tracking and the ultrasound data. Ideally, the tracker should be fast enough to reduce the error introduced. Other than that, unexpected angular sensitivity from a non-orthogonal element (i.e. an element that was placed

at a tilt from the manual fabrication process) could introduce beamforming error.

Future works include building an adaptive image formation algorithm taking into account the known angular sensitivity, and enhancing the SNR of the image. The system will be further tested in more realistic environments such as ex vivo tissue or in vivo.

Part III

Advancements on Translational Photoacoustic Imaging

Chapter 12

In Vivo Photoacoustic Prostate Cancer Imaging Using PSMA-Targeting Contrast Agents

In this chapter, I was responsible for algorithm development, system integration, data collection, analysis and writing. Dr. Ying Chen synthesized the PSMA targeted PA agent. Ala Lisok assisted the animal preparation. Dr. Jeeun Kang provided technical support. Dr. Martin Pomper and Dr. Emad Boctor supervised the project.

12.1 Introduction

Prostate cancer is one of the most common types of cancer and the second leading cause of cancer-related death among men in the United States. In a recent report from 2016, 180,890 men were diagnosed with the prostate cancer, and 26,120 men died [110]. Prostate cancer is known for its high survival rate when it is localized because of its slow tumor growth, but the survival rate drops with the onset of metastasis and subsequent accelerated tumor growth. Therefore, screening has a substantial value for early detection, enabling to treat the cancer in the early stage.

Prostate-specific antigen (PSA) blood test [111] and digital rectal examination have been gold-standard prostate screening methods. After those screenings, a transrectal or transperineal needle biopsy are performed for definite diagnosis of prostate cancer [112]. However, these need biopsy procedures are invasive, and not ideal for early stage screening and repetitive therapeutic monitoring after proctectomy. Therefore, there has been a need to develop a targeted non-invasive imaging screening method that can detect prostate cancer in the early stage with high sensitivity and selectivity.

Molecular imaging differs from traditional anatomical imaging in that biomarkers are used to help image particular targets. Prostate-specific membrane antigen (PSMA) is a type II integral membrane protein that shows its expression on the surface of prostate cancer cell [113, 114]. PSMA has been used as imaging and therapy targets with its advantage of showing the expression in neovascular endothelium of

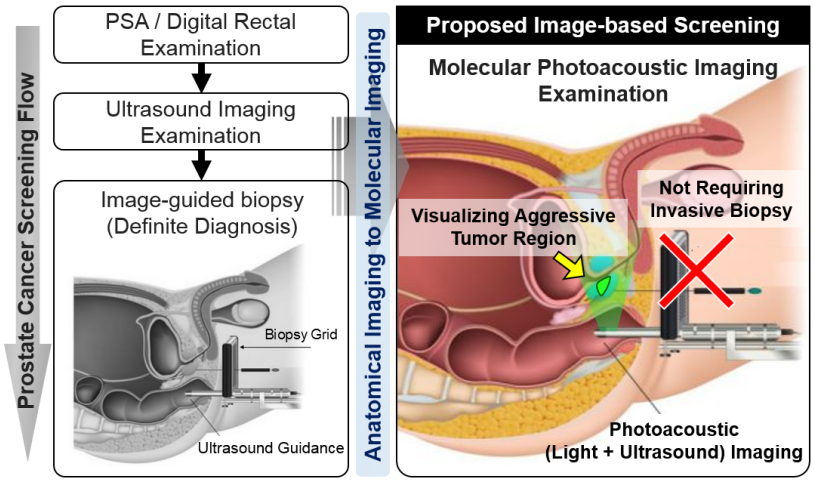

Figure 12.1: Proposed image based prostate cancer screening.

solid tumors but not in normal vasculature [115, 116]. It is also known for showing high affinity with aggressive rather than indolent tumor [117]. PSMA-targeted biomarkers have been developed for many imaging modalities including radionuclide imaging, MRI, and fluorescence (FL) imaging.

Photoacoustic (PA) imaging is a noninvasive and nonionizing hybrid imaging modality combining high optical absorption contrast resolution with high spatial resolution of ultrasound imaging. Using near infrared laser excitation and ultrasound detection enhances the light-penetration and resulting imaging depth by minimizing the absorptive and scattering attenuation during the light propagation through the biological tissue. A number of PA contrast agents have been previously evaluated to selectively visualize tumor tissue or metabolic properties. In particular for prostate cancer screening, Dogra et al. suggested the potential of using of PA imaging as the

modality of imaging PSMA targeting molecules [118]. Yet, the concept has not been demonstrated *in vivo*.

In this work, we propose the PA imaging approach to non-invasively detect PSMA expressing prostate tumor in vivo. For this, we used a PSMA-targeted PA contrast agent, YC-27, a molecule formed with an optical dye, IRDye800CW, and a high-affinity urea-based PSMA ligand Lys-Glu-urea. This molecular linker can specifically bind on PSMA expressed in the prostate cancer to be selectively quantified with spectroscopic PA imaging with material decomposition algorithm.

12.2 Contributions

The main contributions of this chapter are the following:

- Development of in vivo photoacoustic imaging system
- *Invivo* demonstration of PSMA targeted PA imaging
- Differentiation of PSMA positive and negative tumors through imaging mice xenograft

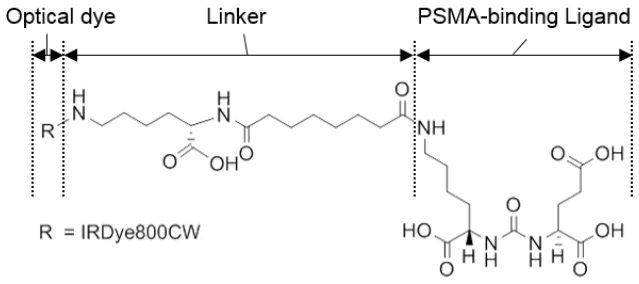

Figure 12.2: Structure of PSMA targeted PA agent.

12.3 Methods

12.3.1 Synthesis of PA Agents

The PSMA-targeted molecule, YC-27, was composed of three functional parts (Figure 12.2). The first component is an optical dye, IRDye800CW. The second component is a high-affinity urea-based PSMA ligand Lys-Glu-urea. The third component is a linker that tethers the PSMA ligand to the bulky optical dyes using a lysine-suberate linker. This agent showed high affinity to PSMA ($K_i < 15$ nM) in in vitro binding assay. The detail synthesis of YC-27 and in vitro assay methodology can be found in [119].

12.3.2 Animal Preparation

Mice xenograft was prepared as the in vivo imaging targets. PSMA+ PC3 PIP and PSMA- PC3 FLU prostate cancer cell lines [116] were grown in RPMI 1640 medium

(Invitrogen, Carlsbad, CA) containing 10 % fetal bovine serum (FBS) (Invitrogen) and 1 % Pen-Strep (Biofl- uids, Camarillo, CA). All cell were cultured in 5 % carbon dioxide (CO2), at 37.0 degree in a humidified incubator. Animal studies were undertaken in compliance with the regulations of the Johns Hopkins Animal Care and Use Committee. Six- to eight-week-old male, non-obese diabetic (NOD)/severe-combined immunodeficient (SCID) mice (Charles River Laboratories, Wilmington, MA) were implanted subcutaneously with 110^6 PC3-PIP and PC3-FLU cells on the back side of mice behind kidneys. Two tumors were placed next to each other to enable to image in ultrasound and PA imaging at the same time (Figure 12.3A). Mice were imaged when the tumors reached 3-5 mm in diameter. A set of PA and ultrasounds images were acquired from both PIP and FLU tumors before injection of the contrast agent. Inhalational anesthesia (isoflurane) was applied on mice through a nose cone attached to the imaging bed. The PA agent of 50 nmol in PBS was injected via tail vein, and the post-injected tumors were imaged at 24 hour, and 13 days for 5 mice. For one of those mice, we fixed the mouse position during the molecule injection, and recorded 2 hour data point for both PA and fluorescence imaging.

12.3.3 Ultrasound Imaging

Ultrasound images were used as the baseline to locate the tumor region. A clinical ultrasound scanner (SonixCEP, Ultrasonix Corp.) was used to collect in vivo mice imaging. A linear array transducer (L14-5/38, Ultrasonix Corp.) with 128 elements

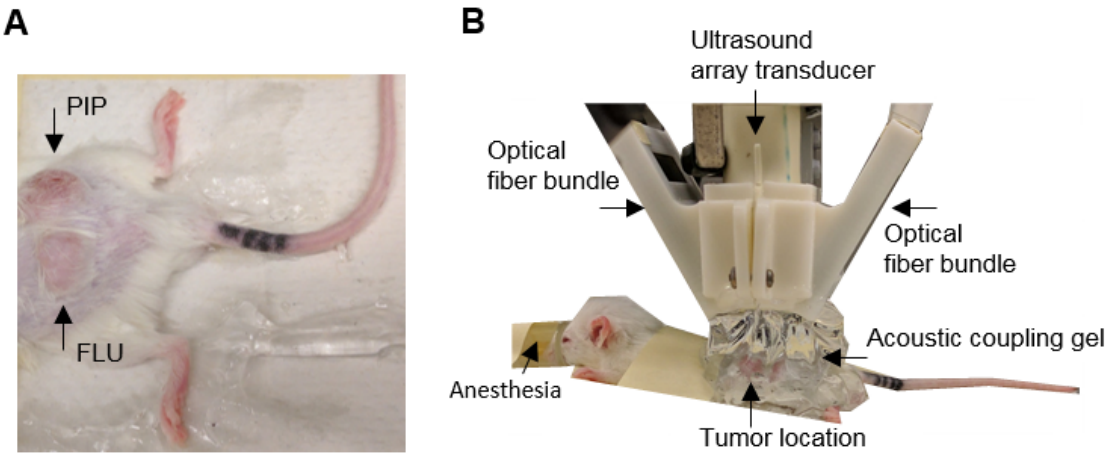

Figure 12.3: (A) Xenograft tumor preparation. The xenograft tumors (PIP and FLU) were inclubaed on the back of mice. (B) Photoacoustic (PA) imaging setup. Laser was illuminated through bar-type fiber bundles, and PA signals were collected by a linear array transducer.

and the pitch of 0.3 mm was used. The mice were anesthetized and placed on a fixation stage while the dorsal was facing up. The ultrasound gel was used to couple the ultrasound probe and mice with tumors. The position of ultrasound transducer was optimized by ultrasound B-mode images to maximize the tumor cross-section.

12.3.4 Photoacoustic Imaging

After determining the ultrasound slice position relative the mice, PA images in the same image field were collected consecutively. A Q-switched Nd:YAG laser integrated with an Optical Parametric Oscillator (OPO) (Phocus Inline and MagicPrism, Opotek Inc.) was used as the light source. The emitted light was coupled with a 4-cm bar-shape optical fiber bundle, which enable the co-registered emission with respect to

the linear array transducer. With the tunability of the laser system, the spectral responses for near-infrared wavelengths (i.e. 700-850 nm at 10-nm interval) were scanned with 20-Hz pulsed repetition frequency and 5 nm pulse duration. At each wavelength, multiple PA data was collected with 64 pulsed laser excitations for frame averaging. The raw PA signals from mice were received by the ultrasound probe, and the data was acquired using data acquisition system (SonixDAQ, Ultrasonix). The raw channel was then beamformed and post-processed to form a PA image for the spectroscopic analysis.

12.3.5 Material Decomposition

The contrast of the reconstructed PA image is consisted by the combination of multiple contrast agents including the dye, blood, and other tissue materials. The process of unmixing each source material from the raw PA intensity utilizing multiple wavelengths is necessary to correctly quantify the exogenous contrast agent intensity. Assuming PA signals is composed with a linear accumulation of multiple signal sources, the received raw PA spectrum is the summation of the multiplication of contrast agent spectrum and quantity. Therefore, the unknown dye and other contrasts m are calculated as

$$\underset{m_{1,2,\ldots,M}}{\arg\min} \left\| p - \sum_{i=1}^{M} m_i \mu_{a,i} \right\|, \tag{12.1}$$

where p is the raw PA spectrum, and i represents the contrast number. μ is the absorption spectrum of the contrast i, and M is the number of contrast-of-interest. In

this work, we assumed three contrasts within the PA image: oxygenated and deoxygenated hemoglobin, and the YC-27 constrast agent. The spectrum of hemoglobin was known from literature [120], and the spectrum of the dye agent was taken from *invitro* experimental results presented in the Result section.

12.3.6 Fluorescence imaging

Fluorescence imaging was recorded as the ground truth of detecting PSMA expressed tumors using Pearl Imager (LI-COR Biosciences). This instrument employs a CCD camera with a field-of-view of 11.2 by 8.4 cm at the surface of the imaging bed. The scan time was less than 30 s to complete white light, 700 and 800 nm channel image acquisition that is optimized for IRDye800CW detection. The output images were displayed a pseudocolor with corresponding scale. All images were acquired at the same parameter settings and are scaled to the same maximum values. Imaging bed temperature was adjusted to 37 degree Celcius. The animal preparation and protocol of YC-27 administration have been mirrored as conducted in our spectroscopic PA recording.

12.4 Results and discussion

PA spectrum of the contrast dye was measured to confirm its spectroscopic characteristics. For this in vitro phantom experiment, IRDye800CW-Ulea diluted with

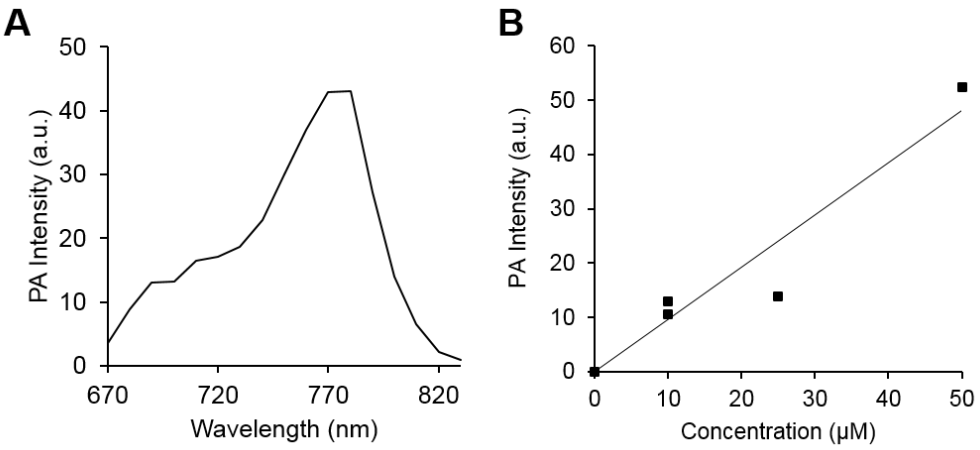

Figure 12.4: PA spectroscopic characteristics. (a) The PA spectrum of IRDye800CW-Ulea. (b) The PA intensity versus the dye concentration.

PBS and was placed in transparent tubes with 1.27-mm diameter (AAQ04133, Tygon, Saint-Gobain Corp.), which were located at around 30 mm depth in the water tank. The YC-27 had the maximum absorption at 780 nm. The PA spectrum of the dye with 50 μM concentration was shown in Fig. 12.4A. The PA intensities at 780 nm wavelength under different dye concentrations from 0.5 to 50 μM were shown in Fig. 12.4B.

The PA and ultrasound images of mice were recorded before and after the dye injection. Figure 12.5 shows the PA and ultrasound images of one mouse under different time points, and the quantified PA agent intensity was plotted. The raw PA contrast was seen at pre-injection due to background blood signals, but there is no YC-27 visible after material decomposition. For the same mouse, a clear YC-27 contrast was seen in both PIP and FLU tumors after 2 hour. This is attribute to the blood circulation around the tumor. After 24 hours from injection, the PA agent in

the blood was washed out, so that the contrast from the FLU tumor was decreased substantially, while a strong agent update was remaining in the PIP tumor. The same trend was observed in fluorescence imaging by comparing the quantitated intensity of PSMA targeted agent.

Figure 12.6 summarizes the quantified PA and fluorescence intensity from YC-27 contrast for both PIP and FLU tumors under different time points. With five mice testing, the PA intensity from YC-27 showed a statistically significant improvement by comparing pre-injection and a24 hour post-injection on PIP tumors ($p < 0.01$), as well as comparing PIP and FLU tumors at 24 hours time point ($p < 0.01$). We also performed the measurement after 13 days from the injection, and the weak YC-27 contrast was remaining in the PIP tumor. The same trend could be observed in fluorescence results (Fig. 12.6B). Then, we compared the correlation between PA and fluorescence intensity using the all data points with different tumor types and time points (Fig. 12.6C).

The result reveals that the PA and fluorescence were strongly correlated, and suggested that PA imaging could serve as a complemental modality of fluorescence. Comparing these two imaging systems, the main different is the dimensionality where PA imaging provides slice-lie tomographic view of tissue, while fluorescence imaging delineate the superficial distribution of the contrast. Therefore, PA imaging hold its unique potential of being used as the non-invasive imaging modality for prostate cancer screening.

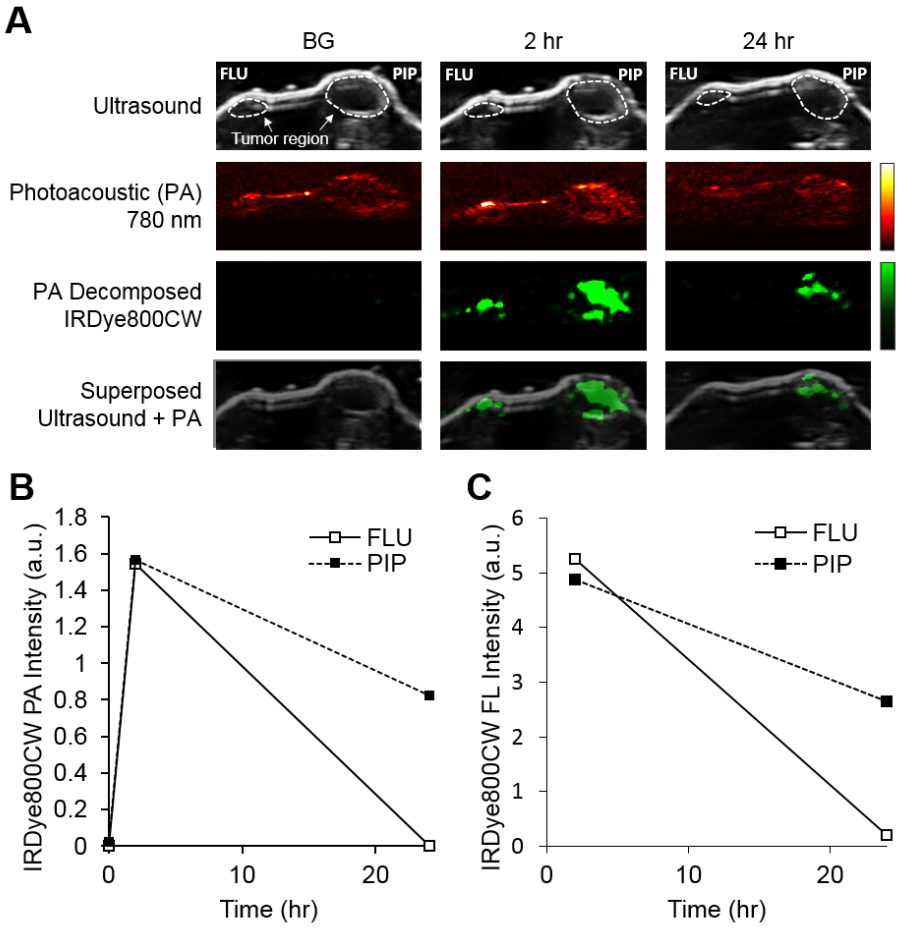

Figure 12.5: PA and ultrasound imaging of PSMA negative (FLU) and positive (PIP) tumors. (a) Image comparison of the tumor before injection and after 2 hours and 24 hours injection. (b) Quantified the PA intensity of FLU and PIP tumors. (c) Quantified the fluorescence (FL) intensity of FLU and PIP tumors.

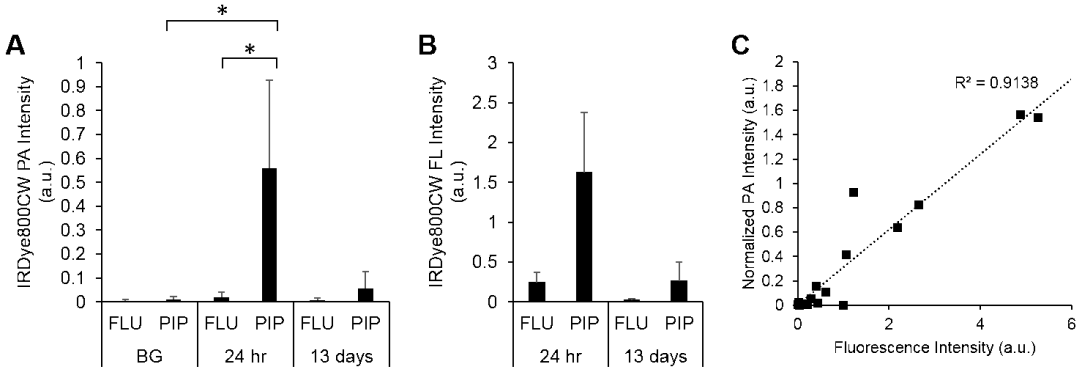

Figure 12.6: (A) PA intensity comparing before injection and after injection 24 hours and 13 days. * stands for p-value lower than 0.01. (B) Fluorescence intensity comparison after injection 24 hours and 13 days. (C) Comparison of PA and fluorescence, and its correlation.

12.5 Conclusions

In this chapter, we used the PSMA targeting PA contrast agent, YC-27, and validated the feasibility of PSMA tumor detection in vivo. PA imaging visualizing a tomographic slice could reveal the similar agent contrast as fluorescence imaging does provide through superficial dorsal angle. These results suggest that PA imaging has as reliable PSMA targeting molecule detection capability as fluorescence imaging in a non-invasive manner.

Chapter 13

Photoacoustic Voltage-Sensitive Dye Recording

This chapter has been published as: *H. K. Zhang*, P. Yan*, J. Kang, D. S. Abou, H. N. D. Le, A. K. Jha, D. L. J. Thorek, J. U. Kang, A. Rahmim, D. F. Wong, Emad M. Boctor**, Leslie M. Loew** (*equal contributions, **co-corresponding author), "Listening to membrane potential: Photoacoustic voltage sensitive dye recording, in Journal of Biomedical Optics, 22(4), 045006, 2017.*

This is a collaborative work done through Brain Initiative effort with multiple PIs across The Johns Hopkins University and University of Conneticut. I was responsible for developing the theoretical model, system integration, lipid vesicle prepration, data collection, analysis and writing. Dr. Ping Yan synthesized the PAVSD800-2, and wrote the method section related to the dye synthesis. Dr. Jeeun Kang and Dr.

Diane Abou assisted the experiment. Dr. Daniel Thorek, Dr. Jin Kang, Dr. Arman Rahmim, Dr. Dean Wong, Dr. Emad Boctor, and Dr. Leslie Loew supervised the project.

13.1 Introduction

The quantification of neurotransmitter (NT) activity with high temporal resolution is essential to build a comprehensive map of brain function. We need to improve upon the low temporal resolution, but high pharmacological specificity, of PET and higher spatial and temporal resolution, but less specific, MRI. Membrane potential measurements utilizing direct electrical recording or by imaging using voltage sensitive dyes (VSD), have been used to observe spontaneous NT events by means of voltage fluctuations caused by ionic currents. In general, imaging approaches have the advantage that patterns of activity can be studied with high resolution over large areas of brain [121]. However, purely optical based detection approaches have several limitations which include a small dynamic range and only shallow penetration depth due to light scattering and absorbance of overlying tissue *in vivo*.

Photoacoustic (PA) imaging is an emerging hybrid imaging modality. Here, non-invasive molecular light absorbance dependent acoustic signal occurs at depths of up to several centimeters in biological tissue [73, 77], with a micro to millimeter special resolution that is limited by the acoustic bandwidth and focusing. The mechanism

behind PA imaging is that upon excitation by a short-pulsed laser, thermal relaxation of the chromophore excited state induces local thermal elastic expansion. Using near infrared laser excitation and ultrasound detection enhances the light-penetration and resulting imaging depth by minimizing the absorptive and scattering attenuation during the light propagation through the biological tissue.

Towards use of this technique for functional brain imaging, previous research has demonstrated PA imaging to be capable of monitoring brain activity based on the blood-oxygen-level dependent (BOLD) signal change. This imaging procedure, which does not rely on the administration of exogenous contrast agent [122–124], is susceptible to several non-linear physiological and biophysical parameters in addition to the NT activity or electrical signaling. As a result, it is regarded as an indirect, semi-quantitative reflection of the membrane potential change in neurons [125, 126]. An alternative approach is needed in order to provide direct readout of membrane potential events in cerebral tissues.

A number of contrast agents have been previously evaluated for use with PA imaging to selectively visualize tumor tissue or metabolic properties [127–129]. Most of the proposed PA contrast agents have been based on the extinction coefficient of the compound used as the materials with a stronger absorbance should provide strong PA intensity. Here, we show how voltage-dependent PA signals may be produced by VSDs. We first develop the theoretical concept whereby the fluorescence quenching of the voltage-dependent dye leads to a reciprocal enhancement of PA intensity. Based on

this concept, we synthesized a novel near infrared PA VSD (PAVSD800-2) whose PA intensity change is sensitive to membrane potential. The performance of the PA-VSD developed was tested with a lipid vesicle test system that allowed us to readily manipulate membrane potential and measure both the PA and spectrophoto/fluorometric response. Importantly, it has near-infrared excitation and emission bands, which would make it appropriate for deep NT activity imaging applications. Furthermore, our theoretical model based on the photophysical properties of the VSD enable us to quantitatively estimate the PA voltage sensitivity. Further development of the ideas described herein promise exogenous contrast agents with high temporal and spatial resolution for deep brain NT activity measurements.

13.2 Contributions

The main contributions of this chapter are the followings:

- Development of photoacoustic based voltage imaging
- Development and validation of photoacoustic voltage sensitive dye
- Theoretical derivation of quenching based photoaoucstic contrast enhancement

13.3 Theory and Principle

13.3.1 Design of a PA-VSD Based on Photophysics and Photochemistry

When a chromophore absorbs a photon to occupy an excited state, it can relax back to the ground state either by emitting a photon or by shedding its energy as heat. The former is termed radiative decay and has a rate, k_r, that depends on the chromophore and its molecular environment; the radiative decay is measured as fluorescence. The thermal decay route, with a rate k_t, also depends on both the structure of the dye molecule and its environment. Specifically, low energy internal vibrational modes can facilitate thermal relaxation; and the environment, including interactions with solvent or with specific interacting partners quenchers also offer non-radiative decay pathways. The PA intensity depends on the thermal decay of chromophores after they are excited by a short intense laser pulse; the resultant rapid and large thermal decay produces a burst of heat that locally increases the kinetic energy of neighboring molecules and can be detected with an ultrasound detector. The key point is that for a given chromophore, the efficiency of thermal (th) (acoustic) and radiative (fluorescence (F) and phosphorescence) decay processes are in competition; for most organic chromophores, phosphorescence can be neglected, leading to simple

relationships:

$$\Phi_F = \frac{k_r}{k_r + k_t}, \Phi_{th} = \frac{k_t}{k_r + k_t}, \tag{13.1}$$

These equations give the theoretical quantum efficiency, Φ, for fluorescence and photoacoustics, corresponding respectively, to the probability that an absorbed photon will be transformed into an emitted photon, detectable as fluorescence, or into a thermoelastic expansion of an absorber, detectable as PA. Both arithmetically and by the principle of conservation of energy, the sum of Φ_F and Φ_{th} must be unity. Indeed, there is experimental evidence of the reciprocal relationship between fluorescence efficiency and PA efficiency. For example, Qin et al. designed a PA contrast agent, in which PA intensity was enhanced by suppressing the fluorescence emission [130].

It has long been known that cyanine dyes have a tendency to form aggregates at high concentrations. The aggregates are non-fluorescent. Waggoner et al. developed a series of highly sensitive VSDs based on cyanine dyes that, because they have delocalized positive charge, redistributed across cell membranes as a function of the membrane potential [131]. Because the charge is delocalized, they are able to permeate through the hydrophobic cell membrane and redistribute according to the Nernst equation. The idea is that the dye molecules will accumulate inside polarized cells at sufficiently high local concentration to produce non-fluorescent aggregates; upon depolarization, the dye molecules will be released and diluted into the larger external volume, favoring fluorescent monomers (Figure 13.1). Indeed, under the right circumstances, depolarization can produce >100 fold increases in cyanine dye fluo-

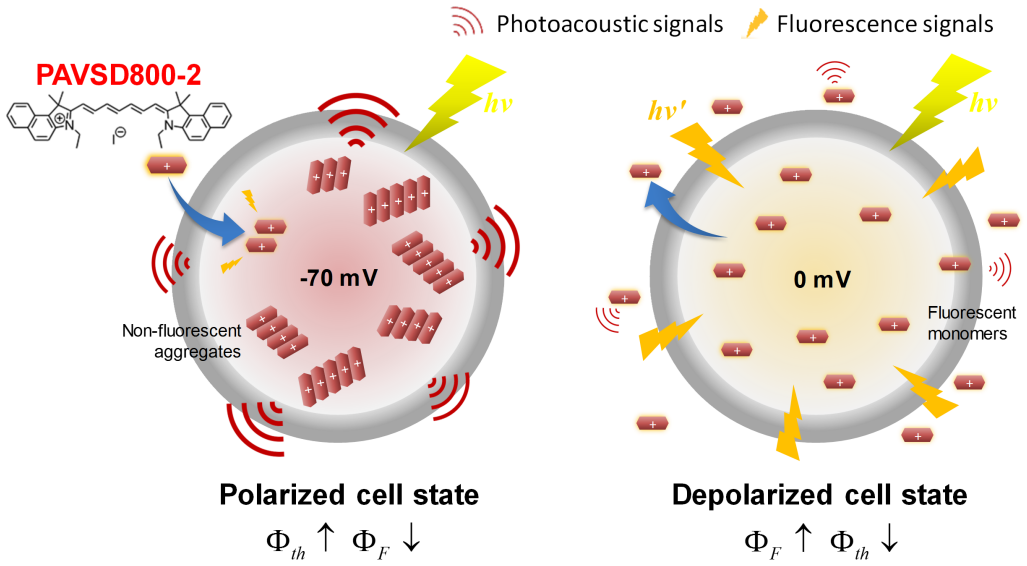

Figure 13.1: The principle of the fluorescence quenching effect on the developed VSD (PAVSD800-2) according to a varying membrane potential: typically -70mV and 0mV in the polarized / depolarized states of neurons, respectively.

rescence [132], because the tendency for the dyes to aggregate shifts the equilibrium for more monomeric dye to be driven in by the membrane voltage.

We reasoned in the present work that there should be a reciprocal relationship between the fluorescence and the PA sensitivity to membrane potential (Figure 13.1) because the aggregated state of the cyanine dyes should favor thermal decay of the excited state. However, previously reported cyanine dyes with superior voltage sensitivity, such as di-SC2(5) [132], absorb around 650 nm or lower. Because the best available laser systems for PA detection are in the near infrared spectral range and because longer wavelengths allow deeper penetration into tissue, we decided to design and synthesize a new cyanine dye specifically for application as PA-VSD. Our first candidate, PAVSD800-2, shows a fluorescence emission in near-infrared region

with the absorbance peak around 800 nm and fluorescence emission at 828nm in the presence of lipid membranes.

13.3.2 Thermal Confinement and Fluorescence Emission

To be able to quantitatively predict the PA response to a change in membrane potential, we derived a more detailed mathematical model to incorporate the PA signal enhancement with the fluorescence quenching effect. This model also accounts for possible changes in dye absorbance. In the classic formulation, the initial PA pressure, p_0, has been modeled based on absorbance as,

$$p_0 = \frac{\beta}{\rho C_v \kappa} \Phi_{th} \mu_a \Upsilon = \Gamma \Phi_{th} \mu_a \Upsilon, \tag{13.2}$$

where β is the thermal compressibility; ρ is the mass density; C_v is the heat capacity; κ is the isothermal compressibility; Φ_{th} is the thermomechanical conversion efficiency, μ_a is the optical absorbance; Υ is the optical fluency, and Γ is the thermodynamic conversion coefficient for PA pressure generation, which is also known as the Grneisen parameter. However, this formulation is not sufficient to model the PA pressure enhancement due to fluorescence change for the purpose of designing VSD. Our new formulation starts from the energy conservation rule based on quantum yield; the total amount of absorbed energy by an absorber (i.e., $E_{abs} = \mu_a \Upsilon$) will be converted into thermal energy (E_{th}), and light re-emission like fluorescence (E_F), and other

photochemical reactions (E_{others}):

$$E_{abs} = E_{th} + E_F + E_{others}, \tag{13.3}$$

and the substitution of Eq. 13.3 into the Eq. 13.2 gives

$$p_0 = \Gamma E_{th} = \Gamma(E_{abs} - E_F - E_{others}). \tag{13.4}$$

Now, the PA pressure change ratio (i.e., C_{PA}) depending on the neural depolarization can be expressed as

$$C_{PA} = \frac{p_0}{p_0'} = \frac{(E_{abs} - E_F)}{(E'_{abs} - E'_F)}, \tag{13.5}$$

where p_0 and p_0' are the initial PA pressures generated by PA-VSD at resting and depolarized states of neurons, assuming E_{others} is negligible compared to E_F. E'_{abs} and E'_F are the total energy amount of absorbance and fluorescence emission in action state, respectively.

Correspondingly, the total amount of absorbance and fluorescence change depending on the depolarization state of a neuron can be given by

$$C_{PA} = \frac{E_{abs}}{E'_{abs}} \tag{13.6}$$

and

$$C_F = \frac{E_F}{E'_F} \tag{13.7}$$

In addition, the ratio of fluorescence energy compared to total optical absorbance in resting state, which is same as the quantum yield Φ'_F can be given by

$$\Phi'_F = \frac{E'_F}{E'_{abs}} = \frac{C_{abs}}{C_F}\Phi_F. \tag{13.8}$$

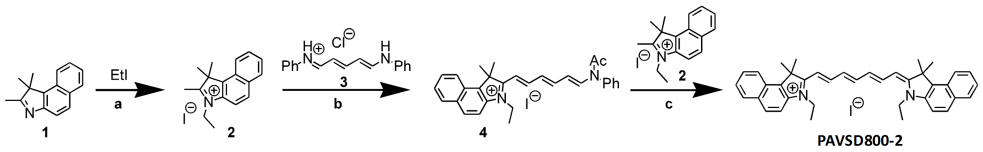

Figure 13.2: PAVSD800-2 synthetic scheme. Conditions: (a) CH_3CN, 130°C, 14 h, 64; (b) Ac_2O, 130°C, 1 h; and (c) 11 Ac_2O/pyridine, 100°C, 40

In all, the PA pressure change ratio in Eq. 13.5 can be reformulated as

$$C_{PA} \simeq \frac{C_F(C_{abs}^2 - \Phi_F)}{C_{abs}(C_F - C_{abs}\Phi_F)} = \frac{C_{abs} - \Phi'_F \cdot C_F}{1 - \Phi'_F}. \tag{13.9}$$

Hence, the PA signal change in response to neuronal depolarization is determined by the combination of the absorbance and fluorescence changes, as well as the ratio of the fluorescence energy and the absorbance energy in the depolarized state.

13.4 Materials and Methods

13.4.1 Synthesis of PAVSD800-2

PAVSD800-2 was synthesized by modified literature methods [133, 134] (refer to Fig. 13.2).

3-Ethyl-1,1,2-trimethyl-1H-benzo[e]indolium iodide (2). [133] 1,1,2-Trimethyl-1H-benzo[e]indole (1, 1.0 g, 4.78 mmol) and iodoethane (2.8 g, 18.0 mmol) were dissolved in 5 mL acetonitrile under nitrogen. The mixture was sealed in a pressure vessel and allowed to react at 130°C for 14 h. Upon cooling down to 5°C, the solids formed were filtered out and washed with acetone to give 2 as gray crystals (1.12 g, 64%).

Intermediate 4. [134] Benzoindolium 2 (128 mg, 0.35 mmol) and glutaconaldehyde dianil hydrochloride (3, 100 mg, 0.35 mmol) were dissolved in 2 mL of acetic anhydride, and the mixture was allowed to react at 130°C in a pressure vessel for 1 h. The solution turned purple. The progress of reaction was followed by absorbance spectra in methanol, which showed a major peak at 501 nm upon completion. This reaction mixture was used for the next step directly.

Cyanine PAVSD800-2. A second equivalent of benzoindolium 2 (128 mg, 0.35 mmol) and 2 mL of pyridine were slowly added to the intermediate (4) in acetic anhydride. The mixture was allowed to react at 100°C for 30 min, and the solution turned green. The progress of reaction was followed by absorbance spectra in methanol, which showed a major peak at 780 nm upon completion. After cooling down, the solvents were removed by rotary evaporation and the residue was purified by chromatography (SiO_2-amino bond, 2:98 MeOH/CH_2Cl_2). Green colored fractions were combined and the solvents were removed by rotary evaporation. The residue was washed with isopropanol (2 10 mL), and then dissolved in 30 mL 1:2 *i*-PrOH/CH_2Cl_2. The solvents were evaporated slowly under vacuum until about 5 mL was left. Precipitates formed were filtered out and washed with 10 mL i-PrOH, and dried to give cyanine PAVSD800-2 as green powders (94 mg, 40%). R_f (silica gel, 1:9 MeOH/CH_2Cl_2) = 0.64; ^{1}H NMR (400 MHz, CD_3OD) δ 1.42 (t, J = 7.2 Hz, 6 H), 1.97 (s, 12 H), 4.23 (q, J = 7.2 Hz, 4 H), 6.32 (d, J = 14 Hz, 2 H), 6.56 (t, J = 12.4 Hz, 2 H), 7.46 (t, J = 6.8 Hz, 2 H), 7.55 (d, J = 8.8 Hz, 2 H), 7.58-7.68 (m,

3 H), 7.95-8.07 (m, 6 H), 8.21 (d, J = 8.8 Hz, 2 H); LCMS: m/z = 537.0 $[M\text{-}I]^+$.

13.4.2 Lipid vesicle preparation

Lipid vesicles were prepared from 25 mg soybean phosphatidylcholine (Type II) suspended in 1 mL of K+ buffer, which contains 100 mM K_2SO_4, and 20 mM HEPES. This suspension was vortexed for 10 min and sonicated in bath-type sonicator for 60 min, yielding a translucent vesicle suspension. A Na^+ buffer containing 100 mM Na_2SO_4, and 20 mM HEPES was prepared. During experiments 10 μL of vesicle suspension was added to 1 mL of Na^+ buffer, resulting in an approximately 100:1 K^+ gradient across vesicle membrane. VSD was added to this suspension. When 2.5 μL of 10 μM valinomycin, a K^+ specific ionophore, was added K^+ ions were transported from inside to outside of vesicle membranes, resulting in a negative membrane potential. This negative potential drives the positively charged VSDs inside the vesicles, which causes aggregation of dyes and quenching of fluorescence. Subsequent addition of 2.5 μL of 1 mM gramicidin, a non-specific monovalent cation ionophore, allows Na^+ cations to move from outside to inside of vesicle membranes to short circuit the membrane potential.

13.4.3 Experimental Setup for Photoacoustic Voltage-Sensitive Dyes Characterization

13.4.3.1 Spectroscopic/fluorometric voltage sensitive dyes characterization

A combined spectrophoto/fluorometer system (Spectramax i3x, Molecular Devices) was used to measure both fluorescence and absorbance of the PA-VSD with 1, 3, 6, and 9 μM concentrations. For fluorescence, the measurement was conducted for the spectral range from 750 nm to 850 nm at 10-nm increment, and the absorbance was measured in the range from 600 nm to 900 nm at 5-nm increment. Note that 720 nm wavelength was used for excitation during spectrofluorometry of the PA-VSD.

13.4.3.2 Phantom experiment setup for photoacoustic voltage-sensitive dyes sensing

The PA sensing system was employed for the characterization of the synthesized PA-VSD (Figure 3); A Q-switched Nd:YAG laser integrated with an Optical Parametric Oscillator (OPO) (Phocus Inline and MagicPrism, Opotek Inc.) was used for PA signal generation. With the tunability of the laser system, the spectral responses for near-infrared wavelengths (i.e. 700-850 nm at 10-nm interval) were scanned with 20-Hz pulsed repetition frequency and 5 nm pulse duration. The light was delivered

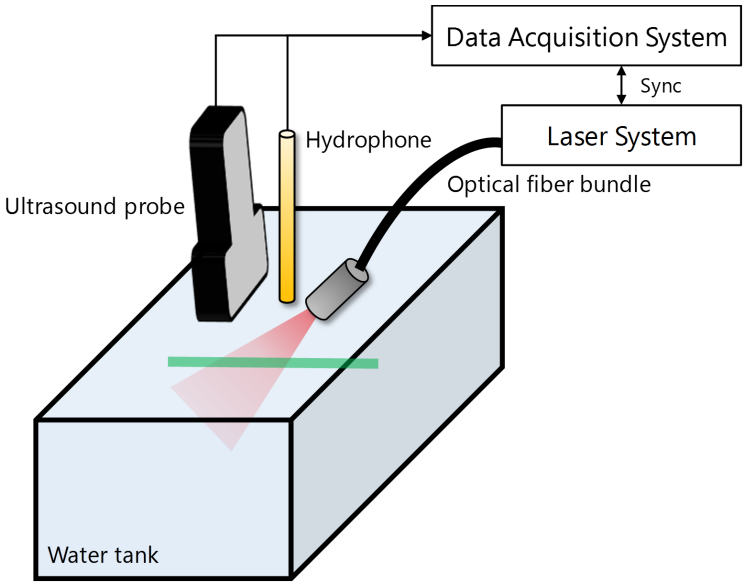

Figure 13.3: Phantom experiment setup for PA characterization of PAVSD800-2. Near-infrared light excited the sample in the tubing (green) through the optical fiber bundle, and the generated PA signals were captured by a clinical linear array transducer (10-MHz center frequency).

through an optical fiber bundle with a 9 mm round shape output, which was aligned with ultrasound receiver. The PA-VSD in the lipid vesicles suspension was loaded into transparent tubes with 1.27 mm diameter (AAQ04133, Tygon®, Saint-Gobain Corp.), which were located at around 30 mm depth in the water tank. Note that the temperature of the water was consistently maintained at 22°C during the experiments.

A 10-MHz linear ultrasound probe (L14-5/38, Ultrasonix Corp.) was used for PA-VSD sensing in practical circumstance with a limited bandwidth (i.e., 75% -6 dB fractional bandwidth). Similarly, a hydrophone with wide flat bandwidth from 250 kHz to 20 MHz (HGL-1000, Onda Corp., CA, USA) was used to collect single line radio-frequency (RF) PA pressure signal. Twenty sets of PA data were collected,

in which nineteen of them were collected using the linear array transducer, and the other was through the hydrophone, and the average and standard deviation values were calculated. The PA signals acquired at the depth of target were used to form an averaged RF signal, which is further processed to present PA intensity at each optical wavelength; this permitted an accurate correlation with the spectrophotometric measurements. For the imaging setup, one set of data was obtained using the linear array transducer from 9 μM PA-VSD at 800-nm optical wavelength, and the differentiation between the resting and polarized states was analyzed.

13.5 Results

13.5.1 Spectrophoto/fluorometric Photoacoustic Voltage-Sensitive Dyes Characterization

The spectrophoto/fluorometric results of the dye with different concentrations are shown in Figs. 13.4-13.6. In the absorbance results, Fig. 13.4(a) shows the absorbance spectrum for PAVSD800-2 at 6 μM concentration, and the peak was determined to be 800 nm. The absorbance slightly decreased in response to the membrane potential at the addition of valinomycin. As the negative control, adding gramicidin into the suspension with valinomycin recovered its absorbance intensity. When the dye concentration of 1, 3, 6, and 9 μM concentrations were tested, a linear

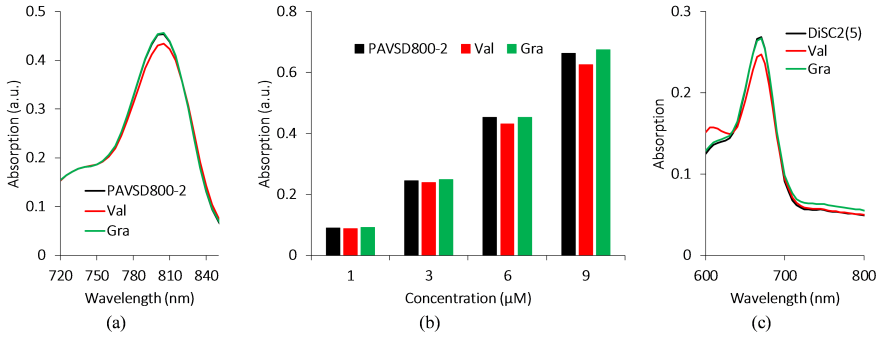

Figure 13.4: The spectrophotometric characteristics of the (a and b) PAVSD800-2 and (c) the di-$SC_2(5)$ at the simulated resting/action states using valinomycin (Val) and gramicidin (Gra). (a) Absorbance spectrum of the dye PAVSD800-2 for the concentration of 6 μM. (b) Absorbance spectra at the wavelength of 800 nm for different dye concentrations. (c) Absorbance spectrum of the dye di-$SC_2(5)$ for the concentration of 6 μM.

trend of absorbance increase was observed by increasing the dye concentration, a slight reduction during depolarization is seen for all concentrations [Fig. 13.4(b)]. A decrease in the primary absorbance peak and an increase in shoulder peak are characteristic of H-aggregation for cyanine dyes [135].

The measured fluorescence spectra with different PAVSD800-2 concentrations are shown in Figs. 13.5(a-c). The fluorescence quenching effect is due to negative membrane potential generated by the addition of valinomycin, a K^+ specific ionophore, and subsequent self-quenching of positive dye molecules accumulating and aggregating inside the vesicles. The effect was reversed when gramicidin, a Na^+ ionophore, was added to depolarize the membrane potential. The spectrum change in fluorescence quenching at 6 μM concentration is shown in Fig. 13.5(a). As negative control, K^+ buffer was used as the external buffer instead of Na^+ buffer. This control condi-

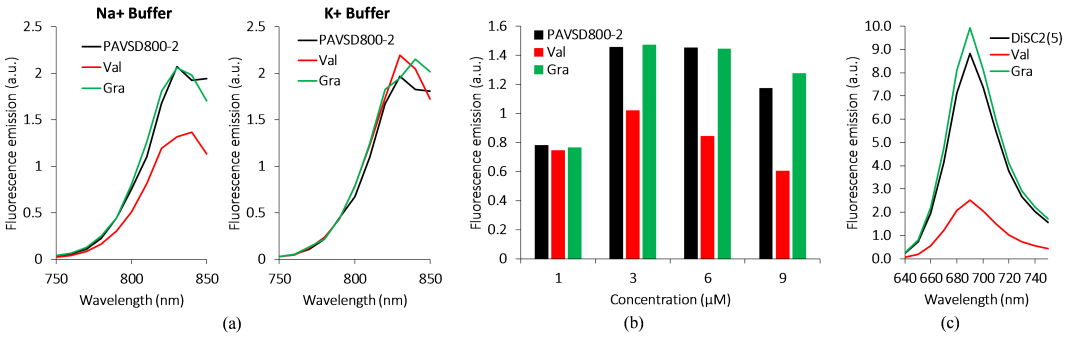

Figure 13.5: The spectrofluorometric characteristics of the PAVSD800-2 (a-b), and the di-$SC_2(5)$ (c). (a) The emission spectrum of the dye PAVSD800-2 at 6 μM concentration. (d) The fluorescence emission at 820 nm for different concentrations. (c) Fluorescence emission spectrum of the dye, di-$SC_2(5)$ at 6 μM concentration.

tion establishes the same concentration of K^+ on both sides of the vesicle membrane, preventing the generation of a polarized voltage when valinomycin is added; the absence of a fluorescence change therefore indicates that the dye does not interact with valinomycin or gramicidin at these concentrations (Fig. 13.5(a), right), but responds only to membrane electrical potential (Fig. 13.5(a), left). The amount of fractional change in fluorescence emission depends on the dye concentration, and the trend at the emission wavelength of 825 nm is shown in Fig. 13.5(b).

A fractional change in absorbance and fluorescence emission for different PAVSD800-2 concentrations are compared and summarized in Fig. 13.6. A small valinomycin-induced absorbance reduction of 2 % to 6 % were observed from 1 to 9 μM concentrations, while the fluorescence quenching up to 49 % was observed for 9 μM concentration. This substantial fluorescence change will contribute to the corresponding PA signal sensitivity to membrane potential.

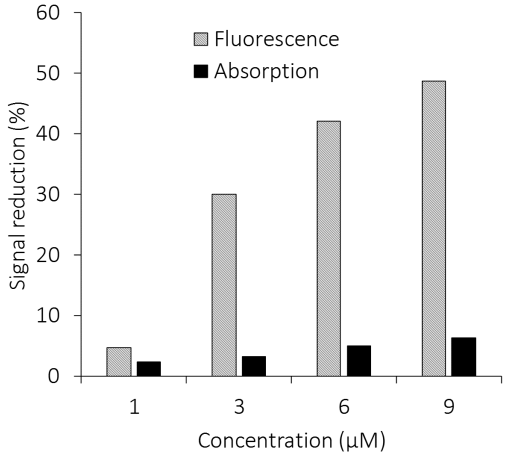

Figure 13.6: The fractional change of absorbance at 800 nm and fluorescence signal at 825 nm between the simulated resting to action states by adding valinomycin.

The absorbance and fluorescence spectrum of the classic VSD, di-$SC_2(5)$, at the concentration of 6 μM are also obtained, and shown in Figs. 13.4(c) and 13.5(c). This result may be regarded as a positive control to verify that the lipid vesicle system was operating as expected. Figure 13.5(c) particularly serves to highlight that the magnitude of the fluorescence response can be dramatically large and that improved versions of the longer wavelength cyanine dyes may be achievable.

13.5.2 Photoacoustic Characterization of the Photoacoustic Voltage-Sensitive Dyes

The PA spectrum of 6 μM PAVSD800-2 is shown in Fig. 13.7(a) for a typical experiment. Valinomycin administration, which polarizes the lipid vesicle membranes, increases the PA signal intensity. Addition of gramicidin restores the PA

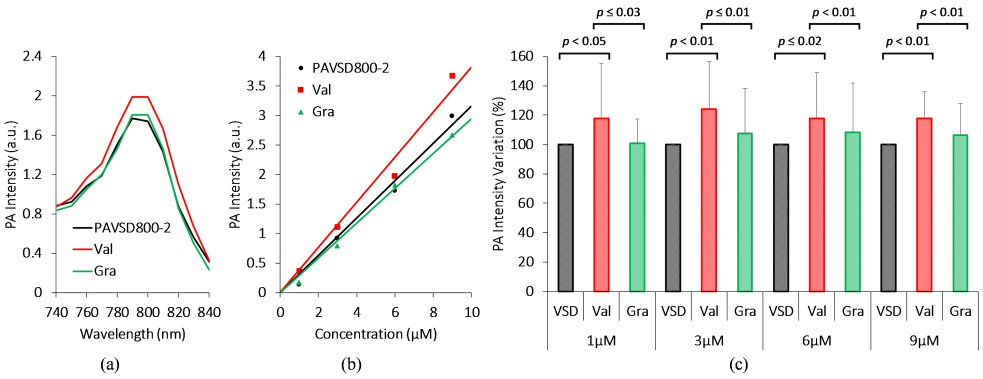

Figure 13.7: (a) PA spectra of the PA-VSD for different concentrations at the prestimulus (black) and stimulated polarized (red) and depolarized (green) states using valinomycin (Val) and gramicidin (Gra). (b) Voltage-dependent PA intensity at 800 nm for different concentrations.

signal intensity close to the original level. In this experiment, the PA intensity at 800 nm wavelength increases by 14 in the polarized state. Different concentrations of PAVSD800-2 were also tested at 800 nm [Fig. 13.7(b)]. As would be expected, an increase in PA intensity is observed with concentration and the effect of polarization (Val, red) and depolarization (Gra, green) is seen at all concentrations. To confirm the statistical significance of the PA enhancement through polarization, 20 samples were measured, and PA intensity variation was computed by normalizing the intensity to the initial dye intensity. Figure 13.7(c) shows the mean and the standard deviation of PA intensity variation under three conditions (prestimulus, stimulated polarized, and depolarized states). Comparing the initial depolarized state and after adding valinomycin, and the valinomycin result and the result after adding gramicidin, p-values were all below 0.05. The fractional PA intensity changes upon polarization at 1, 3, 6, and 9 μM concentrations were 17 %, 24 %, 17 %, and 17 %, respectively.

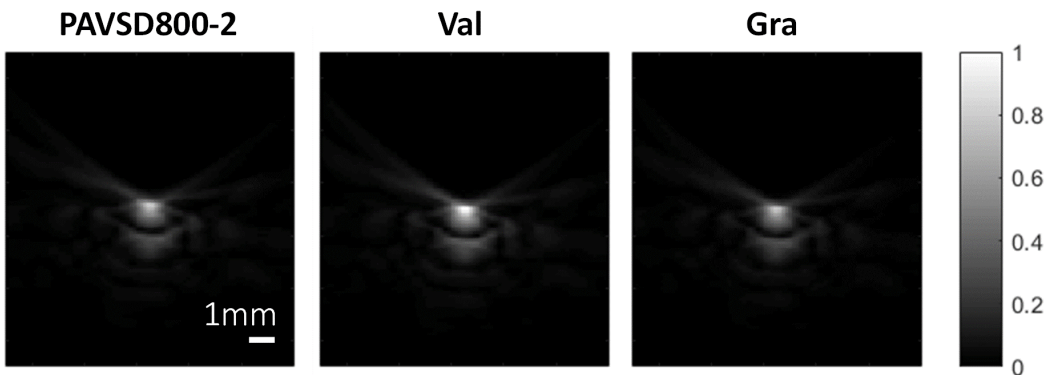

Figure 13.8: The PA images for three conditions: the depolarized state from the PAVSD800-2 only, the valinomycin-induced polarized state, and the gramicidin-reinduced depolarized state.

Figure 13.8 shows the reconstructed PA images with the 800 nm wavelength. A data set at 9 μM concentration, which showed 22.72 % fractional change of PA signals, was chosen to display. The brighter contrast was observed from the tubing in the valinomycin-induced polarized state, and the contrast was restored to the pre-stimulus level in the depolarized state after adding the gramicidin.

To further emphasize the change in PA intensity, the before and after valinomycin difference images are shown in Fig. 13.9. The result after adding gramicidin shows a close intensity to the original data, and it is regarded as the negative control of the evaluation. Note that the same color scale was used on these two results, and a clear enhancement in PA signal intensity was seen at the simulated resting state (i.e. the valinomycin-induced negative potential) compared to that of the depolarized state.

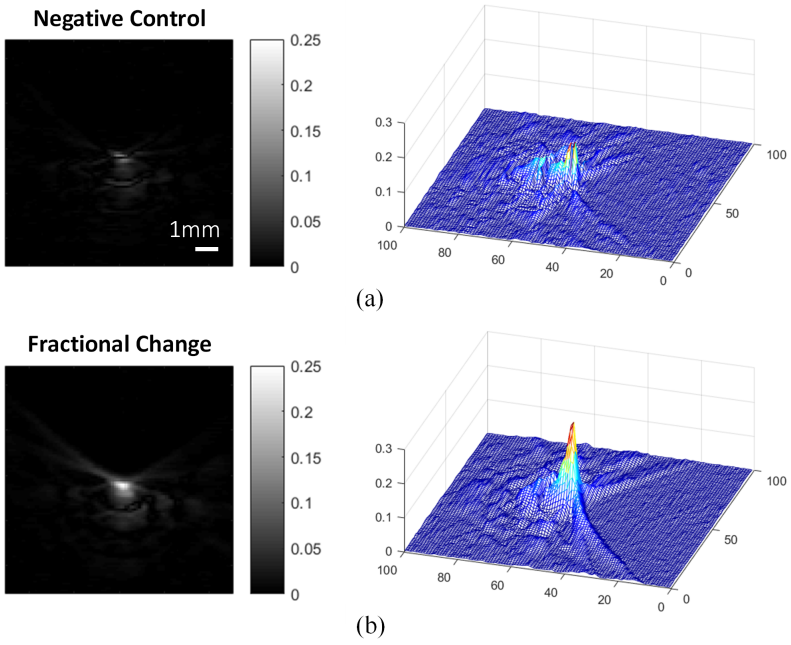

Figure 13.9: Stimulated resting and action state contrast change relative to the pre-stimulus state intensity. (a) Image produced by subtraction of the gramicidin data from the initial PA dye image is considered a negative control. (b) The difference between the initial PA dye image and the valinomycin-induced polarized state. Magnitude represents the fractional change of the intensity relative to the pre-stimulus state intensity.

13.6 Discussion

In this chapter, we report a novel concept for the design of PA-VSDs based on the fluorescence self-quenching mechanism of cyanine VSDs. We then experimentally validated this idea by designing, synthesizing and testing a near infrared absorbing cyanine dye. Based on the results, we demonstrated the promise of PA imaging to detect membrane potential events in real-time.

Our approach relies on the voltage-dependent mechanism of cyanine dye re-distribution through cell membranes. It is important to note that this mechanism can be slow on the timescale of seconds [131, 132, 136]. This is too slow follow the millisecond time scales of neuronal action potentials or electrical events at individual synapses. Studies using 2-photon fluorescence imaging microscopy of fast VSDs or genetically encoded voltage indicators can produce high spatial and temporal resolution, <1 ms and <1 μm [137–140]. Although the cyanine dyes are too slow to capture such single spatially localized events, we believe that the proposed VSD technology integrated with PA imaging promises to allow deep monitoring of brain activity patterns on the sub millimeter spatial scale and second timescale. Spatial resolution in PA imaging mainly depends on the frequency of ultrasound receiver and the focusing aperture size. For example, when the receiving ultrasound probe has center frequency of 10 MHz, the maximally expected resolution is 150 μm in theory. Potentially, 2-photon excitation could permit localized PA detection down to the μm scale. Pronounced electrical events such as seizure patterns should be readily imaged. Additionally, because the

slow VSDs effectively integrate electrical activity over space and time, spatiotemporal patterns in response to prolonged stimulus and neurotransmitter release should also be captured. Of course, the studies presented in this report represent the first generation of PA-VSDs with a simple excitation and detection scheme and are intended to demonstrate our design principles. We will use these principles to develop improved PA-VSDs that will capture faster and/or smaller electrical events.

We cannot be certain of the precise membrane polarization induced by valinomycin in our phantom study, because of some inevitable leakage permeability of the lipid vesicle membranes. Nonetheless, the valinomycin-induced membrane polarization has the upper estimate of -120 mV, which is derived from the 100-fold potassium gradient across the lipid vesicle membranes. From the given polarization, we achieved 24 and 49 of fractional changes in PA and fluorescence at, respectively, 3 and 9 μM PA-VSD. Therefore, the physiological membrane potential changes in the ranges of -20 to -100mV should be readily detectable. This sensitivity is considerably higher than the best fast VSD used for fluorescence monitoring of excitable cells and tissue [140]. Slow VSD mechanisms can, in general, produce much higher sensitivities than fast VSDs with $\Delta F/F$ as high as 500/100mV [132]; we therefore anticipate that we will be able improve the sensitivity of PA-VSDs much further by designing structures with optimized solubility and permeability.

Although the measured absorbance reduction and the fluorescence quenching represent two competing processes to control the magnitude of PA sensitivity, the effect

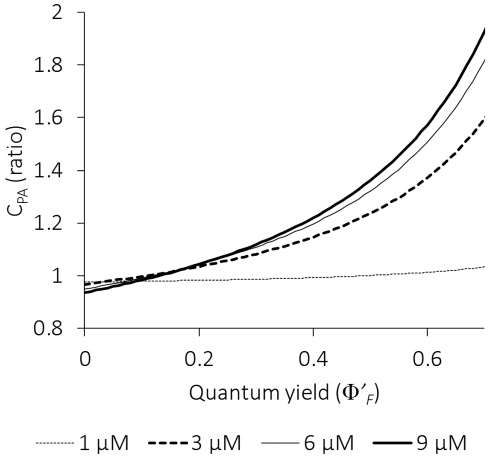

Figure 13.10: The theoretical PA signal change based on the absorbance change and fluorescence change from the experimental data.

of fluorescence quenching was dominant as observed in our experimental results (compare Figs 13.4(a) and 13.5(a)). In general, we would need to have measurements of the quantum efficiency Φ_F in each membrane state to be able to make quantitative prediction of the PA intensity change by applying the theoretical model derived in Eq 13.9. Based on this formulation, Fig. 13.10 shows the PA intensity enhancement for various PAVSD800-2 concentrations over a range of resting Φ_F, where the absorbance and the fluorescence change parameters were taken from the experimental measurement results. This graph demonstrates that the PA intensity change is indeed highly sensitive to the fluorescence quantum efficiency. The quenching effect outweighs the absorption reduction, and leads to PA intensity enhancement when the quantum yield is higher than around 0.1.

The derived theoretical model in Eq. 13.9 provides a quantitative tool to guide optimization of PA-VSD performance for potential applications in transcranial PA

and fluorescence imaging. This model indicates three directions to design a better fluorescence quenching based VSD; (1) higher fluorescence quenching effect, (2) less absorbance reduction or larger absorbance enhancement upon aggregation, and (3) higher fluorescence efficiency Φ_F. It might be counterintuitive that a higher Φ_F would produce a better PA intensity change, but the higher the baseline Φ_F is, the greater the opportunity for large quenching becomes, as more energy transfers into non-radioactive decay. Nevertheless, there should be further optimization between fractional contrast change of PA signals and its sensitivity, which may be lowered by the high Φ_F. Our future work will be focused on enhancing the balanced performance of PA-VSDs guided by the theoretical model.

A limitation of the current theoretical model is that the PA or fluorescence change is based on the assumption of a linear system with respect to the energy. However, some studies suggested that the PA intensity could be non-linearly related to the light energy under certain circumstances [141, 142]. Therefore, the theoretical model can be improved by including potential non-linear sensitivity of the VSD.

In addition to the dye features that would improve PA voltage sensitivity, other important dye attributes will also be needed to produce practical PA-VSDs for brain imaging. Such improvement might include: even longer wavelengths to further enhance deep tissue imaging; greater aqueous solubility to allow higher concentrations to be delivered to neuronal tissues; dyes with faster voltage-dependent redistribution kinetics to allow for sensing of activity down to the timescale of action potentials or

individual NT events. We believe the work described here provides both a theoretical and experimental proof of concept to allow us to further develop photo acoustics as a new modality for imaging electrical activity in the brain.

13.7 Conclusions

In this paper, we presented a PA based VSD, PAVSD800-2, as a potential tool to monitor membrane potential for brain imaging. The design principle of the dye is to manipulate fluorescence quantum yield to enhance PA intensity through voltage-dependent fluorescence quenching, while the total absorbance remains stable. We also derived the theoretical model to predict the PA intensity change based on known phot-physical dye characteristics. This model is experimentally validated, and the reciprocal relationship between PA and fluorescence was demonstrated for different dye concentrations.

Chapter 14

Conclusions

In this dissertation, I introduced enabling technologies and explored associated applications to broaden the impact of translational ultrasound/photoacoustic imaging. The goals of these technologies were; (1) to broaden the accessibility to photoacoustic imaging and demonstrate the translational applicability, (2) to make both ultrasound and photoacoustic imaging be more comprehensive and capable of imaging deep by incorporating co-robotic paradigm, and (3) to explore clinical and scientific applications through molecular photoacoustic imaging.

Along the goals given, three research topics were introduced in this thesis. Part I presented the enabling technique to maximize the access to photoacoustic imaging by using clinical ultrasound scanner and low-cost light source. Part II was the integration of robot with both ultrasound and photoacoustic imaging system through human robot cooperative control to overcome existing challenges in user-dependency and

image quality. Part III was the demonstration of translational photoacoustic imaging on brain imaging and cancer detection. Together, these parts explored the feasibility of co-robotic translational ultrasound and photoacoustic imaging.

Future works include the further refinement of the proposed systems. The SPARE algorithm will be merged to clinical ultrasound scanner for real-time visualization, and the potential of avoiding the usage of line trigger will be investigated to further extend the applicability. This dissertation demonstrated the feasibility of the co-robotic ultrasound system under limited motion and conditions. Therefore, the system performance should be evaluated more by appling more complicated trajectories and variable settings. Finally, these enabling technologies will be tested on the molecular PA imaging to validate the feasibility of low-cost high performance modality.

Appendix A

Technical Terms and Acronyms

1D: One Dimentional

2D: Two Dimensional

3D: Three Dimensional

BME: Biomedical Engineering

FL: Fluorescence

FOV: Field-of-View

IEEE: Institute of Electrical and Electronics Engineers

LCSR: Laboratory for Computational Sensing and Robotics

MAP: Multiple Active-Point

MRI: Magnetic Resonance Imaging

MUSIIC: Medical UltraSound Imaging and Intervention Collaboration

PA: Photoacoustic Imaging

APPENDIX A. TECHNICAL TERMS AND ACRONYMS

RF: Radio Frequency

PLD : Pulsed Laser Diode

ROI : Region of Interest

PRF: Pulse Repetition Frequency

PSA : Prostate-Specific Antigen

PSMA: Prostate-Specific Membrane Antigen

SNR: Signal-to-Noise Ratio

SPIE: Society of Photographic Instrumentation Engineers

STRATUS: Synthetic TRacked AperTure Ultrasound

TOF: Time of flight

TRUS: Transrectal Ultrasound

Appendix B

Supplemental information for Chapter 6

B.1 Tracking Systems and Ultrasound Calibration

Two rigid-body transformations are required to track an ultrasound image: a transformation from the tracking base to the tracking sensor, and a transformation from the tracking sensor to ultrasound image. Various tracking systems can be used to obtain the transformation from the tracking base to the tracking sensor, including electromagnetic (EM), optical, and mechanical tracking systems. EM tracking systems are based on the transmission of an EM field and the EM sensor localizing itself

within this field. The advantages of an EM tracking system are that no line of sight is required, and the sensor size can be small. The drawbacks are interference from ferromagnetic metals, wired EM sensors, and its limited tracking accuracy compared to other tracking systems [143]. Optical tracking systems are based on tracking fiducials or markers using single or multiple optical cameras. The accuracy is typically below 0.35 mm [144, 145], and this number is stable and lower than that of the electromagnetic tracker. The main problem for optical trackers is that line of sight is required. On the contrary, mechanical tracking systems consisting of mechanical linkages can also be used to for tracking. An example of an active mechanical tracking system is a robot arm, which tracks its end-effector or the end of its mechanical linkages. Robot arms have been reported to achieve precisions of 0.05 mm to 0.10 mm [146]. While a robot arm is generally more intrusive than EM or optical tracking systems, it is also able to resolve controlled motions.

The process to acquire the rigid-body transformation between the tracking sensor and the ultrasound image is known as ultrasound calibration, a variation of the classic hand-eye calibration problem [147]. Ultrasound calibration is a pre-operative procedure and would be conducted prior to STRATUS imaging. Many factors can easily affect its accuracy, and the design of calibration phantoms is one of the most important components. A point-based calibration phantom is a classic phantom used by many groups [148,149]. Since it is difficult to fix a single point in three-dimensional space, a cross-wire phantom or stylus phantom are used instead. Other than point-

based calibration, a Z-bar phantom [83] and wall phantom have also been proposed. The performance of ultrasound calibration largely depends on the ultrasound image quality and segmentation method. Point-based calibration is considered to be more accurate than other calibration methods because it is less dependent on image segmentation. The synthetic-aperture technique requires sub-wavelength localization accuracy to merge information from multiple poses, which is challenging to achieve in conventional ultrasound calibration. Therefore, a more accurate calibration technique is in demand.

B.2 Error Terms in Rigid-body Transformation

To express the error in a transformation matrix as a single metric, we defined the precision error expressing the extent of errors in both rotation and translation. Assuming a point location from a transformation coordinate F is p, then the point location from the world coordinate is

$$p_0 = Fp. \tag{B.1}$$

When error in F exists, the point location becomes

$$p_0^e = F\Delta F p. \tag{B.2}$$

The precision error was calculated in units of mm as the standard deviation of p_0^e for multiple F and p combinations, while the global point position p was fixed. To evaluate the contribution from rotational and translational components in ΔF to the precision error, we run a simulation based on Equation B.2.

In this simulation, three components in both rotation and translation were randomized. The rotational components were represented by its three Euler angles, and the translational components were represented by its three-dimensional vector. The norm of the three components in both rotation and translation was used as the input to the simulation to represent the extent of errors. The magnitude of the norm was varied in a range from 0 to 1 degree for rotation and from 0 to 1 mm for translation. Six components in rotation and translation were randomized 100 times, and the mean of 100 trials is shown as the value of the precision error. The result is shown in Fig. B.1. This result represents the magnitude of precision error when certain rotational and translational errors exists in a transformation.

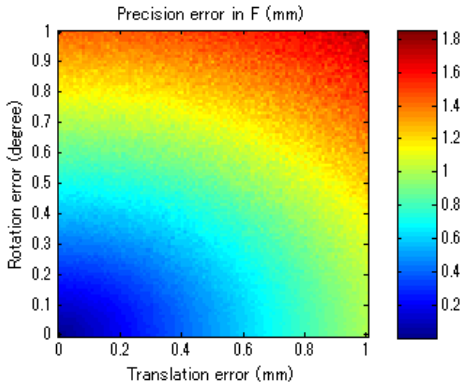

Figure B.1: The relationship between rotational and translational components to the overall precision error.

B.3 Error Propagation Analysis of BXp formulation

RP of a point can be regarded as an indirect way to guess the error in X, but RP is not entirely reliable because RP depends on the motions taken, and on the segmentation error in p. Thus, we conducted a mathematical analysis to derive the connection between the error in X, B and p to estimate the feasible error range of X in the experiment.

In a point-based calibration, a fixed point location po can be expressed as

$$p_0 = BXp, \tag{B.3}$$

$$p_0 = R_B R_X t_p + R_B t_p + t_B, \tag{B.4}$$

where R_B and R_X are the rotational component of the transformation B and X, respectively. t_p, t_X, and t_B are translational components of B and X, respectively; however, in reality, although p_0 is a constant number, BXp suffers from errors. Therefore, under the condition that BXP contains error, the realistic formation becomes

$$p_0 = R_B \Delta R_B R_X \Delta R_X (t_p + \Delta t_p) + R_B \Delta R_B (t_p + \Delta t_p) + t_B + \Delta t_B, \tag{B.5}$$

where Δ represents the error in the component. Rotations can be represented as $R = exp(\vec{n}\theta)$, where $\vec{n}$ is a unit vector for the axis of rotation and θ represents the magnitude. In this case, assuming the rotational error $\alpha = \vec{n}\theta$ stands, Taylors infinite series expansion gives us

$$\Delta(\alpha)\text{skew}(\alpha) \approx I + \text{skew}(\alpha), \tag{B.6}$$

where

$$\text{skew}(\alpha) = \begin{bmatrix} 0 & -\alpha_3 & \alpha_2 \\ \alpha_3 & 0 & -\alpha_1 \\ -\alpha_2 & \alpha_1 & 0 \end{bmatrix}. \tag{B.7}$$

Thus, Equation B.5 can be rewritten as

$$p_0 = R_B(I+\text{skew}(\beta))R_X(I+\text{skew}(\chi))(t_p+\Delta t_p)+R_B(I+\text{skew}(\beta))(t_X+\Delta t_X)+t_B+\Delta t_B. \tag{B.8}$$

Subtracting Equation B.6 from Equation B.4, and assuming that double skew term and multiplication with Δ term small enough to be negligible earns

$$0 = R_B\text{skew}(\beta R_X t_p + R_B R_X\text{skew}(\chi t_p + R_B R_X \delta t_p + R_B\text{skew}(\beta t_X + R_B \Delta t_X + \Delta t_B. \tag{B.9}$$

Rearranging Equation B.9 becomes

$$\begin{bmatrix} -R_B R_X\text{skew}(t_p)^T & -R_B \end{bmatrix} \begin{bmatrix} \chi \\ \Delta t_X \end{bmatrix} = \begin{bmatrix} R_B R_X\text{skew}(t_p)^T R_X^T + R_B\text{skew}(t_X)^T & I & R_B R_X \end{bmatrix} \begin{bmatrix} \beta \\ \Delta t_B \\ \Delta t_p \end{bmatrix}. \tag{B.10}$$

The rotational error χ can be computed by providing error matrix β, Δt_B, and Δt_p. In simulation, the following equation is used to considering realistic pose deter-

mination and corresponding behavior of X,

$$\begin{bmatrix} -R_B^1 R_X \text{skew}(t_p^1)^T & -R_B^1 \\ \vdots & \vdots \\ -R_B^n R_X \text{skew}(t_p^n)^T & -R_B^n \end{bmatrix} \begin{bmatrix} \chi \\ \Delta t_X \end{bmatrix}$$

$$= \begin{bmatrix} (R_B^1 R_X \text{skew}(t_p^1)^T R_X^T + R_B^1 \text{skew}(t_X)^T)\hat{\beta}^1 & \Delta\hat{t}_B^1 & R_B^1 R_X \Delta\hat{t}_p^1 \\ \vdots & \vdots & \\ (R_B^n R_X \text{skew}(t_p^n)^T R_X^T + R_B^1 \text{skew}(t_X)^T)\hat{\beta}^n & \Delta\hat{t}_B^n & R_B^n R_X \Delta\hat{t}_p^n \end{bmatrix} \begin{bmatrix} \|\beta\| \\ \|\Delta t_B\| \\ \|\Delta t_p\| \end{bmatrix}. \quad \text{(B.11)}$$

where n is the number of poses used in calibration, and $\hat{\beta}$, $\widehat{\Delta t_B}$, $\widehat{\Delta t_p}$ are unit vectors of β, respectively. Each pose contributes a single row in the data matrices on either side of Eqation B.11. For each pose, a different B and p will be provided, and the unit vector in β, Δt_B, and Δt_p also changes while its magnitude is fixed.

The rotational error variation in X was analyzed based on both the tracking system and the performance of calibration expressed as the segmentation error. Figure B.2 shows the result of the analytical simulation that describes the contribution of the precision in B and segmentation error to the final rotational component error in X. This result indicates that the segmentation error is less influential compared to the precision error in B for the same magnitude of error. The real segmentation error could be more sensitive to the error in X, because the segmentation error in simulation was chosen as a randomized distribution, and the random distribution could converge when a large number of poses were used. In reality, the segmentation error could be biased in a particular direction due to multiple physical reasons; incorrect speed of

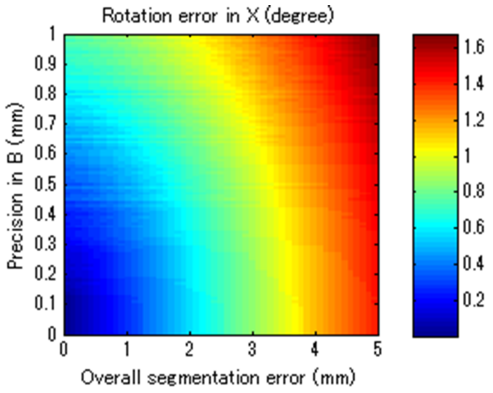

Figure B.2: Result of error propagation analysis based on BXp formulation.

sound estimation could cause error in the axial direction, and the lateral width of the point could be degraded because of the limited aperture size of ultrasound array transducer.

Appendix C

Supplemental information for Chapter 10

C.1 Recovering A using multiple active-point phantom involves 1 DOF deficiency

We will derive the proof that the solution of $AX = XB$ using multiple active points phantom has 1 DOF. Equations - can be rewritten as

$$\Delta A_i^T A^{ij*} \Delta A_j \Delta X X^* = \Delta X X^* B^{ij}. \tag{C.1}$$

Rearranging equation C.1 gives

$$(\Delta A_i \Delta X)^{-1} A^{ij*} (\Delta A_j \Delta X) X^* = X^* B^{ij}. \tag{C.2}$$

By defining $\Delta A_i^* = \Delta A_i \Delta X$ and $\Delta A_j^* = \Delta A_j \Delta X$,

$$\Delta A_i^{*-1} A^{ij*} \Delta A_j^* X^* = X^* B^{ij}. \tag{C.3}$$

This is another formulation binding A and B.

Equation C.1 is a case of Equations C.2 and C.3, when ΔX is identity matrix. When we have n poses, Equation C.2 contains $n+6$ unknown, in which n unknown in unknown rotation ΔA, and one DOF known is ΔX, and five DOF is X^*. However, as Equation C.3, we only can solve for $n+5$ DOF because unknown rotation ΔA and ΔX share the same rotation axis, and these will be solved as one DOF ΔA^*. Therefore, we miss the last one DOF to solve all $n+6$ unknowns.

C.2 Alternative Solution of Recovering A using Multiple Active-Point Phantom

Here, we will discuss the way of computing A from the channel data. The difference compared to previous approach is that instead of using the earliest arrival data, using entire wave form could provide more information to localize the point segmentation. The time-of-flight map of the segmented waveform will be obtained. Next,

using phantom point location and the corresponding distance (computed from time-of-flight), the position of ultrasound array element position from phantom coordinate can be calculated through trilateration.

Each ultrasound array element p_{US} can be computed by

$$p_{US} = \arg\min_{p_{US} \in R^3} \sum_{i=1} N||p^i_{ph} - {}^{ph}p_{US}|| - d^i, \tag{C.4}$$

where N is the number of phantom points and p_{ph} is the point position from the phantom frame.

The transformation of the ultrasound array from phantom coordinate to ultrasound image coordinate is computed through point cloud registration. Note that the recovered A is not fully true because the ultrasound array model is a line, and one DOF rotation is undefined.

$${}^{ph}p_{US} = A'^{US}p_{US}. \tag{C.5}$$

As from different poses can be computed through previous steps, but we need to know one fully defined A to solve X. When one of the pose is forcing the probe to capture the mid-plane of the active point, the unknown one DOF can be recovered as,

$$p_{ph} = -(R'_A \Delta R_A)^{-1} t_A, \tag{C.6}$$

where the elevational dimension of p_{ph} is zero.

Bibliography

[1] M. Xu and L. Wang, "Photoacoustic imaging in biomedicine," *Review of Scientific Instruments*, vol. 77, no. 4, 2006.

[2] S. Park, S. Aglyamov, and S. Emelianov, "Beamforming for photoacoustic imaging using linear array transducer," 2007, pp. 856–859.

[3] B. Yin, D. Xing, Y. Wang, Y. Zeng, Y. Tan, and Q. Chen, "Fast photoacoustic imaging system based on 320-element linear transducer array," *Physics in Medicine and Biology*, vol. 49, no. 7, pp. 1339–1346, 2004.

[4] C.-K. Liao, M.-L. Li, and P.-C. Li, "Optoacoustic imaging with synthetic aperture focusing and coherence weighting," *Optics Letters*, vol. 29, no. 21, pp. 2506–2508, 2004.

[5] R. Kolkman, P. Brands, W. Steenbergen, and T. Van Leeuwen, "Real-time in vivo photoacoustic and ultrasound imaging," *Journal of Biomedical Optics*, vol. 13, no. 5, 2008.

BIBLIOGRAPHY

[6] J. Niederhauser, M. Jaeger, and M. Frenz, "Comparison of laser-induced and classical ultrasound," vol. 4960, 2003, pp. 118–123.

[7] N. Kuo, H. Kang, D. Song, J. Kang, and E. Boctor, "Real-time photoacoustic imaging of prostate brachytherapy seeds using a clinical ultrasound system," *Journal of Biomedical Optics*, vol. 17, no. 6, 2012.

[8] H. Kang, "Software framework of a real-time pre-beamformed rf data acquisition of an ultrasound research scanner," *SPIE Medical Imaging 2012: Visualization, Image-Guided Procedures, and Modeling*, p. 8320, 2012.

[9] T. Harrison and R. Zemp, "The applicability of ultrasound dynamic receive beamformers to photoacoustic imaging," *IEEE Transactions on Ultrasonics, Ferroelectrics, and Frequency Control*, vol. 58, no. 10, pp. 2259–2263, 2011.

[10] C. Frazier and W. O'Brien Jr., "Synthetic aperture techniques with a virtual source element," *IEEE Transactions on Ultrasonics, Ferroelectrics, and Frequency Control*, vol. 45, no. 1, pp. 196–207, 1998.

[11] S. Nikolov and J. Jensen, "Virtual ultrasound sources in high-resolution ultrasound imaging," vol. 4687, 2002, pp. 395–405.

[12] J. Kortbek, J. Jensen, and K. Gammelmark, "Synthetic aperture sequential beamforming," 2008, pp. 966–969.

BIBLIOGRAPHY

[13] K. E. Thomenius, "Evolution of ultrasound beamformers," vol. 2, 1996, pp. 1615–1622.

[14] J. Jensen and N. Svendsen, "Calculation of pressure fields from arbitrarily shaped, apodized, and excited ultrasound transducers," *IEEE Transactions on Ultrasonics, Ferroelectrics, and Frequency Control*, vol. 39, no. 2, pp. 262–267, 1992.

[15] M. Lediju Bell, N. Kuo, D. Song, J. Kang, and E. Boctor, "In vivo visualization of prostate brachytherapy seeds with photoacoustic imaging," *Journal of Biomedical Optics*, vol. 19, no. 12, 2014.

[16] M. Bell, X. Guo, D. Song, and E. Boctor, "Transurethral light delivery for prostate photoacoustic imaging," *Journal of Biomedical Optics*, vol. 20, no. 3, 2015.

[17] L. Xi, G. Zhou, N. Gao, L. Yang, D. Gonzalo, S. Hughes, and H. Jiang, "Photoacoustic and fluorescence image-guided surgery using a multifunctional targeted nanoprobe," *Annals of Surgical Oncology*, vol. 21, no. 5, pp. 1602–1609, 2014.

[18] M. Lediju Bell, A. Ostrowski, K. Li, P. Kazanzides, and E. Boctor, "Localization of transcranial targets for photoacoustic-guided endonasal surgeries," *Photoacoustics*, vol. 3, no. 2, pp. 78–87, 2015.

[19] A. Cheng, H. Kang, H. Zhang, J. Kang, R. Taylor, and E. Boctor, "Ultra-

sound to video registration using a bi-plane transrectal probe with photoacoustic markers," vol. 9786, 2016.

[20] W. Xia, D. Nikitichev, J. Mari, S. West, R. Pratt, A. David, S. Ourselin, P. Beard, and A. Desjardins, "Performance characteristics of an interventional multispectral photoacoustic imaging system for guiding minimally invasive procedures," *Journal of Biomedical Optics*, vol. 20, no. 8, 2015.

[21] N. Dana, L. Di Biase, A. Natale, S. Emelianov, and R. Bouchard, "In vitro photoacoustic visualization of myocardial ablation lesions," *Heart Rhythm*, vol. 11, no. 1, pp. 150–157, 2014.

[22] M.-L. Li, H. Zhang, K. Maslov, G. Stoica, and L. Wang, "Improved in vivo photoacoustic microscopy based on a virtual-detector concept," *Optics Letters*, vol. 31, no. 4, pp. 474–476, 2006.

[23] Y. Tsunoi, S. Sato, R. Watanabe, S. Kawauchi, H. Ashida, and M. Terakawa, "Compact acoustic-resolution photoacoustic imaging system with fiber-based illumination," *Japanese Journal of Applied Physics*, vol. 53, no. 12, 2014.

[24] H. Zhang, K. Kondo, M. Yamakawa, and T. Shiina, "Coded excitation using periodic and unipolar m-sequences for photoacoustic imaging and flow measurement," *Optics Express*, vol. 24, no. 1, pp. 17–29, 2016.

[25] H. Zhang, X. Guo, H. Kang, and E. Boctor, "Photoacoustic reconstruction

using beamformed rf data: A synthetic aperture imaging approach," vol. 9323, 2015.

[26] J. Seabra and J. Sanches, "Modeling log-compressed ultrasound images for radio frequency signal recovery," 2008, pp. 426–429.

[27] R. Prager, A. Gee, G. Treece, and L. Berman, "Decompression and speckle detection for ultrasound images using the homodyned k-distribution," *Pattern Recognition Letters*, vol. 24, no. 4-5, pp. 705–713, 2003.

[28] A. Cheng, J. Kang, R. Taylor, and E. Boctor, "Direct three-dimensional ultrasound-to-video registration using photoacoustic markers," *Journal of Biomedical Optics*, vol. 18, no. 6, 2013.

[29] A. Smith, J. Wolf, G.-Y. Xie, and M. Smith, "Musculoskeletal pain in cardiac ultrasonographers: Results of a random survey," *Journal of the American Society of Echocardiography*, vol. 10, no. 4, pp. 357–362, 1997.

[30] A. Schoenfeld, J. Goverman, D. Weiss, and I. Meizner, "Transducer user syndrome: An occupational hazard of the ultrasonographer," *European Journal of Ultrasound*, vol. 10, no. 1, pp. 41–45, 1999.

[31] A. Priester, S. Natarajan, and M. Culjat, "Robotic ultrasound systems in medicine," *IEEE Transactions on Ultrasonics, Ferroelectrics, and Frequency Control*, vol. 60, no. 3, pp. 507–523, 2013.

[32] N. Koizumi, S. Warisawa, M. Nagoshi, H. Hashizume, and M. Mitsuishi, "Construction methodology for a remote ultrasound diagnostic system," *IEEE Transactions on Robotics*, vol. 25, no. 3, pp. 522–538, 2009.

[33] C. Hennersperger, B. Fuerst, S. Virga, O. Zettinig, B. Frisch, T. Neff, and N. Navab, "Towards mribased autonomous robotic us acquisitions: A first feasibility study," *IEEE Trans Med Imaging*, pp. 1–10, 2016.

[34] S. Salcudean, W. Zhu, P. Abolmaesumi, S. Bachmann, and P. Lawrence, "A robot system for medical ultrasound," *Robotics Research*, 2000.

[35] C. Zandsteeg, D. Bruijnen, and M. Van De Molengraft, "Haptic tele-operation system control design for the ultrasound task: A loop-shaping approach," *Mechatronics*, vol. 20, no. 7, pp. 767–777, 2010.

[36] K. Mathiassen, J. Fjellin, K. Glette, P. Hol, and O. Elle, "An ultrasound robotic system using the commercial robot ur5," *Frontiers Robot. AI*, vol. 3, no. 1, pp. 1–16, 2016.

[37] H. en, A. Cheng, K. Ding, E. Boctor, J. Wong, I. Iordachita, and P. Kazanzides, "Cooperative control with ultrasound guidance for radiation therapy," *Front Robot AI*, 2016.

[38] M. Balicki, A. Uneri, I. Iordachita, J. Handa, P. Gehlbach, and R. Taylor, "Micro-force sensing in robot assisted membrane peeling for vitreoretinal

surgery," *Lecture Notes in Computer Science (including subseries Lecture Notes in Artificial Intelligence and Lecture Notes in Bioinformatics)*, vol. 6363 LNCS, no. PART 3, pp. 303–310, 2010.

[39] X. He, M. Balicki, P. Gehlbach, J. Handa, R. Taylor, and I. Iordachita, "A multi-function force sensing instrument for variable admittance robot control in retinal microsurgery," 2014, pp. 1411–1418.

[40] G. Casiez, N. Roussel, and D. Vogel, "1 € filter: A simple speed-based low-pass filter for noisy input in interactive systems," in *Proceedings of the SIGCHI Conference on Human Factors in Computing Systems*, ser. CHI '12. New York, NY, USA: ACM, 2012, pp. 2527–2530.

[41] M. Gilbertson and B. Anthony, "An ergonomic, instrumented ultrasound probe for 6-axis force/torque measurement," *Conference proceedings : ... Annual International Conference of the IEEE Engineering in Medicine and Biology Society. IEEE Engineering in Medicine and Biology Society. Annual Conference*, vol. 2013, pp. 140–143, 2013.

[42] M. Li, A. Kapoor, and R. Taylor, "A constrained optimization approach to virtual fixtures," 2005, pp. 2924–2929.

[43] H. Zhang, A. Cheng, N. Bottenus, X. Guo, G. Trahey, and E. Boctor, "Synthetic tracked aperture ultrasound imaging: Design, simulation, and experimental evaluation," *Journal of Medical Imaging*, vol. 3, no. 2, 2016.

[44] H. Zhang, R. Finocchi, K. Apkarian, and E. Boctor, "Co-robotic synthetic tracked aperture ultrasound imaging with cross-correlation based dynamic error compensation and virtual fixture control," vol. 2016-November, 2016.

[45] H. Zhang, T. Fang, R. Finocchi, and E. Boctor, "High resolution three-dimensional robotic synthetic tracked aperture ultrasound imaging: Feasibility study," vol. 10139, 2017.

[46] J. Jensen, S. Nikolov, K. Gammelmark, and M. Pedersen, "Synthetic aperture ultrasound imaging," *Ultrasonics*, vol. 44, no. SUPPL., pp. e5–e15, 2006.

[47] L. Nock and G. Trahey, "Synthetic receive aperture imaging with phase correction for motion and for tissue inhomogeneitiespart i: Basic principles," *IEEE Transactions on Ultrasonics, Ferroelectrics, and Frequency Control*, vol. 39, no. 4, pp. 489–495, 1992.

[48] G. Trahey and L. Nock, "Synthetic receive aperture imaging with phase correction for motion and for tissue inhomogeneitiespart ii: Effects of and correction for motion," *IEEE Transactions on Ultrasonics, Ferroelectrics, and Frequency Control*, vol. 39, no. 4, pp. 496–501, 1992.

[49] H. Zhang, E. Ergun, G. Trahey, and E. Boctor, "Synthetic aperture ultrasound imaging with robotic aperture extension," vol. 9419, 2015.

[50] N. Bottenus, W. Long, H. Zhang, M. Jakovljevic, D. Bradway, E. Boctor, and

G. Trahey, "Feasibility of swept synthetic aperture ultrasound imaging," *IEEE Transactions on Medical Imaging*, vol. 35, no. 7, pp. 1676–1685, 2016.

[51] L. B. Rosenberg, "Virtual fixtures: perceptual tools for telerobotic manipulation," 1993, pp. 76–82.

[52] X. Guo, A. Cheng, H. Zhang, H.-J. Kang, R. Etienne-Cummings, and E. Boctor, "Active echo: a new paradigm for ultrasound calibration," *Medical image computing and computer-assisted intervention : MICCAI ... International Conference on Medical Image Computing and Computer-Assisted Intervention*, vol. 17, pp. 397–404, 2014.

[53] X. Guo, H.-J. Kang, R. Etienne-Cummings, and E. Boctor, "Active ultrasound pattern injection system (auspis) for interventional tool guidance," *PLoS ONE*, vol. 9, no. 10, 2014.

[54] P. Detmer, G. Bashein, T. Hodges, K. Beach, E. Filer, D. Burns, and D. Strandness Jr., "3d ultrasonic image feature localization based on magnetic scanhead tracking: In vitro calibration and validation," *Ultrasound in Medicine and Biology*, vol. 20, no. 9, pp. 923–936, 1994.

[55] C. Barry, C. Allott, N. John, P. Mellor, P. Arundel, D. Thomson, and J. Waterton, "Three-dimensional freehand ultrasound: Image reconstruction and volume analysis," *Ultrasound in Medicine and Biology*, vol. 23, no. 8, pp. 1209–1224, 1997.

[56] Q. Huang, Y. Zheng, M. Lu, and Z. Chi, "Development of a portable 3d ultrasound imaging system for musculoskeletal tissues," *Ultrasonics*, vol. 43, no. 3, pp. 153–163, 2005.

[57] A. Krupa, "Automatic calibration of a robotized 3d ultrasound imaging system by visual servoing," vol. 2006, 2006, pp. 4136–4141.

[58] M. Ackerman, A. Cheng, E. Boctor, and G. Chirikjian, "Online us sensor calibration using gradient descent on the euclidean group," *Robotics and automation (ICRA)*, p. 2014, 2014.

[59] G. Ameri, J. Baxter, A. McLeod, U. Jayaranthe, E. Chen, and T. Peters, "Synthetic aperture imaging in ultrasound calibration," vol. 9036, 2014.

[60] J. Den Buijs, H. Hansen, R. Lopata, C. De Korte, and S. Misra, "Predicting target displacements using ultrasound elastography and finite element modeling," *IEEE Transactions on Biomedical Engineering*, vol. 58, no. 11, pp. 3143–3155, 2011.

[61] C. Wachinger, W. Wein, and N. Navab, "Three-dimensional ultrasound mosaicing," *Lecture Notes in Computer Science (including subseries Lecture Notes in Artificial Intelligence and Lecture Notes in Bioinformatics)*, vol. 4792 LNCS, no. PART 2, pp. 327–335, 2007.

[62] P. Abolmaesumi, S. Salcudean, W.-H. Zhu, M. Sirouspour, and S. DiMaio,

"Image-guided control of a robot for medical ultrasound," *IEEE Transactions on Robotics and Automation*, vol. 18, no. 1, pp. 11–23, 2002.

[63] C. Kim, F. Schfer, D. Chang, D. Petrisor, M. Han, and D. Stoianovici, "Robot for ultrasound-guided prostate imaging and intervention," 2011, pp. 943–948.

[64] G. Michailidis, P. Papageorgiou, and D. Economides, "Assessment of fetal anatomy in the first trimester using two- and three-dimensional ultrasound," *British Journal of Radiology*, vol. 75, no. 891, pp. 215–219, 2002.

[65] B. Benoit and R. Chaoui, "Three-dimensional ultrasound with maximal mode rendering: A novel technique for the diagnosis of bilateral or unilateral absence or hypoplasia of nasal bones in second-trimester screening for down syndrome," *Ultrasound in Obstetrics and Gynecology*, vol. 25, no. 1, pp. 19–24, 2005.

[66] H. Neshat, D. Cool, K. Barker, L. Gardi, N. Kakani, and A. Fenster, "A 3d ultrasound scanning system for image guided liver interventions," *Medical Physics*, vol. 40, no. 11, 2013.

[67] S. Wojcinski, A. Farrokh, U. Hille, J. Wiskirchen, S. Gyapong, A. Soliman, F. Degenhardt, and P. Hillemanns, "The automated breast volume scanner (abvs): Initial experiences in lesion detection compared with conventional hand-held b-mode ultrasound: A pilot study of 50 cases," *International Journal of Women's Health*, vol. 3, no. 1, pp. 337–346, 2011.

[68] P. Skaane, R. Gullien, E. Eben, M. Sandhaug, R. Schulz-Wendtland, and F. Stoeblen, "Interpretation of automated breast ultrasound (abus) with and without knowledge of mammography: A reader performance study," *Acta Radiologica*, vol. 56, no. 4, pp. 404–412, 2015.

[69] S. Nikolov and J. Jensen, "3d synthetic aperture imaging using a virtual source element in the elevation plane," vol. 2, 2000, pp. 1743–1747.

[70] H. Andresen, S. Nikolov, M. Pedersen, D. Buckton, and J. Jensen, "Three-dimensional synthetic aperture focusing using a rocking convex array transducer," *IEEE Transactions on Ultrasonics, Ferroelectrics, and Frequency Control*, vol. 57, no. 5, pp. 1051–1063, 2010.

[71] H. Zhang, M. Bell, X. Guo, H. Kang, and E. Boctor, "Synthetic-aperture based photoacoustic re-beamforming (spare) approach using beamformed ultrasound data," *Biomedical Optics Express*, vol. 7, no. 8, pp. 3056–3069, 2016.

[72] H.-P. Brecht, R. Su, M. Fronheiser, S. Ermilov, A. Conjusteau, and A. Oraevsky, "Whole-body three-dimensional optoacoustic tomography system for small animals," *Journal of Biomedical Optics*, vol. 14, no. 6, 2009.

[73] L. Wang and S. Hu, "Photoacoustic tomography: In vivo imaging from organelles to organs," *Science*, vol. 335, no. 6075, pp. 1458–1462, 2012.

[74] R. Ma, A. Taruttis, V. Ntziachristos, and D. Razansky, "Multispectral op-

toacoustic tomography (msot) scanner for whole-body small animal imaging," *Optics Express*, vol. 17, no. 24, pp. 21 414–21 426, 2009.

[75] A. Polo, C. Salembier, J. Venselaar, and P. Hoskin, "Review of intraoperative imaging and planning techniques in permanent seed prostate brachytherapy," *Radiotherapy and Oncology*, vol. 94, no. 1, pp. 12–23, 2010.

[76] Y.-H. Wang and P.-C. Li, "Ultrafast photoacoustic imaging and its application to real-time 3d imaging with improved focusing," *Ultrasonic Imaging*, vol. 33, no. 3, pp. 189–196, 2011.

[77] L. Wang, "Multiscale photoacoustic microscopy and computed tomography," *Nature Photonics*, vol. 3, no. 9, pp. 503–509, 2009.

[78] Y. Okumura, B. D. Henz, S. B. Johnson, T. J. Bunch, C. J. OBrien, D. O. Hodge, A. Altman, A. Govari, and D. L. Packer, "Three-dimensional ultrasound for image-guided mapping and intervention," *Circulation: Arrhythmia and Electrophysiology*, vol. 1, no. 2, pp. 110–119, 2008.

[79] Y. Hu, H. U. Ahmed, Z. Taylor, C. Allen, M. Emberton, D. Hawkes, and D. Barratt, "Mr to ultrasound registration for image-guided prostate interventions," *Medical image analysis*, vol. 16, no. 3, pp. 687–703, 2012.

[80] E. L. Melvær, K. Mørken, and E. Samset, "A motion constrained cross-wire

phantom for tracked 2d ultrasound calibration," *International journal of computer assisted radiology and surgery*, vol. 7, no. 4, pp. 611–620, 2012.

[81] P.-W. Hsu, G. M. Treece, R. W. Prager, N. E. Houghton, and A. H. Gee, "Comparison of freehand 3-d ultrasound calibration techniques using a stylus," *Ultrasound in medicine & biology*, vol. 34, no. 10, pp. 1610–1621, 2008.

[82] J. W. Trobaugh, D. J. Trobaugh, and W. D. Richard, "Three-dimensional imaging with stereotactic ultrasonography," *Computerized Medical Imaging and Graphics*, vol. 18, no. 5, pp. 315–323, 1994.

[83] E. Boctor, A. Viswanathan, M. Choti, R. Taylor, G. Fichtinger, and G. Hager, "A novel closed form solution for ultrasound calibration," vol. 1, 2004, pp. 527–530.

[84] F. Aalamifar, A. Cheng, Y. Kim, X. Hu, H. Zhang, X. Guo, and E. Boctor, "Robot-assisted automatic ultrasound calibration," *International Journal of Computer Assisted Radiology and Surgery*, pp. 1–9, 2016.

[85] H. H. Chen, "A screw motion approach to uniqueness analysis of head-eye geometry," in *Computer Vision and Pattern Recognition, 1991. Proceedings CVPR'91., IEEE Computer Society Conference on.* IEEE, 1991, pp. 145–151.

[86] F. C. Park and B. J. Martin, "Robot sensor calibration: solving ax= xb on

the euclidean group," *IEEE Transactions on Robotics and Automation*, vol. 10, no. 5, pp. 717–721, 1994.

[87] M. K. Ackerman, A. Cheng, B. Shiffman, E. Boctor, and G. Chirikjian, "Sensor calibration with unknown correspondence: Solving ax= xb using euclidean-group invariants," in *Intelligent Robots and Systems (IROS), 2013 IEEE/RSJ International Conference on*. IEEE, 2013, pp. 1308–1313.

[88] K. S. Arun, T. S. Huang, and S. D. Blostein, "Least-squares fitting of two 3-d point sets," *IEEE Transactions on pattern analysis and machine intelligence*, no. 5, pp. 698–700, 1987.

[89] R. Køster-Rasmussen, A. Korshin, and C. N. Meyer, "Antibiotic treatment delay and outcome in acute bacterial meningitis," *Journal of Infection*, vol. 57, no. 6, pp. 449–454, 2008.

[90] C. Armon and R. Evans, "Addendum to assessment: Prevention of post-lumbar puncture headaches: Report of the therapeutics and technology assessment subcommittee of the american academy of neurology," *Neurology*, vol. 65, no. 4, pp. 510–512, 2005.

[91] R. Carroll, *Risk management handbook for health care organizations*. John Wiley & Sons, 2009, vol. 30.

[92] C. Edwards, E. Leira, and P. Gonzalez-Alegre, "Residency training: A failed

lumbar puncture is more about obesity than lack of ability," *Neurology*, vol. 84, no. 10, pp. e69–e72, 2015.

[93] K. Shah, K. Richard, S. Nicholas, and J. Edlow, "Incidence of traumatic lumbar puncture," *Academic Emergency Medicine*, vol. 10, no. 2, pp. 151–154, 2003.

[94] S. Ahmed, C. Jayawarna, and E. Jude, "Post lumbar puncture headache: Diagnosis and management," *Postgraduate Medical Journal*, vol. 82, no. 973, pp. 713–716, 2006.

[95] F. Shaikh, J. Brzezinski, S. Alexander, C. Arzola, J. Carvalho, J. Beyene, and L. Sung, "Ultrasound imaging for lumbar punctures and epidural catheterisations: Systematic review and meta-analysis," *BMJ (Online)*, vol. 346, no. 7902, 2013.

[96] A. Brook, J. Burns, E. Dauer, A. Schoendfeld, and T. Miller, "Comparison of ct and fluoroscopic guidance for lumbar puncture in an obese population with prior failed unguided attempt," *Journal of NeuroInterventional Surgery*, pp. 323–327, 2013.

[97] T. Engedal, H. rding, and O. Vilholm, "Changing the needle for lumbar punctures: Results from a prospective study," *Clinical Neurology and Neurosurgery*, vol. 130, pp. 74–79, 2015.

[98] T. Ungi, P. Abolmaesumi, R. Jalal, M. Welch, I. Ayukawa, S. Nagpal, A. Lasso,

M. Jaeger, D. Borschneck, G. Fichtinger, and P. Mousavi, "Spinal needle navigation by tracked ultrasound snapshots," *IEEE Transactions on Biomedical Engineering*, vol. 59, no. 10, pp. 2766–2772, 2012.

[99] J. Moore, C. Clarke, D. Bainbridge, C. Wedlake, A. Wiles, D. Pace, and T. Peters, "Image guidance for spinal facet injections using tracked ultrasound." *Medical image computing and computer-assisted intervention : MICCAI ... International Conference on Medical Image Computing and Computer-Assisted Intervention*, vol. 12, no. Pt 1, pp. 516–523, 2009.

[100] E. Chen, P. Mousavi, S. Gill, G. Fichtinger, and P. Abolmaesumi, "Ultrasound guided spine needle insertion," *Proc. SPIE*, vol. 7625, p. 762538, 2010.

[101] M. Najafi, P. Abolmaesumi, and R. Rohling, "Single-camera closed-form real-time needle tracking for ultrasound-guided needle insertion," *Ultrasound in Medicine and Biology*, vol. 41, no. 10, pp. 2663–2676, 2015.

[102] X. Wang, P. Stolka, E. Boctor, G. Hager, and M. Choti, "The kinect as an interventional tracking system," vol. 8316, 2012.

[103] S. Nagpal, P. Abolmaesumi, A. Rasoulian, I. Hacihaliloglu, T. Ungi, J. Osborn, V. Lessoway, J. Rudan, M. Jaeger, R. Rohling, D. Borschneck, and P. Mousavi, "A multi-vertebrae ct to us registration of the lumbar spine in clinical data," *International Journal of Computer Assisted Radiology and Surgery*, vol. 10, no. 9, pp. 1371–1381, 2015.

[104] J. Gadsden, M. Latmore, and D. M. Levine, "Evaluation of the ezono 4000 with ezguide for ultrasound-guided procedures," *Expert Review of Medical Devices*, vol. 12, no. 3, pp. 251–261, 2015.

[105] P. J. Stolka, P. Foroughi, M. Rendina, C. R. Weiss, G. D. Hager, and E. M. Boctor, "Needle guidance using handheld stereo vision and projection for ultrasound-based interventions." in *MICCAI (2)*, 2014, pp. 684–691.

[106] H. K. Chiang, Q. Zhou, M. S. Mandell, M.-Y. Tsou, S.-P. Lin, K. K. Shung, and C.-K. Ting, "Eyes in the needlenovel epidural needle with embedded high-frequency ultrasound transducerepidural access in porcine model," *The Journal of the American Society of Anesthesiologists*, vol. 114, no. 6, pp. 1320–1324, 2011.

[107] P.-Y. Lee, C.-C. Huang, and H. K. Chiang, "Implementation of a novel high frequency ultrasound device for guiding epidural anesthesia-in vivo animal study," in *Ultrasonics Symposium (IUS), 2013 IEEE International*. IEEE, 2013, pp. 2049–2052.

[108] Y. Kim, X. Guo, and E. Boctor, "New platform for evaluating ultrasound-guided interventional technologies," vol. 9790, 2016.

[109] E. A. Prince and S. H. Ahn, "Basic vascular neuroanatomy of the brain and spine: what the general interventional radiologist needs to know," in *Seminars*

in interventional radiology, vol. 30, no. 03. Thieme Medical Publishers, 2013, pp. 234–239.

[110] R. L. Siegel, K. D. Miller, and A. Jemal, "Cancer statistics, 2016," *CA: a cancer journal for clinicians*, vol. 66, no. 1, pp. 7–30, 2016.

[111] V. T. Devita Jr, T. Lawrence, and S. A. Rosenberg, *Cancer: Principles & Practice of Oncology: Annual Advances in Oncology*. Lippincott Williams & Wilkins, 2012.

[112] J. A. Webb, K. Shanmuganathan, and A. McLEAN, "Complications of ultrasound-guided transperineal prostate biopsy a prospective study," *BJU International*, vol. 72, no. 5, pp. 775–777, 1993.

[113] X. Huang, M. Bennett, and P. E. Thorpe, "Anti-tumor effects and lack of side effects in mice of an immunotoxin directed against human and mouse prostate-specific membrane antigen," *The Prostate*, vol. 61, no. 1, pp. 1–11, 2004.

[114] N. Schülke, O. A. Varlamova, G. P. Donovan, D. Ma, J. P. Gardner, D. M. Morrissey, R. R. Arrigale, C. Zhan, A. J. Chodera, K. G. Surowitz *et al.*, "The homodimer of prostate-specific membrane antigen is a functional target for cancer therapy," *Proceedings of the National Academy of Sciences*, vol. 100, no. 22, pp. 12 590–12 595, 2003.

[115] H. Liu, P. Moy, S. Kim, Y. Xia, A. Rajasekaran, V. Navarro, B. Knudsen, and

N. H. Bander, "Monoclonal antibodies to the extracellular domain of prostate-specific membrane antigen also react with tumor vascular endothelium," *Cancer research*, vol. 57, no. 17, pp. 3629–3634, 1997.

[116] S. S. Chang, V. E. Reuter, W. Heston, N. H. Bander, L. S. Grauer, and P. B. Gaudin, "Five different anti-prostate-specific membrane antigen (psma) antibodies confirm psma expression in tumor-associated neovasculature," *Cancer research*, vol. 59, no. 13, pp. 3192–3198, 1999.

[117] S. Perner, M. D. Hofer, R. Kim, R. B. Shah, H. Li, P. Möller, R. E. Hautmann, J. E. Gschwend, R. Kuefer, and M. A. Rubin, "Prostate-specific membrane antigen expression as a predictor of prostate cancer progression," *Human pathology*, vol. 38, no. 5, pp. 696–701, 2007.

[118] V. Dogra, B. Chinni, S. Singh, H. Schmitthenner, N. Rao, J. J. Krolewski, and K. L. Nastiuk, "Photoacoustic imaging with an acoustic lens detects prostate cancer cells labeled with psma-targeting near-infrared dye-conjugates," *Journal of biomedical optics*, vol. 21, no. 6, pp. 066 019–066 019, 2016.

[119] Y. Chen, S. Dhara, S. R. Banerjee, Y. Byun, M. Pullambhatla, R. C. Mease, and M. G. Pomper, "A low molecular weight psma-based fluorescent imaging agent for cancer," *Biochemical and biophysical research communications*, vol. 390, no. 3, pp. 624–629, 2009.

[120] S. Prahl *et al.*, "Optical absorption of hemoglobin," 1999.

[121] M. Canepari, O. Bernus, and D. Zecevic, "Membrane potential imaging in the nervous system and heart," *Springer Cham.*, vol. 516, 2015.

[122] S. Hu, "Listening to the brain with photoacoustics," *IEEE Journal on Selected Topics in Quantum Electronics*, vol. 22, no. 3, 2016.

[123] M. Nasiriavanaki, J. Xia, H. Wan, A. Bauer, J. Culver, and L. Wang, "High-resolution photoacoustic tomography of resting-state functional connectivity in the mouse brain," *Proceedings of the National Academy of Sciences of the United States of America*, vol. 111, no. 1, pp. 21–26, 2014.

[124] J. Yao and L. Wang, "Photoacoustic brain imaging: From microscopic to macroscopic scales," *Neurophotonics*, vol. 1, no. 1, 2014.

[125] O. Arthurs and S. Boniface, "How well do we understand the neural origins of the fmri bold signal?" *Trends in Neurosciences*, vol. 25, no. 1, pp. 27–31, 2002.

[126] O. Arthurs, T. Donovan, D. Spiegelhalter, J. Pickard, and S. Boniface, "Intracortically distributed neurovascular coupling relationships within and between human somatosensory cortices," *Cerebral Cortex*, vol. 17, no. 3, pp. 661–668, 2007.

[127] J. Weber, P. Beard, and S. Bohndiek, "Contrast agents for molecular photoacoustic imaging," *Nature Methods*, vol. 13, no. 8, pp. 639–650, 2016.

[128] D. Wu, L. Huang, M. Jiang, and H. Jiang, "Contrast agents for photoacoustic

and thermoacoustic imaging: A review," *International Journal of Molecular Sciences*, vol. 15, no. 12, pp. 23 616–23 639, 2014.

[129] G. Luke, D. Yeager, and S. Emelianov, "Biomedical applications of photoacoustic imaging with exogenous contrast agents," *Annals of Biomedical Engineering*, vol. 40, no. 2, pp. 422–437, 2012.

[130] H. Qin, T. Zhou, S. Yang, and D. Xing, "Fluorescence quenching nanoprobes dedicated to in vivo photoacoustic imaging and high-efficient tumor therapy in deep-seated tissue," *Small*, vol. 11, no. 22, pp. 2675–2686, 2015.

[131] P. Sims, A. Waggoner, C.-H. Wang, and J. Hoffman, "Mechanism by which cyanine dyes measure membrane potential in red blood cells and phosphatidylcholine vesicles," *Biochemistry*, vol. 13, no. 16, pp. 3315–3330, 1974.

[132] L. Loew, L. Benson, P. Lazarovici, and I. Rosenberg, "Fluorometric analysis of transferable membrane pores," *Biochemistry*, vol. 24, no. 9, pp. 2101–2104, 1985.

[133] S. H. Sinha, E. A. Owens, Y. Feng, Y. Yang, Y. Xie, Y. Tu, M. Henary, and Y. G. Zheng, "Synthesis and evaluation of carbocyanine dyes as prmt inhibitors and imaging agents," *European journal of medicinal chemistry*, vol. 54, pp. 647–659, 2012.

[134] R. B. Mujumdar, L. A. Ernst, S. R. Mujumdar, C. J. Lewis, and A. S. Wag-

goner, "Cyanine dye labeling reagents: sulfoindocyanine succinimidyl esters," *Bioconjugate chemistry*, vol. 4, no. 2, pp. 105–111, 1993.

[135] E. McArthur, J. Godbe, D. Tice, and E. Weiss, "A study of the binding of cyanine dyes to colloidal quantum dots using spectral signatures of dye aggregation," *Journal of Physical Chemistry C*, vol. 116, no. 10, pp. 6136–6142, 2012.

[136] L. M. Loew, "Design and use of organic voltage sensitive dyes," in *Membrane Potential Imaging in the Nervous System and Heart*. Springer, 2015, pp. 27–53.

[137] C. D. Acker, P. Yan, and L. M. Loew, "Single-voxel recording of voltage transients in dendritic spines," *Biophysical journal*, vol. 101, no. 2, pp. L11–L13, 2011.

[138] C. D. Acker, E. Hoyos, and L. M. Loew, "Epsps measured in proximal dendritic spines of cortical pyramidal neurons," *Eneuro*, vol. 3, no. 2, pp. ENEURO–0050, 2016.

[139] W. Akemann, M. Sasaki, H. Mutoh, T. Imamura, N. Honkura, and T. Knpfel, "Two-photon voltage imaging using a genetically encoded voltage indicator," *Scientific reports*, vol. 3, 2013.

[140] P. Yan, C. Acker, W.-L. Zhou, P. Lee, C. Bollensdorff, A. Negreane, J. Lotti, L. Sacconi, S. Antic, P. Kohl, H. Mansvelder, F. Pavone, and L. Loew, "Palette

of fluorinated voltage-sensitive hemicyanine dyes," *Proceedings of the National Academy of Sciences of the United States of America*, vol. 109, no. 50, pp. 20 443–20 448, 2012.

[141] H. Chen and G. Diebold, "Chemical generation of acoustic waves: A giant photoacoustic effect," *Science*, vol. 270, no. 5238, pp. 963–966, 1995.

[142] M. Sarimollaoglu, D. Nedosekin, Y. Menyaev, M. Juratli, and V. Zharov, "Nonlinear photoacoustic signal amplification from single targets in absorption background," *Photoacoustics*, vol. 2, no. 1, pp. 1–11, 2014.

[143] J. Hummel, M. Figl, W. Birkfellner, M. Bax, R. Shahidi, C. Maurer Jr., and H. Bergmann, "Evaluation of a new electromagnetic tracking system using a standardized assessment protocol," *Physics in Medicine and Biology*, vol. 51, no. 10, pp. N205–N210, 2006.

[144] R. Elfring, M. De La Fuente, and K. Radermacher, "Assessment of optical localizer accuracy for computer aided surgery systems," *Computer Aided Surgery*, vol. 15, no. 1-3, pp. 1–12, 2010.

[145] A. Wiles, D. Thompson, and D. Frantz, "Accuracy assessment and interpretation for optical tracking systems," vol. 5367, 2004, pp. 421–432.

[146] L. Morten, "Automatic robot joint offset calibration," *Int. Workshop of Advanced Manufacturing and Automation*, 2012.

[147] R. Tsai, "A new technique for fully autonomous and efficient 3d robotics hand/eye calibration," *IEEE Transactions on Robotics and Automation*, vol. 5, no. 3, pp. 345–358, 1989.

[148] L. Mercier, T. Lang, F. Lindseth, and L. Collins, "A review of calibration techniques for freehand 3-d ultrasound systems," *Ultrasound in Medicine and Biology*, vol. 31, no. 2, pp. 143–165, 2005.

[149] P.-W. Hsu, R. Prager, A. Gee, and G. Treece, *Freehand 3D ultrasound calibration: A review*, 2009.

Vita

Haichong "Kai" Zhang was born in China, and raised in Japan. He received a B.S. and M.S. in Human Health Sciences (Laboratory Science) from Kyoto University, Japan in 2011 and 2013, respectively. After completing his master degree, he joined the Ph.D. program at The Johns Hopkins University, and received M.S. in Computer Science in 2015. His research interests include medical imaging related to medical ultrasound, robotics, photoacoustics. In one main research thrust, he aims to create a paradigm shift on ultrasonography by achieving high resolution deep-tissue imaging. Diagnostic ultrasound is notoriously known of having limited clinical value for obese patients, as imaging lacks needed resolution at profound depth. His innovative robotic ultrasound imaging approach will remove this hurdle. He developed synthetic-tracked aperture ultrasound (STRATUS) imaging, in which image quality and field-of-view can be substantially improved by utilizing the information from a human-robot cooperative scanning. He has also been developing photoacoustic imaging, which is a hybrid imaging approach combining sound and light, to achieve molecular contrast visualization toward disease-specific precision medicine. His synthetic

aperture-based photoacoustic re-beamforming (SPARE) algorithm enables photoacoustic imaging using incorrectly beamformed data from clinical ultrasound scanners. He has also involved in projects developing molecular PA agents for brain and cancer imaging applications.